Development of a Tracking Detector and Kinematic Reconstruction Methods for the Electron-Ion Collider

By

Stephen Maple

A thesis submitted to the University of Birmingham for the degree of
DOCTOR OF PHILOSOPHY

School of Physics and Astronomy
College of Engineering and Physical Sciences
University of Birmingham
United Kingdom
July 2024

Abstract

The Electron-Ion Collider (EIC) is a future facility that will be constructed at Brookhaven National Laboratory (BNL) over the next decade, to begin data-taking in the early 2030s.

Studies performed for the optimisation of the tracking system of ePIC, the EIC project detector, are presented. The EIC physics programme places stringent requirements on the tracking system, which must be high precision, low mass and well integrated. Simulations are performed for various tracking geometries, which are implemented in Geant4-based frameworks with varying levels of realism for the geometry and reconstruction, and the performance is evaluated. The design of the tracking system has been iteratively updated in line with such performance studies and projections of the technology, which inform the current ePIC tracking design. It is found that in order to achieve the EIC physics goals with the 1.7 T solenoidal magnetic field to be used in ePIC, large area tracking layers built using high precision and low mass monolithic silicon sensors are required. The performance targets are challenging to meet in the endcap trackers for a 1.7 T field, and so a combination of measurements from the tracking and calorimetry systems will be required.

An accurate reconstruction of the kinematic variables x, y, and Q^2 is essential for the EIC inclusive physics programme. The ability of the ePIC detector to reconstruct the kinematic variables is studied, and the resolutions of the methods optimised throughout the phase space. Conventional reconstruction methods usually rely on two of the four measured quantities (energy and polar angle of the scattered electron and hadronic final state). A novel reconstruction method is presented whereby the kinematic variables, and the energy of possible initial state photon radiation, are reconstructed through a kinematic fit of all measured quantities in a Bayesian framework using informative priors. The method is validated for smeared generated DIS events, fully simulated ePIC events, and is also applied to simulations and data from the H1 experiment at the HERA collider.

Acknowledgements

I could not have made it to this point in my personal and academic life without the help of many people. I owe you all a debt of gratitude, and in the case of the SLC, a debt of money. Words cannot (and to avoid excessive acknowledgements, will not) express my appreciation for all of you. I hereby extend my thanks to all who are not named explicitly, I'll thank you properly in the next thesis.

It is only natural to begin by thanking my supervisors, Laura Gonella and Paul Newman - through your efforts I have achieved far more than I could have imagined when starting out on my PhD journey. Thanks to Paul for your encouragement, and all the interesting opportunities. Laura, you did your job too well, and it seems that the Groundhog PhD must come to an end. I also wish to thank Peter Jones for all of his work for the UK EIC effort. Thanks also to my BILPA compatriots, for their informative discussions and helpful advice. The BlueBEAR High Performance Computing facility has my thanks for all the CPUs and storage space, you'd be a 10/10 supercomputer if you'd just let me access CVMFS.

To all of the PhD students who I've had the good fortune to share E318 with, you played a key role in making the PhD a fun time of my life, thanks for the company and for supplying me with many anecdotes. A special mention goes to Mark, Chris, and Kiran, for their company during (more than) occasional multi-hour lunch breaks.

Life, of course, goes on outside of the office: to Driff lot and 662, your friendship is appreciated, someday I'll explain what I've been doing all this time. To Abigael, thank you for your patience, support, and for sticking by me. Finally, none of this would have been possible if not for my parents, who have supported and encouraged me at every stage of my life.

Declaration

The results presented in this thesis are direct outcomes of my own work. However, the studies conducted for this thesis would not have been possible without the efforts of many people, over many years of development for the EIC project. Figures shown in this thesis were either produced myself, or taken from publicly available resources, in which case this is noted in the figure caption.

Several software tools that are not specific to the EIC were used as part of this work, and so I acknowledge the authors and developers of:

- The ROOT data analysis framework
- The Pythia6, Pythia8, and Djangoh monte carlo event generators
- The Geant4, Fun4All, and DD4hep frameworks for detector simulation
- The Bayesian Analysis Toolkit (BAT)

In Chapter 2, a theoretical background of Deep Inelastic Scattering is presented, and draws from several textbooks and articles, but most notably from "Deep Inelastic Scattering" by R. Devenish and A. Cooper-Sarkar, and "Quarks and Leptons: An Introductory Course in Modern Particle Physics" by F. Halzen and A. Martin.

Chapter 3 gives an overview of the ePIC detector, and shows performance plots that were produced by relevant subgroups within the ePIC collaboration. The description of track reconstruction is informed by the documentation created by the ACTS authors.

Chapter 4 covers simulation studies that were performed as part of the geometry optimisation leading up to the current ePIC tracking detector. Multiple tools were used for simulation and reconstruction in these studies. The starting point for Fun4All studies was the implementation of two Yellow Report tracking detector layouts, which I inherited from a former PhD student, H. Wennlöf. The implementations of

subsequent detector models for ATHENA in Fun4All were my own. The "reference detector" description in Fun4All was created by ECCE members, and modifications made for subsequent studies were my own. The model of the ePIC tracker in the official ePIC software was implemented by members of the ePIC Software Working Group, as was the seed finder used in the realistic seeding studies. All simulations in this chapter, that used either Fun4All or the ePIC software, were performed myself. Radiation maps of the fluence and dose expected in the full detector were produced for separate background sources by members of the ePIC Background Task Force, with my contribution being the processing of these maps such that the integrated dose and fluence from all sources in the region of the silicon tracker is obtained.

Kinematic resolutions at the EIC are first assessed in Chapter 5. The simulated events used in these studies were generated, propagated through the detector, and reconstructed as part of simulation campaigns ran by the ePIC Software Working Group. All analysis and plotting scripts were my own, other than the plotting script used for Fig. 5.7, which was adapted from a script given to me by B. Schmookler.

The reconstruction of DIS events with a kinematic fit in Chapter 6 builds on the work of R. Aggarwal and A. Caldwell, who were the first to study this method using BAT. The kinematic fit studied in Chapter 6 draws inspiration from these studies, but was implemented in BAT and expanded on by myself. Any work requiring either H1 data or MC would not have been possible without the many members of the H1 collaboration who contributed to the design, construction, and operation of the H1 detector. The event selection and analysis code used in the H1 studies was adapted from code used in an H1 event shapes analysis, with the aid of D. Britzger.

Table of Contents

List of Figures

List of Tables

Chapter 1

Introduction

The Electon-Ion Collider (EIC) is a large scale particle accelerator facility which is to be located at Brookhaven National Laboratory in the United States, based on the existing Relativistic Heavy Ion Collider (RHIC) complex. Construction is to commence following the conclusion of RHIC operations in the mid 2020s, with the intention to begin operations and science in the early 2030s. The EIC will study the properties of protons, neutrons, and atomic nuclei with unprecedented precision, variety, and luminosity. The EIC will be capable of colliding beams of polarised electrons with heavy ions, as well as polarised protons and light nuclei, across a large range of centre-of-mass energies, all with high luminosity. To maximise the physics potential of the EIC, a detector that provides the best possible acceptance, resolution, and particle identification capabilities is required. Further to this, analysis techniques that take full advantage of the detector information to facilitate a high quality reconstruction are also necessary.

1.1 Scattering Experiments for Hadron Structure

Modern understanding of the structure of matter at a subatomic level is informed by measurements involving the scattering of charged particles on nuclei. This technique was pioneered by Rutherford, Geiger, and Marsden in their famous 1911 experiment in which α particles were scattered by a gold foil, ultimately leading to the discovery of the atomic nucleus [1]. More recently, electrons have become a typical probe for scattering experiments, given their ease of production and acceleration, point-like nature, and the electroweak interactions involved in their scattering being well understood and calculable.

Hofstadter and colleagues made extensive use of electron scattering in the 1950s and

60s to determine the charge distributions of protons and nuclei and thus measured their radii [2]. In stark contrast to the elastic form factors that were measured during this time, early results with the 20 GeV electron beam at the Stanford Linear Accelerator Center (SLAC) in 1968, found little variation in the structure functions for the area of parameter space under study. This provided the first evidence of a point-like internal structure of nucleons [3]. This internal structure can only be resolved when the wavelength of the electron is sufficiently small that it probes deep inside the hadron target, which subsequently breaks up to give a many particle final state. This interaction is therefore termed Deep Inelastic Scattering (DIS). The experiments performed at SLAC made the first measurements of proton structure functions, as well as providing evidence for Bjorken scaling [4] and the Callan-Gross relation [5]. Experiments using electron beams and unpolarised targets continued at SLAC up to the early 1990s. Further experiments and collaborations were established in this time, such as the European Muon Collaboration (EMC) which probed targets using muon beams from the SPS at CERN [6], and the CCFR experiment at Fermilab, which used a beam of mixed ν_μ and $\bar{\nu}_\mu$ on a Beryllium-Oxide target [7].

The aforementioned experiments were all fixed-target scattering experiments, in which the struck nuclei were stationary in the lab-frame as part of a foil, gas, or liquid. The accessible parameter space depends largely on the centre-of-mass energy, so that the larger centre-of-mass energy possible at a collider experiment is desirable. To date, the only electron-proton collider to have existed was the **H**adron-**E**lectron-**R**ing**a**nlage (HERA) facility at the Deutsches Elektronen Synchrotron (DESY) research centre in Hamburg, which operated from 1992 to 2007. HERA was instrumented by two general purpose detectors, H1 and ZEUS, which recorded $e^{\pm}p$ collisions at centre-of-mass energies of up to 318 GeV, enabling proton structure to be studied in a much wider kinematic range than ever before. The two remaining interaction regions at HERA were instrumented by the HERMES and HERA-B detectors, which were respectively used to study the spin structure of nuclei, and CP violation in the decays of mesons containing heavy quarks. During its operation, HERA collected data which challenged preconceptions about the makeup of protons, observing a high density of gluons and quark-antiquark pairs at small momentum fractions, as well as measuring heavy quarks which could be interpreted as components of the proton. HERA also provided another surprise early in its operation, with protons unexpectly remaining intact following large momentum transfers. This marked the beginning of a whole field of study devoted to exporing this "hard diffraction" signature.

In addition to unpolarised DIS experiments, the spin structure of the nucleon has

been studied using polarised targets. These programmes have been used to measure spin structure functions and test fundamental sum rules associated with Quantum Chromodynamics (QCD) and the quark-parton model (QPM). In the late 1980s, results from EMC indicated that the net spin of the 3 quarks accounts for $< 24\,\%$ of the spin of the proton, rather than the expected $100\,\%$ [8]. This problem, often referred to as the "proton spin crisis" has been further investigated in experiments at several high energy physics laboratories. The EIC will be the first ever collider mode DIS experiment with polarised targets, and so will play a crucial role in extending these studies to a new kinematic region and determining the polarised gluon contribution to the spin of the proton.

1.2 Electron-Ion Collider

The Electron-Ion Collider will be the second ever electron-proton collider, after HERA. It offers an instantaneous luminosity increase of two orders of magnitude compared to HERA, as well as the ability to use polarised targets of protons or light nuclei, or unpolarised heavy nuclei. The design of the EIC was guided by requirements expressed in the EIC White Paper [9], and in its current design provides collisions of polarised protons and polarised electrons with centre-of-mass energies ranging from 20 GeV to 141 GeV, and heavy ion collisions up to 89 GeV per nucleon. The beams collide at a crossing angle of 25 mrad, which allows for the quick separation of the beams, as well as positioning of the focusing beam elements closer to the interaction point, while keeping the synchroton radiation background manageable. The luminosity loss as a result of the crossing angle is recovered through the inclusion of crab cavities in each beam [9]. The collider is to be built using the existing RHIC complex, with one of the ion rings being rebuilt and the other being replaced by an electron storage ring. A schematic diagram of the EIC is shown in Fig. 1.1, including the various rings, pre-accelerators, and injector. Research and development activities for the EIC project detector are ongoing, with a generic detector R&D programme that began in 2011, superceded by project-specific R&D since 2021. The project timeline currently forecasts the construction phase to begin in 2025, following the conclusion of RHIC operations, and data taking to begin in the early 2030s.

The basic design requirements of the EIC are summarised below:

- High ($\sim 70\,\%$) polarisation of electron, proton, and ^{3}He beams
- Large range of ion beams, from deuterons to heavy nuclei such as gold, lead, or uranium

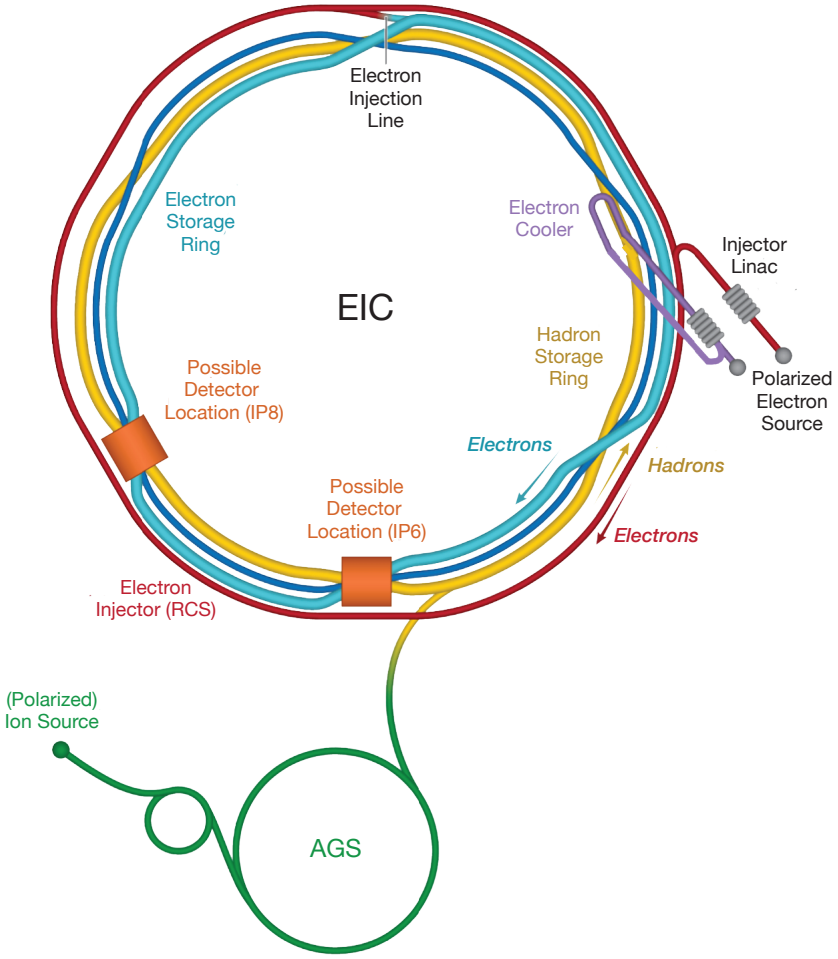

Figure 1.1: Schematic layout of the planned EIC accelerator based on the existing RHIC complex at Brookhaven National Laboratory. The project detector is to be located at interaction point 6 (IP6), and a possible second detector at interaction point 8 (IP8). AGS stands for "Alternating Gradient Synchrotron". Figure taken from [10].

- e-p centre-of-mass energies ranging from 20 GeV to 141 GeV
- e-A collisions up to 89 GeV/nucleon
- High instantaneous luminosity, $\mathcal{L} = 10^{33} - 10^{34}\,\mathrm{cm}^{-2}\,\mathrm{s}^{-1}$

The large range of centre-of-mass energies are achieved through various combinations of an electron beam which may take energies of up to 18 GeV, with protons with energies between 41 and 275 GeV or ions with energies between 41 and 110 GeV/nucleon. The current projected energy combinations for e-p and e-Au collisions are summarised in Table 1.1 and 1.2 [11].

The EIC facility is capable of supporting two interaction points. However, only one detector is forseen to be instrumented as part of the EIC project, the project detector, ePIC, which will be located at IP6. It is the ambition of the wider EIC

Table 1.1: e-p configurations.

E(e) (GeV)	**E(p) (GeV)**	$\sqrt{s}$ **(GeV)**
5	41	28.6
5	100	44.7
10	100	63.2
10	275	104.9
18	275	140.7

Table 1.2: e-Au configurations.

E(e) (GeV)	**E(Au) (GeV)**	$\sqrt{s}$ **(GeV)**
5	41	28.6
5	110	46.9
10	110	66.3
18	110	89.0

community to install a second detector at IP8, with aim to expand the physics programme and mitigate risks through a two detector solution.

The ePIC detector will be the first experiment at the EIC. It consists of a $\sim 10\,\mathrm{m}$ long cylindrical central detector, as well as additional instrumentation along the beamline, up to $\sim 45\,\mathrm{m}$ from the interaction point. The central detector consists of precision tracking and electromagnetic calorimetry systems, and a variety of particle identification systems, all surrounded by a superconducting magnet which provides a 1.7 T solenoidal magnetic field. Beyond the solenoid there are hadronic calorimeters. The beamline instrumentation enables the detection of particles emerging at very small angles relative to the primary beam. The combination of the central detector and beamline instrumentation makes ePIC a detector with near hermetic coverage.

1.2.1 Physics Aims

The EIC seeks to address fundamental questions surrounding the nature of nucleons and nuclei. A brief discussion of the physics processes that may be studied at the EIC is given in Chapter 2. The underlying physics questions that the EIC aims to answer are:

- How are partons and their interactions responsible for nearly all visible matter in the universe?
- How do quarks and gluons and their motion in the proton produce the overall spin structure of the proton?
- What does the internal structure of protons and atomic nuclei look like in position and momentum space?
- How does the distribution of quarks and gluons differ between protons and nuclei?
- How are the dynamics of quarks and gluons affected in a dense nuclear environment – is there a boundary at which gluons saturate?

1.3 Thesis Outline

Chapter 2 describes the physics that may be probed using DIS, starting from an introduction of form factors and leading to the various structure functions associated with protons/nuclei. Chapter 3 describes the detector subsystems that are to be included in the ePIC detector, and gives a detailed description of the tracking subsystem, the tracking resolutions, and track reconstruction.

The work presented in this thesis is divided into two areas of study. The first is the development of the tracking system for the EIC project detector, ultimately leading to the current tracking design of the ePIC detector. Studies are aimed at the optimisation of the tracking geometry, using resolution benchmarks of quantities associated with track reconstruction. Additionally, studies measuring the performance implications of increasing levels of realism in the tracking simulations are presented. This work is covered in Chapter 4.

The second area of study is the reconstruction of kinematic variables associated with the inclusive DIS process. This work is presented in two parts, the first being the evaluation of the kinematic variable reconstruction performance of the ePIC detector, using conventional reconstruction methods, discussed in Chapter 5. The second part, shown in Chapter 6, is the presentation of a novel method for the reconstruction of the DIS variables using a kinematic fit within a Bayesian inference framework. The kinematic fitting method is evaluated in terms of the resolution with which the DIS variables are reconstructed, and the ability of the method to tag initial-state photon radiation that may be emitted by beam electrons prior to a collision. These studies are performed using full simulations of the ePIC detector, as well as simulated and real data from the H1 detector at HERA.

Chapter 2

EIC Physics

The basic process at the EIC is Deep Inelastic Scattering, of which there are several categories, allowing for a variety of physics studies on the nature of protons and nuclei. In this chapter, the theoretical background of DIS and the extraction of proton structure functions with inclusive DIS is presented, as well as a short overview of non-inclusive physics. The form factor derivation presented in this chapter follows and condenses a detailed derivation that can be found in reference [12].

2.1 Form Factors and Elastic Scattering

The Rutherford gold foil experiment of 1911 probed the structure of gold atoms through the scattering of α particles by a gold foil. This experiment measured the non-relativistic scattering cross section

$$\frac{d\sigma}{d\Omega} = \frac{Z_1 Z_2 \alpha^2}{4k^2 \sin^4(\theta/2)}, \tag{2.1}$$

where $\alpha \approx 1/137$ is the fine structure constant, Z_1 and Z_2 are the atomic numbers of the probe and target, k is the momentum of the probe, and θ is its scattering angle in the laboratory frame. The scattering is elastic, so the momentum of the probe after scattering, denoted by k' and used later on, is equal in magnitude to k. Contrary to expectations from the plum pudding model [13], which predicted that the α particles would pass through with negligible deflection, it is clear that while the cross section decreases with increasing scattering angle, a non-negligible fraction of the α particles are scattered at large angles. Rutherford concluded that the majority of the mass was concentrated in a small and positively charged scattering centre, termed the nucleus.

In the Rutherford scattering case, both the probe and the scattering target are point-like. In the case of electrons scattering from a nuclear target, the electron is point-like, but the charge of the nuclear target is distributed over a finite region of space. In order to determine the charge distribution, the angular distribution of the scattered electrons from the charge distribution may be compared to the cross section for scattering on a point charge:

$$\frac{d\sigma}{d\Omega} = \left(\frac{d\sigma}{d\Omega}\right)_{\text{Rutherford}} |F(q)|^2. \tag{2.2}$$

Here, $q = k - k'$ is the (three-vector) momentum transfer between the electron and target, and the charge distribution of the target is described by form factor $F(q)$. The form factor may be deduced using unpolarised electrons scattering from a static (fixed in space and not changing with time), spinless charge distribution $Ze\rho(x)$, normalised such that

$$\int \rho(x) d^3x = 1. \tag{2.3}$$

For a static target, the form factor in Eq. 2.2 is simply the Fourier transform of the charge distribution

$$F(q) = \int \rho(x) e^{iq\cdot x} d^3x. \tag{2.4}$$

The Rutherford scattering equation describes the non-relativistic scattering of point-like spin-0 particles. If the Rutherford scattering case is extended to relativistic spin-1/2 particles, being scattered by the Coulomb field of an atomic nucleus, corrections can be applied to the cross section such that

$$\left(\frac{d\sigma}{d\Omega}\right)_{\text{Mott}} = \left(\frac{d\sigma}{d\Omega}\right)_{\text{Rutherford}} \cdot \frac{E'_e}{E_e} \cdot \cos^2(\theta/2), \tag{2.5}$$

as found by Mott in 1932 [14]. The factor $\cos^2(\theta/2)$ arises from the spin-1/2 of the electron. Relativistic electrons produce significant nuclear recoil, which is described by the factor $\frac{E'_e}{E_e}$, and can also be written as

$$\frac{E'_e}{E_e} = \frac{1}{[1 + \frac{2E_e}{M}\sin^2(\theta/2)]}. \tag{2.6}$$

Given that both the magnetic moment and charge of the proton are involved in the scattering process, and the proton is not static, the above discussion cannot be used directly to yield the structure of the proton. The contribution of the magnetic moment can be accounted for if we consider the proton to be a point charge e with Dirac magnetic moment $e/2M$, in which case one can simply take the known result for electron-muon scattering [12], replacing the mass of the muon by that of the

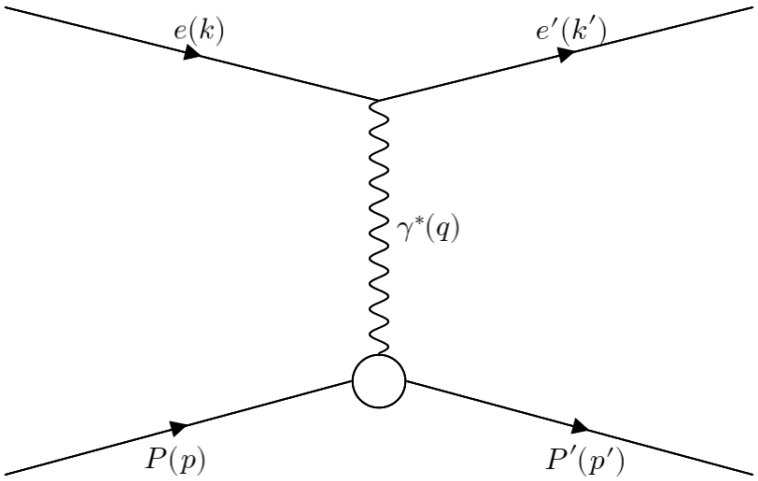

Figure 2.1: Elastic scattering of an electron by a proton.

proton, M:

$$\left(\frac{d\sigma}{d\Omega}\right)_{lab} = \left(\frac{d\sigma}{d\Omega}\right) \cdot \frac{E'_e}{E_e} \cdot \left(\cos^2(\theta/2) - \frac{q^2}{2M^2}\sin^2(\theta/2)\right). \tag{2.7}$$

The spin-1/2 target leads to an additional term $-\frac{q^2}{2M^2}\sin^2(\theta/2)$ representing the magnetic interaction. From here elastic electron-proton scattering, as shown in Fig. 2.1, can be considered, and the derivation will proceed using four-vectors unless otherwise specified. The interaction occurs via the exchange of a virtual photon, with four momentum q. The four momentum of the incoming (outgoing) electron is labelled k (k'), such that $q = k - k'$. The manner in which the virtual photon interacts with the proton with four momentum p relates to the energy of the collision. For lower energies, the most probable occurrence is elastic scattering. In this case the proton remains intact, and the invariant mass W of the final state hadronic system with four momentum p', is simply the mass of the proton.

To calculate the differential cross section for elastic ep scattering, one must consider the transition currents. This is simple for point-like spin-1/2 particles such as the electron. However, for the proton it is necessary to introduce functions parametrising our ignorance of the hadronic current. The proton transition current J^μ must be a Lorentz four vector, so the most general four vector form that can be constructed from p, p', and q is used. With the removal of terms that do not contribute to the cross section, two independent form factors $F_1(q^2)$ and $F_2(q^2)$, known as structure functions remain. Using this parametrisation of the hadronic current to calculate the differential cross section for elastic $e - p$ scattering, the expression

$$\left(\frac{d\sigma}{d\Omega}\right)_{lab} = \frac{\alpha^2}{4E_e^2\sin^4(\theta/2)}\cdot\frac{E_e'}{E_e}\cdot\left[\left(F_1^2 - \frac{\kappa^2 q^2}{4M^2}F_2^2\right)\cos^2(\theta/2) - \frac{q^2}{2M^2}(F_1+\kappa F_2)^2\sin^2(\theta/2)\right] \tag{2.8}$$

is obtained, and is known as the Rosenbluth formula [15]. The nucleon anomalous magnetic moment κ is introduced, which takes a value of 1.79 μ_N for the proton and -1.91 μ_N for the neutron, in the limit where the momentum transfer $q^2 \to 0$, with $\mu_N = e/2M$ denoting the nuclear magneton [16]. The structure functions are chosen so that in the limit $q^2 \to 0$, $F_1(0) = 1$ and $F_2(0) = 1$. It is conventional to write the Rosenbluth formula using linear combinations of F_1 and F_2 known as the "Sachs" form factors G_E and G_M

$$\begin{aligned} G_E &= F_1 + \frac{\kappa q^2}{4M^2}F_2 \\ G_M &= F_1 + \kappa F_2 \end{aligned} \tag{2.9}$$

which are defined so that no $G_E G_M$ interference terms appear in the cross section. G_E is usually referred to as the electric form factor, and G_M the magnetic form factor. The ep elastic cross section can be rewritten as

$$\left(\frac{d\sigma}{d\Omega}\right)_{lab} = \frac{\alpha^2}{4E_e^2\sin^4(\theta/2)}\cdot\frac{E_e'}{E_e}\cdot\left(\frac{G_E^2 + \tau G_M^2}{1+\tau}\cos^2(\theta/2) + 2\tau G_M^2\sin^2(\theta/2)\right), \tag{2.10}$$

where $\tau = -q^2/4M^2$. Data on the angular dependence of $ep \to ep$ scattering can be used to separate G_E and G_M at different values of $-q^2$. The behaviour at low $-q^2$ can be used to extract the root-mean-square (RMS) radius of the proton charge and magnetic moment distributions, with data from ep scattering experiments indicating a radius of $\sim 0.8\,\text{fm}$ for both [17].

2.2 Deep Inelastic Scattering

2.2.1 Unpolarised DIS

As the magnitude of the four momentum transfer, given by $-q^2$, of the incident electron increases, the inelastic regime becomes dominant, in which case excited states of the proton such as a Δ^+ baryon are produced. In such a case, the invariant mass of the hadronic system $\Delta^+ \to p\pi^0$ is given by $W = M_\Delta$. As $-q^2$ is further

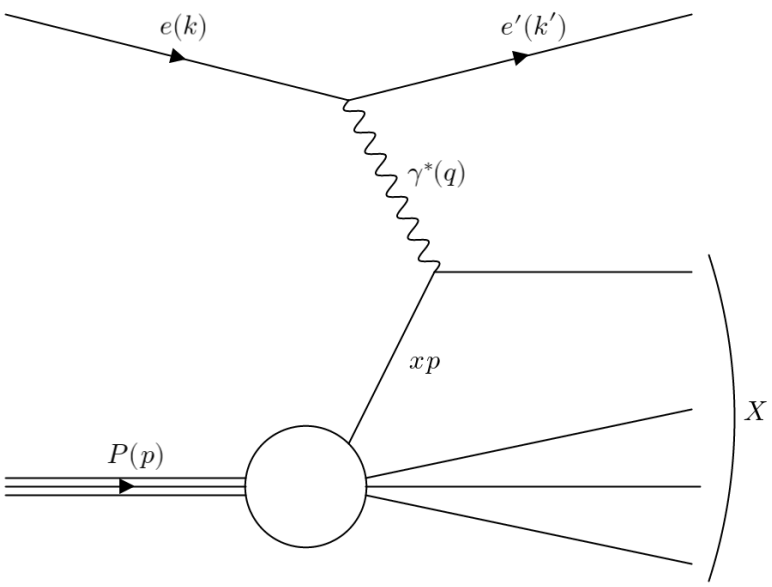

Figure 2.2: Neutral-Current Deep Inelastic Scattering of an electron on a proton.

increased, the proton breaks up into a complicated multiparticle hadronic final state (HFS) with large invariant mass W. This is considered to be the DIS regime, and if no constraint is placed on the type of particles produced in the final state, the process may be referred to as inclusive DIS. The lowest order Neutral-Current (NC) DIS process is shown in the Feynman diagram in Fig. 2.2 and has the form

$$e(k) + P(p) \Longrightarrow e'(k') + X(p'). \tag{2.11}$$

The diagram in Fig. 2.2 describes DIS using the quark-parton model (QPM), in which the electron is elastically scattered by point-like spin-1/2 constituents of the proton (partons). In the QPM, the scattering process is governed by three Lorentz invariant (LI) quantities: x, y, and Q^2, which are defined as

$$Q^2 = -(q \cdot q) \tag{2.12}$$

$$x = \frac{Q^2}{2p \cdot q} \tag{2.13}$$

$$y = \frac{p \cdot q}{p \cdot k}. \tag{2.14}$$

Q^2 is the "virtuality" or "resolving power" of the exchanged boson, giving a scale to the interaction such that larger values of Q^2 resolve smaller transverse distances within the struck proton. The wavelength of the virtual photon is given approximately by $\lambda \sim \hbar c/|Q|$. Using the Heisenberg uncertainty principle, the resolution can be found as $\Delta r \sim 1/|Q|$, where Δr denotes the distance scale probed by the

virtual photon, yielding a resolution of $\sim$0.2 fm at $|Q| = 1\,\text{GeV}$. The most sizeable contribution to the total ep cross section comes from events in which the virtuality is very low ($Q^2 \to 0$), in which the virtual photon is almost real. In the DIS regime, in which Q^2 (and $p \cdot q$) are sufficiently large that the electron is scattered by an individual parton, the Bjorken scaling variable x can be interpreted as the fraction of the proton momentum carried by the struck parton in a Lorentz frame in which the proton is moving fast, and so can only take values between 0 and 1. The inelasticity y is a dimensionless quantity representing the fraction of energy lost by the electron in the proton rest frame; as such it also only assumes values $0 \leq y \leq 1$.

The centre-of-mass energy s is found as $s = (k+p)^2$ which yields, after simplification, $2p \cdot k = s - m_p^2$. It can therefore be seen from the previous definitions of x, y and Q^2 that these variables are related through $Q^2 = (s - m_p^2)xy$. In collider mode DIS experiments such as the EIC and HERA, $s \gg m_p^2$, so the relation becomes

$$Q^2 \simeq sxy. \tag{2.15}$$

The elastic form factors discussed in the previous section were known to fall rapidly as a function of Q^2, due to the finite extent of the charge distribution. It was predicted by Bjorken and later observed by experiments at SLAC that F_2 was independent of Q^2 for x values around $x \sim 0.25$ [18]. The QPM grew from Feynman's attempt to provide a simple physical picture of this scaling.

In the QPM, DIS processes are considered to be the incoherent elastic scattering of electrons from charged partons. It is therefore useful to once again consider elastic electron-muon scattering, the cross section for which is expressed in Eq. 2.16 [18] using the aforementioned LI quantities:

$$\frac{d\sigma}{dy} = \frac{2\pi\alpha^2}{Q^4}[1 + (1-y)^2]s. \tag{2.16}$$

This formalism can be extended such that electron-proton scattering is interpreted as the incoherent sum of electron-parton scatters. For electron scattering by a parton carrying fraction x of the proton's momentum, the ep centre-of-mass energy s is replaced by xs, and an additional factor due to the charge of the struck quark is introduced:

$$\frac{d\sigma}{dy} = \frac{2\pi\alpha^2}{Q^4}[1 + (1-y)^2]xse_i^2, \tag{2.17}$$

where e_i is the charge of the struck quark (anti-quark), and thus may take values of $\frac{2}{3}e$ ($-\frac{2}{3}e$) or $-\frac{1}{3}e$ ($\frac{1}{3}e$). To obtain the electron-proton scattering cross section,

this result must be summed over all partons. A distribution function $q_i(x)$ is introduced, which gives the probability density of the struck quark carrying fraction x of the proton's momentum, with i denoting the flavour of the quark. The momentum distribution is given by $xq(x)$ and is more commonly referred to using the term "parton distribution function" (PDF). The double differential cross section for incoherent scattering from a quark of any flavour, carrying momentum fraction x is thus

$$\frac{d^2\sigma}{dxdQ^2} = \frac{2\pi\alpha^2}{xQ^4}[1 + (1-y)^2] \sum_i e_i^2 x[q_i(x) + \bar{q}_i(x)]. \tag{2.18}$$

To understand this physical interpretation from the QPM in terms of the structure functions, this result is compared to the general cross section formula for inelastic electron-proton scattering, the derivation of which is not presented here, but can be found in reference [18]:

$$\frac{d^2\sigma}{dxdQ^2} = \frac{4\pi\alpha^2}{xQ^4}[xy^2F_1(x,Q^2) + (1-y)F_2(x,Q^2)]. \tag{2.19}$$

The longitudinal structure function is defined as $F_L = F_2 - 2xF_1$, meaning that the cross section may be rewritten as

$$\frac{d^2\sigma}{dxdQ^2} = \frac{2\pi\alpha^2}{xQ^4}[Y_+F_2(x,Q^2) - y^2F_L(x,Q^2)], \tag{2.20}$$

where $Y_+ = 1 + (1-y)^2$. For measurements at ep colliders, it is more common to consider the reduced cross section, which is defined by

$$\sigma_r = \frac{xQ^4}{2\pi\alpha^2 Y_+}\left[\frac{d^2\sigma}{dxdQ^2}\right] = F_2(x,Q^2) - \frac{y^2}{Y_+}F_L(x,Q^2). \tag{2.21}$$

The QPM predicts $F_L(x,Q^2) = 0$, which leads to the parton model result of

$$F_2(x,Q^2) = \sum_i e_i^2 x[q_i(x) + \bar{q}_i(x)]. \tag{2.22}$$

This QPM result predicts Bjorken scaling, as F_2 is independent of Q^2 for fixed x. The prediction $F_L(x,Q^2) = 0$ is known as the Callan-Gross relationship, which is often written as $2xF_1 = F_2$, and results from the nature of spin-1/2 partons [5]. The structure functions F_2 and F_L relate to the total cross sections for the $\gamma^* p \to X$ subprocess, and are given by

$$\begin{aligned} \sigma_T + \sigma_L &= \frac{4\pi^2\alpha}{Q^2(1-x)} F_2 \\ \sigma_L &= \frac{4\pi^2\alpha}{Q^2(1-x)} F_L \end{aligned} \tag{2.23}$$

where σ_T (σ_L) is the cross section for transversely (longitudinally) polarised virtual photon scattering. Real photons are transversely polarised, so $\sigma_L = 0$ as $Q^2 \to 0$. However, this is not necessarily the case for virtual photons. The differential cross section shown in Eq. 2.20 can therefore be expressed in terms of a single structure function F_2, and the photoabsorption ratio $R(x, Q^2) = \sigma_L/\sigma_T = F_L/2xF_1$:

$$\frac{d^2\sigma}{dxdQ^2} = \frac{2\pi\alpha^2}{xQ^4}\left(1 - y + \frac{y^2}{2[1 + R(x, Q^2)]}\right) F_2(x, Q^2). \tag{2.24}$$

The mass terms are once again neglected, though their inclusion may be necessary for low Q^2. The ratio $R(x, Q^2)$ is coupled to the y^2 term in the differential cross section. Given that y runs from 0 to 1, the contribution of the y^2 term to the cross section is small, and thus the sensitivity to $R(x, Q^2)$ (and equivalently to F_L) is limited except at large values of y. In order to extract $R(x, Q^2)$, the differential cross section must be measured for at least two, and ideally more centre-of-mass energies. With a fixed beam energy, the centre-of-mass energy may still be varied through the identification of events containing initial-state QED radiation (ISR), as discussed in Chapter 6. The sensitivity of such an approach is limited by the rarity of hard ISR events, and the precision of the ISR energy measurement. At the EIC, data will be taken at multiple centre-of-mass energies spanning a large lever arm, allowing for the optimal determination of $R(x, Q^2)$. The results of previous measurements of $R(x, Q^2)$ can be evolved using QCD, and F_2 extracted from the measured cross section according to Eq. 2.24. It is also noted that the effect of F_L (or $R(x, Q^2)$) is very small for most y values, and so is often ignored.

Measurements of F_2 made by several experiments are shown in Fig. 2.3, and exhibit some striking features. While Bjorken scaling holds approximately over a wide range of x values, scaling violations are apparent especially at very high and very low x. The F_2 structure function is seen to increase (decrease) with increasing Q^2 for low (high) x values, indicating that for high Q^2 the proton has a greater fraction of low x quarks. At high Q^2 a finer structure is resolved, with this finer structure consisting of gluons being emitted and producing additional $q\bar{q}$ pairs. The rate at which the F_2 structure function grows with Q^2 is therefore indicative of the gluon density. In the Prytz method [20], this relationship is used to approximate the gluon PDFs:

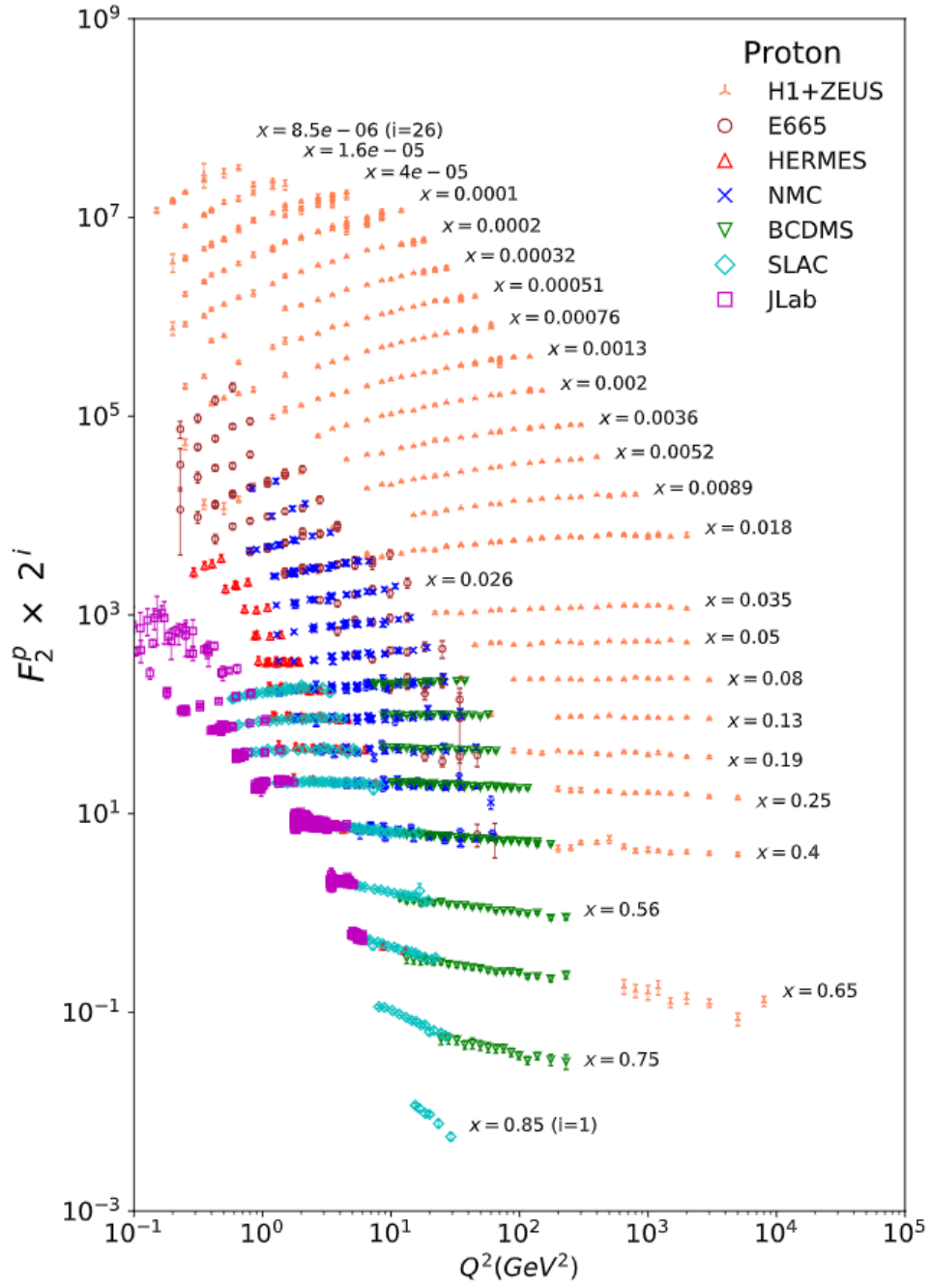

Figure 2.3: Measurements of the proton structure function F_2^p from the scattering of electrons/positrons by protons at the HERA collider (H1+ZEUS), and in fixed target experiments (SLAC, HERMES, JLAB). Also shown are measurements for muon scattering by fixed targets (BCDMS, E665, NMC). Results are plotted as a function of Q^2 for fixed values of x. F_2^p is multiplied by a factor of 2^i to avoid overlapping points, where i is the number of the x bin, ranging from $i = 1$ at $x = 0.85$ to $i = 26$ at $x = 0.0000085$. Figure taken from [19].

$$\frac{dF_2(x,Q^2)}{d\ln Q^2} \approx G(2x,Q^2). \tag{2.25}$$

Formulating this concept in QCD leads to the DGLAP equations [21], which describe the Q^2 evolution of the PDFs. An important behaviour shown in Fig. 2.3 is the substantial rise of F_2 at low x [22]. In the double asymptotic limit (small x and large Q^2), the DGLAP evolution equations can be solved [23] and F_2 predicted to rise as a power of x at low x, eventually being limited by gluon self interactions $gg \to g$. As Q^2 increases, so does the probability of radiating gluons and producing $q\bar{q}$ pairs. The resulting momentum loss shifts the parton distributions to lower x. At high x, which is dominated by the valence quark distributions, this depletes the number of high momentum quarks, leading to a reduction of the value of F_2.

It should be noted that for high energies, W and Z exchange contribute to the cross section and are described by additional structure functions [9]. The Z^0 contribution to the overall cross section is included as an additional term in Eq. 2.21 [24]

$$\sigma_r = \frac{xQ^4}{2\pi\alpha^2 Y_+}\left[\frac{d^2\sigma}{dxdQ^2}\right] = F_2(x,Q^2) - \frac{y^2}{Y_+}F_L(x,Q^2) + \frac{Y_-}{Y_+}xF_3, \tag{2.26}$$

where $Y_- = 1-(1+y)^2$. In the naive QPM, the parity violating structure function xF_3 can be expressed in terms of the quark and anti-quark distributions as

$$xF_3(x,Q^2) \simeq 2x\sum_i e_i a_i [q_i(x,Q^2) - \bar{q}_i(x,Q^2)], \tag{2.27}$$

and is therefore sensitive to the valence quark distributions [25]. The axial vector coupling of the quarks, a_q, is introduced, which takes a value of $+\frac{1}{2}$ for up-type quarks and $-\frac{1}{2}$ for down-type quarks.

The differential cross section for CC e^-p scattering of polarised electrons by unpolarised protons can be expressed as [26]

$$\frac{d^2\sigma_{CC}}{dxdQ^2} = (1-P_e)\frac{G_F^2}{4\pi x}\left[\frac{M_W^2}{M_W^2+Q^2}\right]^2 (Y_+W_2^- + Y_-xW_3^- - y^2W_L^-) \tag{2.28}$$

where G_F is the Fermi coupling constant and P_e denotes the electron beam polarisation ($P_e = 1$ for a fully right handed e^- beam). W_2^-, W_3^- and W_L^- are the structure functions for CC e^-p scattering, where $W_L^- = 0$ in the QPM, and W_2^- and W_3^- can be expressed as the flavour dependent sum and difference between the quark and anti-quark momentum distributions as

$$W_2^- = x(U+\bar{D}), \qquad\qquad xW_3^- = x(U-\bar{D}). \tag{2.29}$$

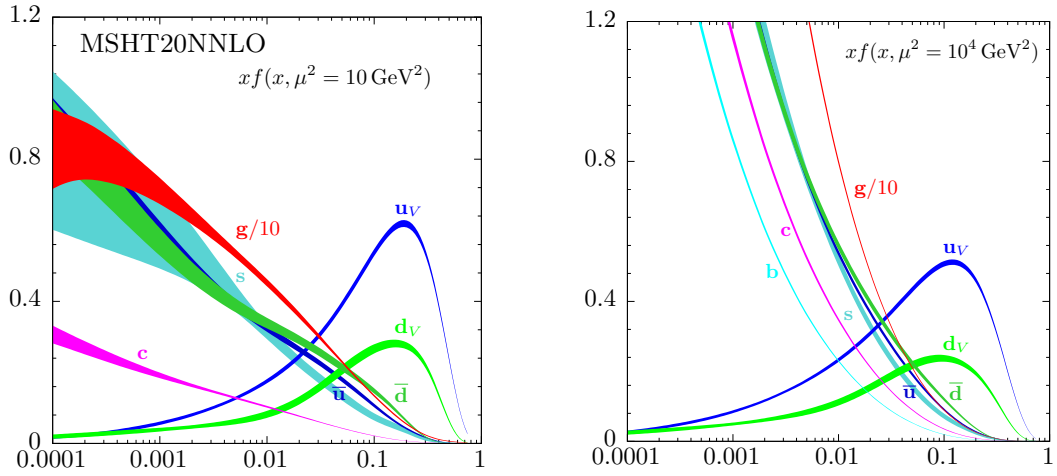

(a) **(b)**

Figure 2.4: x times the unpolarised parton distributions $f(x)$ (where $f = u_v, d_v, \bar{u}, \bar{d}, s \simeq \bar{s}, c = \bar{c}, b = \bar{b}, g$) as obtained from the NNLO MSHT20 global analysis at factorisation scales of (a) $\mu^2 = 10\,\mathrm{GeV}^2$ and (b) $\mu^2 = 10^4\,\mathrm{GeV}^2$. The widths of the bands correspond to a 68 % confidence interval. Figure taken from [27].

Below the b quark mass threshold, the sum of up-type quark densities U can be written as $U = u + c$, and equivalently for the down type quarks $D = d + s$, where u, d, s, and c represent the PDF for the relevant flavour. CCDIS measurements are highly complementary with parity violating NC measurements, as they probe different quark flavour combinations, and so CCDIS measurements play a key role in flavour and quark/anti-quark separation. The opposite charge of W^+ bosons produced in CCDIS with a positron, compared to the W^- bosons that are exchanged during CCDIS with an electron beam, allows for unique flavour combinations to be probed relative to the electron beam case. However, the EIC will focus primarily on the physics that can be achieved using electron beams and, while positron beams can be straightforwardly produced at the facility, measurements using positron beams are not currently planned.

Across the inclusive DIS processes outlined in this section, various quark and gluon PDFs can be extracted and separated. Fig. 2.4 shows the current status of the proton PDFs as obtained by the NNLO MSHT20 global analysis [27] for two different factorisation scales μ (which are typically given by the scale of the probe Q). The gluon PDF is scaled by a factor of 1/10 for visibility. The features are broadly similar at the two scales, though deviations from Bjorken scaling are seen through the rise (fall) of the sea (valence) quark distributions with increasing scale.

2.2.2 Polarised DIS

There have been several experiments that have used the deep inelastic scattering of polarised lepton beams by fixed polarised targets in order to study the spin structure of nucleons [28]. The EIC will be the first polarised target DIS experiment to operate in collider mode, allowing the spin dependent parton substructure of nuclei to be measured with high precision over a greater kinematic range than ever before.

The spin of the proton, like that of the electron and neutron, is equal to $\hbar/2$, or $1/2$ in natural units. Results from EMC in 1988 [8] found that the spin of the three valence quarks account for $< 24\,\%$ of the proton spin, showing there must be other sources which contribute. The proton spin may be decomposed into four individual contributions:

$$\frac{\Delta\Sigma}{2} + L_q + \Delta G + L_G = \frac{1}{2}. \tag{2.30}$$

Here, $\Delta\Sigma/2$ is the intrinsic contribution of the quarks to the proton spin, where the factor of $1/2$ is the quark and anti-quark spin. ΔG is the gluon spin contribution. The angular momentum contributions of the quarks and gluons are given by L_q and L_G, respectively. The intrinsic contribution of quarks and gluons are the integrals of the helicity parton distribution functions for each flavour:

$$\begin{aligned} \Delta q(Q^2) &= \frac{1}{2}\int_0^1 (\Delta u + \Delta\bar{u} + \Delta d + \Delta\bar{d} + \Delta s + \Delta\bar{s})(x, Q^2)dx, \\ \Delta G(Q^2) &= \int_0^1 \Delta g(x, Q^2)dx. \end{aligned} \tag{2.31}$$

The helicity PDFs are experimentally accessible through the spin dependent structure function $g_1(x, Q^2)$, which can be extracted from the difference in scattering cross sections for electrons and protons with their spins aligned and anti-aligned. The difference in cross section for the two polarisation orientations is given approximately by

$$\frac{\Delta\sigma}{2} = \frac{1}{2}\left[\frac{d^2\sigma^{\uparrow\downarrow}}{dxdQ^2} - \frac{d^2\sigma^{\uparrow\uparrow}}{dxdQ^2}\right] \simeq \frac{4\pi\alpha^2}{Q^4} y(2-y) g_1(x, Q^2). \tag{2.32}$$

where $\sigma^{\uparrow\downarrow}$ and $\sigma^{\uparrow\uparrow}$ are the cross sections for aligned and anti-aligned spin directions. To limit the effect of incomplete beam polarisations, measurements of cross section asymmetries are typically used, for which the unpolarised component cancels. The longitudinal double-spin asymmetry is given by

$$A_{||} = \frac{\sigma^{\uparrow\downarrow} - \sigma^{\uparrow\uparrow}}{\sigma^{\uparrow\downarrow} + \sigma^{\uparrow\uparrow}}, \tag{2.33}$$

With the inclusion of an additional depolarisation factor from the virtual photons $D(y)$, given by

$$D(y) = \frac{y(y-2)}{y^2 + 2(1-y)(1+R(x,Q^2))}, \tag{2.34}$$

the spin dependent structure function g_1 can be extracted as

$$A_{||} \simeq D(y)\frac{g_1}{F_1}. \tag{2.35}$$

The gluons drive scaling violations as before, with the gluon helicity distribution being derived from g_1 using the approximation

$$\frac{\partial g_1(x,Q^2)}{\partial \ln Q^2} \simeq -\Delta g(x,Q^2). \tag{2.36}$$

This means that polarised DIS measurements can give insight into the gluon polarisation, with the caveat that a sufficiently large Q^2 range must be available for a given x value [29].

2.2.3 Semi-Inclusive DIS

The one-dimensional quark structure of hadrons is described at leading-twist [30] by three PDFs: the unpolarised quark PDF $f_1(x) = q(x)$, the helicity PDF $g_1(x) = \Delta q(x)$, and the transversity PDF $h_1(x)$ [31]. To describe the three-dimensional structure of hadrons in momentum space, transverse momentum dependent parton distributions (TMDs) are used. Unlike traditional PDFs, which depend only on x and Q^2, TMDs also depend on the transverse momentum of the struck parton, k_T. There are eight independent leading-twist TMDs for quarks and gluons inside a spin-1/2 hadron, which can be measured using Semi-Inclusive DIS (SIDIS) and used to study the dynamics of nucleons.

TMDs have been studied at numerous experiments over the years, using SIDIS as well as other processes [32, 33]. TMDs are usually accessed through asymmetry measurements, most notably the Collins, Sivers, and Boer-Mulders asymmetries. The azimuthal asymmetries that provided the first evidence for the Collins and Sivers effects were measured by HERMES [34], which provided access to the transversity distribution $h_1(x, k_T)$ as well as the Sivers function $f_{1T}^{\perp}(x, k_T)$. Further measurements that constrain these asymmetries, as well as the Boer-Mulders function $h_1^{\perp}$, have also taken place at COMPASS, JLAB, BELLE, and RHIC. The EIC will pro-

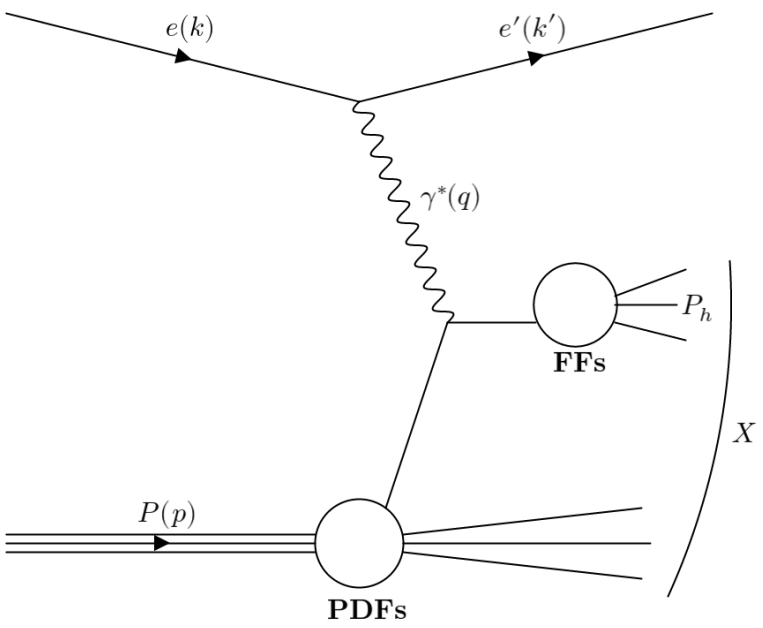

Figure 2.5: Diagrammatic representation of semi-inclusive DIS of an electron by a proton. PDFs refers to parton distribution functions and FFs refers to fragmentation functions.

vide access to TMDs over an unprecedented range in x and Q^2, and allow for the precise extraction of leading-order TMDs, including the less well measured ones such as g_{1T}, $h_{1L}^{\perp}$, and $h_{1T}^{\perp}$.

In SIDIS, information on the particles in the hadronic final state is used in combination with fragmentation functions to extract additional information about the quark flavour decomposition of the nucleon, as pictured in Fig. 2.5. The SIDIS process requires the detection of one or more final state hadrons. For a particular hadron, the fractional momentum it carries is given by $z = (p \cdot P_h)/(p \cdot q)$, where P_h is the four-momentum of the detected hadron, p and q are the incoming hadron four-momentum and q the momentum transfer, as previously defined. The other important quantity in SIDIS measurements is the p_t of the detected hadron. Higher z values are of particular interest, as they have a greater correlation to the flavour and spin of the fragmenting parton. In addition to reconstructing the z of the outgoing hadron, its flavour also needs to be identified, which sets stringent requirements on the particle identification (PID) systems. A more complete discussion of semi-inclusive measurements at the EIC can be found in references [10, 35]

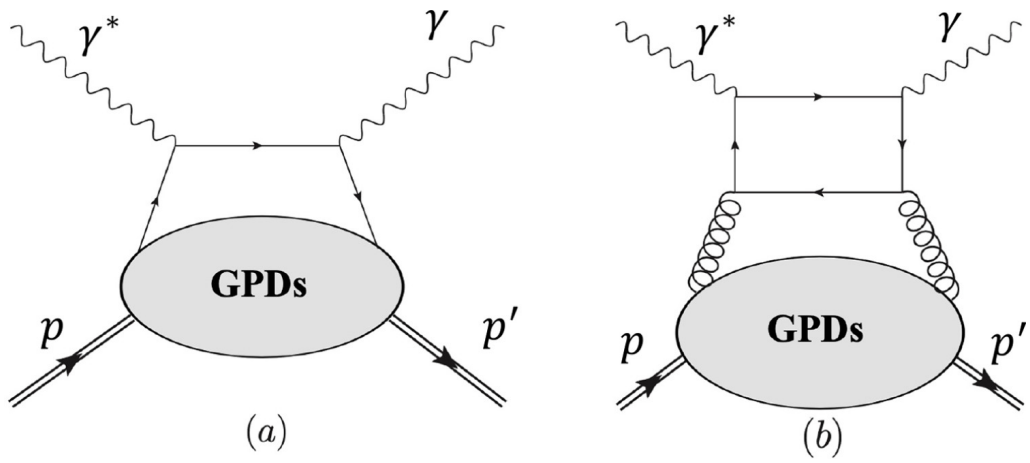

Figure 2.6: Diagrammatic representation of the ep DVCS process, for the (a) quark and (b) gluon contributions to GPDs. GPDs refers to Generalised Parton Distribution functions. Figure taken from [40].

2.2.4 Exclusive DIS

Many processes may be categorised as exclusive; Deeply Virtual Compton Scattering (DVCS) [36], the Sullivan process [37], Timelike Compton Scattering (TCS) [38], and exclusive Vector Meson Production (VMP) [39] to name a few. The commonality between these processes is the requirement that all final state particles in the event be measured, including the intact outgoing proton/ion. Processes in this category often require measurements of scattered protons or other hadron beam particles far beyond the central detector acceptance, and provide much of the motivation for the far-forward and far-backward instrumentation for an EIC project detector.

One of the main goals of the EIC is the determination of the Generalised Parton Distribution functions (GPDs), which are functions describing the positions and momenta of quarks and gluons within the nucleon. GPDs enable the study of the orbital motion of quarks in the nucleon, and describes their contribution to the nucleon spin, which is one of the key questions the EIC seeks to answer. DVCS (see Fig. 2.6) and TCS are key channels that provide insight into the GPDs.

The spatial distributions of gluons in nucleons/nuclei are accessible through the VMP process. This is the only process by which the momentum transfer $t = |p_A - p_{A'}|^2$ may be measured in eA collisions. With the measurement of the coherent VMP differential cross section $d\sigma/dt$, a Fourier transform leads to the impact parameter distribution b, and thus the spatial distribution of the gluons over a range in x [41].

Pions and kaons make up, along with protons and neutrons, the main building blocks

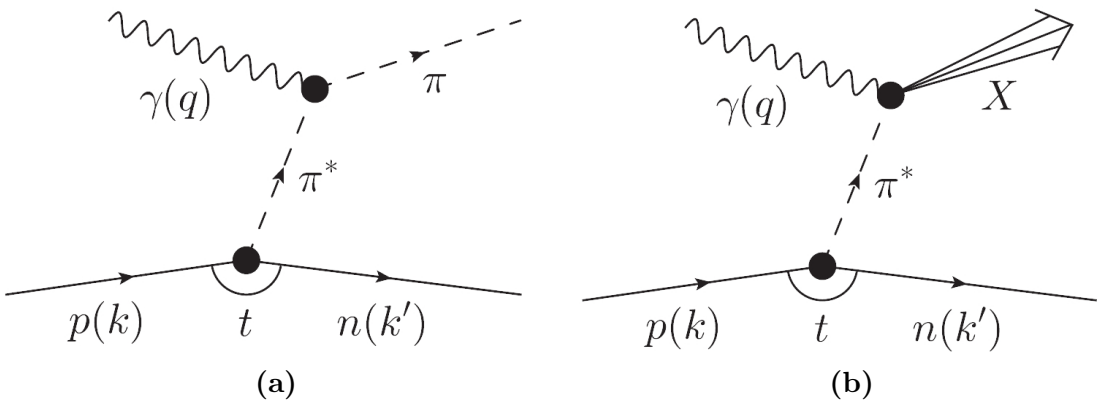

Figure 2.7: Diagrammatic representation of the Sullivan processes where a nucleon's pion cloud provides access to the pions (a) elastic form factor and (b) PDFs. Figure taken from [37].

of visible matter. The distribution of quarks and gluons is expected to be different for pions, kaons, and nucleons. The differences between these distributions is crucial for the understanding of the origin of mass. In Sullivan processes, diagrammatically pictured in Fig. 2.7, scattering occurs from the meson cloud of a nucleon, and so provides access to the meson's elastic form factors and PDFs.

2.3 Kinematic Variable Reconstruction

To determine the proton structure functions using the inclusive DIS process, the cross section is measured as a function of the kinematic variables x, y, and Q^2. These variables can be reconstructed using detector measurements of the scattered electron, the hadronic final state, or a combination of both. Several reconstruction methods have been used previously, with the resolution of such methods depending on the kinematic regime, detector acceptance and resolution effects, and the size of radiative processes. In this section, some of the more popular methods for kinematic variable reconstruction are presented. In Chapter 6 of this thesis, a method that uses all information simultaneously is developed.

2.3.1 Coordinate System

As the particles being collided at facilities such as the EIC and HERA are of different energies and species, it is necessary to make a decision about which direction is "forward" and which is "backward". For the following derivations, the origin is at the nominal interaction point and the positive z-axis is aligned with the proton beam direction, with the $+z$ direction termed "forward". The negative z direction is aligned with the electron beam, and is referred to as "backward". The y-axis points upwards (towards the sky) while the x-axis points horizontally towards the centre

of the collider. Where spherical polar coordinates are used, the azimuthal angle ϕ is measured with respect to the positive x-axis and the polar angle relative to the positive z axis. The four-vectors introduced in section 2.2.1 then have components (E, p_x, p_y, p_z) as

$$k = (E_0, 0, 0, -E_0) \tag{2.37}$$

$$k' = (E_e, E_e \sin\theta_e, 0, E_e \cos\theta_e) \tag{2.38}$$

$$p = (E_p, 0, 0, E_p) \tag{2.39}$$

$$p' = (E_h, p_t^h, 0, p_z^h) \tag{2.40}$$

The masses of the electrons and nuclei are neglected here, and the scattering is chosen to occur in the $x - z$ plane with the electron of energy E_0 scattering through an angle θ_e. E_h, p_t^h, and p_z^h are the energy, transverse momentum and longitudinal momentum of the sum over the hadronic final state.

2.3.2 Electron Method

Perhaps the simplest approach to kinematic reconstruction is the 'electron' or 'electron-only' method, in which x, y, and Q^2 are reconstructed using information from the scattered electron alone. The kinematic variables reconstructed by the electron method are denoted as x_e, y_e, and Q_e^2.

For 'electron-only' reconstruction, the energy E_e and scattering angle θ_e must be measured. Typically the scattering angle is measured by the tracking system and the energy by the calorimeters. However, it is possible to use either of the subdetectors individually and depending on the event kinematics and the resolutions of the subdetectors, this may yield the best reconstruction.

In the electron method, the electron beam energy E_0 is treated as a known quantity. Following the measurement of E_e and θ_e, the virtuality Q_e^2 may be reconstructed using the electron four momenta:

$$q^2 = (k - k')^2 \longrightarrow Q_e^2 = 2E_0E_e(1 + \cos\theta_e) \tag{2.41}$$

The inelasticity y_e is found by evaluating $p \cdot q / p \cdot k$:

$$p \cdot q = E_p[2E_0 - E_e(1 - \cos\theta_e)] \tag{2.42}$$

$$p \cdot k = 2E_pE_0. \tag{2.43}$$

such that

$$y_e = 1 - \frac{E_e(1 - \cos\theta_e)}{2E_0}, \tag{2.44}$$

which may alternatively be written as

$$y_e = 1 - \frac{E_e}{E_0}\sin^2\frac{\theta_e}{2}. \tag{2.45}$$

x_e may then be reconstructed using the relation described in Eq. 2.15. While knowledge of the proton beam energy is not necessary for the reconstruction of y_e and Q_e^2, the proton beam energy is needed in order to calculate the centre-of-mass energy $s = (k + p)^2 = 4E_0E_p$, and so is required in order to calculate x_e.

2.3.3 Hadron Method

In the 'hadron' method, also known as the Jacquet-Blondel or JB method [42], the kinematic variables are reconstructed without using the scattered electron. Instead, only the information from the final state hadrons is used. In the case of CCDIS this is the only available method, as the scattered lepton is a neutrino, which is not measured.

The hadronic final state X consists of all particles associated with the struck quark, as well as the proton remnant. The measurement of all particles in the HFS is a challenging prospect, as particles that are produced at shallow angles to the outgoing proton beam direction will not emerge from the beampipe, and often escape without being reconstructed. To mitigate this effect, the following variables are chosen to describe the hadronic system:

$$\delta_h = (E - p_z)_h = \sum_i E_i - p_z^i \tag{2.46}$$

$$p_t^h = \sqrt{\left(\sum_i p_x^i\right)^2 + \left(\sum_i p_y^i\right)^2}. \tag{2.47}$$

Since the missing hadrons are those at shallow angles relative to the beam axis, their contribution to p_t^h is expected to be small, and as the hadron beam direction is chosen as the positive z-axis, the $E - p_z$ sum of these particles is close to zero.

To obtain y_h, we begin by noting that $p' = q + p$, and find that

$$y = \frac{(p' - p)\cdot p}{k \cdot p} \simeq \frac{p' \cdot p}{k \cdot p} \tag{2.48}$$

neglecting the proton mass. Expanding the numerator, it is found that $p' \cdot p = E_p E_h - E_p p_z^h$, which can be related to δ_h as

$$p' \cdot p = E_p \delta_h. \tag{2.49}$$

Similarly, expanding $k \cdot p$ gives $2E_0 E_p$, so y can be reconstructed as

$$y_h = \frac{\delta_h}{2E_0}. \tag{2.50}$$

The quantities E_h and p_z^h (as well as p_x^h and p_y^h) are obtained from measurements of the energy, momentum, and angle of final state particles by the detector subsystems. To obtain Q^2 using the hadron method we note that the net transverse momentum of the final state must be zero, such that $p_t^h = p_t^e = E_e \sin\theta_e$. Reusing a result from the electron method, it is seen that

$$\begin{aligned} \frac{(p_t^e)^2}{Q_e^2} &= \frac{E_e^2 \sin^2\theta_e}{2E_0 E_e(1+\cos\theta_e)} = \frac{E_e(1-\cos\theta_e)}{2E_0} \\ &= 1 - y_e. \end{aligned} \tag{2.51}$$

Replacing p_t^e by p_t^h, and rearranging for Q^2 gives

$$Q_h^2 = \frac{(p_t^h)^2}{1-y_h}. \tag{2.52}$$

x_h is found from Eq. 2.15 as before.

2.3.4 Σ Method

In many situations it is possible to improve the reconstruction by mixing electron and hadron information, requiring the detector to measure the energy, momentum, and angle of both the scattered electron and the hadronic final state. The Σ method [43] requires that the quantity Σ_{tot}, which is equal to the $E - p_z$ sum over all hadronic final state particles and the scattered electron, be conserved throughout the interaction. It can be seen that for a proton beam travelling in the $+z$ direction and a lepton beam in the $-z$ direction this becomes

$$(E - p_z)_e = 2E_0 \tag{2.53}$$

for the beam electron, in the absence of initial-state QED radiation, and

$$(E - p_z)_p = 0 \tag{2.54}$$

for the proton beam. The total $E - p_z$ before the interaction, Σ_{tot}, is thus $2E_0$. The total after the interaction is given by

$$\Sigma_{tot} = \delta_h + E_e(1 - \cos\theta_e). \tag{2.55}$$

Using the conservation of Σ_{tot} throughout the reaction, equating the quantities before and after gives

$$2E_0 = \delta_h + E_e(1 - \cos\theta_e). \tag{2.56}$$

Replacing the $2E_0$ in the JB method y calculation shown in Eq. 2.50 gives

$$y_\Sigma = \frac{\delta_h}{\delta_h + E_e(1 - \cos\theta_e)}. \tag{2.57}$$

Similarly for Q^2, the JB method calculation in Eq. 2.52 is modified, replacing p_t^h with the electron transverse momentum, and y_h with y_Σ such that

$$\begin{aligned} Q^2_\Sigma &= \frac{p_t^{e'2}}{1 - y_\Sigma} \\ &= \frac{E_e'^2 \sin^2\theta_e}{1 - y_\Sigma}. \end{aligned} \tag{2.58}$$

With y and Q^2 reconstructed, x may once again be found using Eq. 2.15.

2.3.5 $e - \Sigma$ Method

The $e - \Sigma$ method [43], similarly to the Σ method, uses a mixture of electron and hadron information to reconstruct the kinematic variables. In the $e - \Sigma$ method, x is reconstructed entirely using the Σ method as described in section 2.3.4, through a combination of Eq. 2.57 and 2.58. The $e - \Sigma$ method differs from the Σ method in that the Q^2 value is reconstructed purely using the electron method, described by Eq. 2.41. The $e - \Sigma$ method is summarised below:

$$Q^2_{e\Sigma} = Q^2_e \tag{2.59}$$

$$x_{e\Sigma} = \frac{Q^2_\Sigma}{s y_\Sigma} \tag{2.60}$$

$$y_{e\Sigma} = \frac{Q^2_{e\Sigma}}{s x_{e\Sigma}}. \tag{2.61}$$

2.3.6 Double Angle Method

The 'double angle' method (DA method) [44] is a mixed reconstruction method that is especially useful for detectors where the resolution is limited by the energy measurement from the calorimeters. The quantities used in DA method reconstruction are the angle of the scattered electron θ_e and the inclusive angle of the hadronic final state γ_h. The electron scattering angle is directly measured from track information, while the angle γ_h can be calculated from the ratio of quantities δ_h and p_t^h:

$$\frac{\delta_h}{p_t^h} \simeq \frac{E_h(1-\cos\gamma_h)}{E_h \sin\gamma_h}. \tag{2.62}$$

This can be reduced to

$$\frac{\delta_h}{p_t^h} = \tan\frac{\gamma_h}{2}. \tag{2.63}$$

It is useful to define the following quantities based on the angle of the scattered electron and HFS

$$\begin{aligned} \alpha_e &= \tan\frac{\theta_e}{2} \\ \alpha_h &= \tan\frac{\gamma_h}{2}. \end{aligned} \tag{2.64}$$

Starting from Eq. 2.57, and dividing the numerator and denominator by p_t^h, an expression for y in terms of δ_h/p_t^h is obtained, which relates to α_h by Eq. 2.63. Noting that $p_t^h = p_t^e$, the equation

$$y_{DA} = \frac{\frac{\delta_h}{p_t^h}}{\frac{\delta_h}{p_t^h} + \frac{E_e(1-\cos\theta_e)}{p_t^e}} = \frac{\alpha_h}{\alpha_h + \alpha_e}. \tag{2.65}$$

is obtained. As before, Q^2 may be calculated as $\frac{p_t^2}{1-y}$, with p_t being obtained by

$$\begin{aligned} \alpha_e + \alpha_h &= \frac{\delta_h + E_e(1-\cos\theta_e)}{p_t} \\ &= \frac{2E_0}{p_t}. \end{aligned} \tag{2.66}$$

Hence, Q^2 is ultimately found as

$$
\begin{aligned}
Q^2_{DA} &= \frac{4E_0^2}{(1-y_{DA})(\alpha_e+\alpha_h)^2} \\
&= \frac{4E_0^2}{\alpha_e(\alpha_e+\alpha_h)}.
\end{aligned}
\tag{2.67}
$$

x_{DA} may be obtained using Eq. 2.15 as previously.

While calorimeter measurements are used in the determination of δ_h and p_t^h, the ratio δ_h/p_t^h is used for the calculation of α_h, and uncertainties associated with the HFS energy measurement cancel. The DA method is thus insensitive to the overall energy scale of the calorimeters, and so is often used in energy calibrations, as done by ZEUS [45] and H1 [46].

2.4 Detector Requirements

Broadly speaking, the EIC physics programme can be accomplished through the study of inclusive, semi-inclusive, and exclusive DIS processes. At the EIC these will be studied for polarised electron and light nucleon beams, as well as unpolarised beams of electrons and light/heavy nuclei, all for a large range of centre-of-mass energies. The design of the experimental apparatus (both the collider and detector) is based on the needs of these processes, with the experimental requirements becoming increasingly challenging as additional HFS information becomes necessary i.e. when semi-inclusive or exclusive processes are considered. In this section, the requirements these processes impose on the detector design are discussed, with individual treatment given to the tracking subdetector requirements.

2.4.1 General Detector Requirements

The precise measurement and identification of the scattered electron is required for all NCDIS channels. The angle and energy/momentum of the scattered electron and final state hadrons must be measured over a large η range, where η is the pseudorapidity and is defined by

$$
\eta = -\ln\left(\tan\frac{\theta}{2}\right). \tag{2.68}
$$

For this purpose, high precision and large acceptance tracking and calorimetry subsystems are required.

For the semi-inclusive DIS process, additional hadron PID capabilities are needed for light flavour separation across a large range of momenta and η, along with an excellent resolution on the reconstructed vertices for heavy flavour identification. For exclusive channels, all particles in the event need to be reconstructed, including the outgoing intact proton. In these reactions, an excellent resolution for the tracking and calorimetry subsystems in the central detector is required. Also required is the inclusion of additional far-forward detectors such as Roman pots for scattered protons and zero-degree calorimeters, to measure neutrons from nuclear breakup, or other neutral decay products, using a totally hermetic setup.

A precise determination of the delivered luminosity is necessary for the entire experimental programme, which is accomplished using a luminosity monitoring system based on the Bethe-Heitler process $ep \rightarrow ep\gamma$ [47]. The polarisation of the electron and proton/ion beams must also be measured using various polarimeters.

2.4.2 Tracker Requirements

The tracking requirements for an EIC detector as determined from physics simulation studies for the EIC Yellow Report (YR) [10] are shown in Table 2.1. The required momentum resolution, material budget, minimum measurable p_t, and transverse pointing resolution are given for specified ranges in η.

The physics simulation studies that inform these requirements were carried out by members of the physics working groups (PWG) as part of the Yellow Report effort, and will be referred to throughout this thesis using the label "PWG requirement(s)". The basic requirements correspond to those from the EIC detector requirements and R&D handbook [48], which were derived from physics studies and HERA experience. As before, the requirements are driven by the need to precisely measure the scattered electron and HFS systems. The energy and angle of the scattered electron and HFS system are closely related to the DIS event kinematics, as seen in Fig. 2.8. It should be noted that for a given set of beam energies, the lower the event Q^2, the smaller the electron scattering angle, and conversely only at the largest Q^2 values is the electron backscattered ($\eta > 0$). Varying the hadron beam energy does not impact the electron kinematics, while increasing the electron beam energy has the effect of boosting the scattered electron to more negative η. For a detector optimised to measure electrons in a given range, it may be better to vary the hadron beam energy to achieve measurements at different centre-of-mass energies. This would, however, change the hadron kinematics, which may be detrimental for hadron PID if the detectors are optimised for certain kinematic conditions. Most of the charged

Table 2.1: Requirements for the tracking system from the Yellow Report [10].

Tracking requirements from PWGs						
			Momentum res.	Material budget	Minimum pT	Transverse pointing res.
η						
-3.5 to -3.0	Central Detector	Backward Detector	σp/p ~ 0.1%×p ⊕ 0.5%	~5% X0 or less	100-150 MeV/c	
-3.0 to -2.5					100-150 MeV/c	dca(xy) ~ 30/pT μm ⊕ 40 μm
-2.5 to -2.0			σp/p ~ 0.05%×p ⊕ 0.5%		100-150 MeV/c	dca(xy) ~ 30/pT μm ⊕ 20 μm
-2.0 to -1.5					100-150 MeV/c	
-1.5 to -1.0					100-150 MeV/c	
-1.0 to -0.5		Barrel	σp/p ~ 0.05%×p ⊕ 0.5%		100-150 MeV/c	dca(xy) ~ 20/pT μm ⊕ 5 μm
-0.5 to 0						
0 to 0.5						
0.5 to 1.0						
1.0 to 1.5		Forward Detector	σp/p ~ 0.05%×p ⊕ 1%		100-150 MeV/c	dca(xy) ~ 30/pT μm ⊕ 20 μm
1.5 to 2.0					100-150 MeV/c	
2.0 to 2.5					100-150 MeV/c	
2.5 to 3.0			σp/p ~ 0.1%×p ⊕ 2%		100-150 MeV/c	dca(xy) ~ 30/pT μm ⊕ 40 μm
3.0 to 3.5					100-150 MeV/c	dca(xy) ~ 30/pT μm ⊕ 60 μm

hadrons in the HFS will consist of pions and kaons, with the primary difficulty in the hadronic measurement being the separation of these particles using the PID detectors. The yield and average momentum for hadrons is strongly peaked in the outgoing proton beam direction. For JB reconstruction as much of the hadronic recoil as possible must be detected, motivating large forward coverage in the tracker.

The physics aims outlined in Section 1.2.1 set different, and sometimes competing, requirements for the detector. A broad summary of EIC physics measurements and the requirements they set on the tracking subsystem are presented below.

Inclusive Measurements

Inclusive processes provide many physics opportunities, such as the measurement of spin-averaged, spin-dependent, and nuclear PDFs, as well as studies of non-linear QCD and higher twist effects, and searches for Lorentz symmetry and CPT violating effects.

The tracking requirements from the inclusive process are set by the scattered electron. The majority of inclusive channels require $Q^2 > 1\,\mathrm{GeV}^2$. To measure such events with the proposed electron beam energies of $5, 10, 18\,\mathrm{GeV}^2$, the tracker should have coverage down to $\eta = -3.5$ in the backward direction. Additionally, to maintain a good resolution on the reconstructed kinematic variables, a cut of $y < 0.95$ may be applied. The minimum momentum of the scattered electrons after this cut thus ranges from ~ 0.3 to $0.5\,\mathrm{GeV}$, depending on the electron beam configuration [10].

Semi-Inclusive Measurements

A good tracking resolution is required for both the hadrons and the scattered electrons, for the full pseudorapidity range $-3.5 < \eta < 3.5$. When determining the DIS

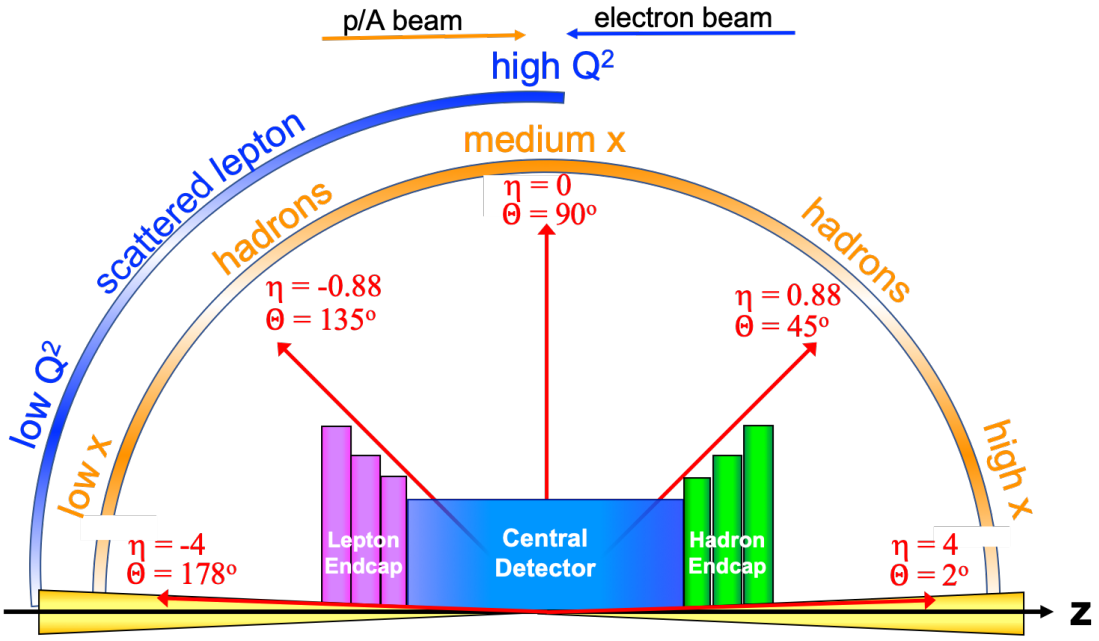

Figure 2.8: Schematic showing the distribution of the scattered electron and HFS particles for different x and Q^2 regions as a function of the detector polar angle/pseudorapidity [10].

kinematics using the HFS, it becomes beneficial to extend the forward coverage to $\eta \sim 4$. For the measurement of Λ baryons, which will be studied via their decay to proton and pion $\Lambda \to p\pi^-$ ($\bar{\Lambda} \to \bar{p}\pi^+$), the majority of the momentum is carried by the decay proton, leading to a spectrum of low energy pions. Any restriction on the minimum measurable p_t significantly reduces the fraction of pions which may be measured, with only 5 % of Λ being reconstructed for measureble $p_t > 300\,\text{MeV}$. A threshold of $p_t > 100\,\text{MeV}$ was determined to be sufficient [10].

Heavy Flavour Measurements

The density of gluons and sea quarks in the proton sharply rises with decreasing x, dominating the structure at low values of x. A growth of the gluon PDFs at small x is predicted by the BFKL (Balitsky-Fadin-Kuraev-Lipatov) equation [49]. As the gluon density becomes large, there may be non-linear effects, with gluon recombination $gg \to g$ competing with gluon evolution $g \to gg$, eventually leading to the saturation of the gluon density. The gluon recombination manifests as an additional non-linear term in the extended evolution equations: the Balitsky-Kovchegov (BK) equation [50] and Jalilian-Marian-Iancu-Mclerran-Weigert-Leonidov-Kovner (JIMWLK) equation [51].

The properties of the saturated gluons may be described using the colour glass condensate (CGC) formalism [52]. Charm jet production in charged current DIS is a

direct probe of the proton's strange quark content, which is an important study in itself, but also directly relates to the gluon density.

The dominant mechanism by which charm quarks are produced in ep collisions is photon-gluon fusion resulting in a $c\bar{c}$ pair [53]. The produced charm quarks subsequently hadronise, forming open charm hadrons (particles with a non-zero charm flavour) such as D mesons, or hidden charm hadrons (particles with equal numbers of charm and anti-charm) such as the J/ψ meson. As the interacting parton is a gluon, this process is sensitive to the gluon density, with the cross section increasing at low x where there is a greater presence of gluons.

Both charm jet and open charm events lead to the production of charmed hadrons, with the decay of this hadron resulting in one or more tracks with a significantly displaced impact parameter relative to the interaction point due to the subsequent weak decay. The transverse pointing resolution requirements in Table 2.1 are largely derived from open charm studies [10]. Charm jet tagging studies have demonstrated that the degradation of the resolutions from these values results in significant losses in charm jet tagging efficiency [54]. The effect of various momentum resolution parametrisations were studied in terms of jet energy resolution and jet energy scale for a number of jet analyses, and resolutions as presented in Table 2.1 determined to be sufficient for jet measurements. A good transverse pointing resolution reduces the background contribution for invariant mass measurements of charmed mesons such as the D meson, while an improved momentum measurement benefits the mass peak resolution [55].

Exclusive Measurements

The process in this category that most directly impacts the tracking requirements is exclusive vector meson production, a parton-level interpretation of which is pictured in Fig. 2.9. As seen in Table 2.1, the asymmetric nature of the EIC leads to asymmetric detector requirements. For the central tracking detector at the EIC, the momentum resolution requirements are far more stringent in the backward direction than forward. The driving force behind these requirements is the t reconstruction in the VMP process, which enables the extraction of the spatial distributions of gluons in nuclei. A precise measurement of the p_t of the vector meson decay products, and at larger Q^2 the scattered electron, is key to an accurate t reconstruction. It has been determined for exclusive J/ψ photoproduction, that a multiple scattering (MS) term of $\sim 0.5\,\%$ or better in the backward direction is required to reconstruct the $J/\psi \to e^+e^-$ decay products [56] with the needed precision. Similarly for the electroproduction case, a MS term of $\sim 0.5\,\%$ is needed at central and backward η

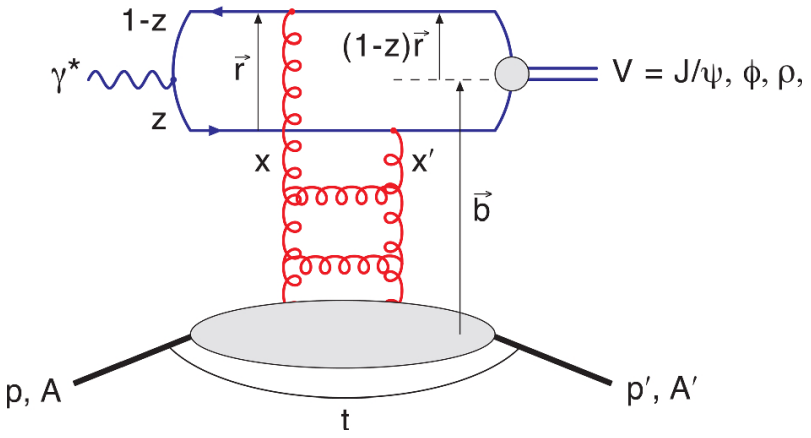

Figure 2.9: Schematic diagram of diffractive vector meson production in the dipole model, and the associated variables. Figure taken from [57].

to sufficiently well reconstruct the scattered electron and J/ψ decay products, such that the reconstructed impact parameter distribution remains accurate. To meet the needs of this process, the backward tracking requirements are reduced relative to the handbook values. The minimum measurable p_t with an EIC detector is determined by the strength of the magnetic field and the inner radii of the tracking layers, with a weaker magnetic field allowing the measurement of lower p_t, at the expense of momentum resolution performance. The ϕ meson decays primarily to a pair of low p_t kaons $\phi \to K^+K^-$, with a broad angular distribution of decay products compared to the leptonic decays of heavier mesons such as the J/ψ [39]. To measure the decay products, a tracking detector with large angular acceptance, and the ability to measure p_t as low as $100 - 150\,\text{MeV}$ is required.

Chapter 3

The ePIC Detector for the EIC

R&D activities for a general purpose EIC detector have taken place over many years, with several different detector designs being considered, depending on the site chosen to host the project, between Brookhaven National Laboratory (BNL) and the Thomas Jefferson National Accelerator Facility (JLAB) [58, 59, 60]. With the confirmation of BNL as the host site in 2020, work focused on the development of an EIC project detector to be situated at interaction point 6 (IP6) of the existing RHIC beamline (see Fig. 1.1).

The EIC Yellow Report [10], which collated physics and detector studies for the EIC, was produced and published in March 2021. The Yellow Report outlines the scientific, technical, and engineering considerations for the EIC, and includes several performance and feasibility studies of individual detector technologies, as well as larger scale simulation studies of detector subsystems and parametrisations of a full EIC detector. Following the completion of the Yellow Report, a call for collaboration proposals for EIC detectors was announced, culminating in the submission of three detector proposals: ATHENA, ECCE, and CORE [61, 62, 63]. The ATHENA and ECCE proposals each featured a design for an EIC project detector to be located at IP6. The CORE proposal presented a potential second detector to be located at IP8.

The EIC reference detector design was chosen in March 2022, with the ECCE proposal as its basis. The ATHENA and ECCE proto-collaborations merged to form a joint team for subsequent project R&D and to move towards realisation of a first EIC detector. This initiated the official formation of what has become the ePIC collaboration, with the ePIC collaboration charter being approved in December 2022. The project detector design has undergone many iterations since this time, with the aim of producing a detector that meets the needs of the physics programme, and

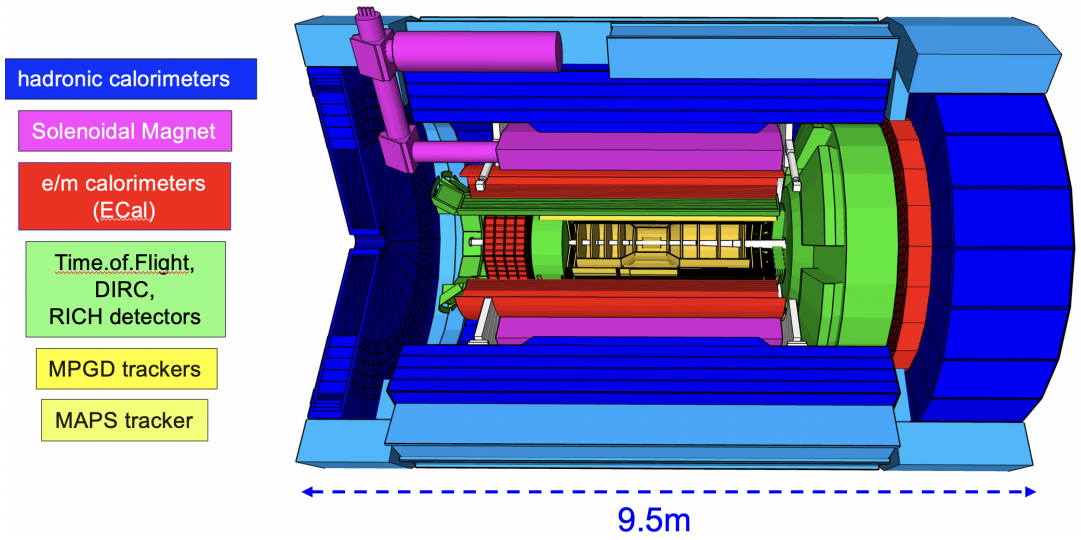

Figure 3.1: The ePIC central detector design with individual subsystems highlighted. The tracking systems are highlighted in yellow, the various PID systems in green, the electromagnetic and hadronic calorimetry subsystems in red and blue respectively, and the solenoidal magnet in magenta. Figure taken from [64].

that can be constructed and operated using technology that will be available at the relevant stages of the project timeline. In this chapter, a high level overview of the design of the ePIC detector at the time of writing is presented, followed by a detailed look at the design of the tracking detector, and the theory behind the reconstruction of charged particle tracks that are the topics of the work of this thesis.

3.1 Overview of Subsystems

The ePIC central detector in its current design is pictured in Fig. 3.1, with individual detector subsystems highlighted for visibility. The region closest to the interaction point is instrumented by a tracking detector that comprises silicon and gaseous detector layers and is responsible for track reconstruction and vertexing. Further from the interaction point there are various PID detectors that enable the separation of pions and kaons (and protons) across a large range of momenta via time-of-flight and Cherenkov angle measurements. Beyond the PID systems there are electromagnetic and hadronic calorimetry systems that are responsible for energy measurements. The barrel tracker, PID systems, and electromagnetic calorimeter are encased by a solenoidal magnet that provides the 1.7 T magnetic field required for tracking measurements. The design is asymmetric, reflecting the asymmetry in the choice of beam particles and their energies. Beyond the central detector there is extensive beam line instrumentation for the measurement of particles at far-forward and far-backward pseudorapidities.

Tracking Subsystem

At its core the ePIC detector has a tracking detector, which is responsible for measuring the momentum of charged particles produced in ep and eA collisions, as well as reconstructing the primary collision vertex, and displaced vertices associated with long-lived particles. A typical tracker design would consist of several layers of segmented silicon or gaseous detectors in a magnetic field, with the momenta of charged particles being found from their resulting curvature. To meet the goals of the EIC physics programme, a tracking detector with high precision vertex and momentum reconstruction and low material budget is required. A comprehensive description of the ePIC tracker is given in section 3.2.

PID Subsystems

The tracking systems provide measurements of the momenta of various particles. If the velocity of a particle is measured separately, the mass of the particle may be found via the relation $\overrightarrow{p} = m\gamma\overrightarrow{\beta}$, and the species of the particle determined according to its mass. The particle identification (PID) systems are the detector components that separate π, K, and p, though another important form of particle identification at the EIC is electron identification, which is denoted as "eID".

The velocity of a particle may be measured directly using a fast timing layer, in a so-called Time-of-Flight or "ToF" measurement, or indirectly through its velocity-dependent interactions. Some examples of velocity-dependent interactions which are commonly leveraged in PID detectors are

- **Specific Ionisation**: The energy loss per unit path length dE/dx is measured, and related to the velocity of the particle through the Bethe-Bloch formula [65].
- **Cherenkov Radiation**: The emission angle of Cherenkov photons relates to the velocity as $\cos(\theta) = 1/n\beta$, where n is the refractive index of the medium.
- **Transition Radiation**: The intensity of transition radiation produced by a particle as it moves between materials relates to its Lorentz factor, γ, and hence to β.

Particle identification at ePIC is accomplished using a combination of ToF and Cherenkov radiation based detector subsystems. Multiple technologies are required to provide coverage at all necessary momenta and pseudorapidities, as illustrated in Fig. 3.2. Full PID coverage is achieved by complementing low momentum PID measurements by ToF detectors (AC-LGADs and HRPPDs), with the higher momentum capabilities of Cherenkov based PID detectors (RICH and DIRC). The Cherenkov

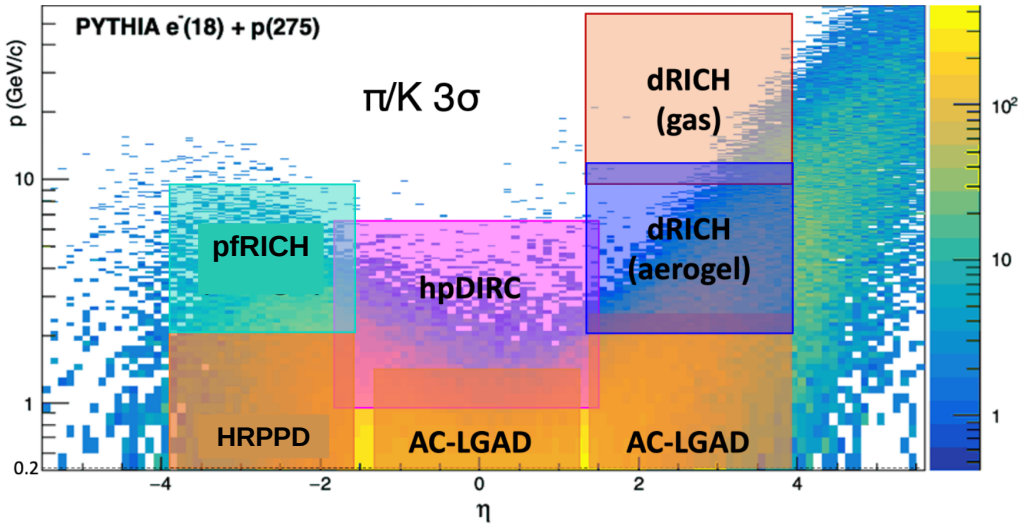

Figure 3.2: Expected regions in $\eta - p$ covered with 3σ π/K separation by ePIC PID subsystems, overlayed on the distribution of pions produced in $18 \times 275\,\mathrm{GeV}^2$ ep events generated in Pythia6. Acronyms: AC-LGAD (AC-Coupled Low-Gain Avalanche Diode), dRICH (Dual-Radiatior Ring Imaging Cherenkov detector), hpDIRC (High Performance Detection of Internally Reflected Cherenkov light detector) , HRPPD (High Rate Picosecond Photodetector), pfRICH (Proximity Focusing Ring Imaging Cherenkov detector). Figure adapted from [62].

based PID systems also aid the suppression of the charged-pion backgrounds that interfere with eID.

PID measurements present one of the major challenges for the detector, and are essential in order to fulfil the needs of the SIDIS programme. To meet the requirements of the physics programme, there must be greater than 3σ $\pi/K/p$ separation, up to 50 GeV in the forward direction, 6 GeV at central pseudorapidities, and 10 GeV in the backward direction.

Regions that achieve the necessary separation are highlighted in Fig. 3.2, with labels denoting the subsystem that provides the separation. The regions are overlayed on mapping of pions produced in $18 \times 275\,\mathrm{GeV}^2$ ep events by Pythia6 [66]. The PID systems provide almost complete coverage in the central detector region for such events (note the logarithmic z-scale). The geometries of the subdetectors were chosen such that they fit the detector while maintaining the necessary performance.

Electromagnetic Calorimetry

Electromagnetic calorimetry systems (EMCALs) measure the energy of particles by exploiting the Bremsstrahlung and pair-production mechanisms that create electromagnetic showers. At ePIC, the EMCALs are responsible for the precision mea-

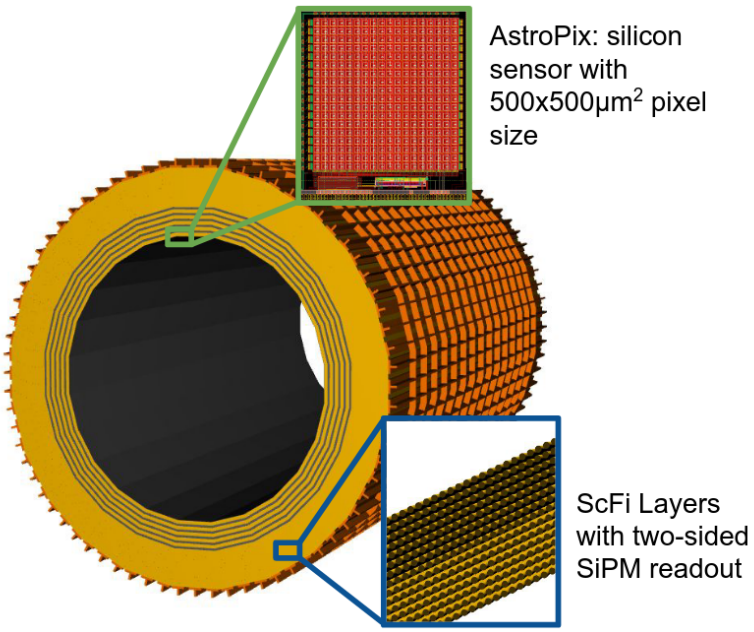

Figure 3.3: Rendering of the ePIC barrel electromagnetic calorimeter. Figure taken from [67].

surement of scattered DIS electrons, and final state electrons and photons, across a wide range in centre-of-mass energy. They also play an important role in eID, where there are stringent requirements for e/h separation in order to distinguish DIS events from the much larger photoproduction background.

For the central detector at ePIC, there must be continuous EMCAL coverage over a large range in pseudorapidity, ideally $-4 < \eta < 4$. This is provided by three EMCAL systems, which are collectively responsible for measurements at backward, central, and forward pseudorapidities. The backward region is instrumented by the EEEMCAL (Electron Endcap EMCAL), which is based on $PbWO_4$ crystals with silicon photomultiplier tube (SiPM) readout. The EEEMCAL offers fast scintillation with high light yield, radiation hardness, and small Molière radius, enabling the precision measurement of scattered electrons at low and moderate Q^2.

The electromagnetic calorimetry in the central region, pictured in Fig. 3.3, consists of an imaging barrel EMCAL, which is made up of 6 layers of AstroPix monolithic silicon sensors [68] interleaved with 5 layers of lead-scintillating fibre sandwich (SciFi/Pb), followed by a larger SciFi/Pb section. The scintillating fibres are read out on both ends by SiPMs. The interleaving of the AstroPix sensors provides excellent position resolution ($\sim 150\,\mu m$), and vertexing potential for photons, as well as the ability to separate photons and π^0 up to momenta greater than 30 GeV [69].

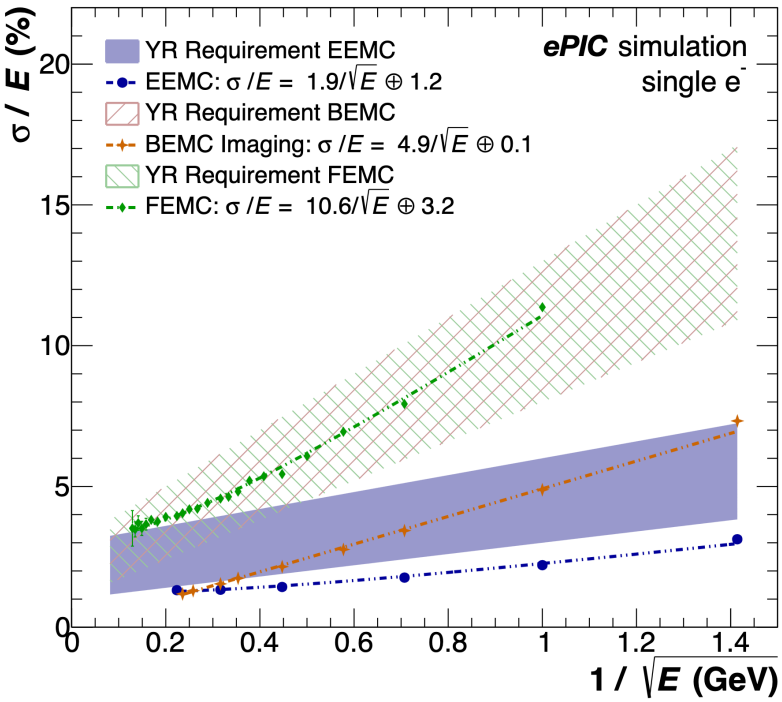

Figure 3.4: Projected resolutions of ePIC EMCAL systems as determined from single e^- simulations, and comparison to Yellow Report requirements. EEMC refers to the electron endcap EMCAL, BEMC to the barrel EMCAL, and FEMC to the forward EMCAL. Figure taken from [69].

The forward EMCAL coverage is provided by a tungsten-scintillating fibre "spaghetti calorimeter" (SpaCal) design [70]. The SpaCal is read out by many SiPMs, and the position resolution offered by the SpaCal design is beneficial for the separation of photons and π^0. The expected performance of the three subsystems is shown in Fig. 3.4, where it can be seen that the PWG requirements from the Yellow Report are either met or exceeded.

Hadronic Calorimetry

Hadronic calorimeters (HCALs) are designed to measure the energy of hadronic particles, typically π, p, n, and K, which do not deposit all of their energy in the EMCAL subsystems. They are the only means of detecting many neutral hadrons. At colliders, HCAL systems serve primarily to measure jets.

As was the case for the EMCAL systems, the HCALs are divided into three systems that cover backward, central, and forward pseudorapidities. In low-x events, hadronic final state particles may be produced in the backward direction and often overlap with the scattered electron in the EMCAL. Hadronic jets produced in photoproduction processes can also fake the scattered electron signature. It was learned from H1 and ZEUS experience that the inclusion of a backward HCAL is useful for

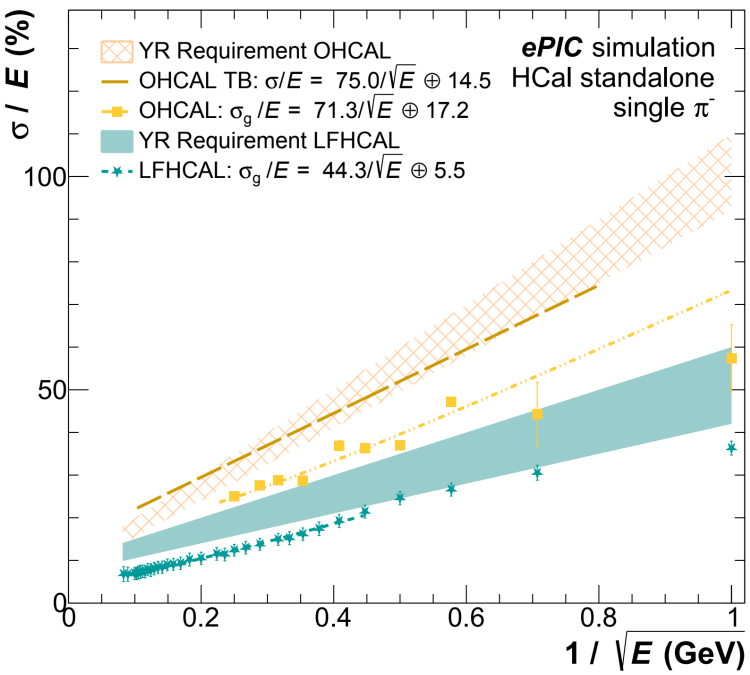

Figure 3.5: Projected resolutions of ePIC HCAL systems as determined from single π^- simulations, and comparison to Yellow Report requirements. OHCAL refers to the barrel HCAL, LFHCAL to the forward HCAL. σ_g indicates that the data point is based on the Gaussian width of the resolution peak, and OHCAL TB denotes the energy resolution is based on a test beam. Figure taken from [69].

e/h separation in such events. The backward HCAL also serves as a tail catcher for low energy neutral particles that escape the EMCAL, and so does not have strict energy resolution requirements, though the position resolution should be good enough to match clusters in the HCAL to the corresponding EMCAL cluster. The design of the backward HCAL is not finalised, but is expected to be a combination of steel and scintillator tiles, with a SiPM readout.

Hadrons produced in the barrel are typically low energy, in which case the charged component is better measured by the tracking system. A barrel HCAL can be used to better measure jets with a large neutral component. The resolution requirements are modest, with a resolution of $\sim 100\,\%/\sqrt{E}$ deemed to be sufficient [10]. ePIC plans to refurbish and reuse the existing sPHENIX barrel HCAL [71], which uses a steel and scintillator tiling design, with SiPM readout. The greatest fluence of hadronic particles is seen in the forward direction, and the hadrons produced in this direction are expected to carry the most energy among the hadrons in the central detector, up to $\sim 150\,\text{GeV}$ [72]. The ePIC forward HCAL consists of highly longitudinally segmented steel and scintillator tiles read out by SiPMs, with an additional high-η HCAL insert to extend the acceptance and capture as much of the hadronic final state as possible.

The performance of the ePIC barrel and forward HCAL systems, labelled OHCAL and LFHCAL respectively, are shown in Fig. 3.5. The YR PWG requirements are also plotted as shaded regions, and it is seen that the energy resolution meets or exceeds the requirements for the considered energy range.

Far-Forward and Far-Backward Detectors

Along the electron beam line, downstream of the interaction point, there are detectors dedicated to the luminosity measurement, as well as the tagging of electrons from Bremsstrahlung and low-Q^2 events. These detectors are positioned as seen on the left-hand side of Fig. 3.6, with the labels "Tagger 1", "Tagger 2", and "Lum. detectors", and are together referred to as the far-backward detectors.

The luminosity acts as a normalisation for all physics studies, and is essential for the determination of absolute cross sections, as is needed in the measurement of e.g. the F_2 structure function. The luminosity may be measured using the Bremsstrahlung process $ep \to ep\gamma$, as was the approach used at H1 and ZEUS [73, 74]. The Bremsstrahlung differential cross-section is precisely known, having been first calculated in the Born approximation by Bethe and Heitler in 1934 [65], with one-loop QED radiative corrections being calculated more recently [75]. As the theoretical uncertainty is small, the scale uncertainty of the luminosity measurement is dominated by the systemmatic uncertainties in counting Bremsstrahlung events. The luminosity was measured at HERA-II by ZEUS with a $\sim 1.5\,\%$ scale uncertainty. However, this may be improved upon with precise understanding of the photon acceptance, and the EIC targets a scale uncertainty of $\sim 1\,\%$.

There are two highly complementary luminosity monitoring systems to be employed at EIC IP6, the Direct Photon Detector (DPD), which counts photons directly, and the Pair Spectrometer (PS), which counts $\gamma \to e^+e^-$ pair conversions. The DPD baseline design consists of a tungsten-scintillating fibre (SciFi/W) spaghetti calorimeter, capable of withstanding the multi-GHz event rates present during nominal EIC running. For the PS, a proportion of the Bremsstrahlung photons are converted to e^+e^- pairs in a thin beryllium converter window, and are then separated by a magnet in the spectrometer. The electrons and positrons are deflected towards detectors consisting of three tracking planes followed by a SciFi/W spaghetti calorimeter, where their energies are measured.

Electrons with small scattering angles relative to the electron beam direction are measured by a low-Q^2 electron tagger, which extends the reach of the central de-

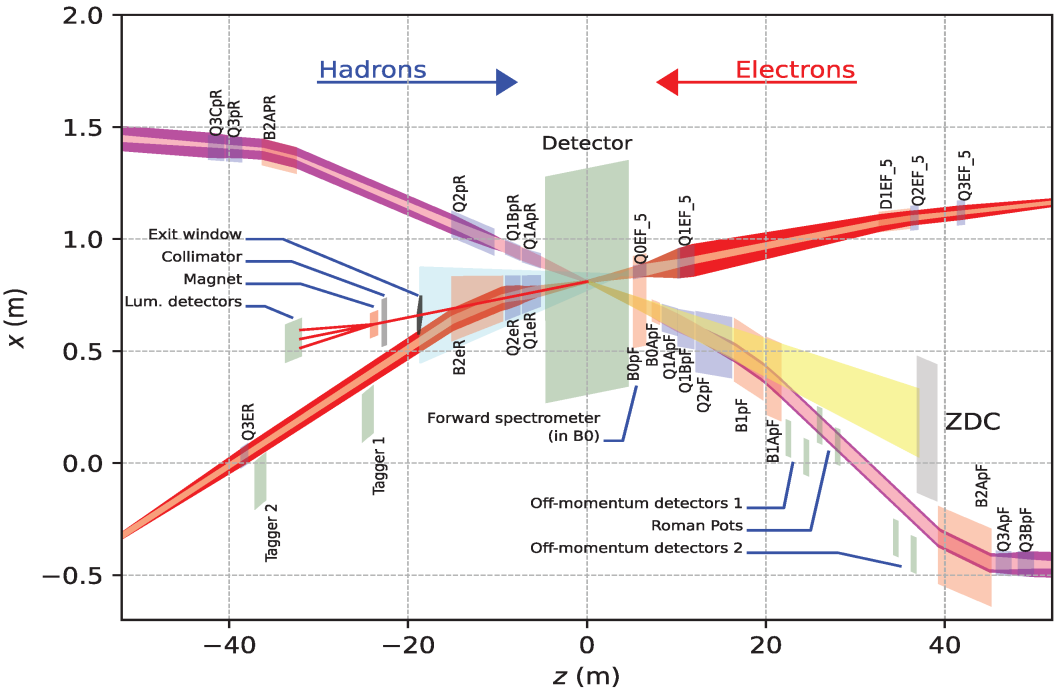

Figure 3.6: Diagram of the layout of EIC IP6. The large green highlighted region is the location of the ePIC central detector. The far-forward (far-backward) region is to the right (left) of the central detector. The B0 Silicon Tracker and Preshower detector is located within the B0pF combined function magnet. Beyond the focusing quadrupoles there are Roman Pots within the beampipe, as well as two sets of off-momentum detectors, and a Zero-Degree Calorimeter outside. In the far-backward direction there are low-Q^2 tagging detectors (Tagger 1 and 2), and luminosity monitoring systems.

tector down to $Q^2 \sim 10^{-6}\,\mathrm{GeV}^2$ [10], enabling the precision measurement of photoproduction events. The low-Q^2 tagger at ePIC consists of two tagger stations, each with four tracking layers and a calorimeter based on the luminosity systems, with the two stations providing coverage for different electron energy ranges. Electrons with less than the nominal beam energy follow a unique path through the magnetic optics, producing a unique electron signature when measured by one of the tagger stations, from which Q^2 can be determined.

Several of the physics channels that are to be studied at the EIC require the tagging of charged hadrons such as protons and pions, or neutral particles such as neutrons or photons, at pseudorapidities far beyond those of the central detector. The far-forward detector subsystems planned for use at the EIC are labelled on the right-hand side of Fig. 3.6, and consist of a Zero-Degree Calorimeter (ZDC), Roman Pots (RP), Off-Momentum Detectors (OMD), and a B0 detector.

The B0 Detector subsystem consists for four tracking planes followed by a crystal EMCAL, embedded in the B0pF combined function magnet. The B0 tracker and EMCAL measure particles with deflections of $5.5 < \theta < 23\,\text{mrad}$, charged particles with $\sim 2 - 4\,\%$ momentum resolution and photons with a $\sim 6 - 7\,\%$ energy resolution [76].

The design strategy for the RP and OMD largely overlap, both taking measurements in tracking planes, and reconstructing particles using a transfer matrix describing the trajectories of charged particles through the magnetic optics. The tracking planes of the RPs are inserted into the beampipe, whereas the OMDs are outside of the beampipe, and so the two systems are sensitive to different momentum ranges. The off-momentum protons from nuclear breakup and decay, which carry a fraction of the beam proton's longitudinal momentum $x_L = p_{z,proton}/p_{z,beam}$, continue past the B0 and are detected in one of the two off-momentum detector stations if $\sim 45 < x_L < 65\,\%$, or in the RP for $\sim 60 < x_L < 95\,\%$ [77].

The trajectories of neutral particles such as neutrons and photons are not affected by the beam line magnets, so these continue along their initial trajectory and are measured in the ZDC. The ZDC for the EIC follows from the ALICE FoCAL design [78], and uses a sampling calorimeter design with lead-silicon followed lead-scintillator layers.

3.2 The ePIC Tracker

The ePIC vertex and tracking detector comprises of layers of silicon Monolithic Active Pixel Sensors (MAPS) closest to the interaction point, complemented by Micro-Pattern Gaseous Detectors (MPGD) further out. The AC-LGAD layers used in the PID systems offer a good spatial resolution ($\sim 30\,\mu\text{m}$), and therefore also contribute to tracking measurements. The AC-LGAD layers are therefore referred to as Timing and Tracking Layers (TTL). The current ePIC detector conceptual design is referred to as "Craterlake", and a visualisation of the tracking system as implemented in simulations is shown in Fig. 3.7, with all relevant subsystems for track reconstruction included. The MAPS based tracker is referred to as the Silicon Vertex and Tracking detector (SVT), and is divided into the Electron Endcaps (EE), Hadron Endcaps (HE), Inner Barrel (IB), and Outer Barrel (OB) components. MPGD tracking layers are present in the barrel and both endcaps. The AC-LGAD ToF layers are present only in the barrel (CTTL) and forward (FTTL) regions.

The ePIC SVT requires sensors with high granularity, low mass, and low power

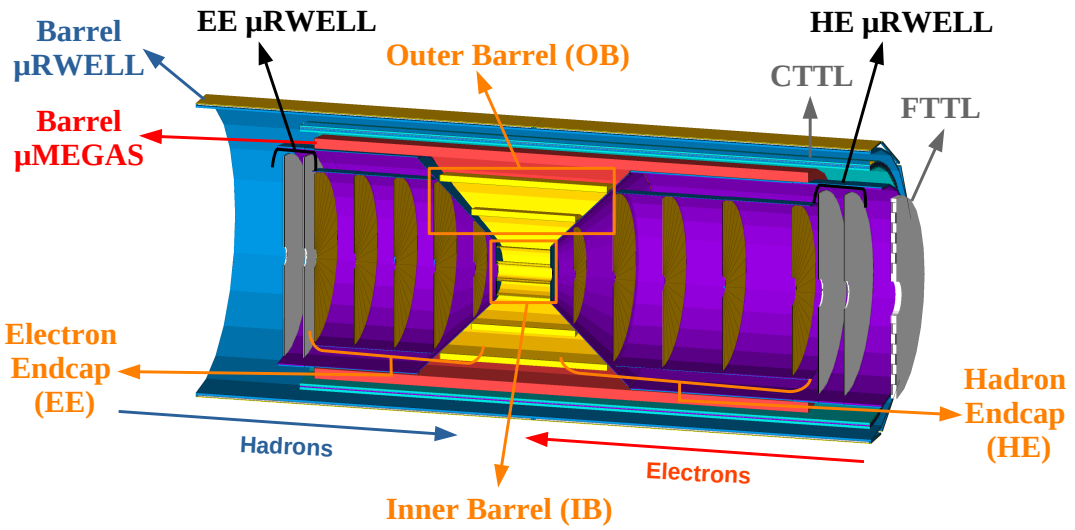

Figure 3.7: Visualisation of the ePIC "Craterlake" tracker conceptual design as implemented in simulations. The gold barrel layers/disks are MAPS, the red barrel layer is the inner barrel MPGD layer, and the subsequent blue layers the barrel ToF and outer barrel MPGD layer. The two silver disks on each side closest to the interaction point are the MPGD disks, and the furthest silver disk in the hadron-going direction the forward ToF. The purple cones and cylinders represent passive material from support and services.

consumption. These requirements are synergistic with the ALICE ITS3 sensor development, and the plan for the ePIC IB is to use the same kind of bent wafer-scale stitched sensors used for ITS3. In sensor stitching, multiple sensor substructures are directly connected on a silicon wafer [79], with material from power distribution and data readout being shifted to the edge of the detector. For stitched sensors that are bent around the beampipe as in ITS3, most of the support material is removed, and if sufficiently low power consumption is achieved then the sensors can be air-cooled. The ITS3 layout is shown in Fig. 3.8. It is made of three cylindrical vertex layers, where each layer comprises two wafer-scale sensors bent around the beampipe. With the removal of material such as kapton and aluminium for circuit boards, carbon and glue for mechanical support, and water for cooling, the remaining material is dominated by the silicon, resulting in a material budget of $\sim 0.05\,\%\ X_0$ per layer.

The sensors in the OB and EE/HE layers are required to cover a larger area compared to the IB, and so factors such as cost and yield are important considerations. A stitched but not wafer-scale sensor, optimised for low cost large area coverage and acceptance is being developed for these layers, and is referred to as the EIC Large Area Sensor (EIC-LAS).

In order to meet the required lengths of the barrel layers, multiple lengths of EIC-

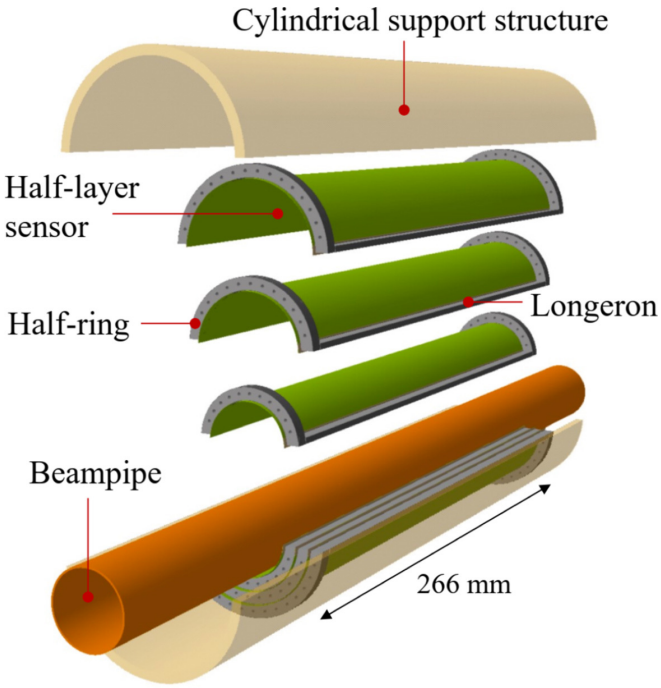

Figure 3.8: Sketch of the ITS3 layout with stitched wafer-scale sensors forming three half-layers (green), along with the beampipe (orange) and support structures (beige). Figure taken from [80].

LAS are required. Work on the development of structures for the OB layers is ongoing, as the design needs to be mechanically rigid and allow for air-cooling, all while keeping the material budget to a minimum. The estimated material budget as implemented in simulations is 0.25 % X_0 for L3, and 0.55 % X_0 for L4, though the material budget in the final mechanical designs is likely to differ from these values, in line with continued R&D efforts. The silicon disks are also to use EIC-LAS, tiled in such a way as to maximise acceptance close to the beampipe. The disks have an estimated material of 0.24 % X_0 per disk in simulations, though this is also expected to change in line with ongoing R&D efforts, see section 4.4.3. The are five disks per side, with the disks in the electron-going direction being labelled ED0-4, and those in the hadron-going direction labelled HD0-4. The full geometry description of the sensitive layers in simulations is outlined in Tables 3.1-3.3.

The MAPS for the inner barrel, outer barrel, and endcap tracking layers, are all to be fabricated using the TowerJazz 65 nm CMOS imaging process. The smaller feature size leads to a smaller pixel size compared to current MAPS such as ALPIDE, which were manufactured using the 180 nm process. While the pixel size has not yet been finalised, the expectation and implementation in simulations is $\sim 20 \times 20\,\mu\text{m}^2$, allowing for a spatial resolution of $\sim 5\,\mu\text{m}$.

The MPGD detectors are based on two technologies: μMegas (Micro-Mesh Gaseous

Table 3.1: Barrel tracker parameters for ePIC "Craterlake" conceptual design as implemented in simulations. The silicon MAPS barrel layers are denoted by L0-4, the two μRWELL layers by Barr MPGD 1/2, and the Barrel AC-LGAD Time-of-Flight layer by CTTL.

Layer	Technology	r (mm)	z_{min} (mm)	z_{max} (mm)
L0	MAPS	36	-135	135
L1	MAPS	48	-135	135
L2	MAPS	120	-135	135
L3	MAPS	270	-270	270
L4	MAPS	420	-420	420
Barr MPGD 1	μMegas	550	-1050	1430
CTTL	AC-LGAD	646	-1125	1740
Barr MPGD 2	μRWELL	725	-1645	1745

Table 3.2: Backward tracker disk parameters for ePIC "Craterlake" conceptual design as implemented in simulations. The silicon MAPS disks are denoted by ED0-4, and the two μRWELL disks by Bwd MPGD 1/2.

Disk	Technology	z (mm)	r_{in} (mm)	r_{out} (mm)
ED0	MAPS	-250	36.76	230
ED1	MAPS	-450	36.76	430
ED2	MAPS	-650	36.76	430
ED3	MAPS	-850	40.06	430
ED4	MAPS	-1050	46.35	430
Bwd MPGD 1	μRWELL	-1100	46.53	500
Bwd MPGD 2	μRWELL	-1200	46.35	500

Table 3.3: Forward tracker disk parameters for ePIC "Craterlake" conceptual design as implemented in simulations. The silicon MAPS disks are denoted by HD0-4, the two μRWELL disks by Fwd MPGD 1/2, and the forward AC-LGAD Time-of-Flight layer by FTTL.

Disk	Technology	z (mm)	r_{in} (mm)	r_{out} (mm)
HD0	MAPS	250	36.76	230
HD1	MAPS	450	36.76	430
HD2	MAPS	700	38.42	430
HD3	MAPS	1000	54.43	430
HD4	MAPS	1350	70.14	430
Fwd MPGD 1	μRWELL	1480	70.14	500
Fwd MPGD 2	μRWELL	1610	70.14	500
FTTL	AC-LGAD	1740	80.00	500

Structure) [81] and μRWELL (Micro-Resistive WELL) [82]. The inner barrel MPGD uses the cylindrical resistive μMegas technology developed for the CLAS12 BMT (Barrel Micromegas Tracker) [83], which provides a spatial resolution of $\sim 150\,\mu m$ and a timing resolution of $\sim 10\,ns$, and provides extra redundancy and pattern recognition for tracking. In the outer MPGD barrel, and for the MPGD disks, layers of planar μRWELLs are used.

An AC-LGAD ToF layer is positioned between the two MPGD layers in the barrel, and an AC-LGAD disk is included in the forward direction. The ToF detectors are the main source of PID at low-p_t. However, due to charge-sharing, an azimuthal resolution of $\sim 30\,\mu m$ can be achieved despite the $500\,\mu m$ segmentation, making these space points also extremely valuable for tracking. The barrel ToF (CTTL) employs a stave-like structure similar to that of the OB MAPS layers, and contributes $\sim 1\,\%$ X_0 to the barrel material budget. The Forward ToF (FTTL) is composed of rectangular modules arranged in horizontal layers to form a disk, and contributes $\sim 2.5\,\%$ X_0 to the material budget in the forward region.

The design outlined here represents the outcome of years of generic and targeted R&D. The choice of technologies, as well as the positions and number of layers, are designed to maximise both the tracking resolutions, and the ability of the full detector to measure the desired physics processes. Studies that have informed the tracker design are a major topic of this thesis, and are outlined in Chapter 4.

3.3 Tracking at Collider Experiments

3.3.1 Spatial Resolution of a Silicon Pixel Detector

The spatial resolution of a segmented silicon detector in a given direction is primarily dependent on its segmentation or pitch in that direction. To find the resolution of such a device, some assumptions are made. A binary readout is assumed, such that when a threshold energy is deposited a "hit" occurs, with no further amplitude information being recorded. The device is also assumed to be uniform and $100\,\%$ efficient over a segment.

For a segmented detector with width d, spanning the range $x = 0$ to $x = d$, the probability of registering a hit on this segment is determined by a normalised uniform probability distribution $f(x)$:

$$f(x) = \begin{cases} \frac{1}{d} & \text{for } 0 \leq x \leq d \\ 0 & \text{otherwise.} \end{cases} \tag{3.1}$$

The standard deviation of this distribution can be found by

$$\sigma = \sqrt{E(x^2) - E(x)^2}, \tag{3.2}$$

where $E(x)$ is the expectation value of the real-valued random variable x, such that

$$E(x) = \int x f(x)\, dx = \int_0^d \frac{x}{d}\, dx = \frac{d}{2} \tag{3.3}$$

and

$$E(x^2) = \int_0^d \frac{x^2}{d}\, dx = \frac{d^2}{3}. \tag{3.4}$$

From Eq. 3.2, the spatial resolution is thus

$$\sigma = \frac{d}{\sqrt{12}}. \tag{3.5}$$

3.3.2 Pointing Resolution

The pointing resolution reflects the accuracy with which the reconstructed collision vertex position is reconstructed. The transverse (longitudinal) pointing resolution is defined as the Gaussian width of the distribution $DCA_{T,reco} - DCA_{T,true}$ ($DCA_{z,reco} - DCA_{z,true}$), where DCA denotes the distance of closest approach of the track to the true vertex, in either the transverse direction (DCA_T) or the longitudinal direction (DCA_z). The distance of closest approach can be derived by considering the innermost layers of a tracking detector. Here, the simplest case of a two-layer detector is considered, with two layers of spatial resolution σ located at radii of r_1 and r_2 from the origin vertex, such that $r_2 > r_1$.

If the position of the track on layer 2 is known with infinite precision, then the position resolution of the reconstructed vertex can be found as a function of the spatial resolution

$$\sigma_{rec,1} = \frac{r_2}{r_2 - r_1}\sigma, \tag{3.6}$$

where $\sigma_{rec,1}$ is the resolution on the reconstructed vertex using only the error on the layer 1 position measurement, and σ is the spatial resolution of a segmented silicon detector. Similarly, if the position on layer 1 is fixed, it can be seen that

$$\sigma_{rec,2} = \frac{r_1}{r_2 - r_1}\sigma, \tag{3.7}$$

and so, combining the contributions to the error from the measurements in each layer, the overall resolution on the reconstructed vertex would be

$$\sigma_{rec} = \sqrt{\sigma_{rec,1}^2 + \sigma_{rec,2}^2}. \tag{3.8}$$

The pointing resolution is a combination of the effects due to the segmented detector's spatial resolutions and radial positions, termed the geometric contribution (See Eq. 3.8), and the uncertainty due to multiple scattering. If there is a beampipe located at radius r_0, then the effective spatial resolution of layer 1, σ_1, becomes

$$\sigma_1 = \sqrt{\sigma^2 + [\sigma_{\mathrm{MS},0}(r_1 - r_0)]^2}, \tag{3.9}$$

where $\sigma_{\mathrm{MS},0}$ represents the angular contribution to the resolution from multiple scattering in the beampipe, which is scaled by the distance to give the positional error at layer 1. The angular error due to multiple scattering is given by [84]

$$\sigma_{\mathrm{MS}} \simeq \frac{13.6\,\mathrm{MeV}}{p \cdot \beta} \cdot \sqrt{\frac{x}{X_0}}, \tag{3.10}$$

where x is the distance traversed in a given medium, X_0 is the radiation length of the medium, and p is the particle momentum. The pointing resolution at layer 2 has contributions from multiple scattering in both the beampipe, and in layer 1, such that

$$\sigma_2 = \sqrt{\sigma^2 + [\sigma_{\mathrm{MS},1}(r_2 - r_1)]^2 + [\sigma_{\mathrm{MS},0}(r_2 - r_0)]^2}. \tag{3.11}$$

The innermost tracking layers are typically designed with low material budget, in which case the contribution to the error of multiple scattering in layer 1 is much smaller than the contribution of multiple scattering in the beampipe. If the multiple scattering contribution of the beampipe is assumed to be much larger than that of layer 1, σ_2 becomes

$$\sigma_2 \simeq \sqrt{\sigma^2 + [\sigma_{\mathrm{MS},0}(r_2 - r_0)]^2}. \tag{3.12}$$

The effective spatial resolutions of layer 1 and layer 2 are given by Eq. 3.9 and 3.12 respectively. Replacing σ in Eq. 3.6 by σ_1, and in Eq. 3.7 by σ_2, the error on the reconstructed vertex position becomes

$$\sigma_{rec} = \sqrt{\left(\frac{r_2}{r_2 - r_1}\sigma_1\right)^2 + \left(\frac{r_1}{r_2 - r_1}\sigma_2\right)^2}. \tag{3.13}$$

However, σ_1 and σ_2 are correlated, and so an additional correlation term must be included

$$\sigma_{rec} = \sqrt{\left(\frac{r_2}{r_2 - r_1}\sigma_1\right)^2 + \left(\frac{r_1}{r_2 - r_1}\sigma_2\right)^2 + 2\left(\frac{r_2}{r_2 - r_1}\sigma_1\right)\left(\frac{r_1}{r_2 - r_1}\sigma_2\right)}, \quad (3.14)$$

which becomes, with the assumption that $r_2 \gg r_1$ and after simplification

$$\begin{aligned}\sigma_{rec} \simeq & \sqrt{\left(\frac{r_1^2}{(r_2 - r_1)^2} + 1\right)\sigma^2 + [\sigma_{\mathrm{MS}}(2r_1 - r_0)]^2} \\ = & \sqrt{\left(\frac{r_1^2}{(r_2 - r_1)^2} + 1\right)\frac{d^2}{12} + (2r_1 - r_0)^2 \frac{(13.6\,\mathrm{MeV})^2}{p^2 \cdot \beta^2} \cdot \frac{x}{X_0}}.\end{aligned} \quad (3.15)$$

Note that σ_{MS} replaces $\sigma_{\mathrm{MS},0}$, and σ is the spatial resolution of a segmented silicon sensor, given by $d/\sqrt{12}$ as before.

It can therefore be seen that the first term of Eq. 3.15 dominates for higher momenta, as the MS term σ_{MS} is negligible at large momenta. The first term depends linearly on the segmentation size d as well as the position of the innermost layer r_1. As such, these parameters should be minimised by mounting the innermost layer as close to the interaction point as possible, as well as using sensors with a fine segmentation. Additionally the inverse dependence on $(r_2 - r_1)$ indicates that this parameter should be maximised, i.e. the first and second layers of a two layer system should be placed as far apart as possible, with no material between them.

The second term of Eq. 3.15 depends on the multiple scattering contribution and dominates at low momenta. It also dominates at large material thickness (from the $\sqrt{\frac{x}{X_0}}$ term). As such, the material in the detector layers and beampipe should be minimised. The linear dependence on the $(2r_1 - r_0)$ term also suggests that the innermost layer should be mounted as close to the beampipe as possible.

3.3.3 Relative Momentum Resolution

To understand the relative momentum resolution of a tracking detector, first consider a detector comprising $N+1$ equally spaced layers with radii $r_0, r_1, ..., r_N$ relative to the interaction point. The "lever arm" of the detector is given by $L = r_N - r_0$, and the spatial resolution of each layer is given by $\sigma = \frac{d}{\sqrt{12}}$, assuming the same pixel pitch. A magnetic field, B, is present along the direction of the beampipe.

The total relative momentum resolution arises from geometric contributions from the detector layout, which are denoted by the subscript "geom", as well as a component due to multiple scattering effects, denoted by the subscript "MS". The momentum is typically reconstructed in two stages: first the transverse momentum is determined by the track's radius of curvature in the magnetic field, and then the polar angle θ is used to calculate the momentum as $p = p_t / \sin(\theta)$. The relative tranverse momentum resolution (relative momentum resolution in the plane perpendicular to the magnetic field) is usually the dominant source of error, and is the focus of the following derivation. The relative transverse momentum resolution can be calculated as the sum in quadrature of the geometric and MS components

$$\frac{\sigma_{p_T}}{p_T} = \sqrt{\left(\frac{\sigma_{p_T}}{p_T}\right)^2_{\text{geom}} + \left(\frac{\sigma_{p_T}}{p_T}\right)^2_{\text{MS}}}. \tag{3.16}$$

At low momenta, this resolution is dominated by multiple scattering effects, with the geometric component dominating at higher momenta. The geometric component is given by [85]

$$\left(\frac{\sigma_{p_T}}{p_T}\right)_{\text{geom}} = p_T \cdot \frac{\sigma}{|q|BL^2} \cdot \sqrt{\frac{720N^3}{(N-1)(N+1)(N+2)(N+3)}}, \tag{3.17}$$

and the multiple scattering component by

$$\left(\frac{\sigma_{p_T}}{p_T}\right)_{\text{MS}} = \frac{1}{|q|B} \frac{13.6\,\text{MeV}}{\beta} \sqrt{\frac{C_N}{X_0 L}}. \tag{3.18}$$

In these equations q represents the charge of the tracked particle, $\beta = v/c$ is its velocity as a fraction of the speed of light, and C_N a dimensionless coefficient related to the uncertainty on the curvature of the track. C_N relates to the number of tracking layers, and ranges from 1.25 for a 3 layer tracker, up to 1.43 for a tracker with infinite layers [84, 86].

It can be seen from the geometric term that the lever arm L should be maximised to achieve a good relative momentum resolution, along with a strong magnetic field and a good sensor spatial resolution. Additionally, the proportionality to the fractional resolution of the p_T term indicates that the resolution degrades at high transverse momenta. The multiple scattering term also improves with a stronger magnetic field and larger lever arm.

3.3.4 Track Reconstruction

Track reconstruction is the process of recovering the properties of charged particles based on measurements made across sensitive volumes of the detector. It is one of the most complex and computationally intensive parts of event processing in high energy particle collider experiments, with the CPU load increasing combinatorially with the track multiplicity [87]. Track reconstruction typically occurs in three stages: reconstructing hit positions, grouping of the hit points into track candidates, then fitting the hit points and extracting the final track parameters.

Reconstructing Space-Points

In the ePIC tracking detector, the sensitive detectors are mostly silicon MAPS. When a charged particle passes through the sensor, it ionises the silicon along its path, producing electron-hole pairs. The pairs are quickly separated by the electric field used to bias the sensors, and in fully depleted MAPS sensors such as those planned to be used in ePIC, the charges move by drift towards the collection electrodes. This produces a signal which can be read out from the sensor, which is considered a "hit" if the signal is larger than a predetermined threshold. A "hit" is defined at the sensor surface initially, but can be mapped to a position in the global detector coordinate system. For a single charged particle traversing several layers and producing a single "hit" per layer, the position resolution of each "hit" in the local coordinate system is given by $d/\sqrt{12}$, as derived earlier (see Eq. 3.5).

The first step of the track reconstruction procedure is the conversion of the raw inputs received from the detector. A binary approach as in the previous example can be used, or the pixel charge can be determined from e.g. time-over-threshold readout. In both cases, pixels in the raw readout should be clustered, i.e. grouped together as a single "hit", to achieve an improved position resolution and to prevent a single charged particle being reconstructed as multiple tracks. Clustering occurs in two dimensions, by successively adding bordering pixels that have registered hits. The average cluster position can be estimated using only the positions of the struck pixels

$$\overrightarrow{r} = \frac{1}{N} \sum_{i=1}^{N} \overrightarrow{l_i} \tag{3.19}$$

or by including the measured charge in each pixel as a weighting factor,

$$\overrightarrow{r} = \frac{1}{\sum_{i=1}^{N} q_i} \sum_{i=1}^{N} q_i \overrightarrow{l_i}\,. \tag{3.20}$$

Here, the average cluster position in local coordinates is given by $\overrightarrow{r}$, while $\overrightarrow{l_i}$ and q_i are the local position and charge of pixel i in the cluster [88]. Knowledge of the location and rotation of sensor surfaces is derived from alignment procedures and included in the geometry description, and may be used to construct a transformation matrix that maps positions in the global coordinate system to the local positions.

Track Finding

There are several techniques available with which collections of space-points may be grouped together into track candidates. In some techniques, referred to as "global" methods, the complete set of all space-points serves as the primary input. An example of this is the Hough transform [89], which was developed in the 1950s for the machine analysis of bubble chamber pictures. In the Hough transform, the space-points are transformed to a parameter space where points originating from the space track share a common intersection. Neural Networks have also been considered for track finding [90, 91], for which there are multiple options for the representation of the data: the 3D positions of clustered space-points can be used as an input, as in traditional "global" methods, or alternatively a "sequential" (local) method could be employed whereby the algorithm works within the discrete space of the pixel sensors. The tracking algorithm for ePIC uses one of the most popular sequential methods, which is the seeding and following approach using a Combinatorial Kalman Filter (CKF) [92].

Track Seeding and Following

In track seeding, a track candidate is built starting from a track "seed", which is a short track segment that provides an initial guess at the parameters associated with a track. Seeds are produced by searching for a triplet of three compatible hits, which are then fitted using e.g. a least squares fit to determine a state vector describing the initial track parameters. The track parameters are described using a "state vector" that has the form $\overrightarrow{x} = (d_0, z_0, \phi, \theta, q/p, t)$, and an associated covariance matrix. Here, d_0 and z_0 are the transverse and longitudinal impact parameters, respectively. The polar angle, defined as the angle between the track and the positive z-axis, is given by θ, while the azimuthal angle in the $x-y$ plane is given by ϕ. The quantity q/p contains the combined information of the charge of the particle and its momentum, and the parameter t denotes the time.

Compatible space-points that can be used to form a seed are found using an orthogonal range search strategy. In an orthogonal range search, seeds are selected constructively rather than destructively: instead of trying a large number of space-

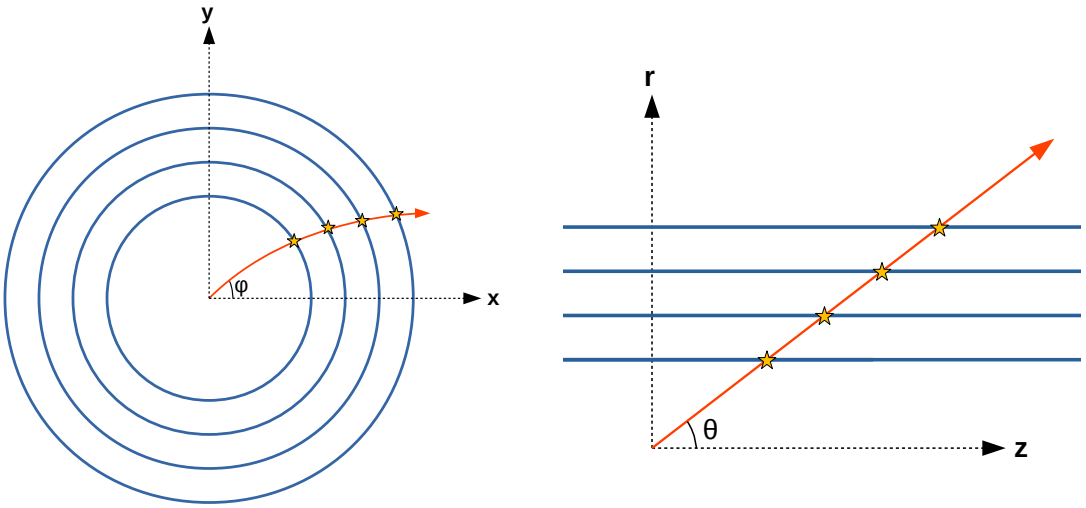

(a) Transverse Plane **(b)** Longitudinal Plane

Figure 3.9: Projection of a track in the a) transverse plane and b) $r-z$ plane. The path of a charged particle is shown in red, with the measurement positions marked where the track meets the detector material (blue).

point groupings and rejecting the majority, the algorithm instead tries to consider only valid seed candidates. The set of space-points acts as the input, and a region of compatibility is defined for each space-point based on the expected behaviour of a particle moving in a uniform magnetic field. The space-points are initially grouped into pairs in adjacent layers, followed by a search for a third space-point in one of the adjacent layers. Triplets of space points are formed.

For a uniform magnetic field directed along the z-axis, the motion of charged particles is circular when drawn in the transverse $(x-y)$ plane, and a straight line in the $r-z$ plane, as shown in Fig. 3.9. A simple fitting procedure, often a least squares fit, is applied occordingly to the two projections, to give a circular fit in the $x-y$ plane and a straight line fit in the $r-z$ plane. The polar angle θ is reconstructed from the angle in the $r-z$ plane, while the longitudinal impact parameter z_0 is found as the z coordinate of the point of closest approach to the origin.

The remaining parameters are determined from the circular fit in the transverse plane. The output of the fit is the radius of curvature of the circular trajectory followed by the charged particle in this projection, ρ, and the coordinates of the centre of the circle, (x_c, y_c). The transverse momentum and charge may be found using the relation $p_t = 0.3B|q|\rho$. The momentum p can thus be calculated as $p_t/\sin\theta$. The sign of the charge, q, can be determined according to the direction of circular motion, as un-like charges spiral in opposite directions. The azimuthal

angle, ϕ is determined from the tangent of the circle at the point closest to the origin $(x, y) = (0, 0)$. The transverse impact parameter, d_0, can be obtained as:

$$d_0 = \sqrt{x_c^2 + y_c^2} - \rho. \tag{3.21}$$

The parameters obtained from the fit can be used to initialise a state vector, $\overrightarrow{x}_0$ (which uses the form described for $\overrightarrow{x}$) with these parameters, and an associated covariance matrix. The seed trajectory is then "followed" through the tracker by extrapolating the track described by $\overrightarrow{x}_0$ to the next tracking plane (accounting for interactions with detector material). At each tracking plane, compatible space-points are searched for and associated with the track candidate, and the state vector (and covariance) updated according to the new hits. This procedure is iterated until the last layer of the tracker is reached. At the end of the track seeding and following process a set of track candidates is found, each being represented by the state vector and covariance matrix determined at the last detector layer.

Track Fitting

With a set of track candidates (and all measurements associated with the candidate) having been found, the parameters of each candidate are refined to achieve the best possible fit. A least squares regression could in principle be used for the fit, but the Kalman filter offers a number of advantages. For track fitting using a Kalman filter, material effects such as multiple scattering and energy loss can be treated locally for each measurement (or layer of material). Fitting using a least squares regression may be computationally taxing due to the need to invert large matrices. Matrix inversion is also required in Kalman fitting, but only small matrices need to be inverted.

For track fitting with a Kalman filter, it is assumed that the surfaces that are crossed by the track, which may be a measurement layer or material layer, have well defined positions and orientations. At the intersection point of the track with layer k, the state vector at this layer is given by $\overrightarrow{x}_k$ and contains information about the local position, direction, and momentum of the track. The uncertainty of the information contained by the state vector is given by the covariance matrix $\mathbf{C}_k$.

Track fitting with a Kalman filter typically occurs in two stages: Kalman filtering and Kalman smoothing. In the filtering stage (the forward pass), the measurements are sequentially processed and the state vector and its covariance updated for each measurement. In the smoothing stage (the backward pass), a second filter is run in the opposite direction, propagating all of the information available at the final

measurement of the forward pass, $\overrightarrow{x}_n$, back to all previous states. The forward pass starts with a prediction step, which is summarised in Eq. 3.22:

$$\overrightarrow{x}_{k|k-1} = \mathbf{f}_{k|k-1}(\overrightarrow{x}_{k-1}), \qquad \mathbf{C}_{k|k-1} = \mathbf{F}_{k|k-1}\mathbf{C}_{k-1}\mathbf{F}^T_{k|k-1}. \tag{3.22}$$

Here, $\overrightarrow{x}_{k|k-1}$ is the prediction of the state vector at surface k, based on the information at surface $k-1$. The function $\mathbf{f}_{k|k-1}$ is the track propagator, which projects the track from surface $k-1$ to surface k according to the equations of motion for a charged particle in a magnetic field. $\mathbf{F}_{k|k-1}$ is the Jacobian matrix for $\mathbf{f}_{k|k-1}$, which collects the derivatives of the track propagator, allowing for an approximate linearised error propagation. It is defined as:

$$\mathbf{F}_{j|i} = \frac{\partial \overrightarrow{x}_j}{\partial \overrightarrow{x}_i}. \tag{3.23}$$

After the prediction step, the state vector at surface k is updated. The amount by which the state vector should be adjusted is encoded in the Kalman gain matrix, which is calculated by comparing the measurement $\overrightarrow{m}_k$ to the prediction of the measurement at surface k, using the extrapolated state vector from surface $k-1$. The update step is summarised in Eq. 3.24:

$$\overrightarrow{x}_k = \overrightarrow{x}_{k|k-1} + \mathbf{K}_k \overrightarrow{r}_k, \qquad \mathbf{C}_k = (\mathbb{1} - \mathbf{K}_k\mathbf{H}_k)\mathbf{C}_{k|k-1}, \tag{3.24}$$

where the Kalman gain for a measurement at surface k, $\mathbf{K}_k$, is given by

$$\mathbf{K}_k = \mathbf{C}_{k|k-1}\mathbf{H}^T_k(\mathbf{V}_k + \mathbf{H}_k\mathbf{C}_{k|k-1}\mathbf{H}^T_k)^{-1}. \tag{3.25}$$

Note that the superscript T denotes the transposition of the associated matrix, and the exponent of -1 denotes its inversion. Here, $\mathbf{H}_k$ is a linear function that maps state vector $\overrightarrow{x}_k$ to a measurement m_k. The difference between the observed and predicted measurement is given by, $\overrightarrow{r}_k$, and $\mathbf{V}_k$ is the covariance matrix associated with the measurement. The full mathematical details are not discussed here, but can be found in references [88, 93].

After both the Kalman filtering and Kalman smoothing steps have taken place, a state vector describing the best fit is obtained, and the final values of the parameters associated with the track are set according to this state vector.

Chapter 4

Tracking Simulations

The design of the ePIC detector described in the previous chapter, is the culmination of performance and feasability studies performed over several years. There have been various detector configurations proposed as part of the development, over the course of the Yellow Report, call for detector proposals, and subsequent optimisation of the chosen reference detector towards the ePIC detector.

The work carried out for this thesis has informed the choices made in the design of the current ePIC tracking system, by applying the lessons learned from studies of the tracking performance with many different tracker configurations. The results of such studies are presented in this chapter.

4.1 Simulation Software Tools

Prior to the development of dedicated software solutions for ePIC simulation, reconstruction, and analysis, many of the software packages used for EIC studies were inherited from other experiments and, where necessary, modified to better suit the needs of the EIC.

The Fun4All framework [94] was originally built for the reconstruction and analysis of real and simulated data in the PHENIX experiment [95]. With the sPHENIX experiment [71] succeeding PHENIX, simulation capabilities were added to Fun4All via the PHG4Reco analysis module, which provides an interface to Geant4 [96].

The Fun4All framework consists of modules based on compiled C++ code, controlled by steering macros in the ROOT software framework [97]. It provides modules that are used to input generated events (either by generating particles directly within

the module or by reading the output of an event generator), propagate particles through the geometry using Geant4, digitise the output, and reconstruct tracks. Track reconstruction is performed by the PHG4TrackFastSim module, which performs "digitisation" by applying a Gaussian smearing according to a chosen position resolution, usually $d/\sqrt{12}$ (see Section 3.3.1), and subsequently reconstructs tracks via an interface to the GENFIT track reconstruction toolkit [98].

Fun4All is particularly convenient for simulations of the tracking detector, as many aspects of the tracking geometry may be edited within the steering macro, avoiding the need for recompilation. This makes Fun4All ideal for the geometry optimisation studies that are a topic of this thesis.

Various tools have been developed for the simulation, reconstruction, and analysis needs of the ePIC experiment, which are collectively referred to as the ePIC software. The detector geometry definition is given by the DD4hep package [99], which describes the geometry in an XML format used both for simulation (via Geant4) and the reconstruction. The reconstruction framework included in the ePIC software stack is EICrecon [100], which includes track reconstruction via the ACTS toolkit [101]. A further discussion of the ePIC software is given in Chapter 5, including the reconstruction of full physics events.

Simulations in this chapter are performed using Fun4All unless otherwise specified.

4.2 Resolution Benchmarking Procedure

The main performance plots produced to benchmark the tracker performance are the relative momentum resolution and transverse pointing resolution, which are labelled on plot axes in this chapter as $\Delta p/p$ and DCA_T (Distance of Closest Approach in the Transverse plane) respectively. These are presented as a function of p or p_T, using the true p or p_T value from the simulation. Where these labels are used, along with labels indicating the plot as a resolution plot, the plotted quantity on axes labelled by $\Delta p/p$ is the Gaussian width of the p_{reco}/p_{true} distribution, and those labelled by DCA_T show the Gaussian width of the $DCA_{T,reco} - DCA_{T,true}$ distribution. Here, the "reco" and "true" subscripts denote the reconstructed and generated values from the simulation respectively. The Gaussian width is determined as the value of σ from a Gaussian fit to the distribution over the range -2σ to 2σ, as pictured in Fig. 4.1. The range restriction serves to exclude the tails of the distributions, and thus gives a better fit to the centroid.

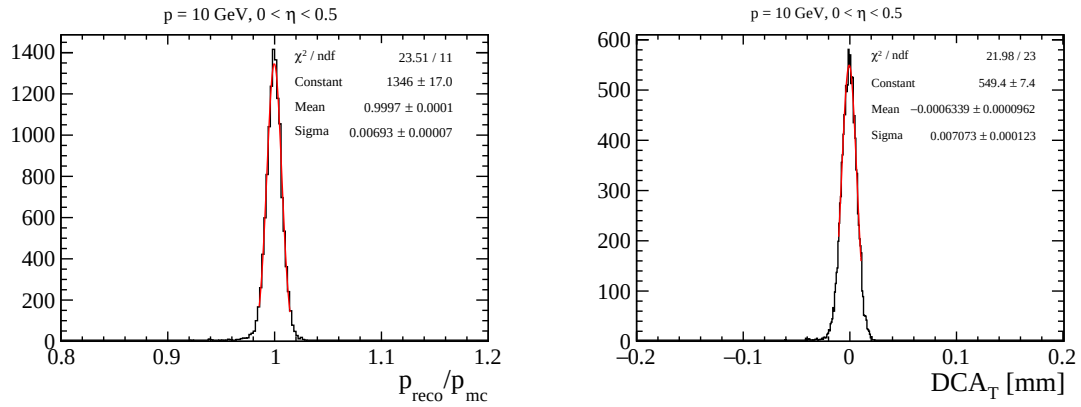

(a) **(b)**

Figure 4.1: Example distributions of (a) p_{reco}/p_{true} and (b) DCA_T, which are used to extract the relative momentum and transverse pointing resolutions respectively. The distributions are shown for electrons with $p_{true} = 10\,\text{GeV}$ that were generated in the range $0 < \eta < 0.5$ and passed through the current ePIC tracking geometry. A Gaussian fit is applied in the range -2σ to 2σ and the width "Sigma" used to set the resolution for a single momentum and η range.

For studies using single generated particles, as is the case for many of the studies in this chapter, the particles are generated according to three possible configurations:

- Generate particles with a flat distribution of generated momenta
- Generate particles with a flat distribution of generated transverse momenta
- Generate particles at fixed momenta

The errors on the plotted p or p_T values are set according to the generation procedure, with no horizontal error bars in plots where particles are generated at fixed momenta, and for those generated with a flat p or p_T distribution horizonal error bars are set as the width of the bin divided by $\sqrt{12}$, corresponding to the standard deviation of a uniform distribution in the chosen bin.

For assessments of tracking performance using single particles, the particles are generated to give a uniform distribution in η, unless otherwise stated. While the relative momentum resolution and transverse pointing resolution are mainly used to benchmark the tracking performance, as the Yellow Report identified resolution requirements for these quantities, other quantities such as the longitudinal pointing resolution (DCA_z), relative transverse momentum resolution, and the polar and azimuthal angle resolutions may be informative. The same fitting procedure extends to any of these quantities, with a Gaussian fit being applied over the range -2σ to 2σ of the relevant distribution.

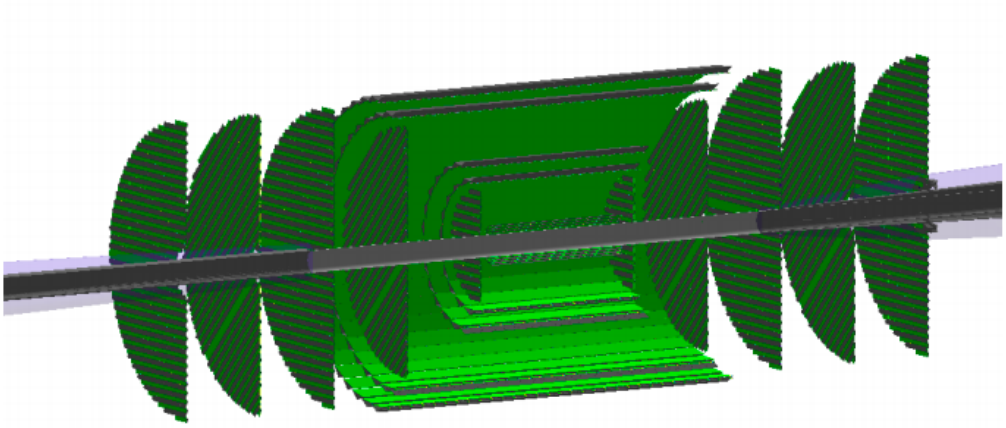

Figure 4.2: All silicon tracker layout as implemented in Fun4All simulations.

4.3 Initial Studies

4.3.1 Performance of Yellow Report Tracking Detectors

The work of this thesis began following the conclusion of the Yellow Report effort, for which there were two potential designs presented for the tracking detector: an "all silicon" design for which silicon MAPS make up the entire tracker, and a "hybrid" design using silicon MAPS for the inner detector, complemented by gaseous detectors for track measurements further from the interaction point. The gaseous detector technologies considered for the "hybrid" tracker design were Micro-Pattern Gas Getectors (MPGDs), and a time projection chamber (TPC). The TPC was chosen for the hybrid-baseline layout.

In addition to the two different tracker designs, two possibilities also existed for the solenoidal superconducting magnets that would be used to provide the necessary magnetic field for the tracking detector. A magnetic field strength of 1.5 T could be achieved through modifications of the BABAR/sPHENIX magnet, or alternatively a new superconducting solenoid could be produced in order to provide a 3 T field.

An overview of the performance achieved by two possible detector configurations from the time of the Yellow Report is given in this section. A visualisation of an all silicon tracker layout as implemented in Fun4All simulations is shown in Fig. 4.2, and a visualisation of the Yellow Report silicon plus TPC hybrid baseline layout in Fig. 4.3. Multiple groups worked on the various detector concepts, and there are some differences between the all silicon configuration presented here and the concept chosen as the Yellow Report all silicon baseline. Notably the all silicon design presented here includes an extra barrel layer compared to the YR all silicon baseline,

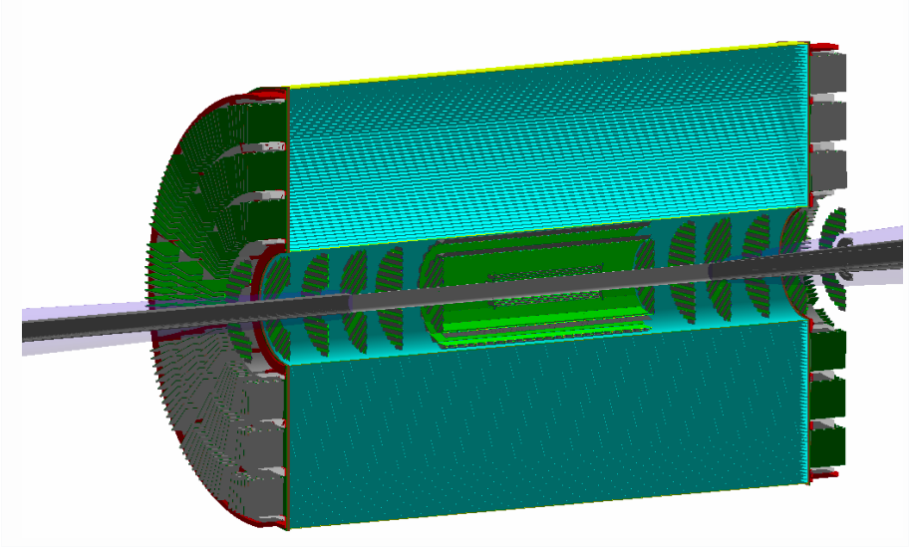

Figure 4.3: Yellow Report hybrid baseline layout as implemented in Fun4All simulations. The silicon layers and disks are shown in green, with the TPC in light blue.

and does not include passive support/service material (further details surrounding the configuration presented here can be found in reference [84]).

The positions of the various active layers in the all silicon layout are summarised in Table 4.1 and Table 4.2, and the YR hybrid baseline is summarised in Table 4.3 and Table 4.4. The parameters of the silicon layers are set according to projections for an EIC sensor based on the ITS3 development. The pixel pitch of the silicon layers in the Fun4All similations is 10 µm (a spatial resolution of $10\,\mu m/\sqrt{12}$), which corresponds to the smallest targeted pixel pitch for ITS3, though it should be noted that multiple pixel sizes are considered during development, with the EIC targeting a sensor that provides ∼5 µm spatial resolution.

The material budget of the various silicon layers are also based on estimates for an EIC sensor based on ITS3 technology. The material budget for the vertexing layers is 0.05 % X_0, arising from the ∼ 50 µm of silicon that makes up almost the entire material budget in an air-cooled, self-supported stitched wafer-scale sensor. The silicon disks target a material budget of 0.24 % X_0, and the larger radius barrel layers 0.55 % X_0, which is assumed to account for the support structure and services.

The TPC in the YR hybrid baseline configuration is based on the compact sPHENIX TPC [102], which spans $20 < r < 78$ cm radially and occupies a length of 211 cm in z. The TPC is filled with a neon and CF_4 gas mixture. The TPC implementation in Fun4All assumes a fixed spatial resolution of 200 µm in ϕ and 500 µm in z, though

Table 4.1: Barrel tracker parameters for all silicon design as implemented in Fun4All simulations.

Layer	Technology	r (mm)	Material (X_0)	Pitch (µm)
L0	MAPS	36.4	0.05 %	10
L1	MAPS	44.5	0.05 %	10
L2	MAPS	52.6	0.05 %	10
L3	MAPS	180	0.55 %	10
L4	MAPS	226.8	0.55 %	10
L5	MAPS	385.5	0.55 %	10
L6	MAPS	432.3	0.55 %	10

Table 4.2: Tracker disk parameters for all silicon design as implemented in Fun4All simulations. The design is symmetric and z refers to the position in the positive and negative z directions. All disks have a material budget of 0.24 %

Disk	Technology	z (mm)	r_{in} (mm)	r_{out} (mm)	Pitch (µm)
D0	MAPS	250	36.4	170	10
D1	MAPS	490	36.4	362.6	10
D2	MAPS	730	49.9	432.3	10
D3	MAPS	970	66.7	432.3	10
D4	MAPS	1210	99.3	432.3	10

Table 4.3: Barrel tracker parameters for YR hybrid baseline design as implemented in Fun4All simulations.

Layer	Technology	r (mm)	Material (X_0)	Pitch (µm)
L0	MAPS	36.4	0.05 %	10
L1	MAPS	44.5	0.05 %	10
L2	MAPS	52.6	0.05 %	10
L3	MAPS	133.8	0.55 %	10
L4	MAPS	180	0.55 %	10
TPC	TPC	200-780	∼2 %	N/A

Table 4.4: Tracker disk parameters for YR hybrid baseline design as implemented in Fun4All simulations. The design is symmetric and z refers to the position in the positive and negative z directions. All disks have a material budget of 0.24 %

Disk	Technology	z (mm)	r_{in} (mm)	r_{out} (mm)	Pitch (µm)
D0	MAPS	220	36.4	71.3	10
D1	MAPS	430	36.4	139.4	10
D2	MAPS	586	36.4	190	10
D3	MAPS	742	49.9	190	10
D4	MAPS	898	66.7	190	10
D5	MAPS	1054	83.5	190	10
D6	MAPS	1210	99.3	190	10

in a realistic TPC the spatial resolution may depend on the drift distance and track angle.

The beampipe is implemented in simulations as a beryllium cylinder with an inner radius of 31 mm and a thickness of 760 µm in the central region, with aluminium extensions further from the interaction point.

Events were generated and propagated through the geometry with the following settings:

- Generated particle: single π^+
- Generated distributions: uniform in p and η
- Ranges: $0 < p < 30\,\text{GeV}$, $-1 < \eta < 3.5$
- Magnetic Field: 1.5 T and 3 T uniform field

The transverse pointing resolution for the two configurations is summarised in Fig. 4.4 for uniform 1.5 T and 3 T magnetic fields, as determined from Fun4All simulations. The equivalent plots for the relative momentum resolution are shown in Fig. 4.5.

The inner layers of both the all silicon and YR hybrid baseline detectors are composed of MAPS, with the same material budget and pixel pitch for the vertexing, barrel, and disk layers between the two layouts. As such, the dominant factors determining the transverse pointing resolution are the distance of the first hit from the interaction point, and the distance between the first and second hit positions (see Section 3.3.2). As the vertexing layers (the first three layers in the barrel) are the same for both configurations, the transverse pointing resolution of each configuration is similar in the central region ($-1 < \eta < 1$).

The first disks (D0/D1) in the all silicon layout are positioned at $z = 250/490\,\text{mm}$, and in the YR hybrid baseline layout they are positioned at $z = 220/430\,\text{mm}$. If Eq. 3.15 is considered, it is predicted that the multiple scattering contribution is responsible for the deterioration in resolution at low p_T. Similarly, the geometry and pixel size dependent term that is responsible for the flat distribution at larger momenta relates to the distance between the first two hits. While D0 in the YR hybrid baseline layout is positioned closer to the interaction point than the D0 in the all silicon layout, the distance between D0 and D1 is smaller, so the all silicon layout gives a slightly better transverse pointing resolution at large transverse momenta for $\eta > 1$.

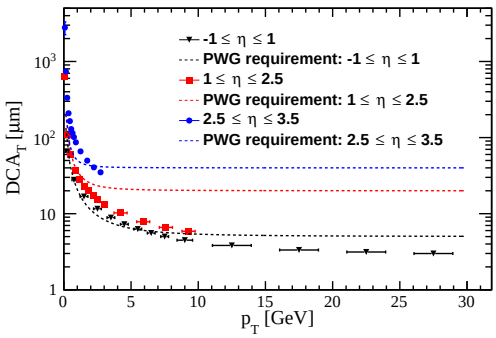

(a) DCA_T resolution: All silicon at 1.5 T

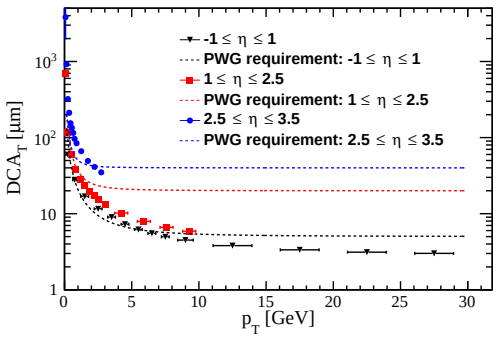

(b) DCA_T resolution: All silicon at 3 T

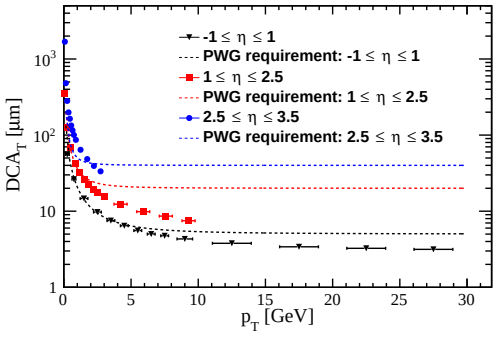

(c) DCA_T resolution: YR hybrid at 1.5 T

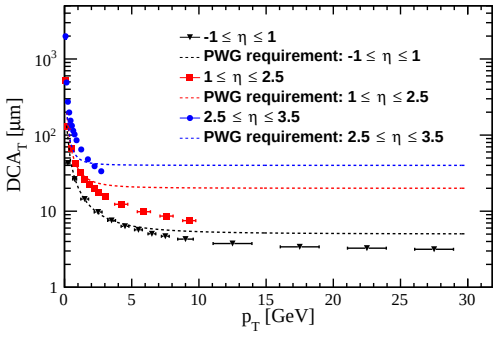

(d) DCA_T resolution: YR hybrid at 3 T

Figure 4.4: Transverse pointing resolution for the (top) all silicon and (bottom) YR hybrid baseline tracker design with magnetic fields of 1.5 T and 3 T.

The relative momentum resolution, similarly to the transverse pointing resolution, is given by individual contributions due to multiple scattering and geometric effects, summed in quadrature. It can be understood from Eq. 3.17 and Eq. 3.18 that the geometric term is proportional to the momentum, while the multiple scattering term is independent of the momentum except at the lowest momenta, where the approximation $\beta \approx 1$ no longer holds true. The relative momentum resolution parametrisation used in the Yellow Report tracking requirements is of the form

$$\frac{\sigma_p}{p} = A \cdot p \oplus B.$$

The YR hybrid baseline layout deviates from this parametrisation when the full momentum range is considered, and may instead be divided into two momentum ranges ($p \lesssim 5\,\text{GeV}$ and $p \gtrsim 5\,\text{GeV}$), for which the MAPS tracker and TPC each dominate the resolution.

In the central region, the relative momentum resolutions of the two configurations are comparable at low momenta. The YR hybrid baseline tracker gives a better resolution for $p \lesssim 3\,\text{GeV}$, as the positioning the MAPS layer L3 at a smaller radius

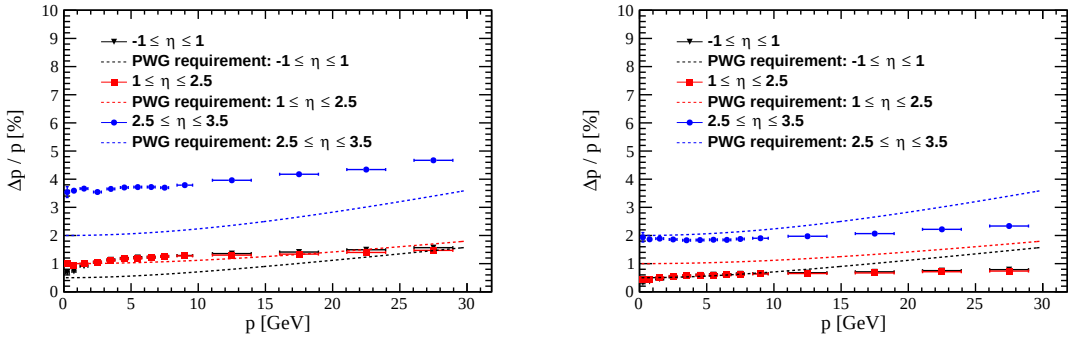

(a) $\frac{\Delta p}{p}$ resolution: All silicon at 1.5 T

(b) $\frac{\Delta p}{p}$ resolution: All silicon at 3 T

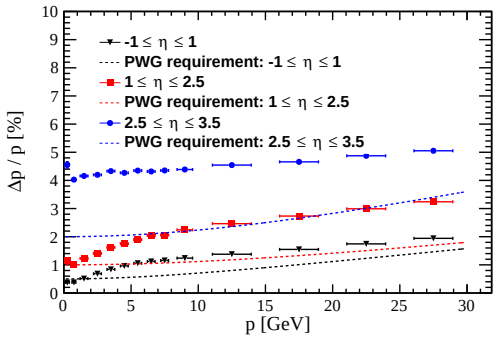

(c) $\frac{\Delta p}{p}$ resolution: YR hybrid at 1.5 T

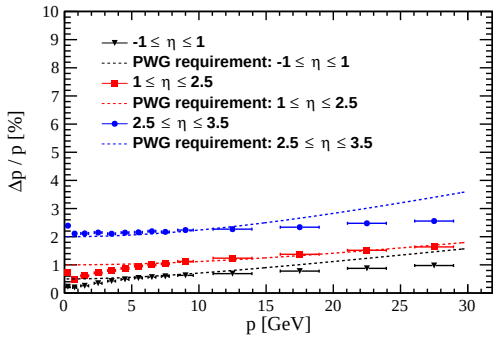

(d) $\frac{\Delta p}{p}$ resolution: YR hybrid at 3 T

Figure 4.5: Relative momentum resolution for the (top) all silicon and (bottom) YR hybrid tracker design with magnetic fields of 1.5 T and 3 T.

compared to the all silicon L3 improves the sagitta measurement in low momentum tracks, where the radius of curvature is small. The barrel of the all silicon configuration has a larger lever arm of high precision MAPS layers compared to the YR hybrid baseline, which in turn leads to a smaller geometric term. Consequently, the relative momentum resolution in the all silicon configuration degrades more gradually with increasing momentum compared to the silicon plus TPC layout, and a better resolution is observed in the all silicon layout for $p \gtrsim 10\,\text{GeV}$ at central pseudorapidities.

The relative momentum resolution of the all silicon configuration at intermediate pseudorapidities ($1 < \eta < 2.5$) is better than that of the YR hybrid baseline across the full momentum range. This owes to the fact that the full lever arm of the silicon disks (432.3 mm) is available in the all silicon layout up to $\eta \sim 1.75$, after which L decreases with increasing η. In the YR hybrid baseline the TPC lever arm decreases with increasing η starting from $\eta \sim 1.1$, corresponding to the outer edge of the TPC.

Both configurations are instrumented by disks using the same MAPS technology in the forward region ($2.5 < \eta < 3.5$), so the relative momentum resolution is determined by the lever arm and material budget. Both layouts occupy the same lever

arm in z, with the final disks positioned at $z = \pm 1210\,\text{mm}$, and so provide a similar relative momentum resolution. The small difference between the relative momentum resolutions of the two configurations in this range is due to the choice of 5 compared to 7 disks. In the hybrid layout, extra disks are included for redundancy in the case that a disk fails. This comes at the cost of added material, which is detrimental to the relative momentum resolution.

To determine whether a tracker configuration is capable of delivering the performance required for the EIC physics programme, the tracking resolutions are compared to the requirements outlined by the Physics Working Groups (PWG) during the Yellow Report, which are summarised in Table 2.1. As the transverse pointing resolution does not directly depend on the magnetic field strength, the resolution obtained for a given layout is compatible for the 1.5 T and 3 T field configurations. It can be seen in Fig. 4.4 that the transverse pointing resolution for each layout is consistent with the PWG requirements.

Unlike the transverse pointing resolution, the multiple scattering and geometric terms that describe the relative momentum resolution depend on the magnetic field strength as $1/B$. Consequently, the relative momentum resolutions for a given layout, using the two magnetic field strengths considered here, differ by a factor of ~ 2. The relative momentum resolution for a given detector concept is therefore determined by the lever arm of the high precision and low material MAPS layers, and the strength of the magnetic field.

If a 1.5 T magnetic field is used, the all silicon layout is consistent with the PWG requirement in the $1 < \eta < 2.5$ range, but not for $2.5 < \eta < 3.5$. The momentum resolution requirement is within reach at 1.5 T for $-1 < \eta < 1$ with the all silicon layout, so meeting the requirement at the lower field strength may be possible with further optimisation, and research into low material solutions. The relative momentum resolution requirements for $2.5 < \eta < 3.5$ are challenging to meet at 1.5 T with the all silicon layout. However, the PWG requirements are met over the full momentum range for $-1 < \eta < 3.5$ with the all silicon layout at 3 T.

The YR hybrid baseline layout does not meet the requirements for any region when using a 1.5 T magnetic field. However, the PWG requirements are met over the full momentum range, for $-1 < \eta < 3.5$ when the 3 T field is applied. As such, it is clear that a tracking detector that delivers the required performance can be achieved, but requires a compromise between the area of silicon (and the associated costs), and the choice of magnet.

If the BABAR/sPHENIX magnet is used, and tracking performed using a 1.5 T field, the chosen tracking detector should use the maximum possible lever arm of high precision and low material MAPS layers. Conversely, if a new 3 T superconducting solenoid is purpose-built for use in an EIC detector, then the area that is instrumented by silicon MAPS may be reduced, and instead a tracking detector comprising a compact silicon tracker complemented by (less expensive) gaseous detectors for large area tracking may be used.

As the two layouts discussed in this section are symmetric in design, the performance at backward pseudorapidities is predicted to match that of the equivalent forward region, i.e. the performance for $-2.5 < \eta < -1$ is equal to that of $1 < \eta < 2.5$, and $-3.5 < \eta < -2.5$ to $2.5 < \eta < 3.5$. The PWG requirements outlined in Table 2.1 are not symmetric, as the scattered electron measurement in some exclusive DIS channels imposes a stringent requirement on the relative momentum resolution in the backward region.

The exclusive VMP process requires that scattered electrons be measured with a resolution of $\sigma_p/p \sim 0.5\,\%$ [56] (no line is drawn on Fig. 4.5 for this requirement). It is clear that neither the all silicon nor the hybrid baseline layout is capable of meeting this requirement in the $-3.5 < \eta < -2.5$ region, even with the larger 3 T field. While the tracker may not be capable of delivering the desired resolution, a high resolution electromagnetic calorimeter is also intended to instrument the backward region. Through the optimal combination of measurements from the tracking and calorimetry systems, it may still be possible to reconstruct the DIS electron with a sufficient resolution for this process.

4.4 Studies for a Hybrid Tracker based on a 3 T Solenoid

Studies conducted throughout the Yellow Report effort provided the groundwork for the development of a specific, optimised detector for EIC IP6. The work presented in this section follows studies that were performed for the optimisation of the tracking system of the proposed ATHENA detector (detailed in the ATHENA detector proposal [61]). A determining factor in the design of the ATHENA detector was the decision to have the magnetic field be produced by a large-bore solenoidal magnet with a maximum field strength of 3 T. The strong field provided by this magnet permits the use of a hybrid silicon plus gas detector tracking system, in the form of a

compact silicon inner tracker, complemented by MPGD barrel layers and disks that provide coverage at large radii. Several configurations that were considered for the ATHENA tracking system are studied in this section, which took place in parallel with the evolution of the tracking design.

4.4.1 Disk Layout Comparison

The tracking resolutions at large η are directly impacted by the number and layout of the silicon disks, with the choice of disk configuration ultimately being a trade-off between resolution, coverage, and redundancy. Here, the results of Fun4All simulation studies, that were performed using an early iteration of the ATHENA tracking system with three different silicon disk configurations, are presented.

The positions and radii of the silicon barrel layers and disks in this early iteration of ATHENA are equivalent to the those of the silicon barrel layers and disks used in the Yellow Report hybrid baseline described in Table 4.3 and Table 4.4. The tracker is composed of five MAPS barrel layers spanning $36.4 < r < 180\,\text{mm}$, and seven MAPS disks spanning $220 < |z| < 1210\,\text{mm}$.

The MPGDs in the barrel region follow a design detailed in the Yellow Report, which is based on the technology developed for the CLAS12 barrel Micromegas tracker [83]. The MPGD tracker consists of two cylindrical layers placed at a radial distance of $\sim 50\,\text{cm}$ from the interaction point, and four outer layers placed at $r \sim 80\,\text{cm}$. Each of the Micromegas layers assume a spatial resolution in $r - \phi$ and z of $150\,\mu\text{m}$, and a material budget in the active area of $\sim 0.3\,\%\ X_0$, with each layer having sufficient length such as to cover $|\eta| < 1$. The MPGDs in the hadron and electron endcaps come in the form of two large-area GEM (Gas Electron Multiplier) stations per side. The inner forward and inner backward GEM stations use three triple-GEM disks each, the outer forward uses two stations, and the outer backward uses one. The simulation assumes a spatial resolution of $50\,\mu\text{m}$ in $r - \phi$ and $250\,\mu\text{m}$ in z, as well as a material budget in the active area of $\sim 0.4\,\%\ X_0$. The outer radii of the GEM disks were chosen such that they provide coverage at $|\eta| > 1.05$.

A visualisation of the tracking system as implemented in the Fun4All simulations is shown in Fig. 4.6. The visualisation shows the 7 silicon disk configuration used in the YR hybrid baseline layout. In addition to this layout, two 5 disk configurations are considered, which occupy the same lever arm as the 7 disk layout, but differ in their spacing. In the first layout, labelled as 5 disk Config 1, the two innermost disks and the outermost disk are positioned as D0, D1, and D6 in the YR hybrid

Table 4.5: Silicon disk parameters for configuration labelled 5 disk Config 1, as implemented in Fun4All simulations.

Disk	z (mm)	r_{in} (mm)	r_{out} (mm)
D0	220	36.4	71.3
D1	430	36.4	139.4
D2	690	57.4	190.0
D3	950	78.3	190.0
D4	1210	99.3	190.0

Table 4.6: Silicon disk parameters for configuration labelled 5 disk Config 2, as implemented in Fun4All simulations.

Disk	z (mm)	r_{in} (mm)	r_{out} (mm)
D0	220	36.4	71.3
D1	468	52.1	151.6
D2	715	67.9	190.0
D3	963	83.6	190.0
D4	1210	99.3	190.0

Table 4.7: GEM disk parameters for configuration used in ATHENA disk layout and gold coating studies, as implemented in Fun4All simulations.

Disk	z (mm)	r_{in} (mm)	r_{out} (mm)
EOG0	-1900	110	1617
EIG2	-1400	100	1037
EIG1	-1350	100	1037
EIG0	-1300	100	1037
HIG0	1300	140	1037
HIG1	1350	140	1037
HIG2	1400	140	1037
HOG0	2950	210	2353
HOG1	3100	210	2353

baseline (Table 4.4), with the two remaining disks spaced equally between D1 and the outermost disk. The second layout, labelled as 5 disk Config 2, retains the disks positioned at D0 and D6 in the YR hybrid baseline, and spaces the three remaining disks equally between them. The 5 disk configurations are summarised in Tables 4.5 and 4.6, the 7 disk configuration is as previously summarised in Table 4.4, and the GEM disks are summarised in Table 4.7.

Previous studies assumed a uniform magnetic field which, while providing a good estimate of charged particle curvature for much of the angular acceptance, loses realism when the more forward/backward regions are considered, as is the case for these studies. In a realistic solenoidal magnet, the field lines curve at further forward/backward angles, resulting in non uniform behaviour and a small loss in

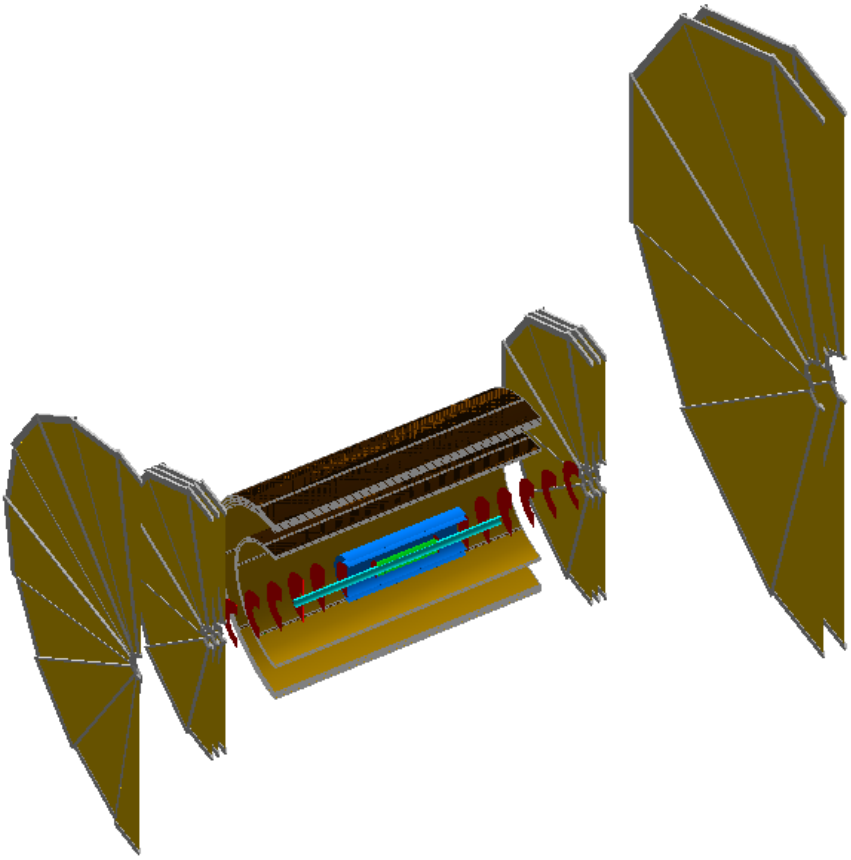

Figure 4.6: An initial ATHENA silicon plus MPGD tracker layout as implemented in Fun4All simulations relating to the disk layout and gold beampipe coating.

performance, which is important to include for studies in this region. The majority of the charged particles measured in the hadron endcaps will be hadronic particles such as $\pi^{\pm}$ and $K^{\pm}$, while in the electron endcaps the most common charged particles to be measured are DIS electrons. Taking these factors into account, the settings used in the Fun4All simulations in this section are:

- Generated particle: single e^{-} ($\eta < -1$), single π^{-} ($\eta > -1$)
- Generated distributions: uniform in p_t and η
- Ranges: $0 < p_t < 30\,\text{GeV}$, $-3.5 < \eta < 3.5$
- Magnetic Field: 3 T solenoidal field map

Comparisons of the three silicon disk configurations in terms of their relative momentum and transverse pointing resolutions, as determined from Fun4All simulations, are shown in Fig. 4.7. As before, the transverse pointing resolution is limited by the position of the first hit, and the distance between the first and second hits.

No significant difference is seen between the transverse pointing resolution of the

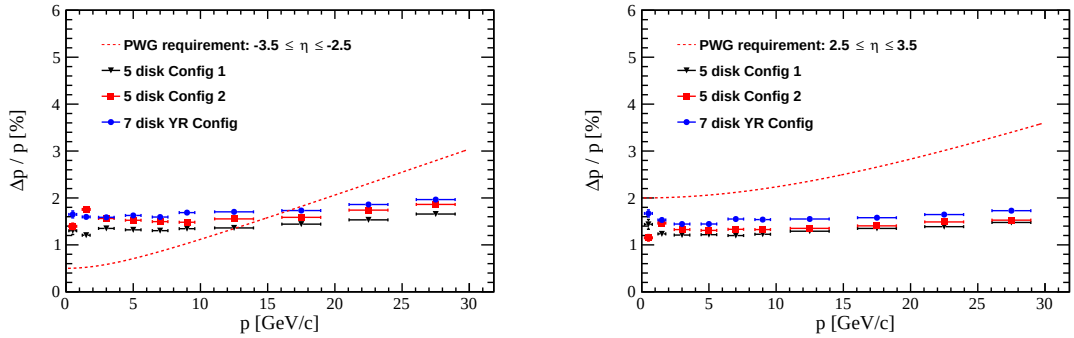

(a) $\frac{\Delta p}{p}$ resolution: Backward disks

(b) $\frac{\Delta p}{p}$ resolution: Forward disks

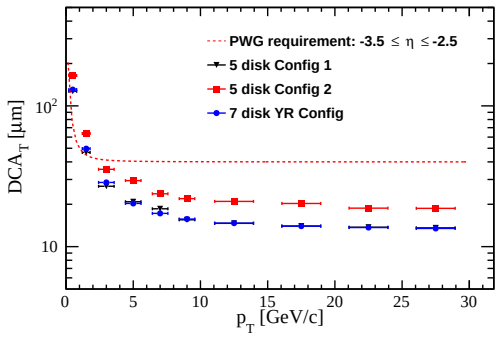

(c) DCA_T resolution: Backward disks

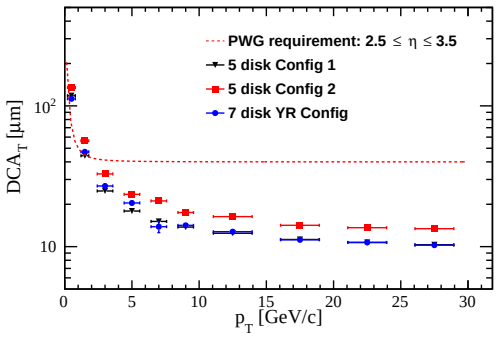

(d) DCA_T resolution: Forward disks

Figure 4.7: Relative momentum resolution and transverse pointing resolution comparison plots for 3 different silicon disk layouts in an initial ATHENA silicon plus MPGD tracker design, using a 3 T solenoidal magnetic field map.

7 disk YR Config and 5 disk Config 1, while a worse resolution is seen for 5 disk Config 2. The first disk, D0, in each configuration only provides coverage in the range $1.85 < |\eta| < 2.5$, so for tracks with $|\eta| > 2.5$, the first hit point is provided by D1. The larger distance between the interaction point and the first hit position at D1 in 5 disk Config 2, leads to a larger geometric term in the transverse pointing resolution, which manifests as a degradation in the pointing resolution across the full p_t range. As such, the disk placement is a compromise between the improvement in transverse pointing resolution that is possible by moving D1 closer to the interaction point, and the loss in η coverage that occurs as a result.

The relative momentum resolution of the three disk configurations in the backward and forward directions are shown in Fig. 4.7a and Fig. 4.7b respectively. The 5 disk configurations each give an improved resolution compared to the original 7 disk configuration, as the momentum resolution at large $|\eta|$ is dominated by the multiple scattering contribution, and the removal of two disks reduces the material traversed. Config 1 outperforms Config 2 in terms of relative momentum resolution, as the distance between D1 and D4 is larger in Config 1. The 7 disk configuration has the same effective lever arm as 5 disk Config 1, and a larger lever arm than Config 2,

but the additional material results in a degraded resolution compared to the 5 disk layouts.

The transverse momentum requirement is not met for $p_t \lesssim 2\,\text{GeV}$ when using 5 disk Config 2, whereas the other configurations are consistent with the requirement for this p_t range. All configurations exceed the PWG requirement for transverse pointing resolution at $p_t \gtrsim 2\,\text{GeV}$. It should be noted that at large pseudorapidities, a particle with a p_t of 2 GeV may have tens of GeV of momentum. Such high energy particles are expected to be infrequent at EIC energies, so it is important to meet the requirements in the $p_t \lesssim 2\,\text{GeV}$ range. 5 disk Config 1 and the 7 disk YR config are the preferred options in terms of transverse pointing resolution, as they provide performance consistent with or exceeding the requirement for the full p_t range.

Each of the three disk configurations exceed the required relative momentum resolution in the forward direction, but the backward requirement (from VMP) is only met for $p \gtrsim 12 - 17\,\text{GeV}$, depending on the configuration. The momentum resolution at large $|\eta|$ is dominated by the multiple scattering contribution. The targeted disk material budget of $0.24\,\%\ X_0$, is already challenging, so it is unlikely that this material budget could be improved upon. In order to reconstruct tracks up to $|\eta| \sim 3.5$, there must be at least three space-points measured at this pseudorapidity. This means that for the necessary coverage, there must be at least three disks with $z \gtrsim 600\,\text{mm}$, while in order to maintain the required transverse pointing resolution, the first two disks at $z = 220/430\,\text{mm}$ are needed. Therefore, the material budget can also not be improved upon by reducing the number of disks, as a minimum of 5 disks are required for the necessary coverage.

As the relative momentum resolution in the forward region is well within the requirements, a configuration with more disks may be beneficial. The extra disks add valuable additional space-points in the hadron going direction, which help with pattern recognition and redundancy, and are beneficial for reconstruction using particle flow techniques.

It can be concluded that, of the options presented here, 5 disk Config 1 offers the best overall performance. A 5 disk layout is best for the backward silicon tracker, while a layout utilising between five and seven silicon disks may be used in the forward tracker. As discussed in the previous section, the backward requirement cannot be met with any disk configuration, and so the required performance will need to be achieved through the combination of measurements from the tracking and calorimetry systems.

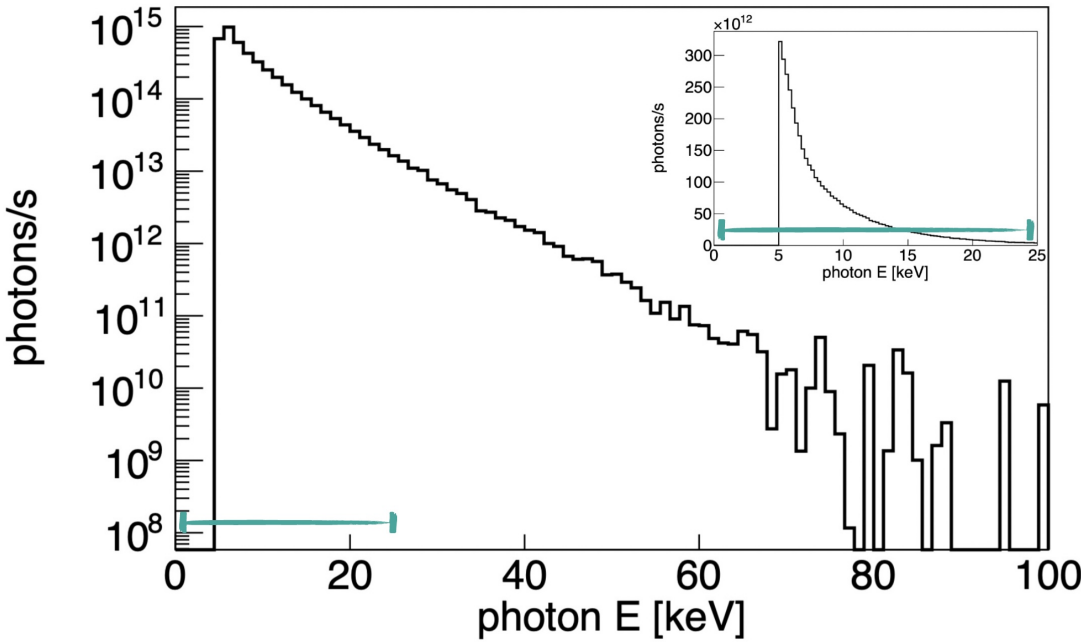

Figure 4.8: Energy spectrum of SR photons generated by Synrad+ using the EIC beamline in the 10 GeV electron beam configuration. A cut is applied to exclude SR with $E < 5\,\text{keV}$. Figure taken from [103].

4.4.2 Gold Coating for the Beampipe

There are several background sources that arise from the electron and proton/ion beams themselves. These background processes often produce additional hits in the tracking layers that interfere with track reconstruction. One such background is the synchrotron radiation (SR) emitted by beam electrons as they pass through magnetic elements along the beamline. Fig. 4.8 shows the flux of SR photons as a function of energy, as determined from simulations of the EIC beamline in Synrad+ with the 10 GeV electron beam energy configuration. It can be seen that the number density of synchrotron radiation photons rises rapidy with decreasing photon energy. To avoid generating an unmanageable number of events, a cut-off is applied below 5 keV, though many SR photons are generated in the range in reality. It is clear from Fig. 4.8 that most SR photons are low energy, and so by coating the inside of the beampipe with a high Z material, the majority of the SR photons can be absorbed.

For this purpose, it was proposed that a gold coating be applied to the interior of the beampipe. Such a coating should be thick enough to absorb the SR photons, while avoiding a large negative impact on the tracking resolutions. In this section, the effect of the gold coating is considered only in terms of the relative momentum resolution and transverse pointing resolution, and the impact on hit occupancy due to SR is not discussed. The hit occupancy due to SR, and other beam backgrounds,

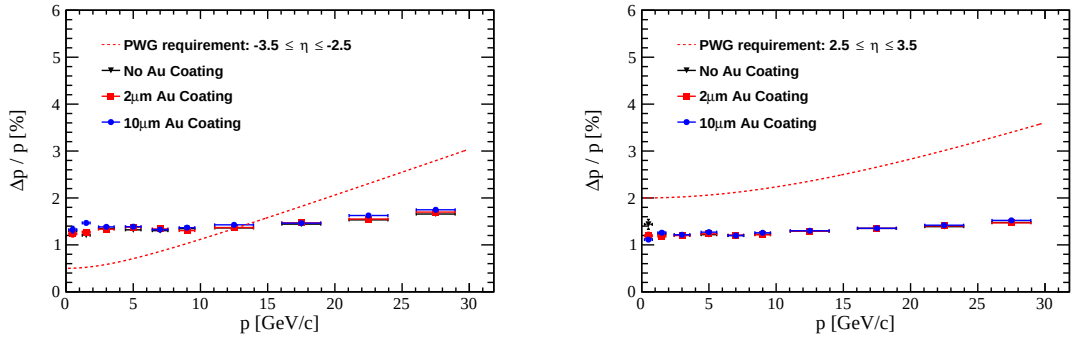

(a) $\frac{\Delta p}{p}$ resolution: Backward disks

(b) $\frac{\Delta p}{p}$ resolution: Forward disks

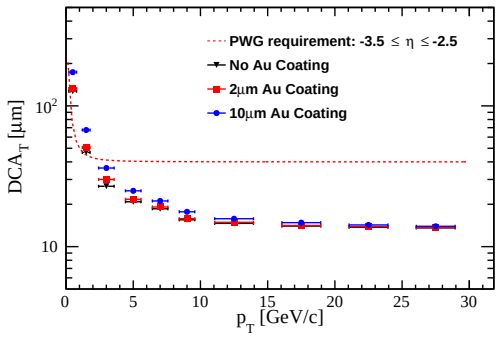

(c) DCA_T resolution: Backward disks

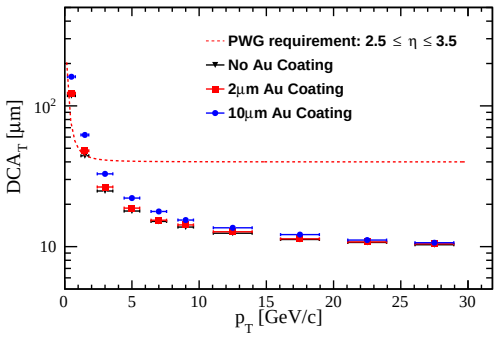

(d) DCA_T resolution: Forward disks

Figure 4.9: Relative momentum resolution and transverse pointing resolution comparison plots for the silicon plus MPGD tracker design with 3 T solenoidal magnetic field with 3 levels of gold coating.

is covered in Section 4.5.7. The amount of extra material traversed by particles originating at the interaction point is maximal at large $|\eta|$ values, and so the impact on the tracking resolutions should be largest in the endcap regions.

The geometry implementation in Fun4All is the same as in the previous section, and uses the 5 disk Config 1 layout described in in Table 4.5. The same parameters were also used for generation, summarised as:

- Generated particle: single e^- ($\eta < -1$), single π^- ($\eta > -1$)
- Generated distributions: uniform in p_t and η
- Ranges: $0 < p_t < 30\,\text{GeV}$, $-3.5 < \eta < 3.5$
- Magnetic Field: 3 T solenoidal field map

A comparison of the relative momentum resolution and transverse pointing resolution in the disk regions, as extracted from Fun4All simulations with three levels of gold coating, is shown in Fig. 4.9. The three thicknesses of gold coating are 0 µm (no coating), 2 µm, and 10 µm. Here, the 2 µm coating provides a lower bound for the absorber thickness that may be applied, and the 10 µm coating provides an upper

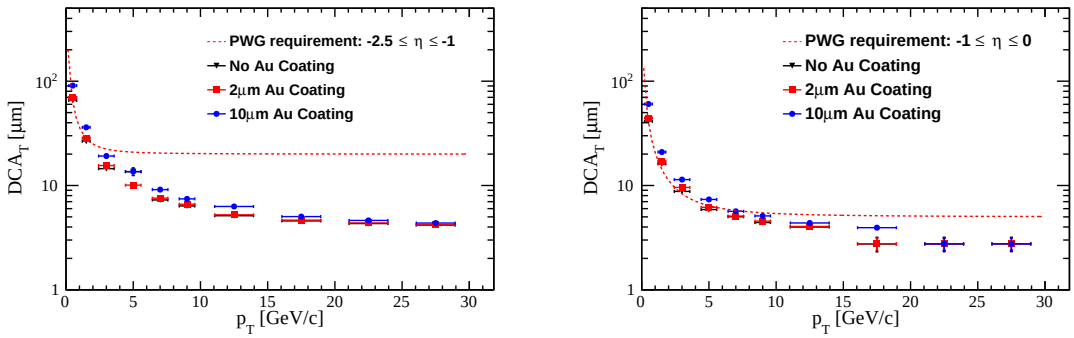

(a) DCA_T resolution: $-2.5 < \eta < -1$ **(b)** DCA_T resolution: $-1 < \eta < 0$

Figure 4.10: Transverse pointing resolution comparison plots for the silicon plus MPGD tracker design with 3 T solenoidal magnetic field for 3 levels of gold coating in the range a) $-2.5 < \eta < -1$ and b) $-1 < \eta < 0$.

bound. The final thickness of gold coating will be chosen in line with dedicated studies of the amount of SR entering the central detector.

No significant difference is observed for the relative momentum resolution between the three configurations, in both the forward and backward regions for which the additional material traversed is greatest.

The transverse pointing resolutions using the three thicknesses are equivalent at large p_t, but a degradation in the resolution is observed at low p_t. The transverse pointing resolution with the 2 µm gold coating applied is comparable to the resolution with no coating. However, the degradation in resolution when a 10 µm coating is applied is significant for $p_t \lesssim 3$ GeV.

It has been verified that the relative momentum resolution does not change with the application of a gold coating with thickness < 10 µm in the region where $|\eta| < 2.5$, so relative momentum resolution plots are not shown for this region. Comparisons of the transverse pointing resolution for the three gold thicknesses in the regions $-2.5 < \eta < -1$ and $-1 < \eta < 0$ are shown in Fig. 4.10a and Fig. 4.10b respectively. Only the plots for $\eta < 0$ in the central region are pictured, as the detector layout is symmetric in all aspects other than the outermost GEM stations, which do not affect the transverse pointing resolution. Hence, the transverse pointing resolution is the same between the $\eta < 0$ ranges and the equivalent range for $\eta > 0$. Similar behaviour is seen in the transverse pointing resolution plots for $-2.5 < \eta < -1$ as was seen for $|\eta| > 2.5$: the resolutions from 0 µm (no coating) and 2 µm simulations are similar, and the 10 µm coating noticeably degrades the resolution.

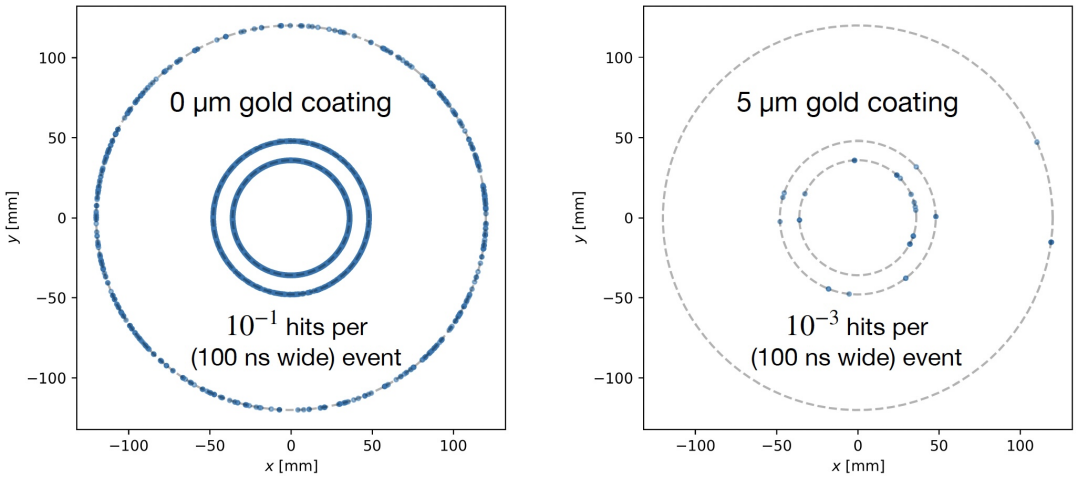

Figure 4.11: Hits in the vertex layers of the ePIC detector with and without the application of a 5 µm gold coating to the beampipe. The hits were collected from 100 ns wide events simulated in the ePIC software. Figure taken from [103].

The transverse pointing resolution requirement is generally matched or exceeded across the full p_t and η ranges of $0 < p_t < 30\,\text{GeV}$ and $-3.5 < \eta < 3.5$ for the 0 µm and 2 µm coating configurations. When the 10 µm coating is applied, the requirement is no longer met for $p_t \lesssim 7\,\text{GeV}$ in the most central region ($-1 < \eta < 1$).

At intermediate ($1 < |\eta| < 2.5$) and forward ($2.5 < |\eta| < 3.5$) pseudorapidities, the requirement is no longer met for $p_t \lesssim 2\,\text{GeV}$ with the 10 µm coating applied. As particles produced at intermediate and forward pseudorapidities generally have lower p_t, it is important to get as close to the requirements as possible at low p_t. A 10 µm gold coating significantly degrades the transverse pointing resolution, so a coating thickness of < 10 µm should be targeted. A 2 µm gold coating does not significantly degrade the transverse pointing resolution (or the relative momentum resolution) and so would be acceptable to use when considering tracking resolutions alone. The drawback of using a thinner gold coating is that more SR photons may make it through the beampipe and into the tracking detector. Hence, the thickness of the gold coating should be made as thick as possible without degrading the resolutions to an unacceptable level.

The impact of the gold coating on the hit occupancy of the vertexing layers has since been investigated in the context of the ePIC detector in studies conducted by members of the ePIC Background Task Force. These studies found that a 5 µm gold coating was sufficient to reduce the hit hit occupancy in these layers by two orders of magnitude, as is shown in Fig. 4.11 for a 100 ns wide event. Such an occupancy is low enough that the impact of SR on track reconstruction is expected to be minimal. As such, a 5 µm gold coating has been chosen for use in ePIC conceptual designs.

The ATHENA proposal was written before these studies by the ePIC Background Task Force took place, and the tracking studies shown here were used to inform the thickness of gold coating for ATHENA. Therefore, for the remaining ATHENA studies that are shown in this chapter, a 2 µm gold coating is applied to the beampipe.

4.4.3 Disk Material Comparison

The targeted material budget for the silicon disks is 0.24 % X_0 per disk. To best meet the relative momentum resolution requirements at large $|\eta|$, a realistic mechanical disk design that gives a material budget of as close to the targeted 0.24 % X_0 as possible is required. In a realistic mechanical disk design, factors such as the layout of support structures, the routing of services, and the integration of the disks in the larger detector all need to be taken into account. The choices made in the mechanical design directly impact the overall material budget of the disks, and hence the tracking resolutions.

Services (power, cooling etc) are expected to dominate the material budget for the MAPS disks. The material budget estimates for the silicon tracking layers in the Yellow Report and beyond are based on extrapolations from existing technologies made by engineering experts within the collaboration [104, 105]. A reasonable approximation of the material budget is obtained by scaling the services load with the silicon surface area, based on the choice of sensor technology. To obtain the 0.24 % X_0 material budget estimate for the disks used in the Yellow Report (and subsequent) configurations, an extrapolation is made from the known material budget of the ALICE ITS2 inner layer staves. With an appropriate scaling for disks with a diameter of more than 30 cm, this gives an estimated material budget of $\sim$ 0.3 % X_0 for ITS2-like disks with diameters of up to 60 cm. To obtain the value for a disk composed of sensors based on the ITS3 technology, a scaling is applied to the ITS2-like disks based on power, cooling, and sensor thickness estimates which leads to the Yellow Report disk material estimate of 0.24 % X_0. This same procedure is also used to obtain the 0.55 % X_0 material estimate for the barrel layers.

Four conceptual mechanical layouts for disks composed of sensors derived from ITS3 are shown in Fig. 4.12. A similar estimation procedure to the one described above is employed for the material budgets of these conceptual layouts, detailed in reference [106]. The layout shown in Fig. 4.12a consists of sensors mounted radially along the disk to both sides of a low-mass half-disk plate. Such a design gives close to full coverage around the beampipe, at the cost of a high mass ($\sim$ 0.53 % X_0 per disk).

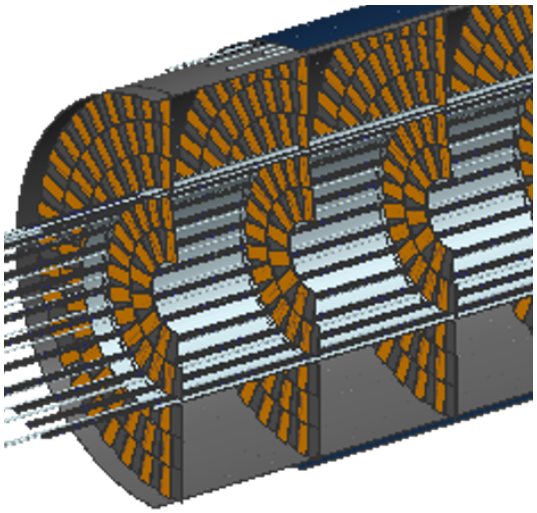

(a) Double sided half-disk plates with radial sensor distribution

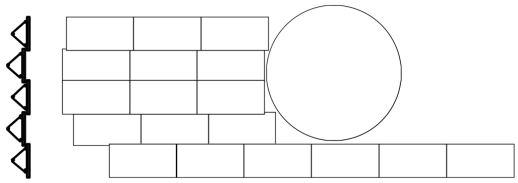

(b) Half-disks composed of parallel overlapping staves

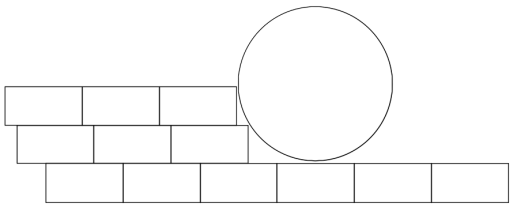

(c) Single sided half-disk plates with sensors in linear array

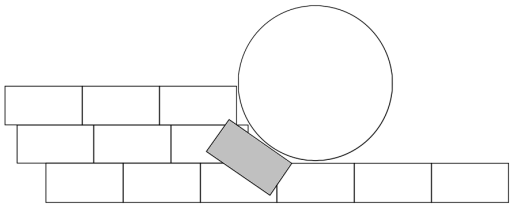

(d) Single sided half-disk plates with sensors in linear array, and additional sensors providing coverage at high η

Figure 4.12: Illustrations of four different disk conceptual mechanical layouts with sensors derived from ITS3 technology. Figures taken from [106].

Fig. 4.12b shows a layout consisting of overlapping "stave" structures that run parallel to each other, and are arranged such that they occupy the maximum area within the disk envelope. Arranging the sensors in this way leaves gaps at high η, but if the subsequent disks are rotated to prevent the gaps in coverage from aligning, it should be possible to prevent high η particles from missing more than one disk. The stave-based design gives a material budget per disk that is equivalent to ITS2 staves, adjusted for ITS3 derived sensors, of 0.29 % X_0.

The layouts shown in Fig. 4.12c and Fig. 4.12d both consist of sensors mounted in a linear array to a single side of a low-mass half disk plate. However, the design shown in Fig. 4.12d uses additional sensors (shown in grey) on the back of the plate to cover the acceptance gaps around the beampipe. Both layouts offer a lower mass

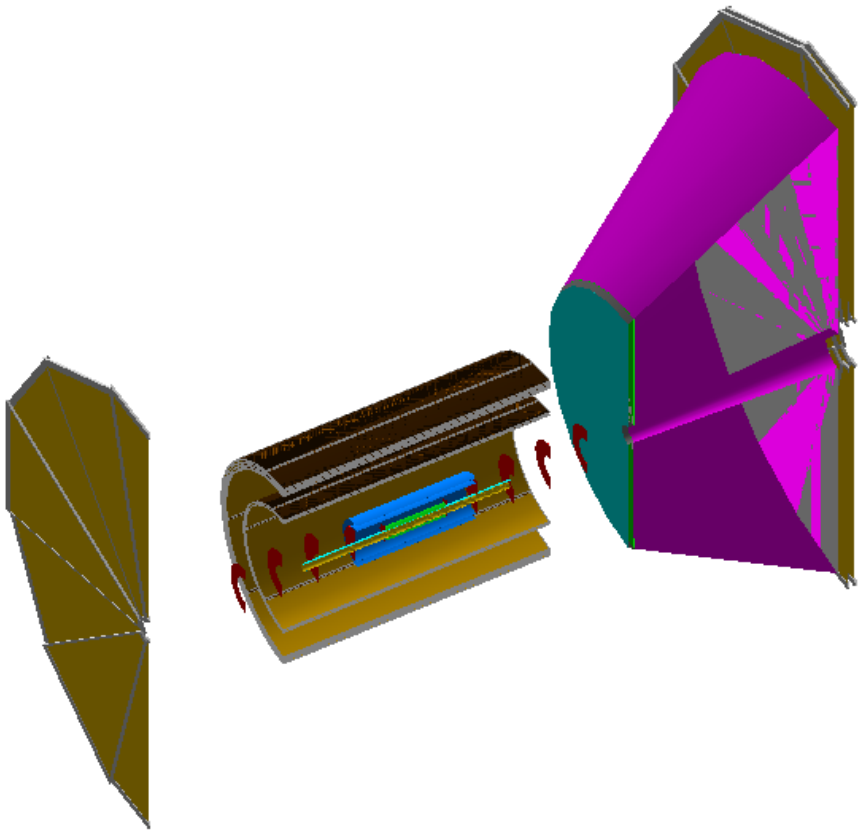

Figure 4.13: An early ATHENA silicon plus MPGD tracker layout as implemented in Fun4All simulations relating to the disk material budget.

when compared to the double sided design. No overlap of sensors is possible in these layouts, and coverage is lost at high η due to gaps around the beampipe, as was the case in the stave-based design. The sensors mounted to the back in the design shown in Fig. 4.12d minimise the loss of coverage, at the cost of extra mass being added at high η (though the mass of the disks is still expected to be lower than the double sided design). The extra mass at high η is not included in the material estimate, so both single sided half disk plate designs have an estimated material of $0.4\,\%\ X_0$.

A visualisation of the geometry implementation in Fun4All simulations for these studies is shown in Fig. 4.13, and is identical to the 5 disk Config 1 layout described in the previous sections, with the exception of the number, size, and positioning of the GEM disks. The configuration of the GEM disks consists of one GEM disk in the backward direction and two in the forward direction, after a RICH detector, as summarised in Table 4.8.

The implementation in Fun4All simulations assumes disks with circular inner and

Table 4.8: GEM disk parameters for configuration used in ATHENA disk material, as implemented in Fun4All simulations.

Disk	z (mm)	r_{in} (mm)	r_{out} (mm)
EIG0	-1900	110	1700
HOG0	3050	210	2100
HOG1	3100	210	2100

outer radii, with the material distributed uniformly across the disk. As such this study does not take into account the differences in the acceptances between the various layouts, nor does it account for additional material present in specific regions of the disks, as in Fig. 4.12d. The simulation settings are unchanged from the previous section were used, and are therefore summarised as:

- Generated particle: single e^- ($\eta < -1$), single π^- ($\eta > -1$)
- Generated distributions: uniform in p_t and η
- Ranges: $0 < p_t < 30\,\text{GeV}$, $-3.5 < \eta < 3.5$
- Magnetic Field: 3 T solenoidal field map

The relative momentum and transverse pointing resolutions are compared for disks assuming the YR material estimate (0.24 % X_0), and disks assuming the material estimates of the conceptual mechanical layouts described in this section. The comparisons are shown in Fig. 4.14. The transverse pointing resolution degrades with increasing disk material, though the degradation in performance is small and present only at low p_t. The multiple scattering term primarily depends on the material present before the second hit position, i.e. in the beampipe and the first disk. At large η, the material of the disks only contributes to fraction of the material traversed by the charged particles, which is dominated by the beampipe (and gold coating). While the difference in transverse pointing resolutions is small, there is tension with the requirement at $p_t \lesssim 2\,\text{GeV}$, even with the lowest material configuration studied (0.24 % X_0 per disk).

The relative momentum resolution shows a more obvious dependence on the disk material budget, with the 0.53 % X_0 configuration leading to a $\sim 0.5 - 0.8$ % degradation in resolution compared to the YR 0.24 % X_0 estimate. Each disk material configuration meets the momentum resolution requirement in the forward direction. However, the 0.53 % X_0 configuration gives a resolution comparable to the forward requirement at low momenta, so the inclusion of additional disks in the hadron endcap may not be possible, as a 6 or 7 disk layout is unlikely to meet the requirement.

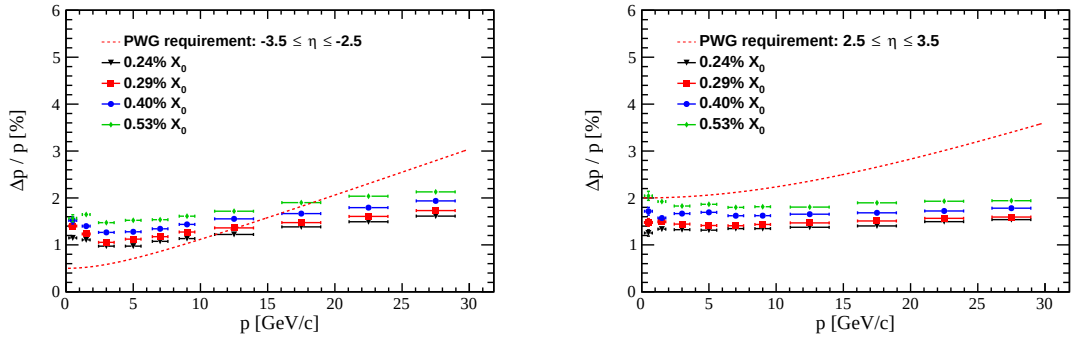

(a) $\frac{\Delta p}{p}$ resolution: Backward disks

(b) $\frac{\Delta p}{p}$ resolution: Forward disks

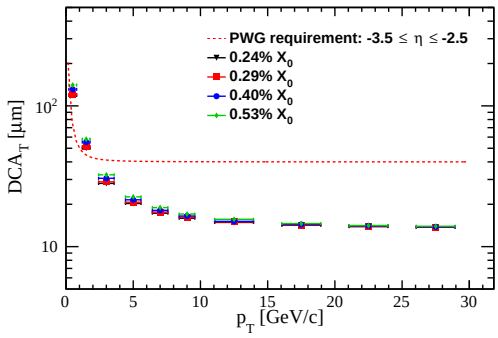

(c) DCA_T resolution: Backward disks

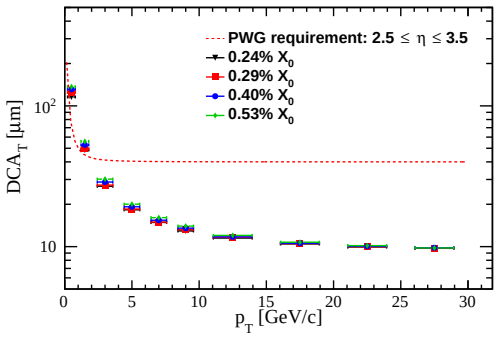

(d) DCA_T resolution: Forward disks

Figure 4.14: Relative momentum resolution and transverse pointing resolution comparison plots for a silicon plus MPGD tracker design with 3 T solenoidal magnetic field for silicon disks with material budget from 0.24 % X_0 to 0.53 % X_0 per layer.

The relative momentum resolution requirement in the backward region is not met across the full p_t range for any configuration, as seen in previous studies. Lower material budget disk designs meet the requirement for a larger part of the momentum range: the requirement is met for $p \gtrsim 11$ GeV with 0.24 % X_0 disks, but $p \gtrsim 18$ GeV for the 0.53 % X_0 configuration. Therefore, the resolution of the 0.24 % X_0 configuration would be sufficient for $y \lesssim 0.4$ in the 18 GeV electron beam configuration, but is insufficient for the 5 GeV or 10 GeV beam configurations. As before, an electron reconstruction that incorporates information from the calorimetry systems is needed in order to meet the requirements in this region.

4.4.4 Pixel Pitch Comparison

Given that MAPS for an EIC detector are planned to be derived from ITS3, the final outcomes of the ITS3 development will directly inform the properties of the MAPS used at the EIC. A range in pixel pitches are explored for ITS3, with an initial target of 10 µm, and more realistic pitches of $18 - 22.5$ µm implemented in prototypes [107, 108].

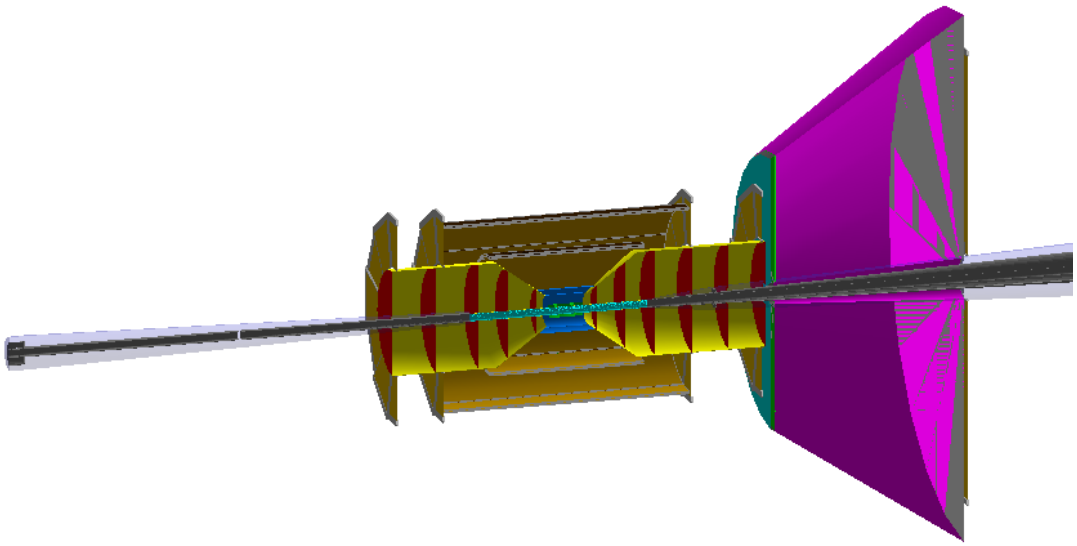

Figure 4.15: A visualisation of the final ATHENA silicon plus MPGD tracker layout, as implemented in Fun4All simulations relating to the pixel pitch.

In this section, the results of simulations performed to study the impact on the tracking resolutions that not meeting the targeted 10 µm pixel pitch for ITS3, which was assumed for studies presented so far in this chapter, are shown. Tracking resolutions using the standard 10 µm pixel pitch are compared to those using 18 µm and 22.5 µm pitches explored as part of the ITS3 development. The 28 µm pitch of the ALPIDE sensor that is used for ITS2 [109, 110] is also considered.

A Fun4All implementation of the tracker design presented in the ATHENA detector proposal [61] is used for these studies. A visualisation of the simulated geometry is shown in Fig. 4.15. The barrel region consists of 5 layers of silicon MAPS with a maximum radius of $\sim 18\,\text{cm}$, complemented by 4 layers of Micromegas at larger radii. The hadron endcap is instrumented by 6 silicon MAPS disks with maximum radii of $\sim 43\,\text{cm}$, augmented by a pair of triple-GEM detectors with inner and outer radii of $\sim 45\,\text{cm}$ and $\sim 90\,\text{cm}$, to provide additional space-points in the range $1.1 < \eta < 2$. A μRWELL is positioned behind the dRICH detector in the hadron endcap, with the main purpose of seeding the dRICH ring finder, while also improving the momentum resolution at large η. In the electron endcap, a similar design is used consisting of 5 silicon MAPS disks with maximum radii of $\sim 43\,\text{cm}$, complemented by a pair of GEM stations. The positions and sizes of all sensitive detectors for tracking in the Fun4All simulation are summarised in Tables 4.9-4.11.

Table 4.9: Barrel MAPS tracker and MPGD tracker parameters for ATHENA design as implemented in Fun4All simulations.

Layer	Technology	r (mm)	Length (mm)
L0	MAPS	33	280
L1	MAPS	43.5	280
L2	MAPS	54	280
L3	MAPS	133.4	344.4
L4	MAPS	179.6	466.8
ML0	Micromegas	477.2	1274.7
ML1	Micromegas	495.7	1274.7
ML2	Micromegas	756.1	2019.8
ML3	Micromegas	774.6	2019.8

Table 4.10: Forward MAPS and GEM disk parameters for ATHENA design as implemented in Fun4All simulations.

Disk	Technology	z (mm)	r_{in} (mm)	r_{out} (mm)
HD0	MAPS	250	31.8	186.2
HD1	MAPS	490	31.8	365.0
HD2	MAPS	730	34.7	432.3
HIG0	GEM	1030	446.8	885
HD3	MAPS	1036.5	50.8	432.3
HD4	MAPS	1343.4	65.8	432.3
HIG1	GEM	1617.4	446.8	885
HD5	MAPS	1650	81.6	432.3
HOG0	μRWELL	3320	193.4	1955

Table 4.11: Backward MAPS and GEM disk parameters for ATHENA design as implemented in Fun4All simulations.

Disk	Technology	z (mm)	r_{in} (mm)	r_{out} (mm)
ED0	MAPS	-250	31.8	185.0
ED1	MAPS	-490	31.8	362.6
ED2	MAPS	-730	31.8	432.3
EIG0	GEM	-1030	446.8	885
ED3	MAPS	-1090	39.5	432.3
EIG1	GEM	-1417.4	446.8	885
ED4	MAPS	-1450	52.6	432.3

Passive material arising from supports/services is included in the simulation in the form of conical/cylindrical aluminium support and service structures (shown in yellow in Fig. 4.15). The conical section is projective along $\eta \sim 1.1$ up to $|z| \sim 60\,\text{cm}$, after which the structure is cylindrical.

The material budget of the silicon MAPS layers use the YR estimates as before: $0.05\,\%$ X_0 per vertex layer, $0.55\,\%$ X_0 per MAPS barrel layer, and $0.24\,\%$ X_0 per MAPS disk. The MPGD subsystems assume a material budget of $0.4\,\%$ X_0. For simulations labelled "ALPIDE" in the performance plots, the material budget of the vertex layers and MAPS disks are increased to $0.3\,\%$ X_0 per layer/disk, in line with the minimum material budget achieved in ITS2 [110]. Simulations were performed with the following settings:

- Generated particle: single π^-
- Generated distributions: uniform in p_t and η
- Ranges: $0 < p_t < 30\,\text{GeV}$, $-3.5 < \eta < 3.5$
- Magnetic Field: 3 T solenoidal field map

A comparison of the relative momentum resolution as determined from Fun4All simulations is shown in Fig. 4.16. For $|\eta| < 2.5$, the relative momentum resolution of the four setups are compatible at low momenta, and diverge at higher momenta, with the larger pixel pitches giving a worse resolution at large p. At $2.5 < |\eta| < 3.5$, there is also separation at low momenta between the three ITS3-based configurations and the ALPIDE configuration, as multiple scattering effects dominate the momentum resolution at large $|\eta|$, and so the extra material present in the silicon disks degrades the resolution.

A comparison of the transverse pointing resolutions of the four configurations is shown in Fig. 4.17. For $p_t \lesssim 2\,\text{GeV}$, the three ITS3-based configurations give the same transverse pointing resolution, while the resolution using the ALPIDE configuration degrades by $\mathcal{O}(10\,\mu\text{m})$. As such, it is clear that the increased material in the ALPIDE layout directly impacts the pointing resolution at low p_t for all η ranges. The separation of the resolutions at high p_t is predicted by Eq. 3.15, and demonstrated in Fig. 4.17, where the configurations using a larger pitch are outperformed at large p_t by those with a smaller pitch.

The relative momentum resolution requirements are met in the range $-2.5 < \eta < 3.5$ for all pitches, while the $-3.5 < \eta < -2.5$ requirement is not met with any pitch.

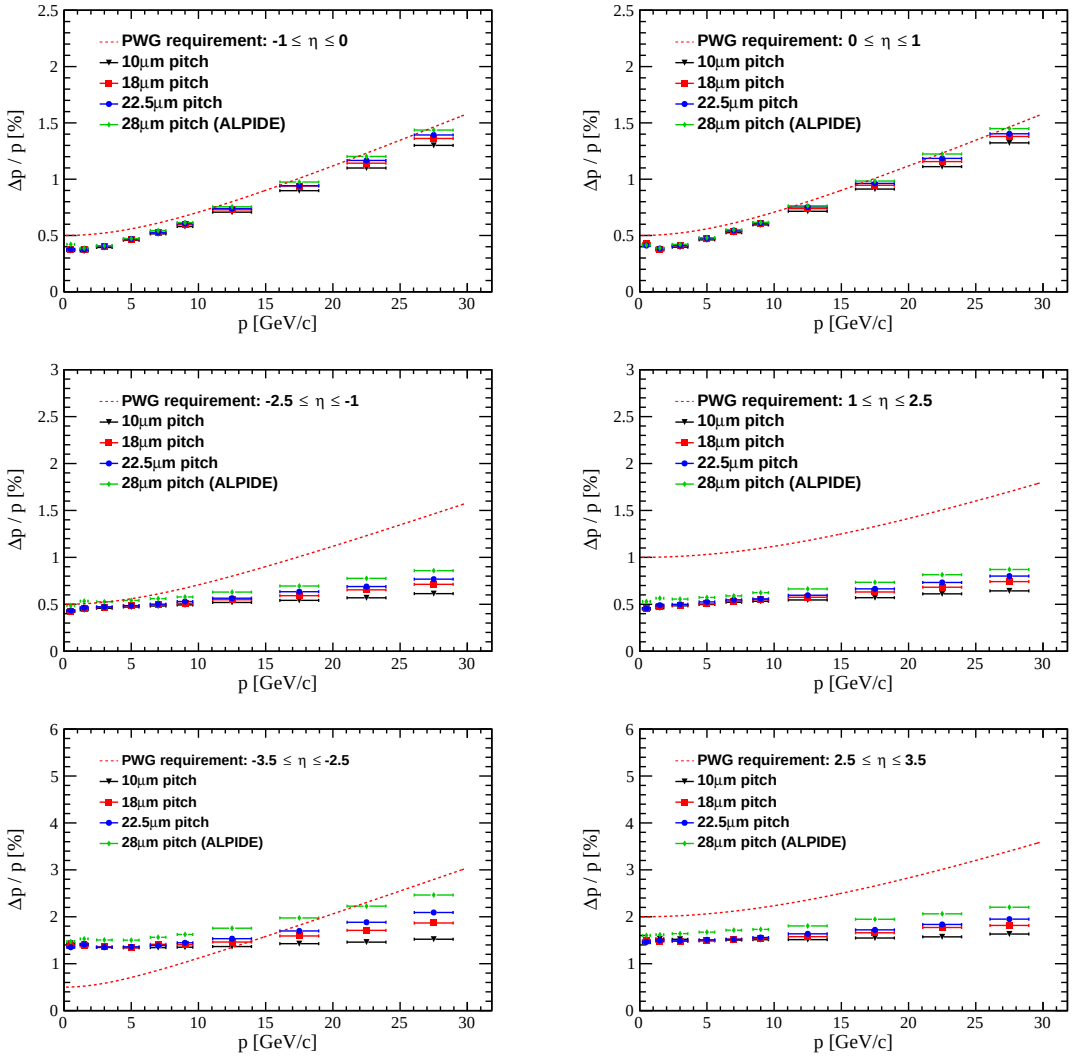

Figure 4.16: Relative momentum resolution comparison plots for the tracker layout used in the ATHENA proposal for MAPS barrel and disk detectors with pixel pitch from 10 µm to 28 µm, using a 3 T solenoidal magnetic field. Resolutions are compared for central (top), intermediate (middle), and forward (bottom) pseudorapidities.

The minimum momentum threshold at which the $-3.5 < \eta < -2.5$ requirement is met increases with increasing pixel pitch: ~ 12 GeV with 10 µm, $14 - 15$ GeV with 18 µm and 22.5 µm, and up to ~ 20 GeV with ALPIDE.

The transverse pointing resolution in the $|\eta| < 1$ region is consistent with (or better than) the requirement for the 10 µm and 18 µm pitch configurations. The 22.5 µm pitch configuration is also close to the requirement, being only ~ 2 µm above it for much of the p_t range. The ALPIDE configuration does not meet the requirement anywhere in the considered p_t range.

In the $1 < |\eta| < 2.5$ interval, the transverse pointing resolution requirement is met for all configurations based on ITS3. The extra material (and increased pitch) of

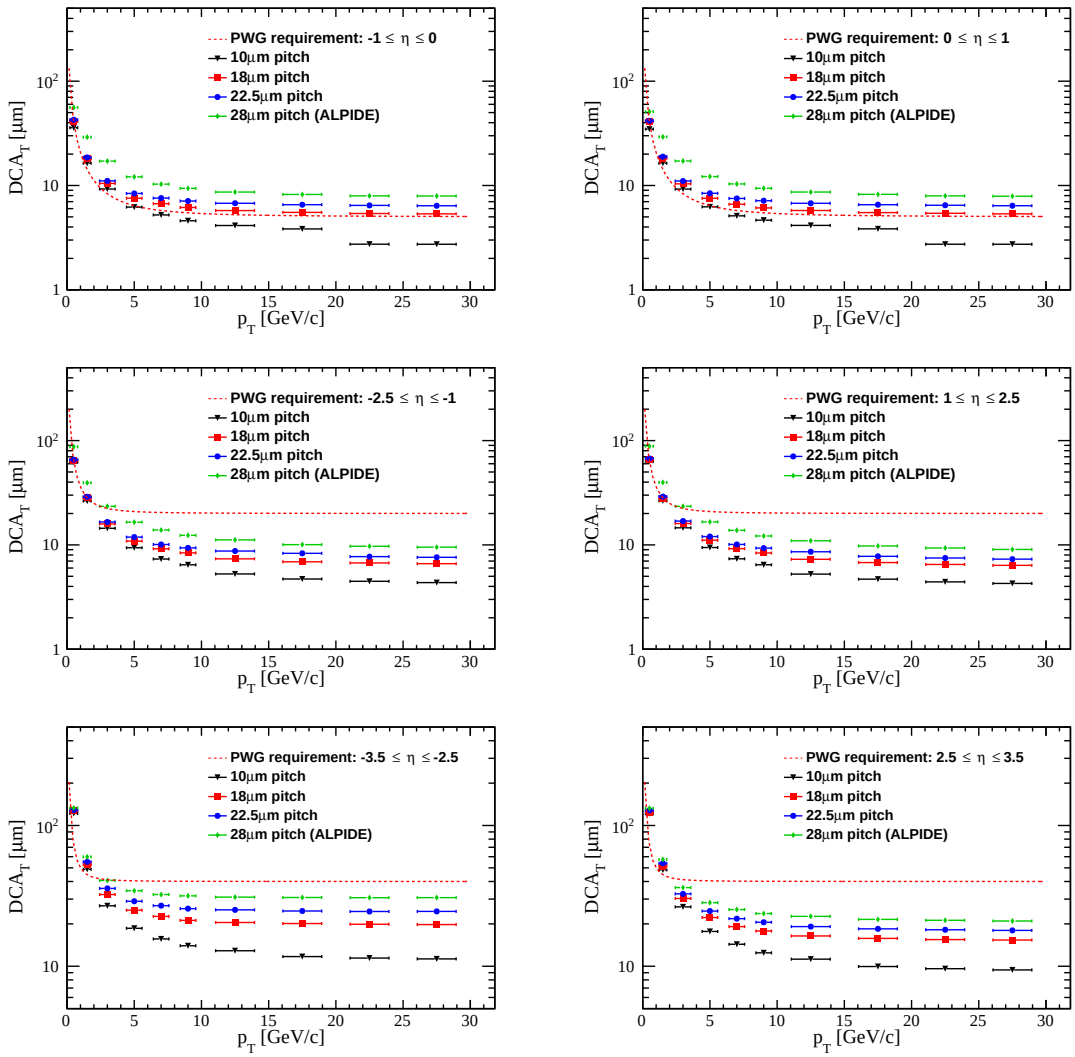

Figure 4.17: Transverse pointing resolution comparison plots for the tracker layout used in the ATHENA proposal for MAPS barrel and disk detectors with pixel pitch from 10 µm to 28 µm, using a 3 T solenoidal magnetic field. Resolutions are compared for central (top), intermediate (middle), and forward (bottom) pseudorapidities.

the ALPIDE configuration results in the requirement not being met for $p_t \lesssim 2\,\text{GeV}$ with this technology. The requirement is met for all pixel sizes in the $2.5 < |\eta| < 3.5$ interval for $p_t \gtrsim 2\,\text{GeV}$, however there is tension with the requirement at $p_t \lesssim 2\,\text{GeV}$ for all pixel sizes. Dedicated studies will be required to determine whether the observed resolution is adequate for the physics needs of the EIC.

4.4.5 Impact of AC-LGAD Layer on Tracking in the Barrel

For PID detectors based on Cherenkov radiation, the region for which PID coverage is provided depends on the Cherenkov threshold for different particles in the medium. For kaons in synthetic fused silica (the material used in the ATHENA DIRC), the momentum threshold is $\sim 0.47\,\text{GeV}$. To extend the PID coverage to

lower momenta, an AC-LGAD time-of-flight (ToF) layer is placed at a radius of 52.5 cm (after the first set of Barrel MPGDs). The reduced radius of the AC-LGAD layer compared to the DIRC enables the detection of charged particles down to $p_t \sim 0.23\,\text{GeV}$.

Beyond its application for PID, an AC-LGAD ToF detector also provides a position measurement that may benefit the tracking resolution. The position resolution depends on the strip pitch, with laser measurements of Resistive AC-Coupled Silicon Detectors (RSDs) reaching a spatial resolution of $\sim 5\,\%$ of the inter-pad distance: $\sim 5\,\mu\text{m}$ with $150\,\mu\text{m}$ pitch [111]. For ATHENA, the barrel AC-LGAD layer consists of a single layer of $1.1\,\%\ X_0$, with 200 cm length and a radius of 52.5 cm, comprising strips of $500\,\mu\text{m}$ in $r\phi$ and 2.5 cm in z.

In this section, the impact of the AC-LGAD layer on the tracking resolutions is assessed using Fun4All simulations of the ATHENA tracking system. The tracking layout is as described in Section 4.4.4, with an additional AC-LGAD ToF layer that provides a spatial resolution of $15 - 30\,\mu\text{m}$. The barrel ToF spans $|\eta| < 1.44$, so events were only generated for $|\eta| < 1.5$. The simulation settings are thus:

- Generated particle: single π^-
- Generated distributions: uniform in p_t and η
- Ranges: $0 < p_t < 30\,\text{GeV}$, $-1.5 < \eta < 1.5$
- Magnetic Field: 3 T solenoidal field map

Fig. 4.18 shows a comparison of the relative momentum resolutions between the ATHENA configuration with no ToF layer, and with the inclusion of an AC-LGAD ToF of 15 or $30\,\mu\text{m}$ resolution. For $|\eta| < 1$, no difference is observed between the three configurations at low momenta where multiple scattering dominates the resolution, but an improvement in the momentum resolution is seen at large momenta with the inclusion of the ToF.

In addition to its role as a PID detector, a barrel ToF layer with good spatial resolution demonstrates the ability to significantly improve the momentum resolution at high momenta at central pseudorapidities. A $15\,\mu\text{m}$ resolution ToF provides a factor of ~ 2 improvement at $p \sim 27\,\text{GeV}$ compared to the configuration with no ToF. No significant difference is seen for the relative momentum resolution at $1 < |\eta| < 1.5$ with the three configurations.

The only difference between the three configurations is the ToF layer at $r \sim 50\,\text{cm}$.

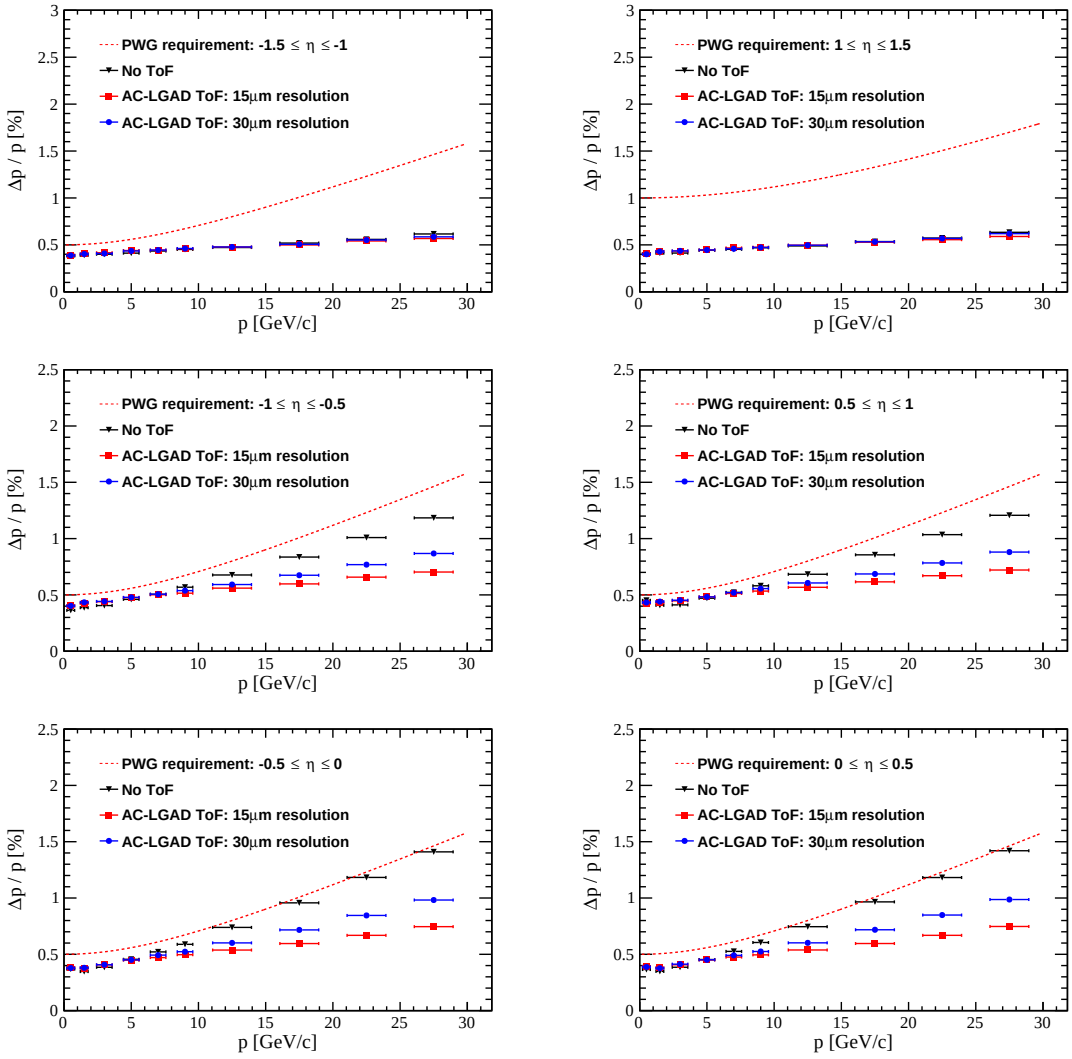

Figure 4.18: Relative momentum resolution plots comparing the tracker layout used in the ATHENA proposal to the same layout with an additional AC-LGAD ToF layer with a resolution of 15/30 µm in $r\phi$.

The transverse pointing resolution is determined by hits closer to the interaction point, and is therefore unchanged between the three configurations, so the corresponding resolution plots are not shown.

4.4.6 Summary of Findings

The results of the various studies conducted as part of the development process for the ATHENA detector proposal provide important lessons that may be applied to the design of any future detector for the EIC.

It was demonstrated by performance studies of various silicon disk configurations that the momentum resolution in the detector endcaps, for a fixed magnetic field strength, is primarily determined by the amount of material per disk, and conse-

quently the number of disks. As such, in the backward region where the momentum resolution requirement is most stringent, the number of disks should be minimised while maintaining adequate redundancy and angular acceptance. For the beampipe configuration at IP6, this is best achieved by using 5 disks. It was shown that to measure scattered electrons in the backward endcap, with a sufficiently high resolution as required by the physics, is not possible with tracking alone. Therefore, the combination of tracking information with an energy measurement from a high resolution electromagnetic calorimeter in the backward endcap will be key in order to achieve the EIC physics goals. The momentum resolution requirements in the forward region are less stringent compared to backward, so the required performance may still be achievable with more than 5 disks when using a 3 T field.

It has been shown that the thickness of gold coating applied to the interior of the beampipe, to attenuate synchrotron radiation entering the main detector, may significantly impact the transverse pointing resolution at low p_t and large η. The tested coating thicknesses of 2 µm and 10 µm provide lower and upper bounds for the coating that may be applied. The 2 µm coating does not significantly degrade the resolutions, though further studies are required to determine an optimal thickness of this coating, such that a balance between SR entering the detector and the transverse pointing resolution is achieved.

The final pitch of the sensors that will be used in the vertexing layers, and the large area sensors used in the MAPS barrel and disk layers, depends on the final results of the ITS3 development process. A degradation in momentum resolution from increased pixel size appears at higher momenta. The momentum resolution requirement also increases (is less stringent) at higher momenta, so a design that meets the momentum resolution requirements at lower momenta will usually also meet the requirements at higher momenta.

The pixel pitch strongly impacts the transverse pointing resolution, particularly at high p_t. It is clear that in order to meet the pointing resolution requirements at high momenta, the final pixel pitch should be $\sim 20 \times 20\,\mu\text{m}^2$ or less (i.e. the pixel should offer a spatial resolution of $\sim 5 \times 5\,\mu\text{m}^2$). It is seen that the extra material introduced when using an ITS2-like MAPS tracker degrades the transverse pointing resolution at low p_t, such that the requirement cannot be met. The transverse pointing resolution does not directly depend on the magnetic field strength, so these considerations apply to any detector to be located at IP6, regardless of which magnet is chosen.

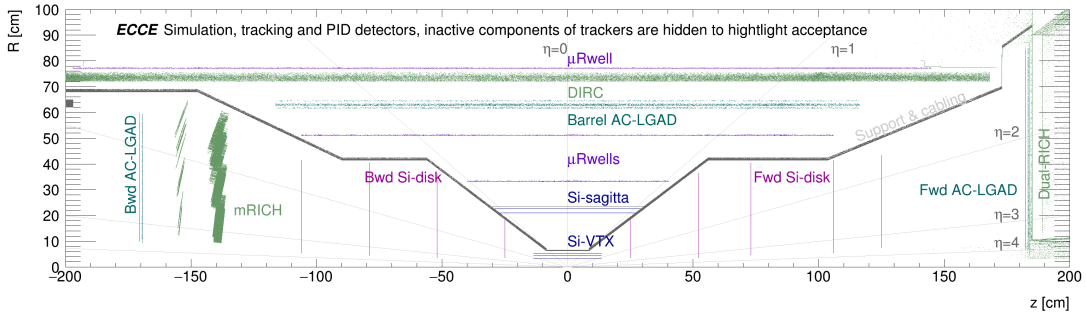

Figure 4.19: Schematic diagram of the reference detector tracker design, composed of MAPS and AC-LGAD barrel and disk layers, μRWELL barrel tracking layers, and the RICH and DIRC PID systems that are also present in the tracker envelope. Figure taken from [62].

The EIC physics programme imposes challenging PID requirements. A barrel ToF layer based on AC-LGADs is an appealing option for low momentum PID. Such a detector may also provide a good spatial resolution in $r\phi$, depending on the strip pitch, and so can benefit the tracking measurements. If position measurements from an AC-LGAD ToF with $\sigma_{r\phi} \leq 30\,\mu\text{m}$ are included in track reconstruction, the momentum resolution is dominated by the ToF layer for $p \gtrsim 5\,\text{GeV}$ at central pseudorapidities ($|\eta| < 1$), and improved by up to a factor of ~ 2 at $p \sim 27\,\text{GeV}$.

4.5 Studies for the ePIC Detector

As of March 2022, a new reference detector design for a detector to be located at IP6 was chosen, with the design presented in the ECCE proposal as its basis [62]. This reference design has since evolved in line with subsequent optimisation, based on the needs of the physics and improved understanding of the chosen technologies. The ePIC detector as described in Chapter 3 represents the current status of the design at the time of writing. The tracking system of the reference detector shares some similarities with the ATHENA tracking system discussed in the previous section, utilising a design based on a central silicon MAPS tracker augmented by MPGDs. However, a key difference between the tracking systems of the reference detector and ATHENA, is the choice of magnet, with the reference detector opting for a magnet based on the BABAR/sPHENIX solenoid, which provides a $\sim 1.5\,\text{T}$ magnetic field. The rest of this chapter shows studies that were performed to optimise the tracking geometry, an assessment of the kinematic coverage, and the introduction of increased realism to the simulations, as well as an evaluation of the beam related backgrounds.

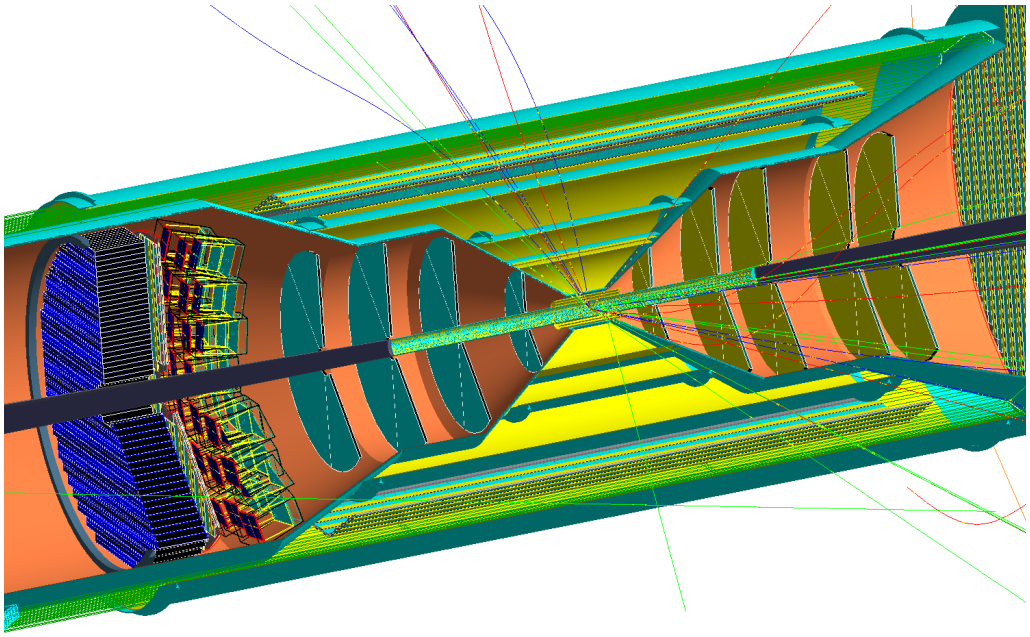

Figure 4.20: Visualisation of the reference detector tracking system as implemented in Fun4All simulations. Components that do not directly contribute to tracking (forward/backward RICH detectors, barrel DIRC, and backward electromagnetic calorimeter) are also included in the visualisation. Support and service material are included as a copper-coloured cone structure. Figure taken from [62].

4.5.1 Tracking System of the Reference Detector

While the technology choices made for the tracker of the ATHENA proposal and the reference detector overlap, there are some notable differences in the size and positioning of the various MAPS and MPGD layers.

Fig. 4.19 shows a schematic view of the tracking system for the reference detector, and a visualisation of the tracking system in Fun4All is shown in Fig. 4.20. The design consists of four MAPS disks in the electron endcap and five in the hadron endcap, each complemented by an AC-LGAD Timing and Tracking Layer (TTL) disk at larger $|z|$, which simultaneously provide tracking measurements and PID via time-of-flight. The barrel tracker is composed of five MAPS layers spanning $33 < r < 227\,\text{mm}$, complemented by three μRWELL layers spanning $331 < r < 770\,\text{mm}$ for large area tracking, and an AC-LGAD TTL at $r \sim 64\,\text{cm}$. The size and positions of all active tracking layers are summarised in Table 4.12-4.14.

The MAPS layers in the barrel region are implemented in the Fun4All simulation with a material budget of $0.05\,\%$ X_0 per layer, while the MAPS disks have $0.24\,\%$

Table 4.12: Barrel MAPS, MPGD, and AC-LGAD tracker parameters for the reference detector design as implemented in Fun4All simulations.

Layer	Technology	r (mm)	Length (mm)
L0	MAPS	33	270
L1	MAPS	43.5	270
L2	MAPS	54	270
L3	MAPS	210	540
L4	MAPS	226.8	600
RWL0	μRWELL	331.4	800
RWL1	μRWELL	510	2120
CTTL	AC-LGAD	640	2800
RWL2	μRWELL	770	3420

Table 4.13: Forward MAPS and AC-LGAD disk parameters for the reference detector design as implemented in Fun4All simulations.

Disk	Technology	z (mm)	r_{in} (mm)	r_{out} (mm)
HD0	MAPS	250	35	185
HD1	MAPS	490	35	365
HD2	MAPS	730	45	405
HD3	MAPS	1060	55	415
HD4	MAPS	1250	75	435
FTTL	AC-LGAD	1820	70	870

Table 4.14: Backward MAPS and AC-LGAD disk parameters for the reference detector design as implemented in Fun4All simulations.

Disk	Technology	z (mm)	r_{in} (mm)	r_{out} (mm)
ED0	MAPS	-250	35	185
ED1	MAPS	-520	35	365
ED2	MAPS	-790	45	405
ED3	MAPS	-1060	55	415
ETTL	AC-LGAD	-1690	80	640

X_0 per disk. The barrel μRWELLs assume a material budget per layer of 0.3 % X_0, while the AC-LGAD TTLs assume material budgets of 1 %, $\sim$ 6 %, and $\sim$ 7 % in the barrel (CTTL), electron endcap (BTTL), and hadron endcap (FTTL) regions respectively [112].

The spatial resolutions assumed for the various sensitive detectors in the Fun4All simulation are as follows: $\sim$ 3 µm ($10/\sqrt{12}$) in the MAPS barrel and disk layers, 30 µm in the AC-LGAD barrel and disk TTLs, and 55 µm for the barrel μRWELL layers. The barrel μRWELL resolution was determined from measurements with a test beam incident perpendicular to a planar μRWELL prototype [113], which gives a best case scenario. For inclined tracks, or in the presence of a strong magnetic

field, the spatial measurement using the Charge Centroid method for MPGDs deteriorates. However, it may be possible to recover much of the resolution by combining information on the amplitude of the induced signals on the strip readout with the time of arrival [114].

Fun4All simulations were conducted to assess the relative momentum resolution and transverse pointing resolution of the reference detector with a 1.5 T magnetic field. The following settings were used for the simulations:

- Generated particle: single π^-
- Generated distributions: uniform in p_t and η
- Ranges: $0 < p_t < 20\,\text{GeV}$, $-3.5 < \eta < 3.5$
- Magnetic Field: 1.5 T solenoidal field map

Fig. 4.21 shows the relative momentum resolution and transverse pointing resolution as determined by Fun4All simulations. The momentum resolution is consistent with the PWG requirements in the range $-1 < \eta < 2.5$. It is noted in the ECCE proposal that while ECCE, which shares the design of the reference detector, does not meet the requirement in the backward region where $\eta < -1$ (and particularly for $\eta < -2.5$) the physics performance may still be achieved by employing the excellent electromagnetic calorimetry available in the integrated detector. It should also be noted that if the most forward η bin ($2.5 < \eta < 3.5$) is separated into two bins covering 0.5 units of pseudorapidity each, the range for which the momentum resolution requirement is met is extended to $-1 < \eta < 3$.

The transverse pointing resolution is shown to be in agreement with or to exceed the PWG requirements for the majority of the p_t range, for all η bins. Deviations from agreement are seen where $p_t \lesssim 2\,\text{GeV}$ in the range $|\eta| > 2.5$, and $1 \lesssim p_t \lesssim 10\,\text{GeV}$ in the central region ($|\eta| < 1$). The transverse pointing resolution is most relevant in heavy flavour studies, and so dedicated physics studies were performed to evaluate their feasibility with the detector, with the outlined layout determined to provide sufficiently good pointing resolutions for heavy flavour measurements [62].

The reference detector design was therefore deemed, in the form shown here, to be capable of delivering the EIC physics programme. However, such a design must be updated in accordance with improved understanding of the performance and construction of the chosen technologies, as the development of these technologies progresses.

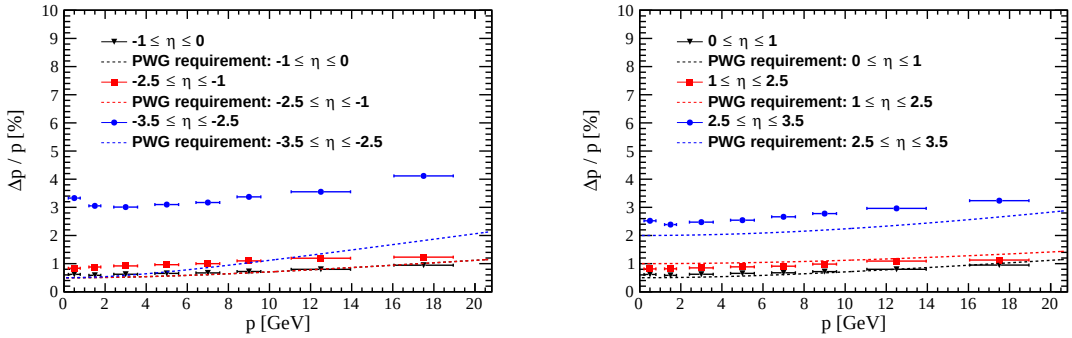

(a) $\frac{\Delta p}{p}$ resolution: Backward η **(b)** $\frac{\Delta p}{p}$ resolution: Forward η

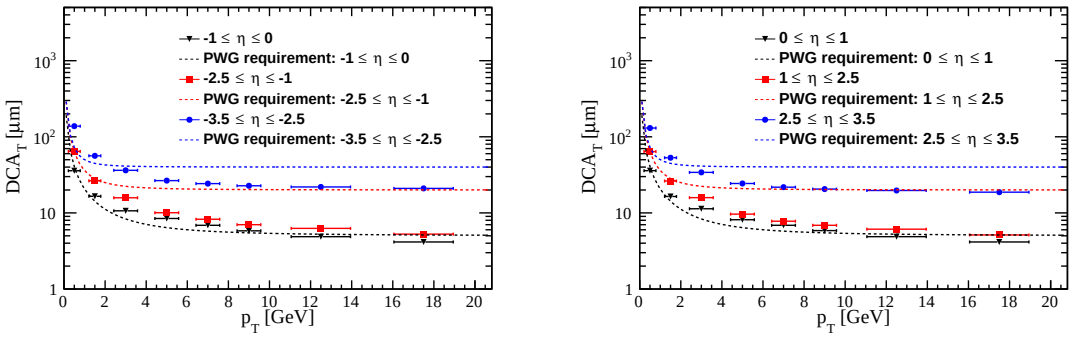

(c) DCA_T resolution: Backward η **(d)** DCA_T resolution: Forward η

Figure 4.21: Relative momentum resolution and transverse pointing resolution comparison plots for the reference detector design, using a 1.5 T solenoidal magnetic field map.

4.5.2 Silicon Barrel Optimisation

The reference detector uses an aggressive target for the material budget of the MAPS barrel layers of 0.05 % X_0 per layer. Such a target for the outer silicon barrel layers at $r \sim 20\,\text{cm}$, henceforth referred to as "sagitta layers", is not compatible with the experiment resources and timeline. When the material of these layers is updated to 0.55 % X_0, which represents an estimate of the material from the procedure outlined in Section 4.4.3, the relative momentum resolution in the central region sees a significant degradation, shown in Fig. 4.22. With the updated material budget, the momentum resolution approximately doubles the requirement.

These results highlighted the need for a design optimisation in the barrel, as well as a new approach to the stave design, to lower material below 0.55 % per layer.

The vertexing layers in the reference detector design are 27 cm long and positioned at radii of $r = 3.3/4.35/5.4\,\text{cm}$. The tracking detectors are to be installed prior to the installation of the beampipe in the central detector. In order to remove water molecules and other contaminants from the interior of the beampipe after installa-

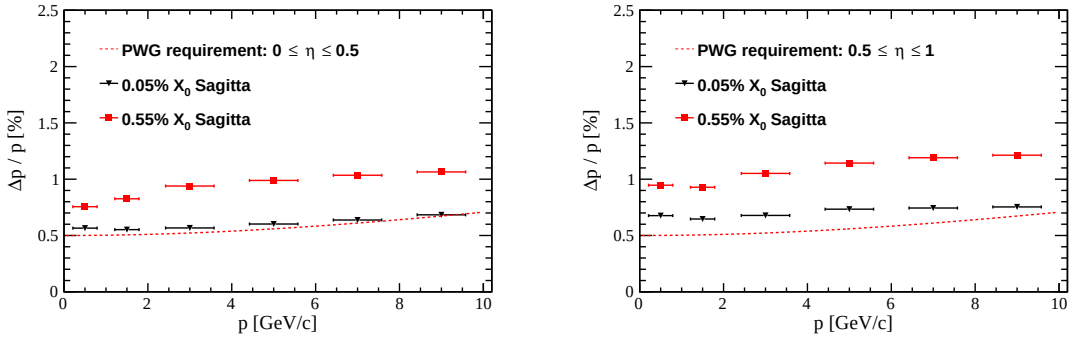

Figure 4.22: Comparison of the relative momentum resolution in the central region ($0 < \eta < 1$) for the reference detector design with a material budget per layer in the MAPS Sagitta layers (L3 and L4) of 0.05 % X_0 and 0.55 % X_0.

tion, the beampipe must undergo bake-out, where gas with a temperature in excess of 100 °C (required to break H_2O bonds) is pumped through the beampipe. For the best possible vertexing resolution, the first silicon layer must be positioned at a radius as near to the beampipe outer radius of 31.8 mm as possible. However, with the current understanding of the temperature profile between the beampipe and L0 during bakeout, and the cooling capability, studies using Ansys fluid simulations [115] indicate that the distance between the beampipe and first layer should be $\gtrsim 5$ mm [116, 117].

The radii at which the 3 vertexing layers can be positioned is determined by the size of the stitched sensors. Because of the way the sensor is designed and stitched, its length and width are multiples of 30 mm and 18.85 mm respectively. As the production process uses a silicon wafer of 300 mm diameter, the sensor length can be up to a maximum of 27 cm, with a corresponding width of ~ 9.4 cm. For a cylindrical layer comprising two bent stitched sensors, this limits the maximum radius to ~ 30 mm, which is smaller than the radius of the beampipe. There are therefore two possibilities for the design of the vertexing layers. The maximum length of the sensor can be reduced to 24 cm, giving a corresponding width of up to ~ 15 cm, and the layers placed at $36 < r < 48$ mm. Alternatively, the 27 cm maximum length can be maintained, and the cylindrical layers constructed from four sensors, allowing for layers to be positioned at $36 < r < 60$ mm.

Vertexing layers based on realistic sensor dimensions, as well as bake-out considerations, are studied in terms of the transverse pointing resolution in the central region, through the comparison of four vertex layouts. These layouts are described in Table 4.15, and the transverse pointing resolution of the reference detector in the central region with these layouts is compared in Fig. 4.23. The Fun4All simulations

Table 4.15: Parameters of four different vertex configurations implemented in Fun4All simulations. "Reference" is the implementation in the reference detector. "Reference + bake-out" is the reference detector shifted by 3 mm to give sufficient separation to bake-out the beampipe. "2 sensors per layer" and "4 sensors per layer" are two possible designs based on realistic sensor dimensions.

Layout	r_{L0} (mm)	r_{L1} (mm)	r_{L2} (mm)	Length (mm)
Reference	33	43.5	54	270
Reference + bake-out	36	46.5	57	270
2 sensors per layer	36	42	48	240
4 sensors per layer	36	48	60	270

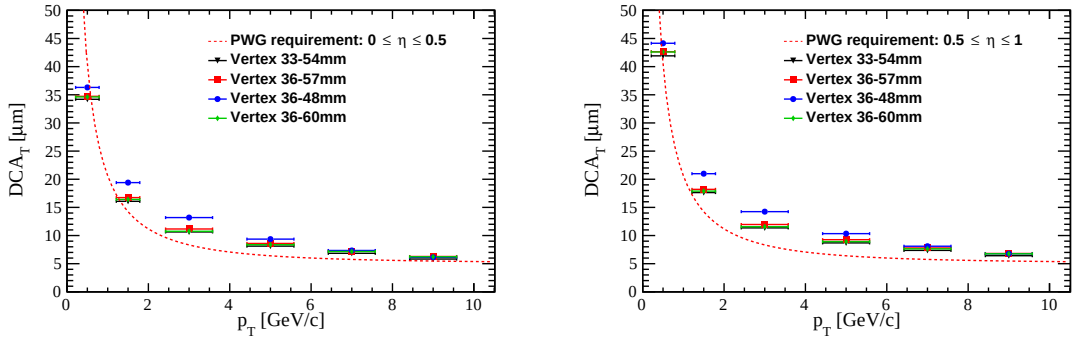

Figure 4.23: Transverse pointing resolution comparison plots for the central region ($0 < \eta < 1$) of the reference detector design, using 4 different configurations of the vertexing layers.

determining the resolutions used the same settings as in the previous section, but with a reduced p_t range:

- Generated particle: single π^-
- Generated distributions: uniform in p_t and η
- Ranges: $0 < p_t < 10\,\text{GeV}$, $-3.5 < \eta < 3.5$
- Magnetic Field: 1.5 T solenoidal field map

The "Reference", "Reference + bakeout", and "4 sensors per layer" layouts each have compatible transverse pointing resolutions, though it should be noted that the two "Reference" configurations are not achievable using realistic sensors without introducing overlaps. The "2 sensors per layer" configuration gives worse performance at low p_t, as a consequence of the shorter lever arm between L0 and L1. Hence, the "4 sensors per layer" layout is preferred in terms of performance between the two realistic layouts.

Having updated the positioning of vertexing layers such that they represent realistic configurations based on the technology, the next goal is the optimisation of the

Table 4.16: Parameters of three different vertex configurations implemented in Fun4All simulations. "Reference" is the implementation in the reference detector. "ATHENA" is the implementation in the ATHENA proposal. "Combination" is a custom positioning which shares one layer positioning with both the reference detector and ATHENA layout.

Layout	r_{L3} (mm)	r_{L4} (mm)	L3 Length (mm)	L4 Length (mm)
Reference	210	226.8	540	600
ATHENA	133.4	179.6	344.4	466.8
Combination	133.4	210	344.4	540

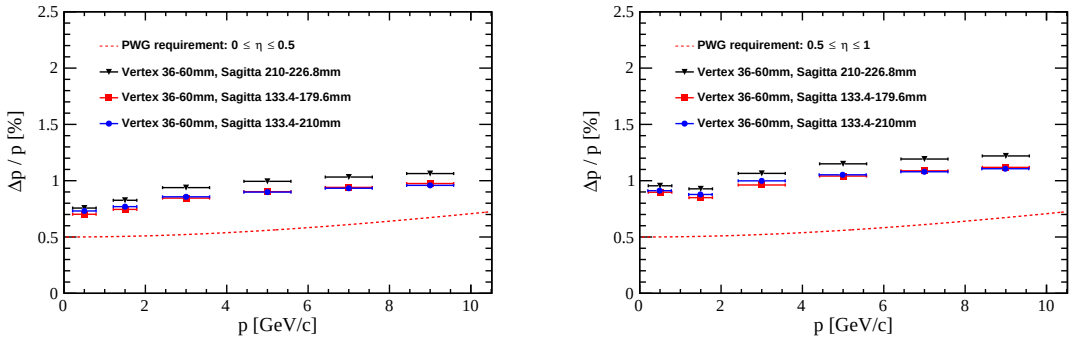

Figure 4.24: Relative momentum resolution comparison plots for the central region ($0 < \eta < 1$) of the reference detector design, using 3 different configurations of the sagitta layers, and the previously described vertex layout with layers at 36/48/60 mm.

outer barrel layers for the recovery of the momentum resolution in the central region. Fun4All simulations are performed for three different configurations of the silicon sagitta layers (sagitta layers referring to L3 and L4). The same particle generation and magnetic field settings as the previous study of the vertexing layers are used. The vertexing layers are positioned with radii 36/48/60 mm as in the "4 sensors per layer" configuration, and the sagitta layer positions are as described in Table 4.16.

Fig. 4.24 shows the relative momentum resolutions achieved by the three barrel configurations. The reference detector design is outperformed by the other two configurations, which each share a layer positioned at $r \sim 13$ cm. This is due to the extra space-point at $r \sim 13$ cm aiding the sagitta measurement, thus improving the momentum resolution.

While these alternatives to the reference detector layout provide a $\sim 0.1\,\%$ improvement in the momentum resolution, the requirement is still missed by $0.3 - 0.4\,\%$ for the momentum range shown. It is therefore clear that further efforts are needed to bring the performance back in line with the requirement, which may be provided by: an increase in magnetic field strength, a reduction in barrel material, or an increase

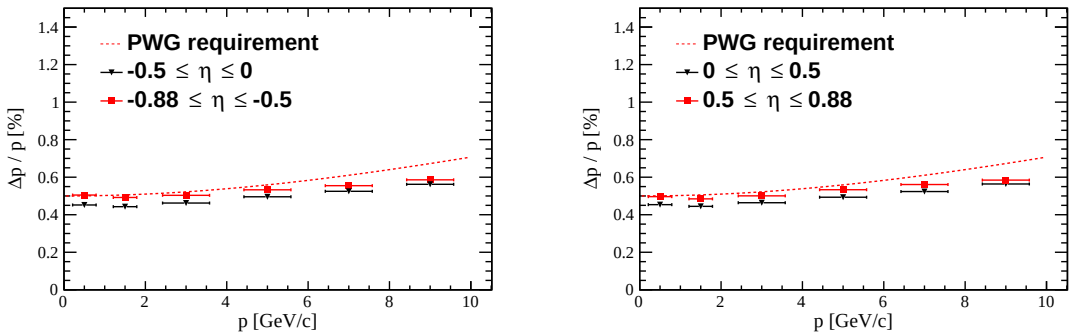

Figure 4.25: Relative momentum resolution comparison plots for the barrel region ($-0.88 < \eta < 0.88$) of the current ePIC tracker design with an assumed magnetic field strength of 1.7 T.

in the lever arm of the high precision MAPS layers.

The ePIC barrel tracker has since undergone a redesign that incorporates the knowledge gained from these studies, leading to the current layout as described in Table 3.1 in Chapter 3. In this redesign, the radius of the third vertexing layer, L2, was doubled from 60 mm to 120 mm, by assuming a layer composed of 8 sensors. The layer therefore contributes to the sagitta measurement, while maintaining the very low (0.05 % X_0) mass of a thin, low power stitched wafer-scale sensor.

The two MAPS outer barrel layers are pushed out to 27 cm and 42 cm respectively, doubling the lever arm of high precision MAPS layers. Previously the service cone had an angle of $\sim 37°$ ($\eta \sim 1.1$), while in the redesign this angle is changed to $45°$ ($\eta \sim 0.88$). The steeper cone angle means that a stave of a given length may be placed at a larger radius, such that layer L3 has a length of 540 mm (twice the maximum sensor length) at a radius of 270 mm. The motivation for this design is the avoidance of services running along the stave, which add to the material budget and are detrimental to the momentum resolution. If the staves are serviced from a single side, then a material budget of 0.25 % X_0 should be possible for L3, extrapolating from the material budget of the ITS2 staves. The material budget of the outer barrel layers depend on the final design for the staves, so this estimate may change if it becomes necessary to run services along the staves.

Even with the reduction of material in the barrel layers, and the increase of silicon lever arm, the momentum resolution requirement is challenging to meet. In order to fully recover the momentum resolution, a stronger magnetic field is required. The magnetic field stretch goal was set to 2 T, with a minimum of 1.7 T determined to be sufficient for the required barrel momentum resolution [118]. Fig. 4.25 shows

Table 4.17: Means and widths of Gaussian fits to the expected primary vertex distribution for *ep* collisions at $18 \times 275\,\mathrm{GeV}^2$, obtained using the transport model.

Fit parameter	x (mm)	y (mm)	z (mm)
μ	0.001	-0.00008	-0.31
σ	0.1894	0.01	32.92

Table 4.18: Geometry of the MAPS disks in an ePIC tracker layout. The disks are symmetric in z, but have different inner radii. ED/HD r_{in} marks the inner radii of the disks in the electron/hadron endcap.

Disk	$\lvert z\rvert$ (mm)	ED r_{in} (mm)	HD r_{in} (mm)	r_{out} (mm)
E/HD0	250	36.8	36.8	230
E/HD1	450	36.8	36.8	430
E/HD2	700	36.8	38.4	430
E/HD3	1000	42.6	53.4	430
E/HD4	1350	51.4	65.1	430

the relative momentum resolution of the ePIC barrel tracker following all of these adjustments, where it can be seen that the performance is now consistent with or better than the PWG requirement for the full momentum range. The η range is restricted to $-0.88 < \eta < 0.88$ for these plots, corresponding to the region inside of the service cone, to ensure a fair comparison with previous configurations.

4.5.3 Impact of Beamspot

In previous simulations shown in this chapter, single particles have been generated and propagated from the origin vertex, $(0, 0, 0)$ in the global detector coordinate system. In reality, the beams are made up of bunches of extended longitudinal length and a small, but non-zero, transverse beam size. The bunch lengths in turn lead to an extended distribution of primary vertex positions, dependent on the longitudinal and transverse sizes of the electron and proton/ion bunches. The region of space within which primary vertices are contained is referred to as the "beamspot". The beamspot is parametrised by Gaussian distributions in x, y, and z, according to a transport model. The transport model creates electron and proton/ion bunches prior to the collision, and integrates the overlap of the bunches as they collide [119]. Table 4.17 shows this parametrisation for the $18 \times 275\,\mathrm{GeV}^2$ *ep* setting.

It is important that the tracking resolutions continue to meet the requirements with a more realistic primary vertex distribution. Fun4All simulations were conducted with the following settings in order to study the impact of the beamspot on tracking performance:

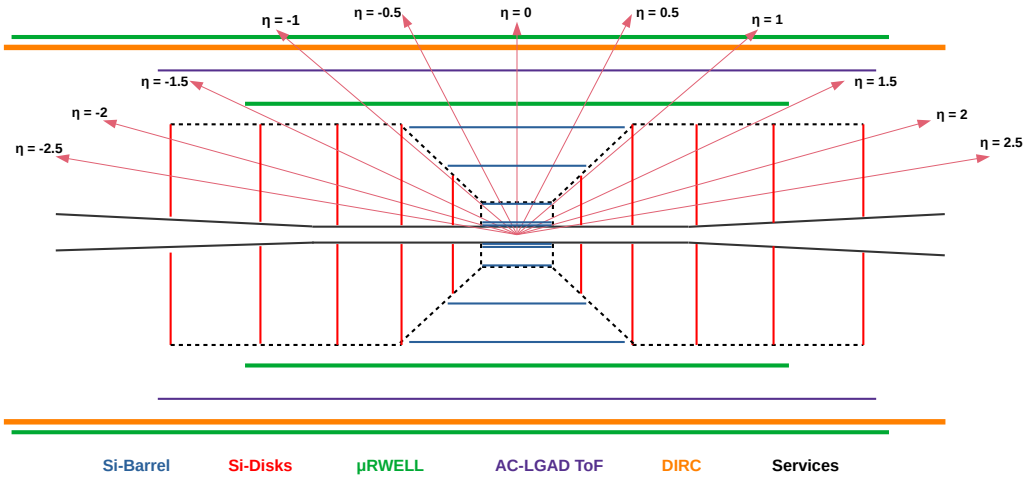

Figure 4.26: Diagram of an ePIC central tracker layout with symmetric disk positions. Arrows marking the pseudorapidity of particles produced at the origin are drawn. Note that while the AC-LGAD disks are not drawn in the diagram, they are included in the simulations.

- Generated particle: single π^-
- Generated distributions: uniform in p_t and η
- Generation vertex: origin or Gaussian distributed within beamspot
- Ranges: $0 < p_t < 10\,\text{GeV}$, $-3.5 < \eta < 3.5$
- Magnetic Field: 1.7 T solenoidal field map

In the standard particle generation, single particles are generated with the momentum and angle being set by randomly sampling uniform distributions of η and p_t, and the particles propagated from the origin vertex. The sampling of η and p_t in the beamspot studies is similar, but an additional stage occurs where the three Gaussian distributions describing the beamspot are each sampled from, and used to set the x, y, and z coordinate of the generation vertex.

The geometry of the barrel region is the final optimised layout described in the previous section, that is summarised in Table 3.1. The MAPS disks use a symmetric layout of five disks per endcap, which is described in Table 4.18, while the AC-LGAD TTLs are positioned as in the reference detector. An illustration of the tracker layout is shown in Fig. 4.26, with arrows indicating the coverage of various intervals in pseudorapidity.

The relative momentum resolution and transverse pointing resolution are compared for generation at the origin and within the beamspot, as shown in Fig. 4.27 and Fig. 4.28. When the two generation approaches are compared in coarse η bins, any

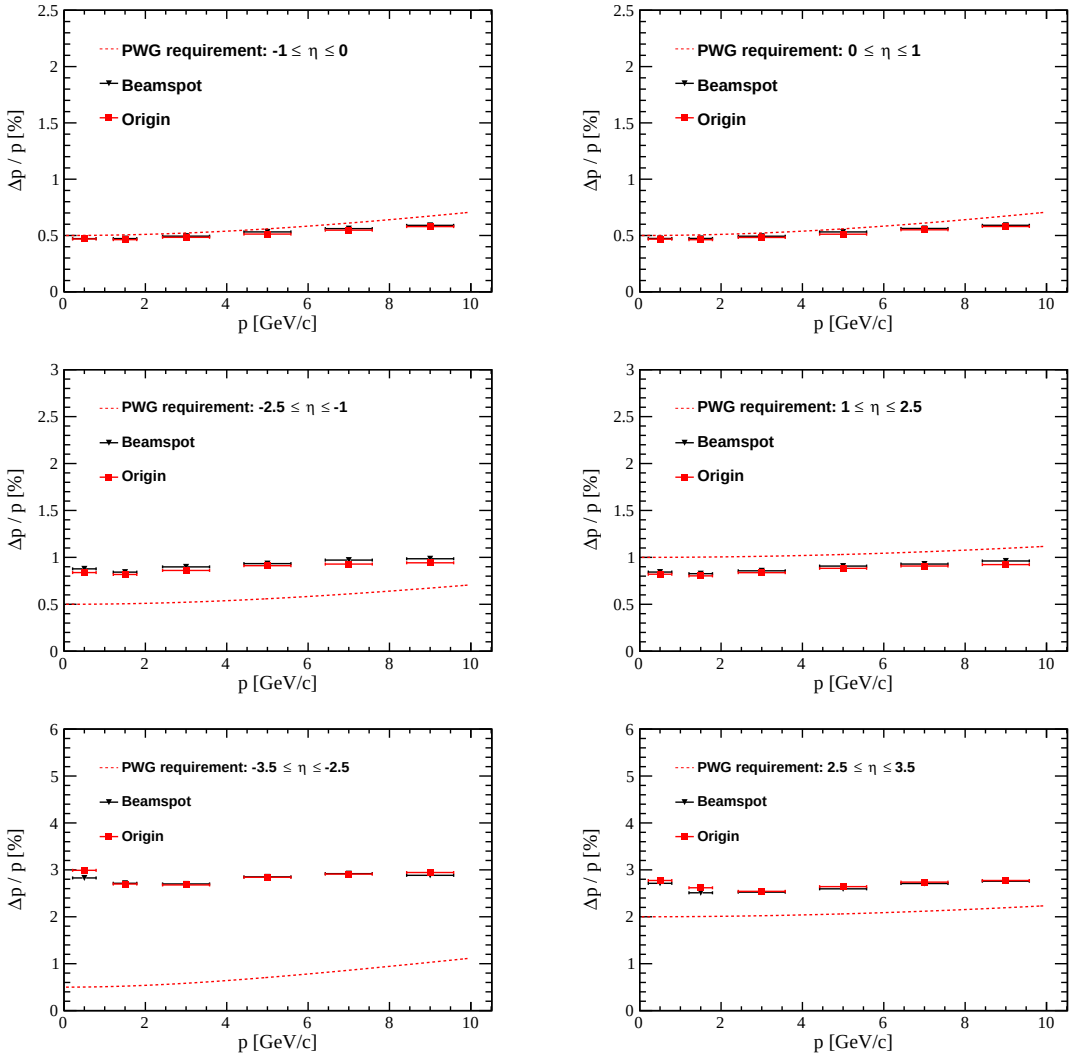

Figure 4.27: Relative momentum resolution comparison for single pions generated at the origin of the coordinate system (Origin), and by a Gaussian approximation of the beamspot (Beamspot), for a version of the ePIC tracking layout using a 1.7 T solenoidal magnetic field.

differences between the two setups are small, and the beamspot does not significantly impact the tracking performance when integrated over a large η range.

The maximum displacement of the interaction vertex in the transverse plane is much less than the radius of the innermost detectors ($\sim 36\,\text{mm}$), and the beamspot appears as point-like in $x - y$. The most significant difference between the "Origin" and "Beamspot" configurations is the large range in z of the generation vertices. Much of the tracker is designed to be projective from the nominal interaction point, notably the transition between the silicon barrel and disks regions at $|\eta| \sim 0.88$, and the service cone that bridges the gap. The service cone introduces a significant amount of material over a very small range in pseudorapidity. However, for particles that are generated $\gtrsim 1\,\text{cm}$ from the origin, the polar angle subtended by the service

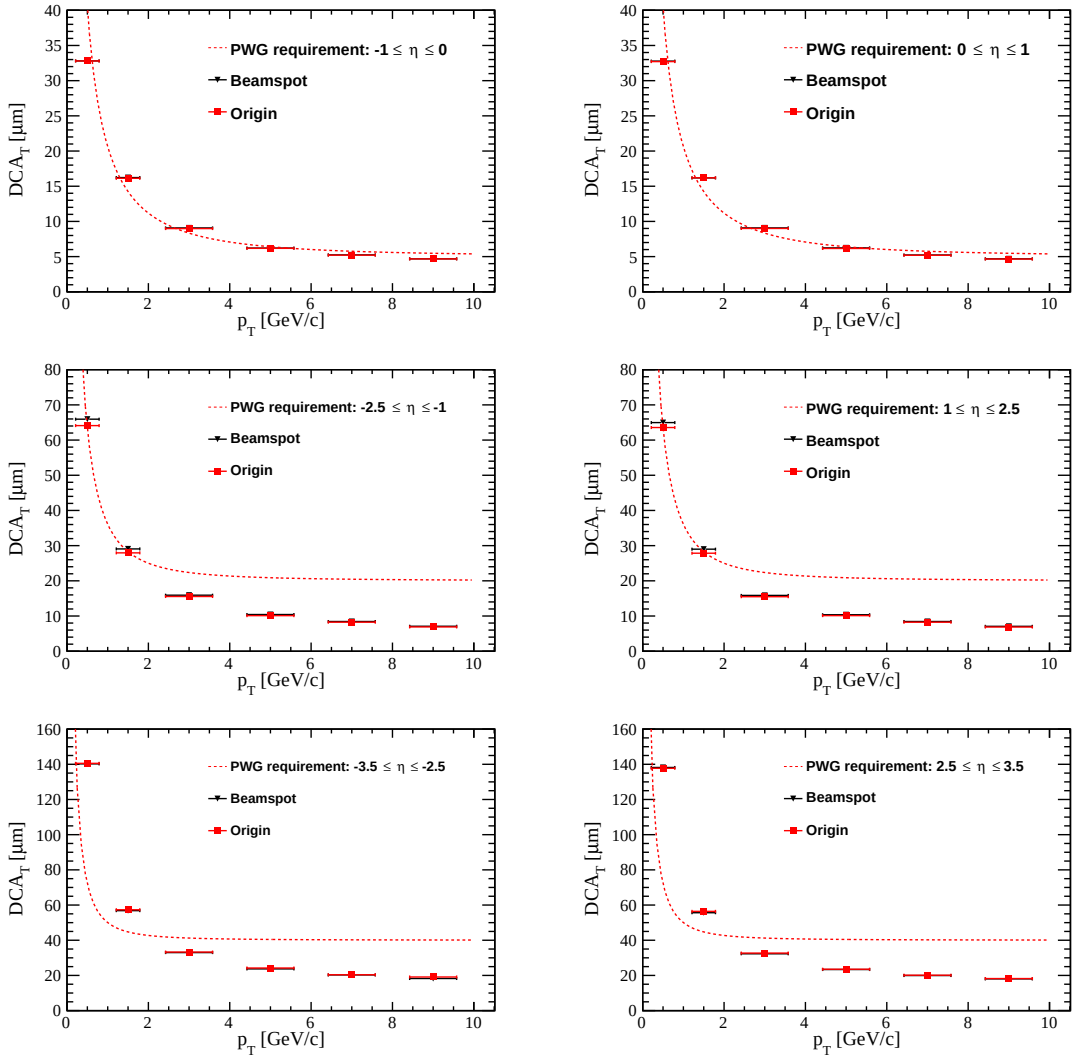

Figure 4.28: Transverse pointing resolution comparison for single pions generated at the origin of the coordinate system (Origin), and by a Gaussian approximation of the beamspot (Beamspot), for a version of the ePIC tracking layout using a 1.7 T solenoidal magnetic field.

cone may be $\gtrsim 5°$, and an appreciable fraction of particles may traverse the service cone during measurement.

To evaluate the impact this may have on the tracking performance, the momentum resolution is plotted as a function of η in bins 0.05 units wide in pseudorapidity, for particles generated at the origin and in the beamspot, shown in Fig. 4.29. Also shown in Fig. 4.29 is the ratio of the relative momentum resolution for the beamspot simulations to those with generation at the origin vertex, $(\frac{\Delta p}{p})_{beamspot}/(\frac{\Delta p}{p})_{origin}$. The ratio is ~ 1 for much of the η range, though two distinct peaks appear for $0.8 \lesssim |\eta| \lesssim 1.1$, with the maximum value of the ratio being ~ 1.25 at $|\eta| \sim 0.97$. For particles generated in the range $0.8 < \eta < 1.1$, depending on which side of the beamspot in z it is generated, the particle may cross the service cone from

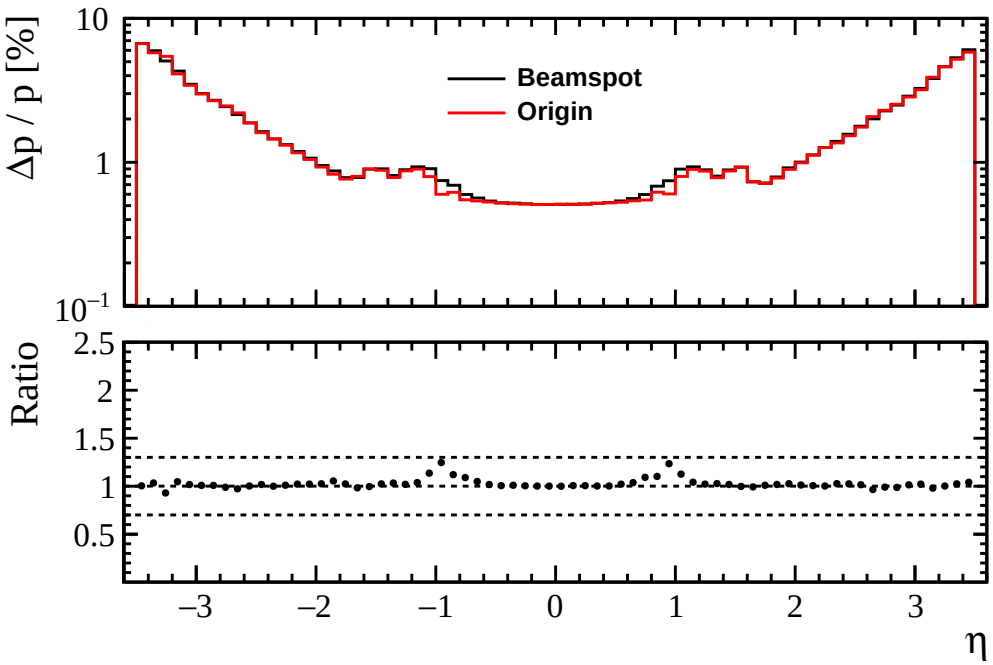

Figure 4.29: (Top) Relative momentum resolution as a function of pseudorapidity for single pions with $0 < p < 10\,\text{GeV}$, generated at the origin of the coordinate system (Origin), and by a Gaussian approximation of the beamspot (Beamspot), for a version of the ePIC tracking layout, using a 1.7 T solenoidal magnetic field. (Bottom) Ratio of the relative momentum resolution with "Beamspot" to "Origin" for each η bin.

the barrel to the disk region or vice versa. The increased average material seen by particles generated in this range deteriorates the momentum resolution at specific pseudorapidities.

4.5.4 Role of Barrel μRWELL

In simulations conducted up to this point, each active layer is assumed to have a 100 % single hit efficiency. In a realistic detector this is unachievable, due to the possibility of bad modules, inefficiencies at the edges of the sensors, the masking and removal of noisy pixels from consideration, and so on. It is important to understand the role that each layer plays in the tracking subsystem as a whole, in terms of whether the layers impact the resolution, offer redundancy, or are solely for pattern recognition. This can be determined through simulation studies with inefficient tracking layers, with such studies being performed in this section with the aim of establishing the role of the μRWELL in the barrel tracker, as well as providing insight on the tracking performance when one or more layers fails to record a hit.

Fun4All simulations were conducted using the barrel geometry that is summarised

Table 4.19: Radial positions, material budgets, and resolutions of the active and passive layers present in the barrel region of an ePIC tracker layout.

Layer	r (mm)	x/X_0 (%)	Resolution (µm)
Beampipe	31	0.36	N/A
L0	36	0.05	$10/\sqrt{12}$
L1	48	0.05	$10/\sqrt{12}$
L2	120	0.05	$10/\sqrt{12}$
Support	135	0.04	N/A
L3	270	0.25	$10/\sqrt{12}$
L4	420	0.55	$10/\sqrt{12}$
μRWELL	550	0.5	150×150
CTTL	640	1.0	30×3000

in Table 4.19, for particles generated with the following settings:

- Generated particle: single π^-
- Generated distributions: uniform in p_t and η
- Generation vertex: origin
- Ranges: $0 < p_t < 10\,\text{GeV}$, $0 < \eta < 0.5$
- Magnetic Field: 1.7 T solenoidal field map

In the simulations, either all MAPS layers are active, or a single layer fails to record a hit and the space-point of the particle at this layer is not passed to the track reconstruction algorithm. For each silicon layer setting, the space-points associated with the CTTL and μRWELL may both be used, both be removed, or only one of the two space-points be used in track reconstruction. The relative momentum resolution with various dead layer combinations is shown in Fig. 4.30.

The relative momentum resolution for the four configurations of active/inactive CTTL and μRWELL layers form two bands for each MAPS setting. When the CTTL is active (black and blue points on the plots) a better momentum resolution is achieved compared to when CTTL is dead (red and green points). This is because the CTTL dominates the momentum resolution, due to its large lever arm and high resolution in $r\phi$ (30 µm). When the CTTL does not record a hit, the tracking layer with the next largest lever arm is the μRWELL at $r = 55\,\text{cm}$. The geometric component of the relative momentum distribution relates to the lever arm L and the spatial resolution in $r\phi$, σ as $\frac{\sigma_p}{p} \propto \frac{\sigma}{L^2}$ (see Eq. 3.17). The spatial resolution of the μRWELL (150 µm) is significantly larger (worse) than the $\sim 3\,\mu\text{m}$ spatial resolution of the MAPS layers. The difference in spatial resolution is such that that the outermost MAPS layer, L4, gives a smaller (better) value of σ/L^2, despite oc-

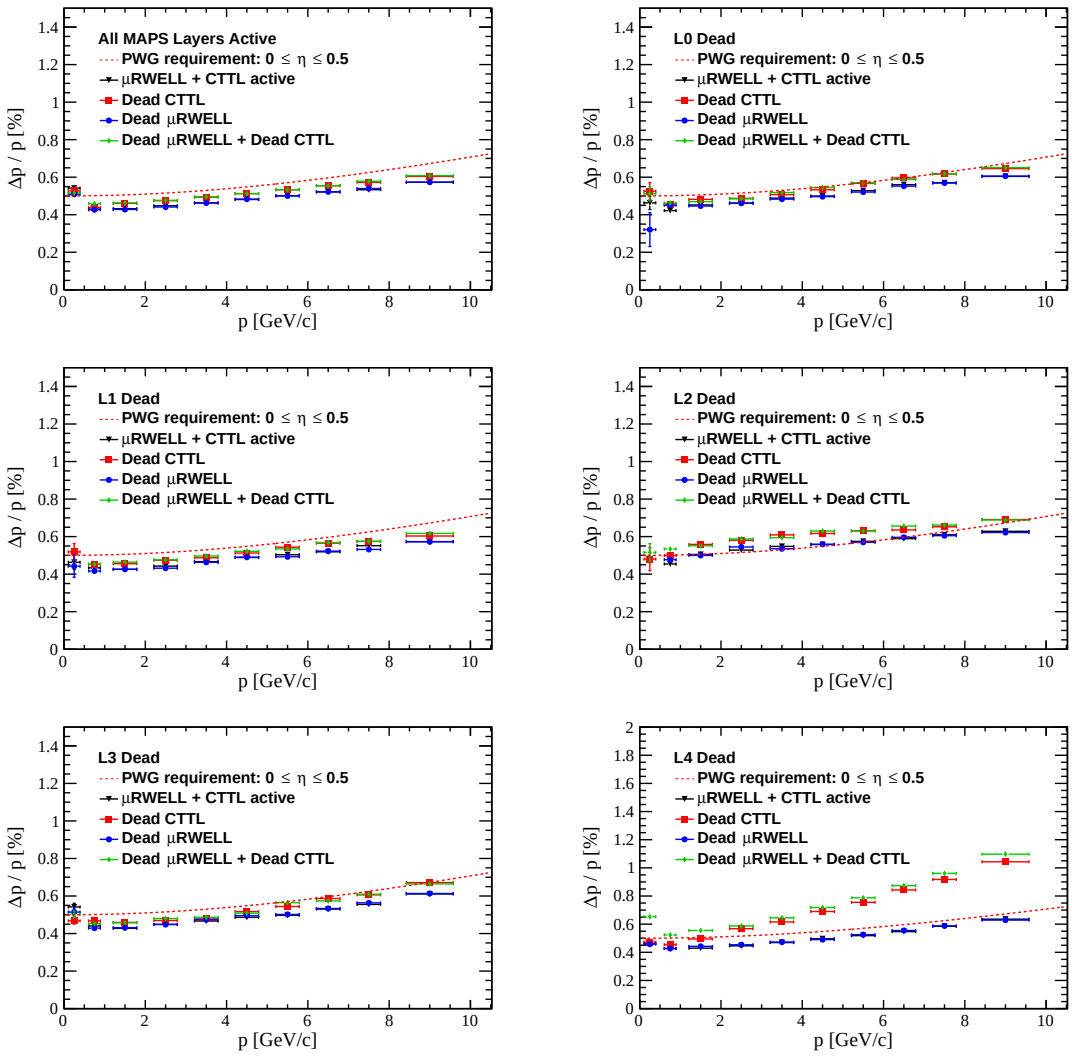

Figure 4.30: Relative momentum resolution comparison for a version of the ePIC barrel tracker with different combinations of dead layers. For each plot (except "All MAPS Layers Active") a single MAPS layer is inactive but the material is still present, and the four combinations of active and inactive for the AC-LGAD CTTL and μRWELL layers considered.

cupying a smaller lever arm than the μRWELL layer. Consequently, the outermost silicon layer dominates the momentum resolution in the case that the CTTL does not record a hit.

The difference between the CTTL active and dead configurations is most pronounced when the MAPS layer L4 does not record a hit. The two configurations with the CTTL active have compatible momentum resolutions, and perform better than the other configurations with CTTL dead. If no hit is measured by L4 and the CTTL, the momentum resolution is significantly degraded, and the configuration with an active μRWELL provides a slightly better performance compared to the configuration with the dead μRWELL (in addition to the dead CTTL and L4).

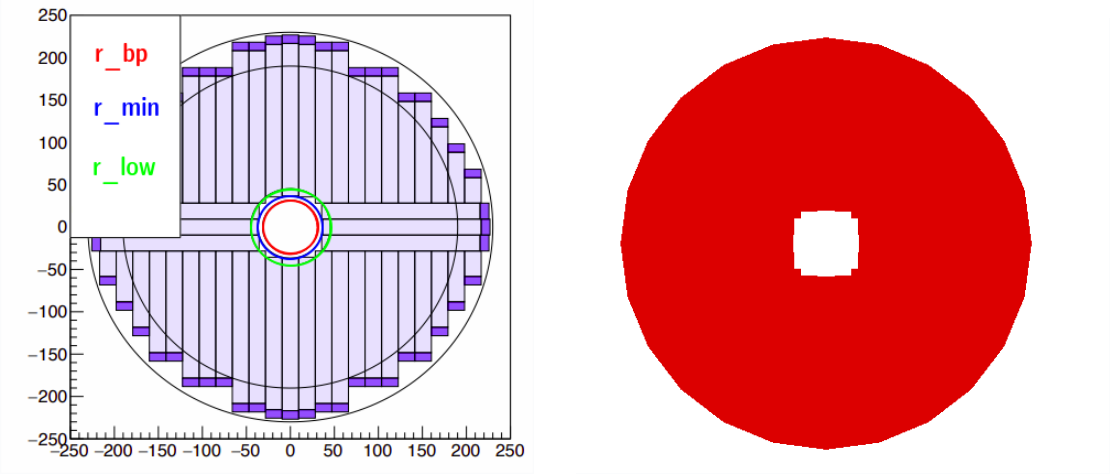

(a) (b)

Figure 4.31: (a) A conceptual disk design for the innermost disk, where sensors of different lengths are arranged in a central cross, and the remaining sensors placed parallel to one arm of the cross. The axes give the disk dimensions in units of mm. (b) A visualisation of a Geant4 implementation of the innermost disk, where the inner opening replicates the inner opening of the conceptual disk design.

There are therefore two conclusions that can be drawn from this, the first being that the μRWELL layer does not result in an improved momentum resolution when all other layers are functional and measure hits. As the momentum resolution is not improved by the presence of the μRWELL when one MAPS layer and/or the CTTL do not record hits, it can also be seen that the μRWELL does not provide redundancy. These results indicate that that the primary role of the barrel μRWELL is pattern recognition.

4.5.5 Large $|\eta|$ Acceptance Studies

Realistic Disk Opening

In the ePIC simulations presented so far, the disks have been constructed as cylinders, with perfectly circular inner and outer radii. For such disks, a single disk provides continuous coverage up to a certain polar angle, after which there is no coverage. As the sensors that will be tiled to construct the disks are rectangular, disk designs that rely on linear arrays of sensors (which are typically required to minimise material budget, see designs in section 4.4.3) do not provide full azimuthal coverage at the inner radii of the disks. Instead, the inner openings of the disks in such a design usually resemble a jagged square (see Fig. 4.31), as opposed to the circular opening used in simulations.

Another consideration for the inner opening of the disk is the presence of a 25 mrad crossing angle between the beams, and the resultant offset in the x-axis of the centre of the beampipe at $|z| \gtrsim 70\,\text{cm}$. Consequently, the inner openings of disks ED3 and ED4 in the electron endcap, and disks HD2 to HD4 in the hadron endcap, are offset from $(x, y) = (0, 0)$.

The partial azimuthal coverage of the inner disk radii and the offset of the inner opening both have the effect of introducing regions of partial coverage at fixed polar angles. Consider a value of η for which there is full geometric acceptance (the track intersects all disks). If η is increased then eventually a region of partial acceptance is reached i.e. the track intersects a disk between r_{min} and r_{low}. Here, r_{min} is the smallest radius that can be instrumented (beampipe radius +5 mm), and r_{low} is the smallest radius where full azimuthal coverage is provided, see Fig. 4.31a.

In previous simulations, the disk openings have been circular and centred on $(x, y) = (0, 0)$, with inner radii such that the perigee of the opening is at least 5 mm from the beampipe, due to the bake-out requirement. In this case, the inner radius, r_{in}, is given by

$$r_{in} = r_{bp} + |x_{offset}| + 5\,\text{mm}, \tag{4.1}$$

where r_{bp} is the outer radius of the beampipe, and x_{offset} is the x coordinate of the centre of the beampipe at a given z.

To evaluate the coverage offered by an endcap tracker with disks composed of tiled rectangular sensors, Geant4 implementations of disks with a realistic inner opening were produced (an example is pictured in Fig. 4.31b). The inner opening in the Geant4 implementation was designed to recreate the same inner opening shapes as the disks produced by a sensor tiling algorithm, described in reference [120]. These disks were imported into Fun4All and studied with single particle simulations. Particles were generated with the following settings:

- Generated particle: single e^- ($\eta < -2.5$), single π^- ($\eta > 2.5$)
- Generated distributions: uniform in p_t and η
- Generation vertex: origin
- Ranges: $0 < p_t < 10\,\text{GeV}$, $2.5 < |\eta| < 4$
- Magnetic Field: 1.7 T solenoidal field map

The parameters associated with the inner openings of the disks are summarised in

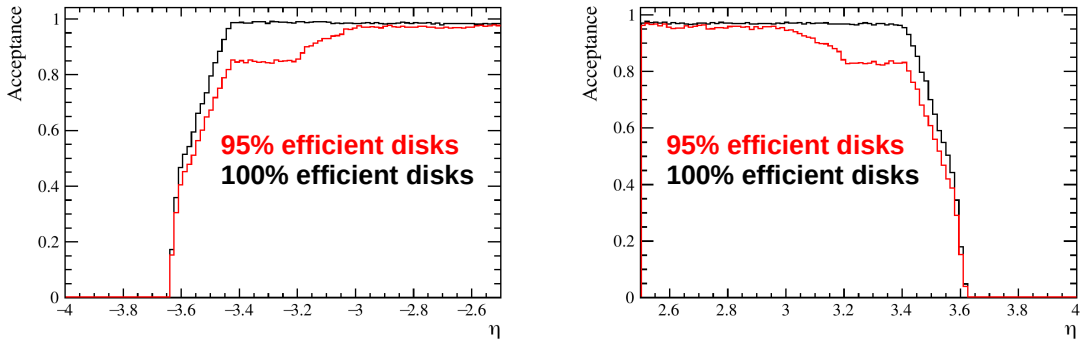

Figure 4.32: Tracking acceptance as a function of η, with 95 % and 100 % efficient (a) backward MAPS disks and (b) forward MAPS disks with a realistic inner opening, as determined from Fun4All simulations.

Table 4.20. A full track reconstruction treatment is not used, instead the track is deemed to be successfully reconstructed if three or more hits are measured by the disks, and so the (geometric) acceptance is defined as

$$\text{Acceptance} = \frac{\text{Number of events with 3 or more hits}}{\text{Total number of events}}. \tag{4.2}$$

Fun4All simulations were performed with the geometry and generation settings described, and the acceptance evaluated as a function of η for the forward and backward disks, assuming single hit detection efficiencies of 95 % and 100 %. The results of these simulations are shown in Fig. 4.32.

For disks configured as described by Table 4.20 with 100 % single hit detection efficiency, full acceptance is provided up to $|\eta| \sim 3.4$, beyond which partial acceptance is provided up to $|\eta| \sim 3.6$. EIC physics studies typically assume coverage in the region $|\eta| < 3.5$. An acceptance of $\gtrsim 80\,\%$ is achieved for $3.4 < |\eta| < 3.5$. If the disk design does not allow for overlaps between sensors, the single hit efficiency will inevitably be reduced due to dead areas between the sensors. Dedicated studies will need to be performed to evaluate the single hit efficiency of the disks at a later stage of the development timeline, and so a conservative value of 95 % is studied.

When the disk single hit efficiency is 95 %, a loss of acceptance occurs initially at $|\eta| \sim 3$, with a gradual decrease in the acceptance from 1 to ~ 0.86 at $\eta \sim 3.2$. This corresponds to the region for which E/HD1 goes from providing partial acceptance, to only E/H2-4 being hit. If only three disks are in the charged particle's path, the acceptance is reduced by the probability that one (or more) of the three disks fails, so Acceptance $= 0.95^3 \simeq 0.86$. This acceptance is maintained until the partial

Table 4.20: Disk parameters of the ePIC tracker layout used in Fun4All disk acceptance studies.

Disk	z (mm)	x_{offset} (mm)	r_{min} (mm)	r_{low} (mm)
ED4	-1350	-5.3	46.1	56.5
ED3	-1000	-1.81	40.8	53.3
ED2	-700	0	36.8	45.4
ED1	-450	0	36.8	45.4
ED0	-250	0	36.8	45.4
HD0	250	0	36.8	45.4
HD1	450	0	36.8	45.4
HD2	700	0.56	37.9	46.3
HD3	1000	7.85	45.6	56.1
HD4	1350	16.02	54.2	67.8

acceptance region of E/HD2 is reached at $|\eta| \sim 3.4$, after which there is once again a drop to 0 at $|\eta| \sim 3.6$.

The acceptance as a function of η can be used to create a mapping to the acceptance of a given $x-Q^2$, by applying a weight based on the pseudorapidities of the scattered electrons in a given $x-Q^2$ bin. For this purpose, a DIS event generator sample for the $18\times275\,\mathrm{GeV}^2$ beam configuration, generated using Pythia8 [121] with $Q^2 > 1\,\mathrm{GeV}^2$, is considered. The following procedure is used to determine the acceptance in a given $x - Q^2$ bin:

1. Determine x and Q^2 for the event
2. Sample random value v between 0 and 1 from a uniform distribution
3. Find η of scattered electron: If $v <$ Acceptance(η), the event is reconstructed
4. Acceptance of an $x - Q^2$ bin is the number of events "reconstructed" divided by the number generated in the bin

The tracking acceptance as a function of x and Q^2 is shown in Fig. 4.33. A binning scheme of 5 bins per decade in x and Q^2 is used for the $x - Q^2$ acceptance plots. The Q^2 range is restricted by the generation and reconstruction conditions to $1 < Q^2 \lesssim 8.7\,\mathrm{GeV}^2$, as $8.7\,\mathrm{GeV}^2$ is the upper Q^2 threshold for electrons scattered at $\eta \sim -2.5$, with $E_e \sim 18\,\mathrm{GeV}$.

The acceptance vs Q^2 plot in Fig. 4.33c maps to the equivalent plot against η in Fig. 4.32a due to the strong correlation between Q^2 and η. Here, the drop to 86 % acceptance occurs at $Q^2 \sim 2\,\mathrm{GeV}^2$, and the drop to no acceptance just above $Q^2 \sim 1\,\mathrm{GeV}^2$, though it should be noted that the minimum Q^2 generation threshold

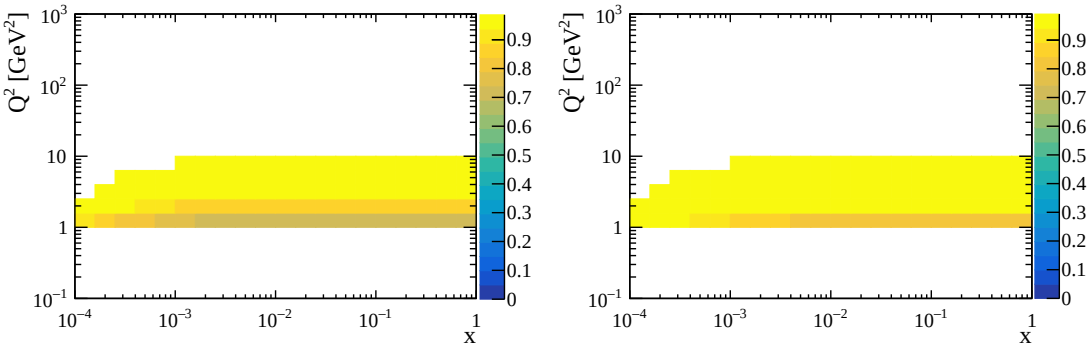

(a) Acceptance vs $x - Q^2$ with 95 % efficient disks

(b) Acceptance vs $x - Q^2$ with 100 % efficient disks

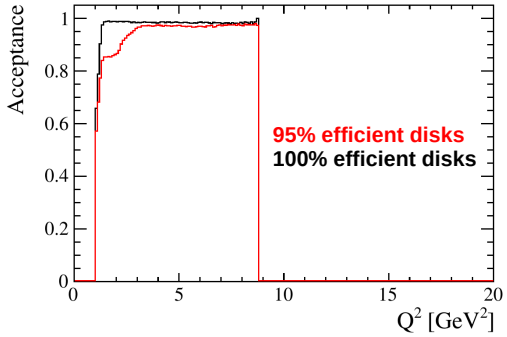

(c) Acceptance vs Q^2 with 95 % and 100 % efficient disks

Figure 4.33: Tracking acceptance as a function of x and Q^2, with 95 % and 100 % efficient MAPS disks, for an $18 \times 275\,\mathrm{GeV}^2$ DIS sample generated using Pythia8.

of $1\,\mathrm{GeV}^2$ means that partial coverage provided below $Q^2 \sim 1\,\mathrm{GeV}^2$ is not seen due to the lack of events generated in this range.

The most significant acceptance losses in the $x - Q^2$ plots are seen in the lowest Q^2 bins, which span $1 < Q^2 \lesssim 1.6\,\mathrm{GeV}^2$, and at large values of x. The acceptance is reduced to $\sim 70\,\%$ in the low Q^2, high x bins in the 95 % efficiency configuration, and $\sim 80\,\%$ in the 100 % efficiency configuration. It should be noted that for several of these bins, the corresponding inelasticity y is less than 0.01, and such bins would often be excluded in DIS analyses.

Electron Beam Energies

Continuous coverage over a large Q^2 range is necessary to achieve the goals of the EIC physics programme. It is challenging to provide this coverage for a single electron beam energy, as a gap in η coverage between the central detector and the far backward detectors is inevitable due to the presence of the beampipe. For this rea-

son, among others, multiple electron beam energies are to be employed at the EIC. For this study, and all subsequent studies in this chapter, simulations are performed using the ePIC software unless otherwise stated.

To evaluate the coverage of the central detector, the ePIC software is used to generate single electron events, propagate the electrons through the ePIC geometry, and reconstruct the tracks using an implementation of ACTS in the software. The tracking geometry is as described in Section 3.2. It should be noted that the disks implemented in the geometry for this study are cylindrical, and therefore do not account for the beampipe offset or sensor tiling scheme. Additionally, the thickness of the gold coating applied to the beampipe is updated from 2 µm to 5 µm in accordance with studies conducted by the ePIC Background Task Force [103]. This coating thickness is used in all subsequent studies using the ePIC detector in this thesis. The simulation uses the following settings:

- Generated particle: single e^-
- Generated distributions: uniform in p_t and η
- Generation vertex: origin
- Ranges: $0 < p_t < 0.5\,\text{GeV}$, $-4 < \eta < 4$
- Magnetic Field: 1.7 T solenoidal field map

A map of the reconstruction efficiency using the ePIC software, as a function of η and p_t, is shown in Fig. 4.34. The efficiency in a given $\eta - p_t$ bin is determined as the fraction of events in that bin where a single electron is successfully reconstructed by the ePIC software, with no requirements placed on the resolution of the reconstruction. In an electron finding algorithm, electron candidates are typically selected from tracks that have a matched cluster in the electromagnetic calorimeters. As such, in these simulations the electrons are deemed to be successfully reconstructed if a track is reconstructed, and one or more energy deposits are found in the electromagnetic calorimeters for the event.

The reconstruction efficiency in Fig. 4.34 is only drawn for the $0.01 < y < 0.99$ region of the kinematic plane for each of the three electron beam energies (5 GeV, 10 GeV, and 18 GeV), as beyond this region it is difficult to precisely reconstruct the event kinematics. Isolines are drawn for different Q^2 and y values at a given electron beam energy (the proton beam energy is only required in order to calculate x). It should be noted that the DIS cross section decreases with increasing y (refer to Eq. 2.24), so the highest statistics are available closer to the $y = 0.01$ isoline.

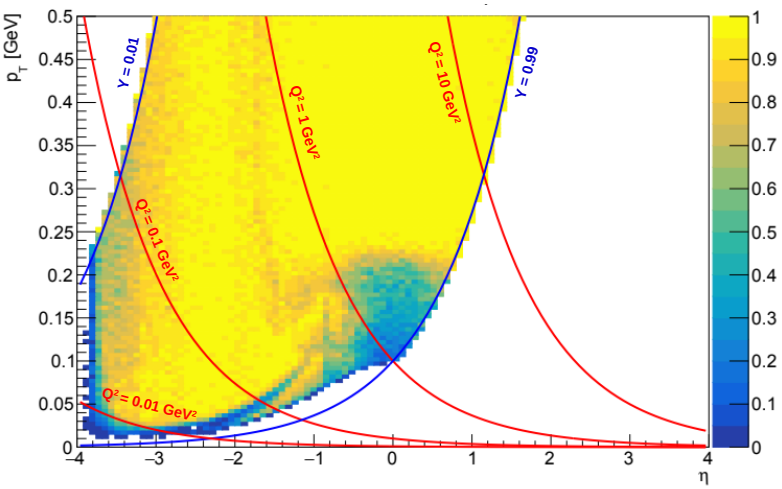

(a) 5 GeV e^- beam

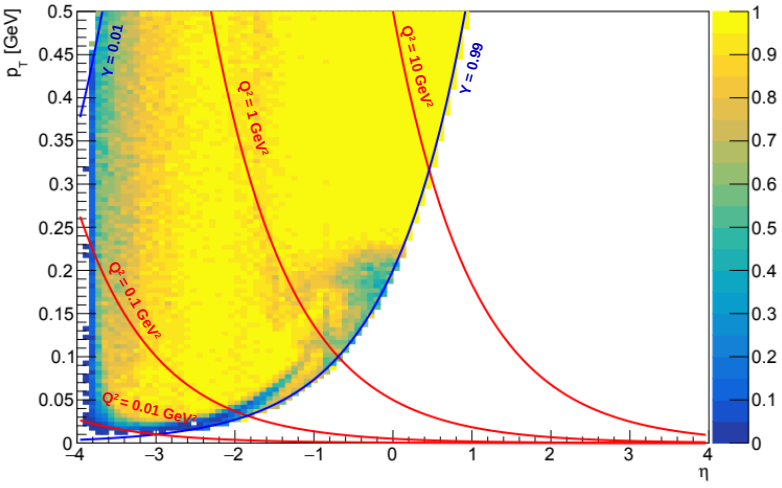

(b) 10 GeV e^- beam

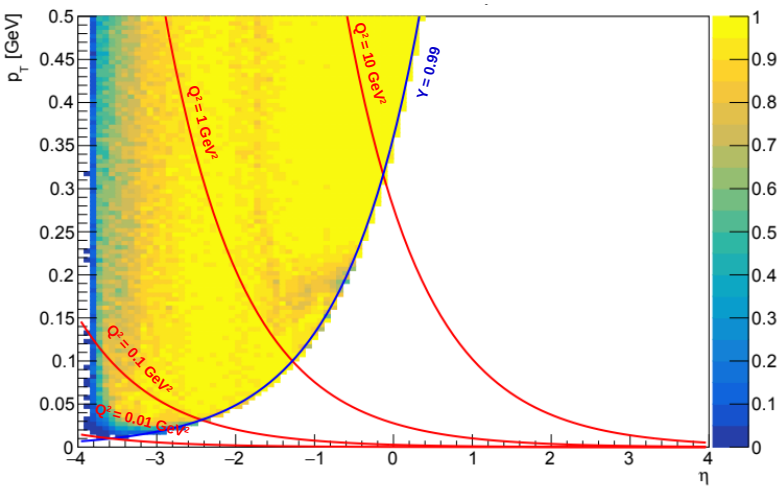

(c) 18 GeV e^- beam

Figure 4.34: Track reconstruction efficiency as a function of η and p_t for single electron events reconstructed using the ePIC software. Isolines are drawn for different values of Q^2 and y for three electron beam energies: (a) 5 GeV, (b) 10 GeV, and (c) 18 GeV. The efficiency is only drawn for events with $0.01 < y < 0.99$.

There are some areas of reduced efficiency, that are most obvious for the 5 GeV electron beam configuration in Fig. 4.34. The ACTS implementation used in these simulations relies on a truth-seeding approach. In truth seeding, the initial track parameters prior to fitting are set according to the generated values of the track, and selection criteria chosen to discard tracks that are unlikely to be reconstructed by a realistic track reconstruction algorithm. One criterion imposed by the ACTS truth seeding implementation in the ePIC software is a minimum momentum for seeding of $p = 0.1\,\text{GeV}$. Generated particles that have momenta of less than 0.1 GeV do not produce a valid seed, and are therefore not reconstructed. This is responsible for the region of 0 efficiency at low p_t and high y in the 5 GeV beam configuration.

A region of degraded efficiency ($\lesssim 60\,\%$) is present at central pseudorapidities for $0.1 \lesssim p_t \lesssim 0.2\,\text{GeV}$. It is possible to attribute much of this to the requirement for a calorimeter measurement, as the minimum transverse momentum required to reach the barrel electromagnetic calorimeter at $r \sim 80\,\text{cm}$ is $\sim 0.2\,\text{GeV}$ when a 1.7 T magnetic field is present. A small drop in efficiency is also seen at $\eta \sim -1.7$, which corresponds to the transition between the barrel and electron endcap calorimeters.

At least partial η coverage is provided up to $\eta \sim -3.7$, though the efficiency begins to drop for $\eta \lesssim -3.5$. For lower electron beam energies, the electrons are less boosted, and the region of the kinematic plane within the chosen y cuts is more central in pseudorapidity. The minimum Q^2 that can be accessed therefore varies with the electron beam energy, with high levels of coverage being provided down to $Q^2 \sim 0.1\,\text{GeV}^2$ in the 5 GeV beam configuration, and down to $Q^2 \sim 1\,\text{GeV}^2$ in the 18 GeV beam configuration. $Q^2 > 1\,\text{GeV}^2$ is often chosen as a cut in inclusive DIS analyses, to interpret results within a perturbative QCD (pQCD) framework. Partial coverage is also provided down to $Q^2 \sim 0.01\,\text{GeV}^2$ in the 5 GeV beam configuration. Between the three electron beam energy configurations, it should be possible to cover the gap in acceptance between the central and far-backward detectors for a single beam energy.

4.5.6 Realistic Track Seeding in ePIC Software

The track reconstruction algorithms used in the ePIC software are still under development. The eventual aim is that the software should provide full track and vertex reconstruction for events containing many charged particles, as well as beam backgrounds. As the development of seeding and vertexing algorithms for multi-particle events is ongoing, simulations of full physics events use a "Truth Seeding" approach.

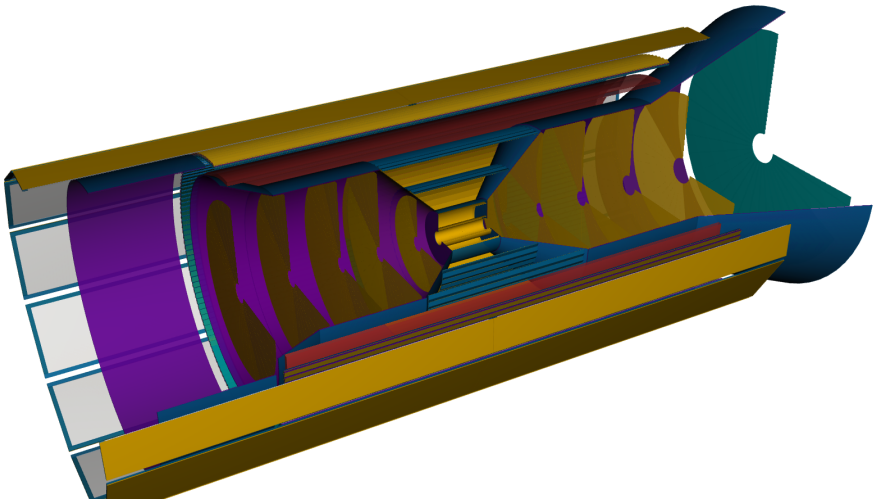

Figure 4.35: Visualisation of the ePIC tracking system as implemented in the ePIC software at the time of the track seeding studies.

For track recognition based on the seeding and following approach, described in Section 3.3.4 and used for ACTS track reconstruction in the ePIC software, a starting initial set of track parameters describing a track candidate called a "seed" is required. In the truth seeding implementation in the ePIC software, one seed is initially produced for each charged particle in the Monte-Carlo (MC) event record, with the track parameters of each seed set to those of the corresponding MC particle. Seeds are removed if their pseudorapidity or vertex position would see the tracks produced outside of the detector acceptance. Finally, the momentum of the seeds are smeared by a factor (10 % by default) to avoid biasing the track fit.

The tracking geometry used in these studies, for which a visualisation is shown in Fig. 4.35, is an earlier iteration of the design presented in Section 3.2. The notable differences are in the positions of the backward disks, and the lack of additional μRWELL disks in both endcaps. The layer dimensions and positions are summarised in Table 4.21 and 4.22.

It is important to understand the behaviour of the truth seeding algorithm, such that the realistic seeding algorithm can be benchmarked against it. The impact of the momentum smearing factor applied during truth seeding, on the momentum resolution of the final reconstructed track, is studied using a sample of simulated events produced using the ePIC software. The tracks are reconstructed from seeds with three different levels of momentum smearing. The generation was performed for single electrons with fixed momenta, with the full settings summarised as:

Table 4.21: Disk parameters of the ePIC tracker layout used in ePIC software seeding studies.

Disk	z (mm)	r_{in} (mm)	r_{out} (mm)
ED4	-1150	46.4	430
ED3	-900	40.1	430
ED2	-650	36.8	430
ED1	-450	36.8	430
ED0	-250	36.8	230
HD0	250	36.8	230
HD1	450	36.8	430
HD2	700	38.4	430
HD3	1000	43.4	430
HD4	1350	70.1	430
FTTL	1920	85.0	670

Table 4.22: Disk parameters of the ePIC tracker layout used in ePIC software seeding studies.

Layer	r (mm)	z_{min} (mm)	z_{max} (mm)
L0	36	-135	135
L1	48	-135	135
L2	120	-135	135
L3	270	-270	270
L4	420	-420	420
μRWELL	550	-1050	1430
CTTL	646	-1125	1740

- Generated particle: single e^-
- Generated distributions: Fixed p, uniform in η
- Generation vertex: origin
- Ranges: $0 < p < 13.75\,\text{GeV}$, $0 < \eta < 3$
- Magnetic Field: 1.7 T solenoidal field map

A comparison of the relative momentum resolution with different seed momentum smearing factors, ranging from no smearing to 10 % smearing, is given for forward pseudorapidities ($0 < \eta < 3$) in Fig. 4.36. While the three smearing factors give compatible results at central pseudorapidities, tracks with $\eta > 1$ give a worse momentum resolution at low p for smeared truth seeds compared to those with no smearing. Additionally, the momentum resolution of tracks reconstructed from unsmeared truth seeds improves as $p \to 0$. Such an improvement in the momentum resolution is unphysical, as the multiple scattering contribution is flat for much of the momentum range, and deteriorates the resolution at very low momenta as $1/\beta$ (see Eq. 3.18).

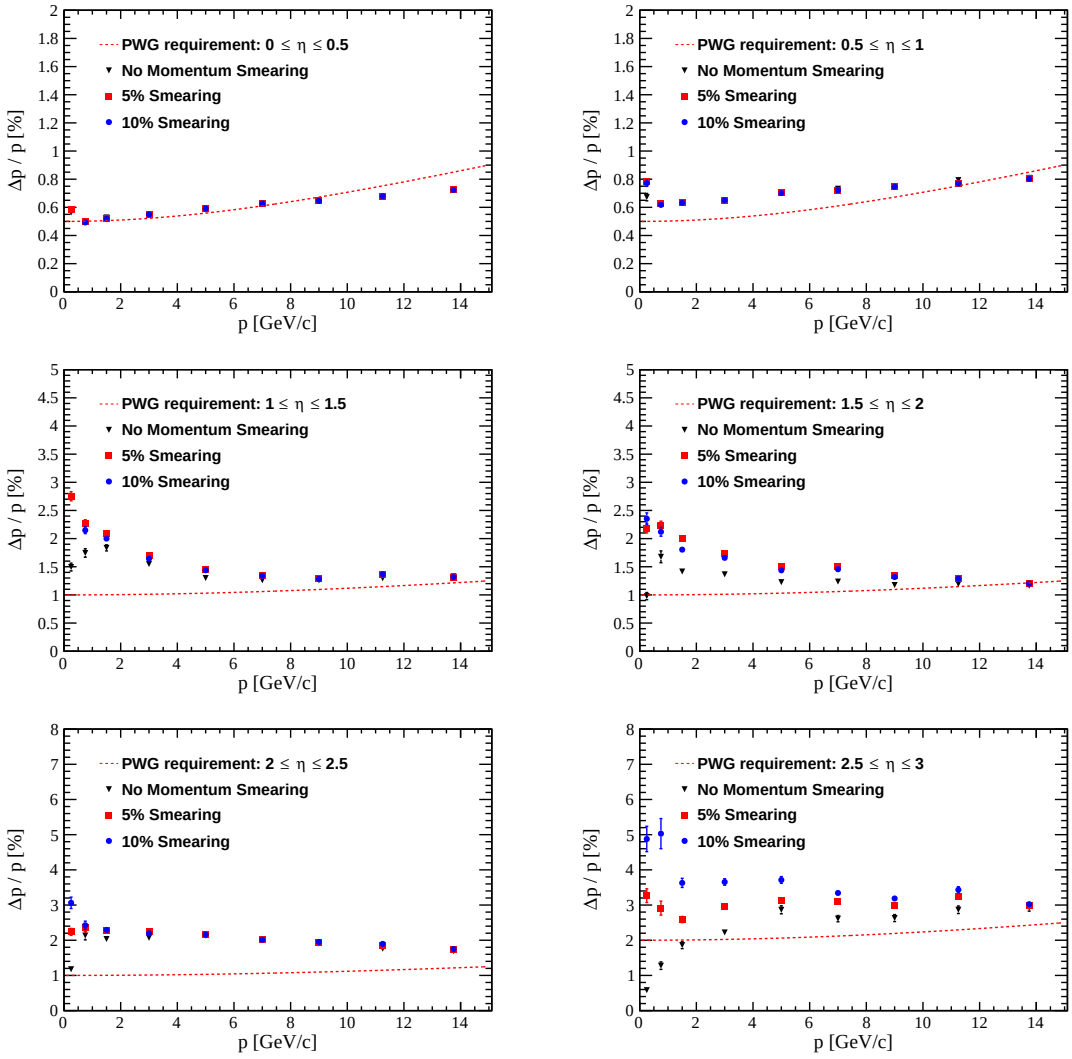

Figure 4.36: Comparison of the relative momentum resolution using truth seeding with momentum smearing factors of 0 %, 5 %, and 10 %, for single electron events simulated in the forward region of a description of the ePIC tracker in the ePIC software.

If all parameters associated with the seed are correctly set, the fitted tracks should be the same regardless of the initial momentum smearing on the track. The discrepancy between the performance with the three smearing factors can be understood by considering the covariance matrices associated with track seeds. In a "realistic" seeding algorithm, initial fits are performed, and the covariance of the six parameters associated with the seed ($\overrightarrow{x} = (d_0, z_0, \phi, \theta, q/p, t)$) can be extracted from the fit. In the truth seeding implementation in the ePIC software, no fit is performed, and the seed covariance matrix is set to values that do not depend on the momentum smearing of the MC particle acting as the seed. If the covariance matrix of the seed is too strict, the measurements will not pull the track parameters sufficiently far from the initial parameters set by the seed.

At larger pseudorapidities and lower momenta, where the errors on a realistic seed are often large, the covariance of the truth seed parameters are often underestimated, so the momentum resolution final fitted tracks tends towards the momentum resolution of the seeds: 0 %, 5 %, and 10 % in this case.

Truth seeding is currently the only approach available in the ePIC software for track reconstruction in full physics events, and it is desirable that a track reconstruction algorithm using realistic seeds be developed for ePIC. The development is ongoing, and is currently able to be used for the reconstruction of single particles. For a set of three seed points, the seed parameters are reconstructed as follows:

1. Project the positions of the seed points in the $x - y$ plane and perform a circle fit.
    - Transverse momentum is found as $p_t = B\rho$.
    - ϕ is found from the tangent to the circle at the point closest to $(0, 0)$.
    - Charge q is found from the direction of the first two hits relative to $(0, 0)$.
2. Project the positions of the seed points in the $r - z$ plane and perform a linear fit.
    - θ is found as the slope of the line
    - momentum is found as $p = p_t \cosh \eta$.

The triplets (sets of three seed points) that become seeds are chosen from among all space-points measured in the MAPS barrel and disk layers. The triplets must be composed of bottom, middle, and top space-points, where bottom/middle/top refers to their ordering radially. A requirement is imposed that less than 40 cm of radial distance separates the middle space-point from the other two. This requirement is set in order to consider seeds of as many space-point combinations as possible for these initial studies. The number of seeds produced for a single charged particle can be reduced by reducing the permitted radial separation of space-points.

The number of hits in the MAPS tracking layers produced by single muons with momenta $0.5 < p < 20$ GeV is shown as a function of η in Fig. 4.37a, while the number of seeds produced by the electrons with the previously described generation settings is shown in Fig. 4.37b. The ePIC software allows for a given space-point to act as the middle space-point only once, so the number of seeds produced with these settings relates to the number of hits produced by the track N, as $N - 2$ (due to the

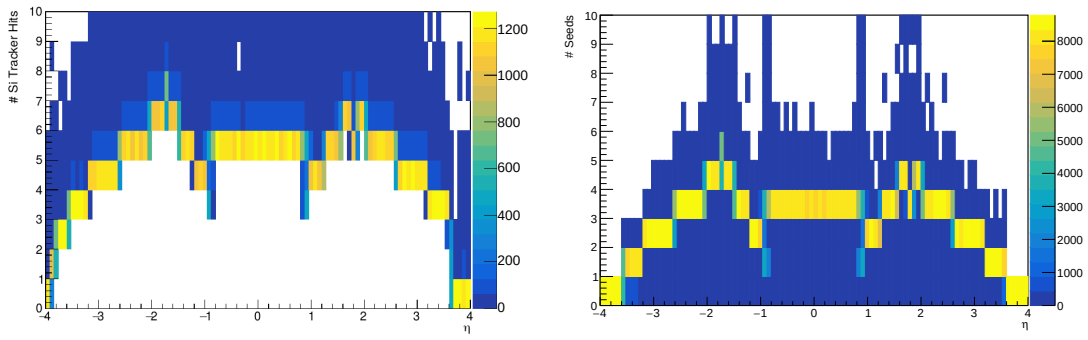

(a) **(b)**

Figure 4.37: (a) Histogram showing the number of hits in the silicon tracking layers for a given muon against the generated η of the muon. (b) The number of seeds produced by electrons generated at a given pseudorapidity.

fact that neither the innermost nor outermost layer can be the middle space-point). When interactions occur that produce secondary particles, and therefore additional space-points in a given layer, more than $N-2$ seeds may be found. Conversely, fewer seeds may be found if space-points are missing from a layer or no seed can be constructed that meets the seeding conditions. Two or more seeds are usually produced for the region $|\eta| \lesssim 3.2$, though a drop in seeding efficiency is noted at $|\eta| \sim 0.88$, where the service cone is present. For $|\eta| \gtrsim 3.2$, only one seed is possible as the MAPS tracker only sees hits in the three outermost disks at these pseudorapidities, with these disks providing coverage up to $|\eta| \sim 3.5$.

The seeds produced by the same particles, but using triplets composed of space-points in different layers, should give a similar result for the final fitted track. Fig. 4.38 shows the relative momentum resolution from single electron events in the forward direction, using the realistic seeding implementation in the ePIC software. The seed that reconstructs the track with the closest momentum value to the true track is compared to seeds chosen at random from the available seeds.

The momentum resolution is the same at central pseudorapidities ($0 < \eta < 1$) regardless of the chosen seed. Some discrepancies are seen between the different seed choices at large η and low p. The momentum resolution with the realistic seeding implementation is comparable to those obtained with the various truth seeding approaches, indicating that the realistic seeding approach outlined in this section works as intended. The natural continuation of this work will be the development of a method that selects a single seed that gives the best initial guess for track reconstruction from the multiple seed candidates produced by a single particle.

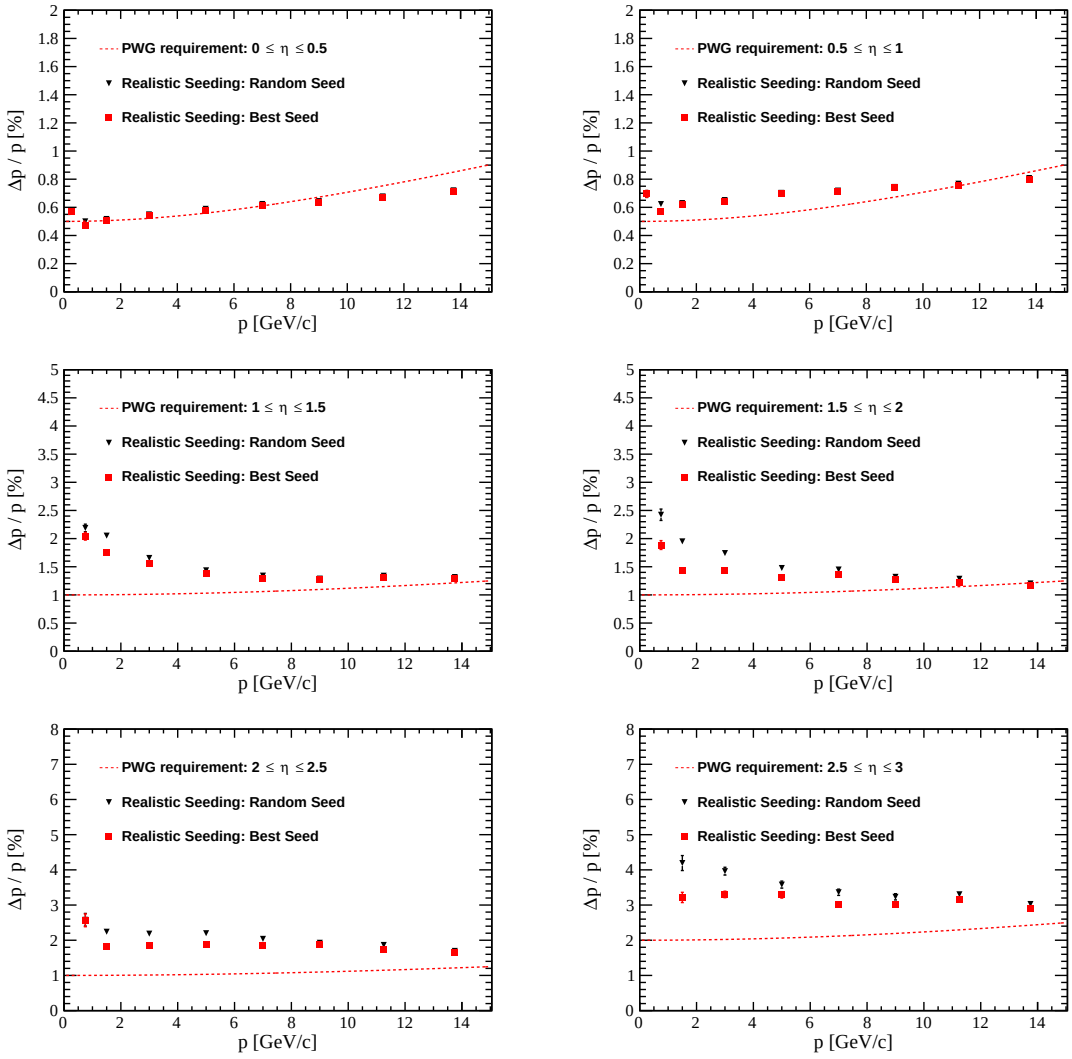

Figure 4.38: Comparison of the relative momentum resolution using realistic seeding for the seed that reconstructs the track with the best momentum resolution, and for a randomly selected seed from among the seed candidates.

4.5.7 Beam Backgrounds

In addition to the particle rates from DIS collisions, for which a maximum rate of $\sim$ 500 kHz is anticipated (with the highest instantaneous luminosity $\mathcal{L} = 10^{34}\,\mathrm{cm}^{-2}\,\mathrm{s}^{-1}$ in the $10 \times 275\,\mathrm{GeV}^2$ ep beam configuration), two major background sources contribute to the particle rates at the EIC. Interactions of the beam electrons and protons with residual gas in the beampipe, termed beam-gas interactions, result in a combined hit rate in the MAPS tracker at the MHz level. The hit rate due to synchrotron radiation is $\sim$ 1 MHz in the absence of gold beampipe coating, but can be reduced to $\sim$ 10 kHz with the 5 µm coating applied [103].

Radiation levels (total ionising dose and 1 MeV neutron equivalent fluence) due to DIS and beam-gas background events have been estimated by the ePIC Background

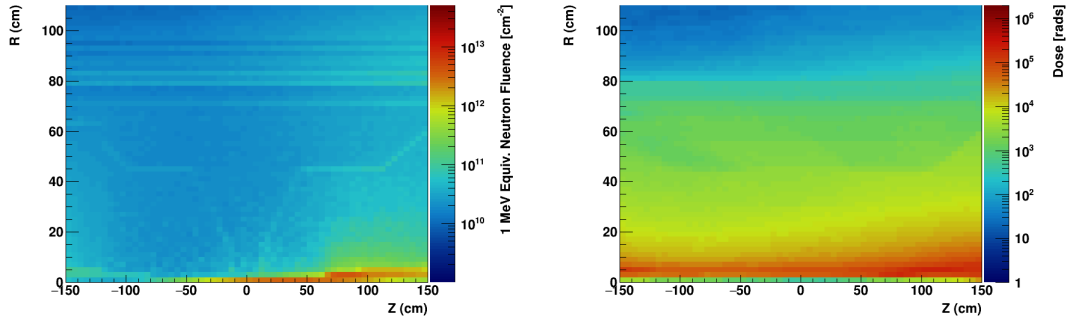

(a) **(b)**

Figure 4.39: (a) 1 MeV neutron equivalent fluence and (b) total ionising dose as a function of r and z in the region of the ePIC tracker. 10 years of running at top luminosity for 6 months per year are assumed.

Task Force for a running period of six months at the top instantanous luminosity configuration ($\mathcal{L} = 10^{34}\,\mathrm{cm}^{-2}\,\mathrm{s}^{-1}$, $10 \times 275\,\mathrm{GeV}^2$ e on p) [122]. The radiation simulations were conducted using the Starsim environment [123], with hadron transport provided by the GCALOR package [124] for Geant3. The 1 MeV neutron equivalent fluence is calculated according to the NIEL scaling hypothesis using the damage function for silicon [125]. The simulations were conducted individually for DIS events, 275 GeV proton beam-gas events, and 10 GeV electron beam-gas events.

Worst case estimates of the dose and fluence that one might see at ePIC are produced by combining and scaling the inputs provided by the task force, assuming that all runs are performed at the top luminosity, for 6 months of running per year over a 10 year period, shown in Fig. 4.39.

The maximum fluence levels are seen in the hadron going direction, though the region of maximum fluence is concentrated within the beampipe, and the majority of the MAPS tracking layers experience less than $\sim 10^{11}$ n_{eq} cm^{-2}, with some regions at smaller radii experiencing up to $\sim 10^{12}$ n_{eq} cm^{-2}. The dose levels are similarly maximal in this region of the beampipe. In these conditions, some regions of the MAPS tracker at lower radii experience a dose of the order of 100 krad, with the majority experiencing $\sim$ 10 krad or less. Even in this worst case estimate, the dose and fluence are at acceptable levels, as the ITS3 development requires sensors capable of functioning under radiation loads of up to 10^{13} n_{eq} cm^{-2} and 10 kGy (1000 krad) [126].

The rates of the various sources of particle production are summarised in Table 4.23. As the accelerator accumulates run time, the vacuum conditions improve and the rate of beam-gas interactions is reduced as a result, and so the rates are presented

Table 4.23: Rates in kHz for the various sources of particle production, limited to those produced in the $-4.5 < z < 5$ m region. Luminosity values are as in Table 3.3 of the EIC Conceptual Design Report [11], and the total cross section is taken from Pythia6.

Rate (kHz)	5×41	5×100	10×100	10×275	18×275	Vacuum
DIS ep	12.5	129	184	500	83	-
p beam-gas	12.2	22.0	31.9	32.6	22.5	10 000 A h
p beam-gas	131.1	236.4	342.8	350.3	241.8	100 A h
e beam-gas	2181.97	2826.38	3177.25	3177.25	316.94	10 000 A h

for the vacuum conditions after 100 A h and 10 000 A h of running.

Studies by the ePIC Background Task Force have also seen the hit rates in different ePIC subdetectors evaluated for DIS, SR and beam-gas interactions from 10 GeV electrons, and proton beam-gas interactions at 275 GeV.

In the following study, the hit rates on individual SVT layers for combined DIS, beam-gas, and SR events are evaluated in the $10 \times 100\,\mathrm{GeV}^2$ beam configuration. To give a worst case estimate, the maximum rates for this beam configuration are used: 184 kHz for DIS, 342.8 kHz for proton beam-gas, and 3177.25 kHz for electron beam-gas.

An event sample for which each event consists of particles generated by DIS and background processes in a 2 µs integration window (frame) is created by sampling from separate event samples. The event samples contained minimum bias DIS events, particles produced by electron and proton beam-gas interactions, and SR photons. The number of events of a given type that are placed in a frame of the merged sample is determined by sampling from a Poisson distribution with the mean set according to the event rates in Table 4.23. The output of SynRad+, which is used to generate the SR, gives a flux of photons rather than individual photons. The average SR rate determines the poisson μ for the number of SR photons in a frame, and individual photons are drawn from the sample using their flux as a weight.

The merged event sample is passed through the ePIC geometry using the ePIC software, with the layout described in Section 4.5.6. The hit rates due to DIS events and DIS+Background events are extracted, and shown for each of the silicon barrel and disk layers in Fig. 4.40. Rates of $\sim 3 - 5$ MHz are measured in the two innermost barrel layers and the disks, while the rates in the remaining barrel layers are below 1 MHz. The rates are dominated by hits from background particles, which result in an order of magnitude increase in the rate for many of the layers. An

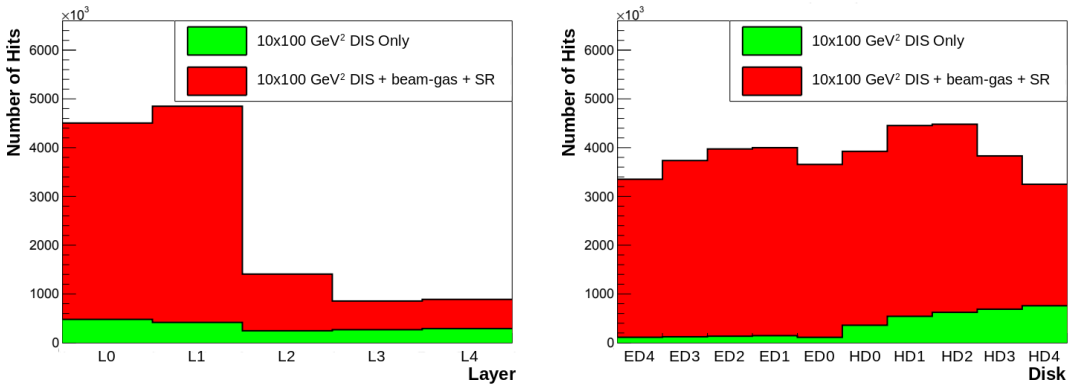

(a) Barrel **(b)** Endcaps

Figure 4.40: Number of hits measured in 1 s by the (a) barrel and (b) endcap tracking layers in the $10 \times 100\,\mathrm{GeV}^2$ beam configuration, for DIS events only, and DIS + beam related backgrounds.

Table 4.24: Average hit occupancy of barrel MAPS tracking layers.

Layer	Hit rate (MHz)	Area (cm^2)	Hits / s / cm^2	Hits / pixel / frame
L0	4.50	610.73	7.38×10^3	7.00×10^{-8}
L1	4.85	814.30	5.96×10^3	5.65×10^{-8}
L2	1.41	2035.75	6.91×10^2	6.56×10^{-9}
L3	0.86	9160.88	9.33×10^1	8.85×10^{-10}
L4	0.89	22167.08	4.01×10^1	3.80×10^{-10}

Table 4.25: Average hit occupancy of MAPS disks in the electron endcap.

Disk	Hit rate (MHz)	Area (cm^2)	Hits / s / cm^2	Hits / pixel / frame
ED0	0.37	1767.11	2.07×10^3	1.96×10^{-8}
ED1	4.00	5368.16	7.45×10^2	7.07×10^{-9}
ED2	3.97	5536.32	7.18×10^2	6.81×10^{-9}
ED3	3.74	5532.26	6.75×10^2	6.40×10^{-9}
ED4	3.35	5524.62	6.07×10^2	5.76×10^{-9}

Table 4.26: Average hit occupancy of MAPS disks in the hadron endcap.

Disk	Hit rate (MHz)	Area (cm^2)	Hits / s / cm^2	Hits / pixel / frame
HD0	3.92	1767.11	2.22×10^3	2.11×10^{-8}
HD1	4.45	5368.16	8.30×10^2	7.87×10^{-9}
HD2	4.48	5533.75	8.10×10^2	7.68×10^{-9}
HD3	3.83	5513.51	6.95×10^2	6.59×10^{-9}
HD4	3.25	5486.76	5.92×10^2	5.62×10^{-9}

average hit occupancy is determined by scaling the hits in a given layer according to the area of the layer and of the pixels. The pixel dimensions are assumed to be $20.8 \times 22.8\,\mu m^2$ (currently forseen for the ITS3 sensor). The hit occupancies are summarised in Tables 4.24-4.26, where it is seen that the average occupancy of the pixels per readout frame ranges from 10^{-10} to 10^{-8} in the barrel region, and is of the order of 10^{-9} in the endcaps. These estimated hit occupancy levels do not pose a challenge for the sensor and readout electronics.

4.5.8 Current Status of ePIC Tracker

The most current ePIC tracker design, which is informed by the studies presented in this chapter, as well as by the many studies performed by members of the collaboration over the course of several years, is as described in Section 3.2, with the geometry outlined in Tables 3.1-3.3. To reflect the current status of the ITS3 development, with the recent sensor submissions using pixels with $\sim 20\,\mu m$ pitch, the pitch assumed in simulations using the ePIC software is $20 \times 20\,\mu m^2$.

The performance of the tracker configuration is evaluated, as before, in terms of its relative momentum resolution and transverse pointing resolution. Simulations are performed using the ePIC software with the following settings:

- Generated particle: single e^-
- Generated distributions: Fixed p, uniform in η
- Generation vertex: origin
- Ranges: $0 < p < 20\,\text{GeV}$, $-3.5 < \eta < 3.5$
- Track Seeding: Realistic
- Magnetic Field: 1.7 T solenoidal field map

The track reconstruction utilises the realistic track seeding method described in Section 4.5.6. The relative momentum and transverse pointing resolutions, extracted from these simulations and plotted for intervals of 0.5 in pseudorapidity, are shown in Fig. 4.41 and 4.42 respectively.

The PWG requirement for the relative momentum resolution is achieved in the central region, owing to the silicon barrel optimisation discussed in Section 4.5.2. The momentum resolution requirement in the forward direction is within reach for much of the η and p range, while the backward requirement is challenging to meet with the available magnetic field. A deterioration in the momentum resolution at large $|\eta|$ is unavoidable. As the target material budget for the MAPS disks is already ambitious,

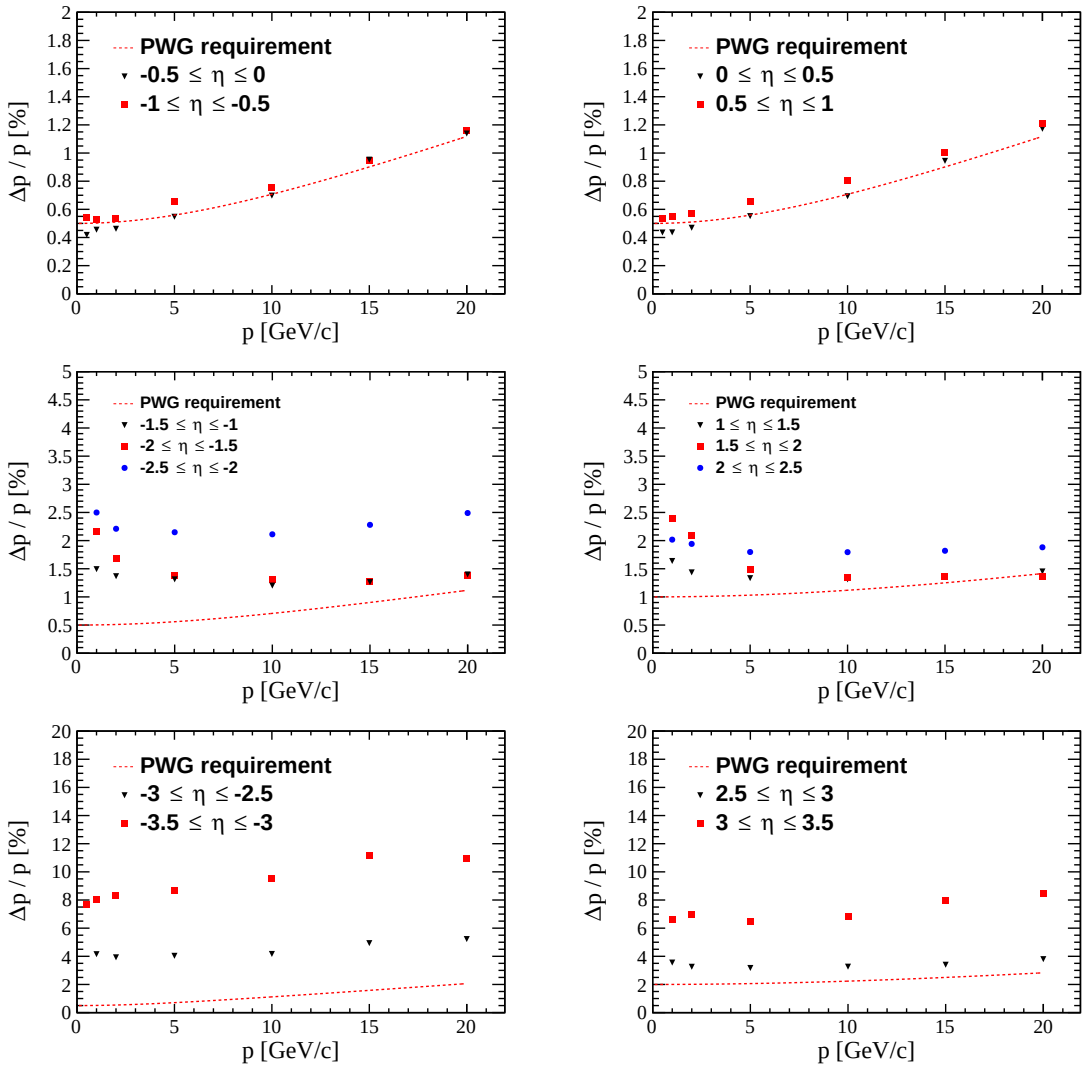

Figure 4.41: Relative momentum resolution as determined from single electron events propagated through the current ePIC tracking geometry and reconstructed using the ePIC software. A realistic track seeding algorithm is used for reconstruction.

and the full available lever arm is being used, the momentum resolution requirement in this region cannot be met by the tracking systems alone. The calorimetry systems provide an opportunity to recover the performance in this region, by combining the energy measurement from the calorimeters with the angular measurement from the tracker. This is beneficial in the forward direction, and essential in the backward direction, in order to achieve the EIC physics goals.

The transverse pointing resolutions in the central region are comparable to the PWG requirements. The large beampipe radius, and the clearance requirement from bake-out, prevent the vertexing layers from being placed any closer to the interaction point. The radii at which the layers may be placed are determined by the sensor size. As such, further optimisation of the transverse pointing resolution

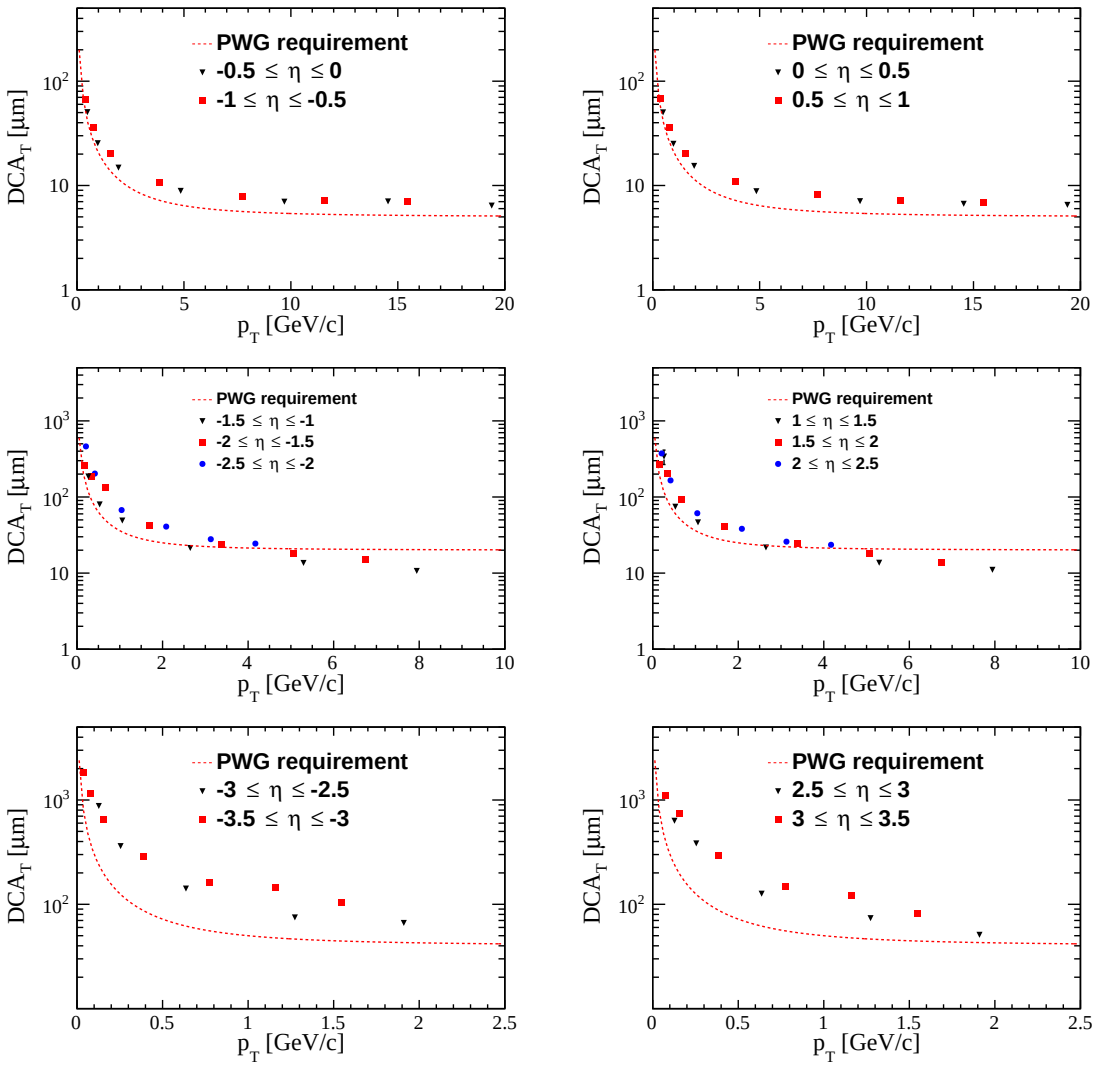

Figure 4.42: Transverse pointing resolution as determined from single electron events propagated through the current ePIC tracking geometry and reconstructed using the ePIC software. A realistic track seeding algorithm is used for reconstruction.

in the central region is not possible with current technology. The requirements are met in the intermediate region ($1 < |\eta| < 2.5$) for $p_t \gtrsim 4\,\text{GeV}$, but they are not met in the forward/backward region ($2.5 < |\eta| < 3.5$) for $p_t < 2.5\,\text{GeV}$.

4.5.9 Summary of Findings

Dedicated R&D has occurred since 2022, that expands on the reference detector design, leading to the current ePIC tracking design which aims to provide a performance that is capable of delivering the EIC physics programme, using technology that will be available on the time-scale of the EIC.

The aggressive $0.05\,\%\ X_0$ material budget targeted for the silicon outer barrel layers

was deemed to be incompatible with the timeline and resources of the experiment. Updating the material to a more realistic 0.55 % X_0 per layer leads to a significant degradation of the momentum resolution in the barrel region, to the extent that the PWG requirements are no longer met. A full reconfiguration of the barrel region has taken place, such that the PWG requirements can be met with realistic technology choices.

The radial positions available for the vertexing layers are determined by the sensor dimensions, and beampipe bake-out considerations. Of the possible radial positions for the vertexing layers, the configuration with the larger distance between the first and second vertexing layers has been found to give the better transverse pointing resolution. Hence, the configuration with the innermost vertexing layers at radial positions of 36 mm and 48 mm is chosen. It has also been established that in order to provide the required relative momentum resolution in the central region with the chosen magnetic field, the high precision MAPS barrel layers should provide coverage up to $r \sim 40$ cm. Additionally, the material budget of the sagitta layers is to be minimised. This is achieved by positioning the third vertexing layer at a larger radius of $r \sim 12$ cm, to contribute to the sagitta measurement while preserving the low material budget of 0.05 % X_0.

The effect of the beamspot, which causes origin vertices to be distributed over an extended z range, on the tracking resolutions, has been evaluated. It is found that the relative momentum resolution and transverse pointing resolution are not impacted for majority of the angular range. However, a degradation in the momentum resolution by a factor of ~ 1.25 is observed at η values corresponding to the angles at which the service cone is projected.

The role of the μRWELL detector in the barrel tracker has been investigated in terms of its contribution to the tracking resolutions and redundancy. It is found that for a barrel tracker design that includes an AC-LGAD timing and tracking layer at $r \sim 60$ cm, the μRWELL layer does not contribute to the resolution except in the case that neither the outermost MAPS layer nor the AC-LGAD TTL register a hit. The results of this study indicate that the μRWELL's main role is pattern recognition.

The acceptance of the tracking layers at large $|\eta|$ has been evaluated for single particles as a function of both pseudorapidity, and the kinematic variables x and Q^2. It is found for a realistic disk implementation, that includes the offset of the disk central opening and the tiling of sensors in the disk envelope, that partial accep-

tance is provided up to $|\eta| \sim 3.6$. It is also noted that, in the case of disks with $< 100\,\%$ efficiency, a drop in the acceptance occurs for $|\eta| \gtrsim 3.2$. The size of the drop depends on the disk efficiency, as only three hits in the MAPS layers can occur, and tracks can not be reconstructed from fewer than three hits. The acceptance as a function of η is used to create a mapping to x and Q^2, where it is seen that, in the $18 \times 275\,\mathrm{GeV}^2$ beam configuration, the acceptance for scattered DIS electrons drops for Q^2 below $\sim 3\,\mathrm{GeV}^2$ for $< 100\,\%$ efficient disks. Coverage is provided down to $Q^2 \sim 1\,\mathrm{GeV}^2$, which is sufficient for many inclusive DIS measurements.

The effect of beam related background radiation on the tracking detector has been studied, and it is seen that both the fluence and the total ionising dose are within acceptable levels for the SVT, based on a worst case estimate of 10 years of running for 6 months per year at top luminosity. The hit occupancy due to beam related backgrounds has also been studied, and is shown to cause an order of magnitude more hits in the tracking layers than DIS event in the $10 \times 100\,\mathrm{GeV}^2$ beam configuration. Despite the high rate of hits due to background processes, the overall rates do not pose a challenge for the sensor and readout electronics.

Finally, the tracking performance of the current design of the ePIC tracking detector has been shown. The resolutions are consistent with, or within reach of, the PWG requirements for much of the η and p range. For regions in which the tracking requirements cannot be met, most notably the backward region, the tracking measurements can be supplemented by calorimeter information, and charged particles reconstructed with a resolution that is sufficient for the challenging measurements targeted by the EIC.

Chapter 5

Kinematic Resolutions at the EIC

To achieve the physics goals of the EIC, a detector capable of precisely reconstructing DIS kinematics is required. Such a reconstruction can be obtained from measurements of the energies and angles of the scattered electron, the overall hadronic final state (HFS), or a combination of both. A precise angle and momentum measurement in the tracker, combined with excellent energy resolution in the calorimeters is necessary for the precision measurement of the scattered electron, while the hadronic final state measurement requires good tracking and calorimeter performance, and an algorithm for the optimal combination of their measurements.

The quality of kinematic reconstruction, and hence the related physics performance of a given detector configuration, can be optimised through dedicated physics studies using full detector simulations. The results of such studies are presented in this chapter.

5.1 ePIC Software

Software for the ePIC collaboration has been developed and continues development by the ePIC Software and Computing working group. The simulation is performed using the DD4hep software framework [99], which provides a full detector description (geometry, materials, readout, visualisation etc). DD4Hep builds from existing software components such as the ROOT geometry package; a tool for building, navigating and visualising detector geometries [97], and the Geant4 simulation toolkit, which is used to simulate the detector response as particles are propagated through the geometry [96]. Simulated physics events are passed through a DD4hep simulation, and a realistic detector output is produced. This output is then processed by the EICrecon framework [100], which is responsible for the digitisation and recon-

struction of the raw detector response. The EICrecon framework currently supports ACTS based tracking [101], calorimetry reconstruction, and some particle identification (PID). For the full simulation studies presented in this section, simulated full events from the Pythia6 event generator are passed through the ePIC detector geometry, processed by EICrecon, and the resulting output files analysed.

5.2 Event Reconstruction

In the initial stages of the EICrecon reconstruction chain, charged particle tracks are reconstructed using ACTS. The track reconstruction method employed for full physics events is broadly similar to the method described in Section 3.3.4, but with a different track seeding procedure. In a "realistic" track seeding algorithm, an initial guess of the track parameters is made using a preliminary fit of a triplet of space-points measured across different layers, which serves as the starting point for the full track fitting procedure. There are many tracks corresponding to different charged particles in a full physics event, and consequently there are many combinations of different space-point triplets that could be formed, which often do not correspond to the trajectory of a charged particle. To reconstruct tracks in full physics events, there needs to be an ambiguity resolution procedure to reduce the number of "fake" tracks being reconstructed.

The triplet-seeding based track reconstruction in EICrecon is still in the development stages, and is not ready for application to full physics events. For the studies in this chapter, an alternative seeding approach based on truth information is used instead. In the truth-seeding approach, all final-state charged particles are identified using the Monte-Carlo (MC) event information, and the seed track parameters set as the true values. Starting the track fit from the true values may bias the resulting fit, so the momentum of the seed is smeared according to a Gaussian distribution with a width of 10 % of the momentum, in order to mitigate this effect.

The matching of tracks to calorimeter clusters is also in the development stage for EICrecon, so an approach that leverages truth information is once again used. In the truth information based track-cluster matching procedure used by EICrecon, the Monte-Carlo ID (mcID) of the particle responsible for a given energy deposit in the calorimeters is compared to the mcID of all final-state particles in the event record, and used to form an association with the related MC particle. Energy deposits that share a common mcID are grouped into a calorimeter cluster. The mcID of the charged particle responsible for a given reconstructed track is identified by comparison of the track direction to the MC particle direction. Tracks and calorimeter

clusters that have the same associated mcID are set as a matched track-cluster pair.

In the final list of reconstructed particles, the charged particle parameters are set according to the track information, which provides the momentum and angle. The mass, and hence energy, of the reconstructed charged particles is determined using the PDG ID of the MC particle that is associated with the track. The energy and angle of reconstructed neutral particles are determined from the energy and angle of the calorimeter clusters not associated with a track. The mass of a given reconstructed neutral particle is determined from the PDG ID of the MC particle that is associated with the cluster.

In order to reconstruct the event kinematics, the scattered electron should first be identified. This is usually accomplished using an electron-finding algorithm, which produces a list of electron candidates based on the features of the detector measurements, such as the energy or p_t of an EMCAL cluster, whether the cluster has a matching track, and the ratio of energy deposition in the EMCAL to the HCAL. The aim of the studies in this chapter is to evaluate the kinematic resolutions, so the efficiency of an electron-finding algorithm is a separate problem. Instead of a full electron-finding approach, the track corresponding to the scattered electron is chosen by comparison to the true energy and angle of the Monte-Carlo scattered electron. The inclusive HFS is determined as the summed four-momenta of all reconstructed particles other than the identified scattered electron.

Beam conditions, such as event-by-event momentum fluctuations, and the presence of a crossing angle, impact the reconstruction of kinematic variables at the EIC. During event generation, head on collisions with fixed energy beams are produced. Beam effects are introduced to the generated events using an "afterburner", which applies the 25 mrad crossing angle as well as the beam divergence, energy spread, and bunch size. The kinematic reconstruction methods use the energy of one or both beams during reconstruction, but beam energy fluctuations are not known for a given event, so the reconstruction methods use the nominal beam momenta instead. As a result of the crossing angle, the direction of the proton/ion beam is not aligned with the z-axis and thus has a non-zero transverse momentum in the lab frame. This affects reconstruction methods that rely on the HFS variables. To correct for this, a combination of Lorentz boosts is applied to the reconstructed HFS four-vector. First, there is a boost by the sum of beam four-momenta to get to the centre-of-momentum frame, then a rotation about the y-axis to eliminate the x component of momentum. Finally, there is a boost back along the z-axis to restore the original beam energies.

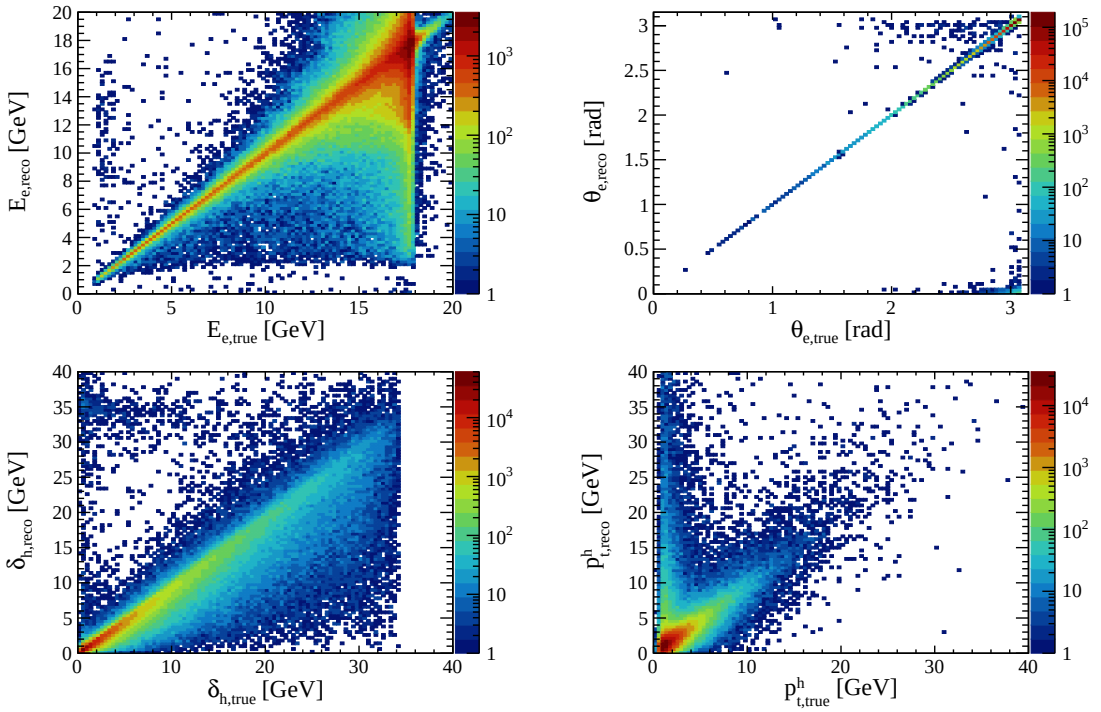

Figure 5.1: Correlation between the true scattered electron and HFS quantities, and the quantities reconstructed by the detector.

5.3 Resolutions and Bin Migration

Resolutions on the kinematic variables x, y, and Q^2 across the kinematic range are presented for the maximum ($18 \times 275\,\mathrm{GeV}^2$) centre-of-mass energy beam configuration. The "resolution" refers to the precision with which a given method reconstructs the three inclusive DIS variables, and is defined here as the RMS of the distribution $\Delta x/x$, $\Delta y/y$, or $\Delta Q^2/Q^2$. The variables are closely linked, with their relation described in Eq. 2.15. Therefore, for a fixed value of Q^2, the "high y" region is the same as the "low x" region. For the methods considered, x is calculated from Q^2 and y, as such the x resolution directly relates to the y and Q^2 resolutions.

When determining the proton structure functions, for example, the choice of reconstruction method used to calculate Q^2 and y impacts the size of systematic errors, acceptance, and radiative corrections. For these studies, the resolution on y, and secondarily the Q^2 resolution, are chosen as the quantities to be optimised and act as metrics for the detector's ability to perform an inclusive DIS measurement.

The quantities measured by the detector, and entering the reconstruction methods, are the scattered electron's energy and angle, E_e and θ_e, as well as the $E - p_z$ sum of all HFS particles, δ_h, and the transverse momentum of the HFS, p_t^h. The resolution of the reconstructed DIS quantities are then limited by the resolution of the detec-

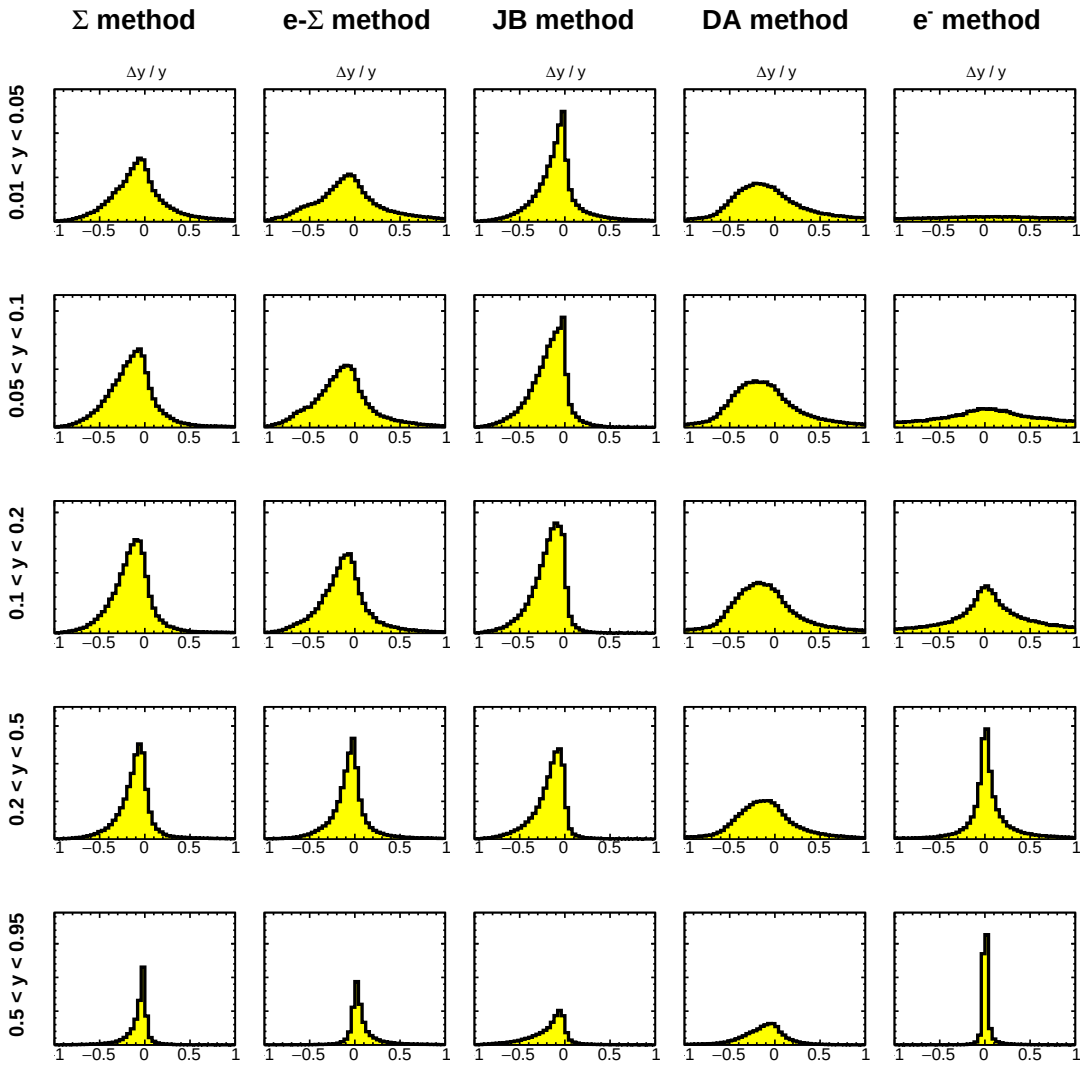

Figure 5.2: Distributions of $\Delta y/y = (y_{reco} - y_{true})/y_{true}$ for different ranges in y_{true}, when reconstructed using several reconstruction methods. The Q^2 range is $1 < Q^2 < 10\,\mathrm{GeV}^2$ and the beam configuration is $18 \times 275\,\mathrm{GeV}^2$ e^- on p.

tor quantities. Fig. 5.1 shows the correlation between the truth and reconstructed detector quantities for events with $Q^2 > 1\,\mathrm{GeV}^2$ and $0.01 < y < 0.95$. The scattered electron energy is strongly peaked around the electron beam energy of 18 GeV, due to the increasing cross section as $y \to 0$. The DIS cross section also decreases as $1/Q^4$, meaning that smaller scattering angles are more probable (note that the electron beam is aligned with $-z$, therefore $\theta_e = \pi$ indicates no scattering). The Q^2 dependence similarly manifests in the p_t^h distribution which peaks at $p_t^h \approx 1\,\mathrm{GeV}$ due to the $Q^2 > 1\,\mathrm{GeV}^2$ requirement. δ_h directly relates to y, as $y = \delta_h/2E_0$, so is analagous to the generated y distribution which increases as $y \to 0$.

Fig. 5.2 shows a summary of $\Delta y/y$ distributions for a fixed region of the kinematic plane where $0.01 < y < 0.95$ and $1 < Q^2 < 10\,\mathrm{GeV}^2$, for y reconstruction using

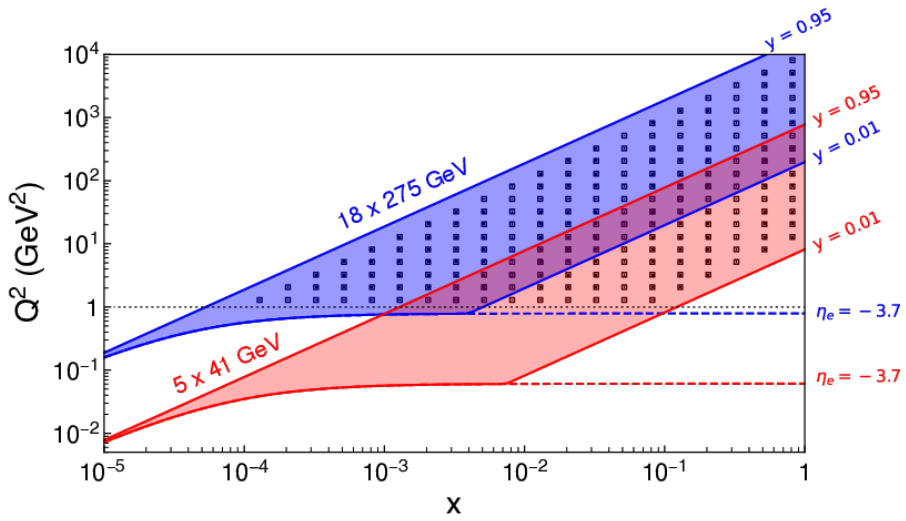

Figure 5.3: Kinematic coverage of EIC $e-p$ events at the minimum and maximum centre-of-mass energies. The markers indicate bin centres for a possible binning scheme of five logarithmically spaced bins in x and Q^2, subject to selection requirements $Q^2 > 1\,\mathrm{GeV}^2$ and $0.01 < y < 0.95$ [61].

several methods in the $18 \times 275\,\mathrm{GeV}^2$ beam configuration. $Q^2 > 1\,\mathrm{GeV}^2$ is a standard requirement for inclusive channels in order to interpret them within a pQCD framework. All methods deteriorate as y decreases, so a cut on $y > 0.01$ is imposed to maintain a sufficiently good reconstruction on the kinematic variables. A cut on the maximum value of y is applied, $y < 0.95$, in order to maintain a good Q^2 resolution and clean conditions for electron identification.

The distributions themselves are clearly non Gaussian, often being asymmetric with long tails, and in some cases showing bias from the central value of 0. In cases such as this, the RMS value does not give the full picture of the quality of reconstruction, and needs to be considered together with the mean of the distribution. An example is when reconstructing using the JB method, where y is given by $\delta_h/2E_0$. Since δ_h is the $E-p_z$ sum of all particles in the HFS, a reconstructed y value greater than the generated value will occur when the measured $E-p_z$ sum is larger than the generated value, typically as a result of detector resolution effects. The longer tail where $\Delta y/y < 0$, which occurs when $E-p_z$ is underestimated, can often be attributed to the HFS particles produced outside of the main detector acceptance, which are unmeasured and do not contribute to the $E-p_z$ sum. This effect is lessened as Q^2 increases, since the transverse momentum increases with Q^2, meaning fewer HFS particles go unmeasured. These effects are also present for the y reconstruction using the Σ and $e-\Sigma$ methods, however the skewing as a result of this effect is reduced by the replacement of the denominator $2E_e$ by $\delta_h + E'_e(1-\cos\theta_e)$ in the Σ method (this replacement is also implicit in the $e-\Sigma$ method). In these methods, when δ_h is

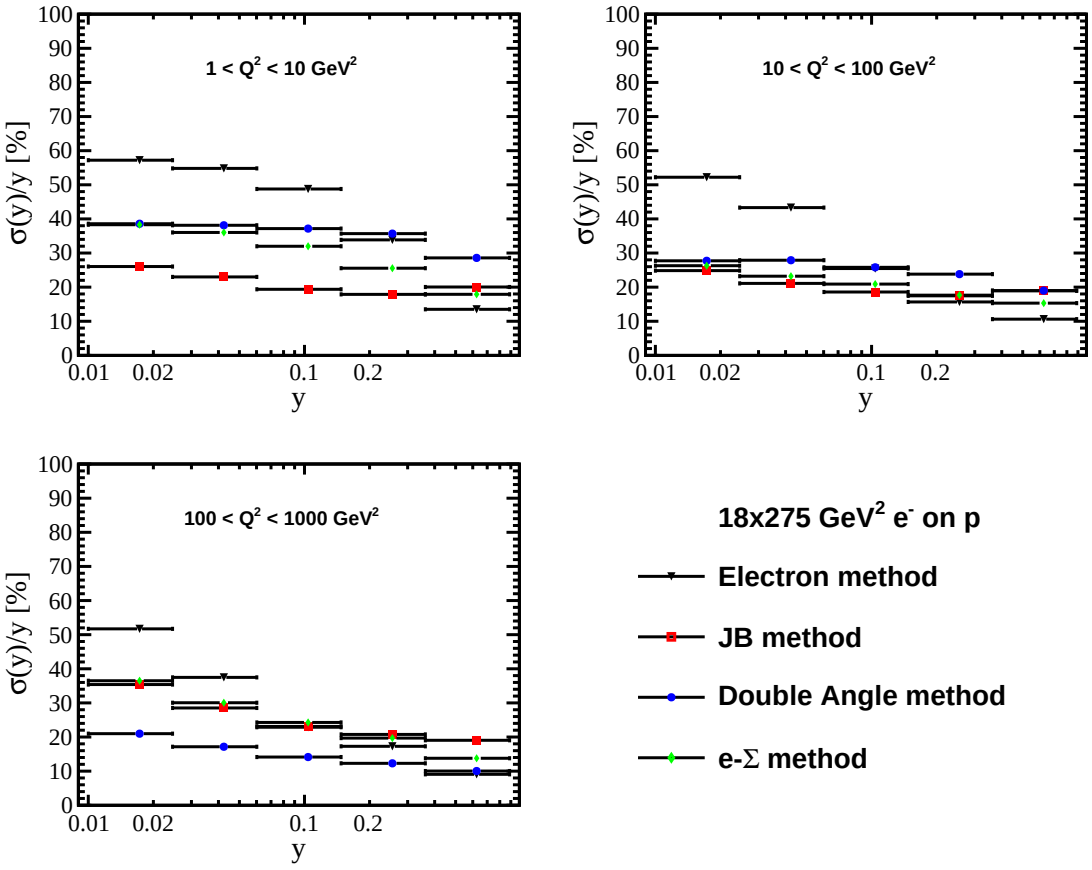

Figure 5.4: RMS of the $\Delta y/y = (y_{reco} - y_{true})/y_{true}$ distributions for several reconstruction methods as a function of y_{true}, for 3 different ranges in Q^2_{true}.

underestimated as a result of unmeasured particles, the value of $\delta_h + E'_e(1-\cos\theta_e)$ is also underestimated, reducing the skew on the y distribution. For low Q^2 events, a bias is also apparent in the DA method. This can also be attributed to unmeasured HFS particles, and the subsequent underestimation of $\alpha_h = \delta_h/p_t^h$. The skewing present in the JB and Σ methods, as well as the bias in the DA method, are greatly reduced when considering larger Q^2 events, where both the electron and HFS are well measured.

While it may be possible to obtain a kinematic variable resolution sufficient for analyses for $y < 0.01$, the variable centre-of-mass energies that will be possible at the EIC render this unnecessary. The kinematic coverage of the most extreme energy configurations at the EIC is shown in Fig. 5.3, where it can be seen that the low y region at $18 \times 275\,\mathrm{GeV}^2$ overlaps with the moderate-to-high y region at $5 \times 41\,\mathrm{GeV}^2$. These extend the coverage of the well reconstructed high y measurements, and increase the possible reach of interesting F_L measurements for which the cross section contribution is greater at high y.

Plots of y resolution against y for three intervals in Q^2, with the $18 \times 275\,\mathrm{GeV}^2$ beam configuration, are shown in Fig. 5.4, and the equivalent plots showing the means of the distributions are shown in Fig. 5.5. These allow for direct comparison of the performance of the four methods. The Σ method is omitted in favour of the $e - \Sigma$ method due to the superior Q^2 reconstruction of the $e - \Sigma$ method and otherwise equivalent approach. It becomes clear that for $y \gtrsim 0.4$, and $1 < Q^2 < 1000\,\mathrm{GeV}^2$, the best reconstruction is provided by the electron method, yielding an average resolution of $\sim 10\,\%$ in this bin. In the electron method, the y resolution (and correspondingly the x resolution) diverges as $y \to 0$. This can be understood from the study of the equations in section 2.3.2, as for low y the scattered electron's energy is close to that of the beam electron, meaning that in the y calculation a large number is subtracted from a similarly large number, giving a large uncertainty on the resulting quantity. As a result, the electron method is increasingly outperformed by other methods with decreasing y. The performance of the Double Angle method is optimal when the angle of the scattered electron, and the angle of the hadronic final state, are well measured. The angle of the scattered electron is closely correlated with Q^2, with larger values of Q^2 corresponding to larger scattering angles. The result is an improvement of the DA reconstruction with increasing Q^2 (and y), ranging from $\sim 50\,\%$ at low y and Q^2, to $\sim 10\,\%$ in the highest y and Q^2 bins considered. The $e - \Sigma$ method, being a mixed method, similarly benefits from both the scattered electron and the HFS being well measured. The $e - \Sigma$ method uses the full HFS information, however, and so is more effective in regions where the scattered electron is not as well measured, at lower y and Q^2.

If the y resolution alone is considered, it would be possible to conclude that for low values of y and Q^2, the JB method provides the best reconstruction. However, the y resolution is not the only determining factor in the quality of the reconstruction, as it can be seen from Fig. 5.5 that the JB method has the largest bias. To determine the full event kinematics, it is also necessary to consider the resolution on the reconstructed value of Q^2. The Q^2 resolution from the four reconstruction methods is shown in Fig. 5.6 for the same Q^2 intervals as previously. The JB method here exhibits a Q^2 resolution that is larger than $\sim 40\,\%$ while the Q^2 resolution from the other methods is $\sim 10 - 20\,\%$. The Q^2 reconstruction of the electron and $e - \Sigma$ methods are identical by definition, and are similar in resolution to reconstruction by the DA method. It can be concluded that, for Neutral Current DIS, the event kinematics are not best reconstructed by the JB method. It should also be noted that the most effective method is dependent on the event kinematics, as well as detector acceptance and resolution effects, and the size of radiative processes which were not available here.

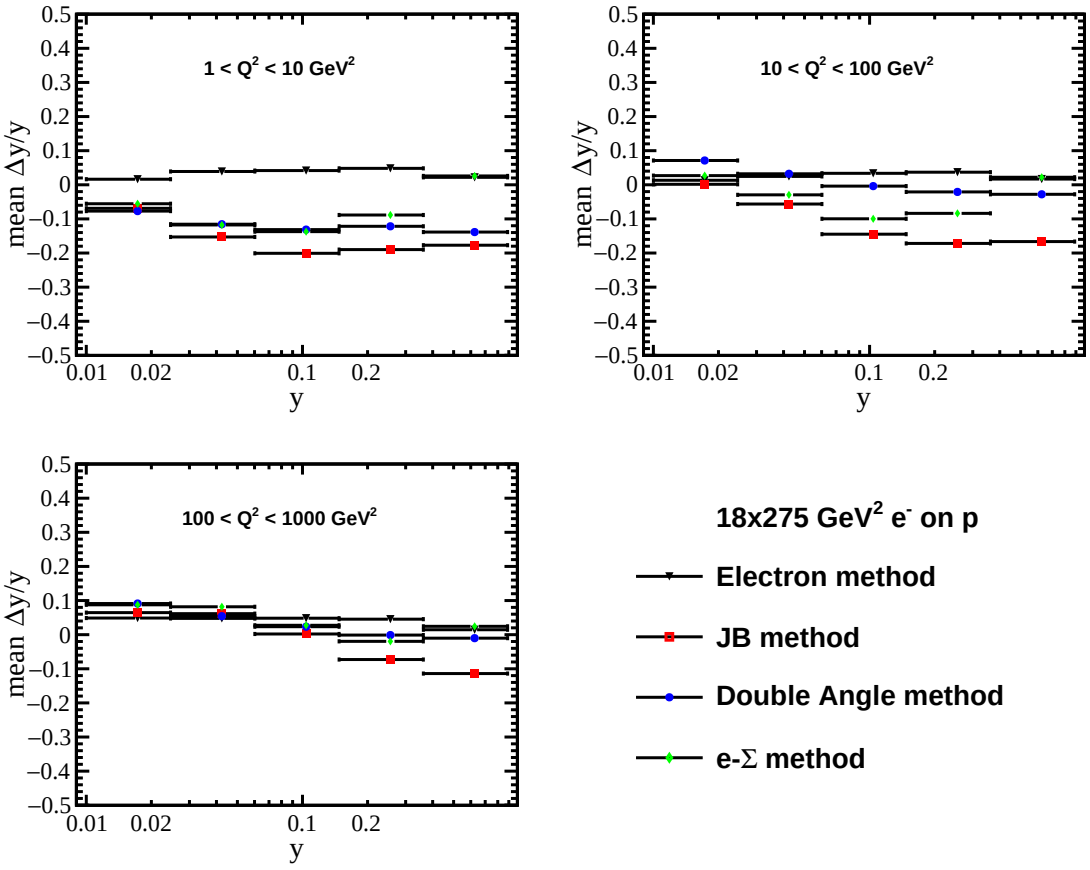

Figure 5.5: Mean of the $\Delta y/y = (y_{reco} - y_{true})/y_{true}$ distributions for several reconstruction methods as a function of y_{true}, for 3 different ranges in Q^2_{true}.

Fig. 5.7 summarises the y resolution as a function of x and Q^2 for the $18 \times 275\,\mathrm{GeV}^2$ beam configuration, if the best method (the method with the smallest RMS for y reconstruction) is chosen at each point. While, as can be seen from Fig. 5.4, there are regions of the phase space in which the JB method exhibits the best y resolution (the smallest RMS), the JB method is not considered as an option when choosing the best reconstruction method for y in Fig. 5.7 on account of its large bias and poor Q^2 reconstruction. The electron method has an excellent resolution in the high y region, at the sub 10 % level for many of the $x-Q^2$ bins. The excellent resolution with which ePIC reconstructs the hadrons means that as the electron method degrades as $y \to 0$, the $e-\Sigma$ method and DA methods take over and continue to provide a high quality reconstruction in that region. The y resolution for all reconstruction methods degrades at low y and especially at low y and Q^2, with the resolution from both the $e-\Sigma$ and DA method being $\sim 40\,\%$. The similar, large, y resolution for the methods in this part of the phase space gives rise to fluctuations in the measured resolution, which is seen in Fig. 5.7 as a low Q^2, high x bin where the DA method gives the best y resolution.

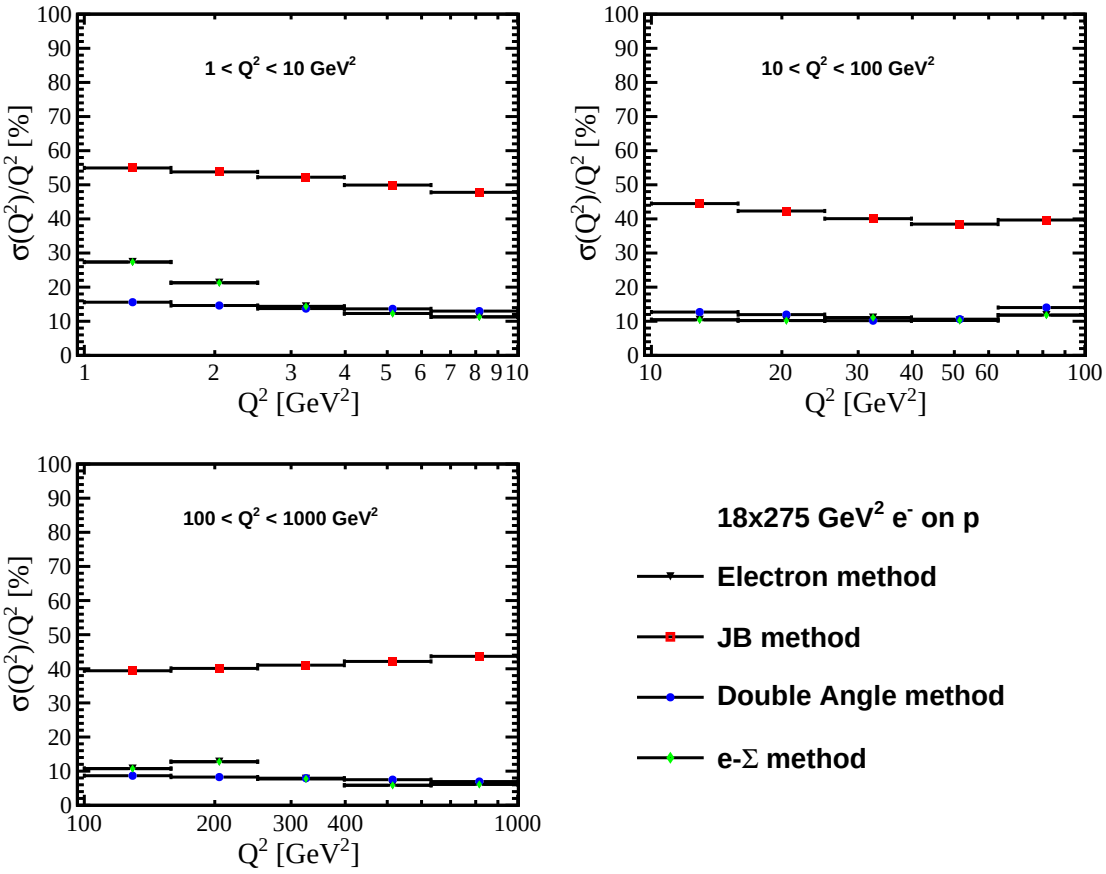

Figure 5.6: RMS of the $\Delta Q^2/Q^2 = (Q^2_{reco} - Q^2_{true})/Q^2_{true}$ distributions for several reconstruction methods as a function of Q^2_{true}, for 3 different ranges in Q^2_{true}.

In a typical inclusive DIS analysis, the $x - Q^2$ plane is separated into bins, and the reduced cross section σ_r is determined for each bin. The cross section measurement is subject to bin migration effects, in which events that were generated in a given bin migrate to one of the surrounding bins, and vice-versa. Having established the resolutions on the kinematic variables throughout the kinematic plane, one can begin to consider the purities and stabilities of a possible binning scheme to be used at ePIC. The purity is the fraction of events that were reconstructed in a given bin which were generated in the same bin. It is a measure of the migration of events originating from outside a given bin to that bin. The stability is the fraction of events which were generated in given bin that were also reconstructed in that bin. It is a measure of the migration of events that were generated in that bin to outside bins. Purity and stability are thus defined by

$$Purity = \frac{N_{rec\&gen}}{N_{rec}} \tag{5.1}$$

and

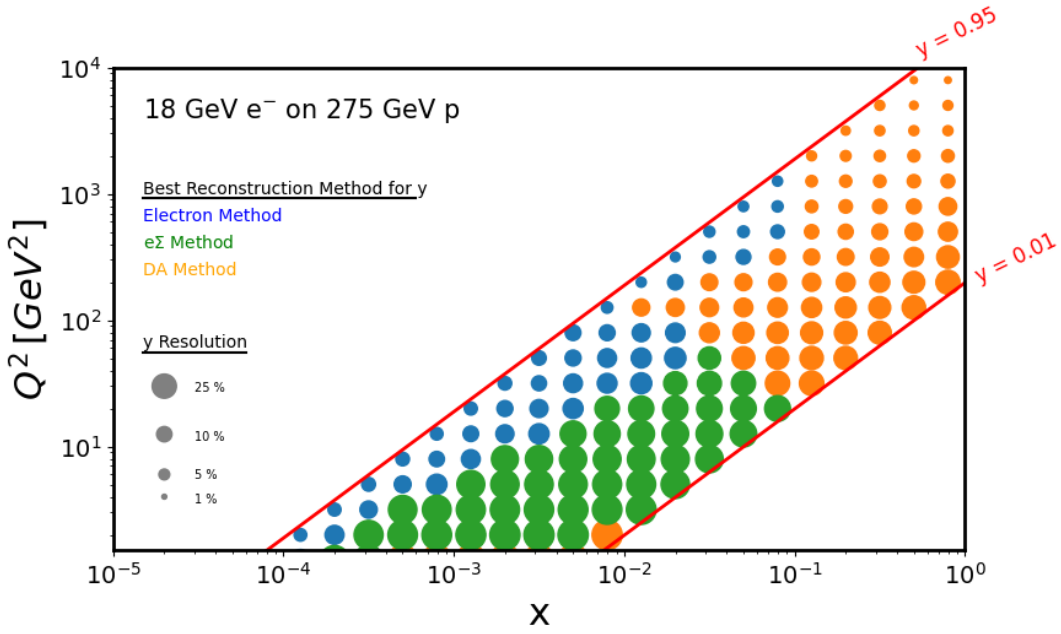

Figure 5.7: Variation of the estimated resolution on y, with x and Q^2, for 18 GeV electrons colliding with 275 GeV protons. At each point in the kinematic plane, the best performing reconstruction method is chosen and indicated by the colour of the corresponding marker, while the size of the marker indicates the magnitude of the resolution obtained.

$$Stability = \frac{N_{rec\&gen}}{N_{gen}}, \tag{5.2}$$

where N_{rec} (N_{gen}) is the number of events that were reconstructed (generated) in a given bin, and $N_{rec\&gen}$ is the number of events that were reconstructed in the same bin as the one in which they were generated.

Purity and stability are functions of the binning scheme. The choice of binning should be adjusted as part of an analysis to give satisfactory values of purity and stability across the region of interest, with the aim of minimising the size of systematic errors associated with kinematic corrections. For HERA analyses, a lower limit of 30 % was often deemed acceptable, though larger values are preferable. Purities and stabilities for a sample binning scheme are shown in Fig. 5.8, where the binning is chosen to be four logarithmically spaced bins per decade in x and Q^2. It can be seen that, for this binning scheme, a purity and stability of at least 30 % can be achieved for all bins with $Q^2 > 1\,\text{GeV}^2$ and $0.01 < y < 0.95$ when an appropriate reconstruction method is chosen.

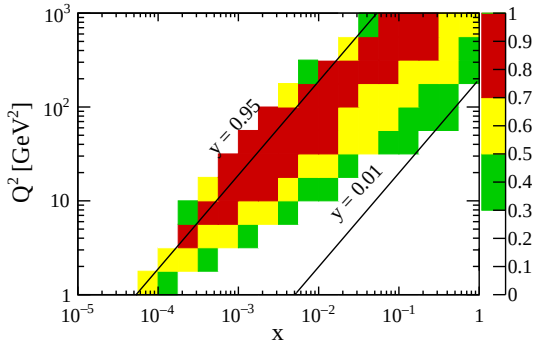

(a) e^- Method Purity

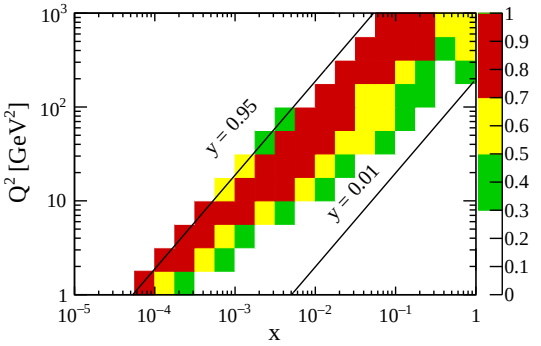

(b) e^- Method Stability

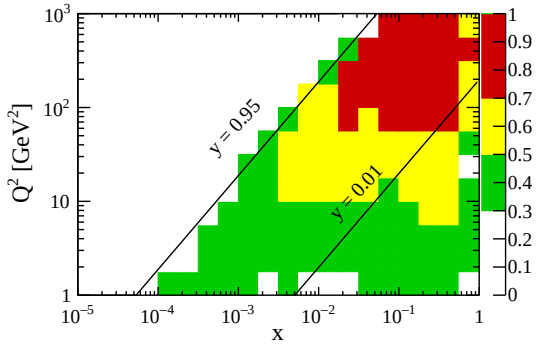

(c) DA Method Purity

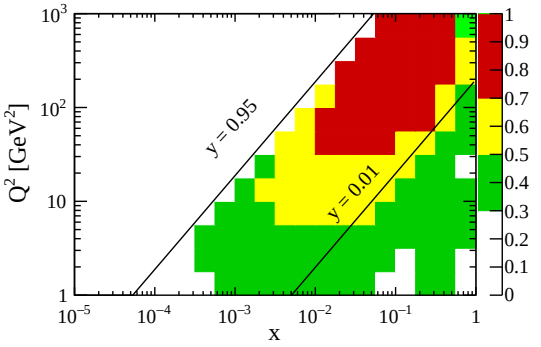

(d) DA Method Stability

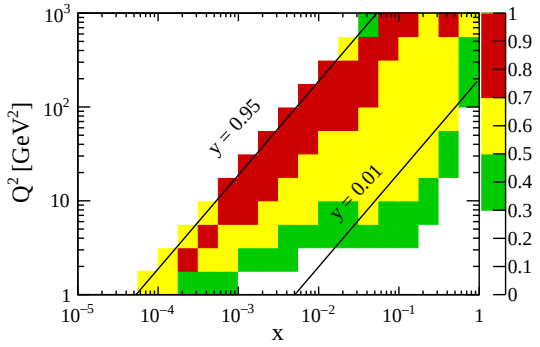

(e) $e - \Sigma$ Method Purity

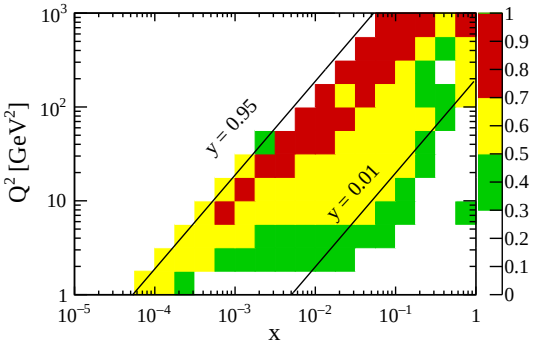

(f) $e - \Sigma$ Method Stability

Figure 5.8: Purities and stabilities for a sample binning scheme for use at ePIC. Four logarithmically spaced bins are present per decade in x_{true} and Q^2_{true}.

Chapter 6

Kinematic Fitting for DIS Reconstruction

There are four measured quantities that may be used to reconstruct the kinematic variables x, y, and Q^2: the energy and angle of the scattered electron, the $E - p_z$ sum of all particles in the HFS, and the transverse momentum of the overall HFS. The resolutions of the conventional reconstruction methods, that were studied in the previous chapter, usually rely on two or three of the measured quantities. In this chapter, a method which uses all four measured quantities simultaneously, as part of an event-by-event kinematic fit, is presented. The over-constraint of the measured quantities means that in addition to estimates of the kinematic variables, the energy of a possible initial state radiation photon may be inferred. The performance of this method is evaluated in terms of the kinematic resolutions and the reconstruction of ISR, in ePIC simulations and H1 simulations and data.

6.1 QED Radiative Effects

If detector acceptance and resolution effects are disregarded, and all final state particles are perfectly measured, then each of the previously listed reconstruction methods yields equivalent results. However, calculations based on the leading order description as pictured in Fig. 2.2 do not adequately describe physics observed in measurements. For this purpose, higher order QED processes, which manifest as a correction to the leptonic tensor, must be included. For their implementation in Monte-Carlo event generators, QED radiative events may be classified as being either initial-state or final-state photon radiation (ISR or FSR), as pictured in Fig. 6.1, with an effective coupling used to determine the probability of a given event class occurring.

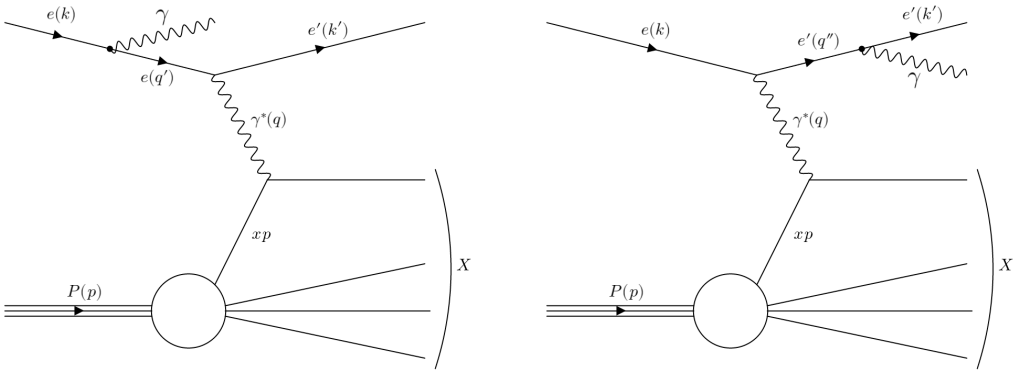

(a) Initial state radiation **(b)** Final state radiation

Figure 6.1: Higher order QED corrections as implemented in Monte-Carlo event generators.

These corrections may significantly impact the reconstructed kinematics, as the relation $q = k - k'$ no longer holds true. For events containing FSR, the corrected four vector of the scattered electron, q'', can be obtained by summing the four vector of the FSR photon with the outgoing electron's four vector. The angular separation between the radiated photon and radiating electron is typically small, meaning that in the case of FSR the radiated photon is often measured together with the scattered electron in the calorimeters.

ISR photons are similarly generated at small angles to the radiating electron, which in this case is aligned with the electron beam axis, and therefore the ISR photons continue down the beamline, often remaining unmeasured. With the assumption that ISR photons are emitted collinear to the electron beam axis, ISR events may be treated as non radiative DIS events in which an electron of four-vector q' and energy $E_e - E_\gamma$ (where E_γ is the energy of the radiated photon) scatters from a proton of energy E_p. Depending on which reconstruction method is used, ISR may strongly bias the values of the reconstructed kinematic variables. The number of events containing hard (which throughout this chapter refers to high energy) ISR for a sample can be reduced by placing a cut on the measured value of Σ_{tot}. As defined in Chapter 2, Σ_{tot} is the summed $E - p_z$ of all particles in the event, which should be equal to twice the reduced electron beam energy $\Sigma_{tot} = 2(E_e - E_\gamma)$ if the ISR photon is excluded from the sum.

A third event class that may be present in Monte-Carlo event generators is QED Compton, in which a quasi-real photon is emitted from the quark line and subsequently undergoes compton scattering $e\gamma \to e\gamma$, typically at a large angle. The

transverse momentum of the scattered photon is balanced by the transverse momentum of the other particles in the event. A topological cut can therefore be imposed to veto such events.

6.2 KF Method

The four measured quantities in a neutral current DIS event are given by $\overrightarrow{D} = (E_e, \theta_e, \delta_h, p_t^h)$. As seen in conventional reconstruction methods, the event kinematics can be reconstructed using only two quantities, so in neutral current events where there are four measurements, the reconstruction is over-constrained. However, the best reconstruction possible is achieved by using the four measured quantities in $\overrightarrow{D}$ simultaneously to exploit the full information available. There are multiple methods that could be used to achieve this, one possibility being the training of deep neural networks to reconstruct kinematic variables given the full event information, which has been studied and shows promising results [127, 128]. Another approach, which will be detailed in this section, uses a kinematic fit (KF) to find the most probable values of the kinematic variables, while also leveraging the over-constraint to infer the energy of a possible ISR photon. The KF method has the advantage of being transparent when compared to a method such a neural network, as the weights given to the input variables in the KF can be clearly understood relating to their resolutions.

The output quantities from the kinematic fit are $\overrightarrow{\lambda} = (x, y, E_\gamma)$, with Q^2 being found using a modified version of Eq. 2.15

$$Q^2 = 4E_p(E_e - E_\gamma)xy, \tag{6.1}$$

correcting the centre-of-mass energy. Bayes' theorem [129] is employed for the extraction of $\overrightarrow{\lambda}$ in which

$$P(\overrightarrow{\lambda}|\overrightarrow{D}) = \frac{P(\overrightarrow{D}|\overrightarrow{\lambda})P_0(\overrightarrow{\lambda})}{P(\overrightarrow{D})} \tag{6.2}$$

where $P(A|B)$ is the conditional probability of event A occurring given B is true. $P(\overrightarrow{D}|\overrightarrow{\lambda})$ is the probability of measuring a set of observables $\overrightarrow{D}$ for an event with kinematics $\overrightarrow{\lambda}$, and is referred to as the likelihood function. The counterpart $P(\overrightarrow{\lambda}|\overrightarrow{D})$ is referred to as the posterior probability. $P_0(\overrightarrow{\lambda})$ is the prior probability, and represents the probability of an event with kinematics λ occurring without any other conditions.

The likelihood function can be written as

$$P(\overrightarrow{D}|\overrightarrow{\lambda}) = P(E_e, \theta_e, \delta_h, p_t^h | x, y, E_\gamma) \tag{6.3}$$

where the electron and HFS variables can factorised to give

$$P(\overrightarrow{D}|\overrightarrow{\lambda}) = P(E_e|x,y,E_\gamma)P(\theta_e|x,y,E_\gamma)P(\delta_h|x,y,E_\gamma)P(p_t^h|x,y,E_\gamma). \tag{6.4}$$

It is important to note that there is a strong correlation between the two hadronic variables δ_h and p_t^h, as a net positive fluctuation in the energy measured in the calorimeters would result in a net positive fluctuation in the measured values of both δ_h and p_t^h. Similarly, the electron variables E_e and θ_e have correlations that should be accounted for. The factorisation in Eq. 6.4 treats the four measured quantities independently, which is acceptable for initial studies, with the goal of including a full treatment of correlations in more detailed future studies. Ignoring correlations, Eq. 6.4 can be written as

$$P(\overrightarrow{D}|\overrightarrow{\lambda}) = P(E_e|E_e^\lambda)P(\theta_e|\theta_e^\lambda)P(\delta_h|\delta_h^\lambda)P(p_t^h|p_t^\lambda), \tag{6.5}$$

where E_e^λ, θ_e^λ, δ_h^λ, p_t^λ are the "true" values of these quantities for an event with kinematic variables described by the set $\overrightarrow{\lambda}$. If the spread of the measured quantities is assumed to follow a Gaussian distribution, centred on the true value, with standard deviation σ, the likelihood can be rewritten as

$$\begin{aligned} P(\overrightarrow{D}|\overrightarrow{\lambda}) = & \frac{1}{\sqrt{2\pi}\sigma_E}\exp -\frac{(E_e - E_e^\lambda)^2}{2\sigma_E^2} \times \frac{1}{\sqrt{2\pi}\sigma_\theta}\exp -\frac{(\theta_e - \theta_e^\lambda)^2}{2\sigma_\theta^2} \times \\ & \frac{1}{\sqrt{2\pi}\sigma_{\delta_h}}\exp -\frac{(\delta_h - \delta_h^\lambda)^2}{2\sigma_{\delta_h}^2} \times \frac{1}{\sqrt{2\pi}\sigma_{p_t^h}}\exp -\frac{(p_t^h - p_t^{h\lambda})^2}{2\sigma_{p_t^h}^2}. \end{aligned} \tag{6.6}$$

The prior distribution, $P_0(\overrightarrow{\lambda})$ reflects the basic features of the DIS cross section in terms of x and y. Starting from the cross section equation shown in Eq. 2.24, neglecting the F_L contribution and any constants we obtain

$$\frac{d^2\sigma}{dxdQ^2} \propto \frac{1+(1-y)^2}{x^3y^2}F_2. \tag{6.7}$$

The F_2 structure function varies only logarithmically with Q^2 for moderate and large x values, but it does display a power-like x dependence. The x dependence of F_2 has been studied at HERA [22] and, within certain limits, can be modelled by the parametrisation $F_2(x,Q^2) \propto x^{-\lambda(Q^2)}$. For values of λ close to zero, as observed at moderate Q^2, the variation of F_2 with x is small. Neglecting the variation of F_2 with x, the DIS cross section contribution to the prior distribution, may thus be

taken simply as $\frac{1+(1-y)^2}{x^3y^2}$. The slow variation of F_2 with x was not included for these studies, due to its complexity and the minimal impact on the fit result. Hence the final DIS contribution to the prior is

$$P_0(\overrightarrow{\lambda}) = \frac{1+(1-y)^2}{x^3y^2}. \tag{6.8}$$

A prior for ISR is applied by means of the QED splitting function, which represents the probability of emitting a photon of a certain energy

$$P(z) \propto \frac{1+z^2}{1-z}, \tag{6.9}$$

where $z = 1 - \frac{E_\gamma}{E_0}$ [130]. Combining the factorised DIS and ISR priors gives the total prior distribution of

$$P_0(\overrightarrow{\lambda}) \propto \frac{1+(1-y)^2}{x^3y^2} \cdot \frac{1+(1-E_\gamma/E_0)^2}{E_\gamma/E_0}, \tag{6.10}$$

and a suitable normalisation is applied based on the ranges of the parameters.

6.3 Bayesian Analysis Toolkit

The Bayesian Analysis Toolkit (BAT) [131] is a software tool for data analysis and is based on Bayes' theorem. Through BAT, the full posterior probability distribution is extracted using Markov Chain Monte-Carlo (MCMC) methods [132].

Markov Chains are sequences of random numbers for which the probability distribution for the next element in the sequence depends only on the current state. MCMC methods are particularly useful for Bayesian inference, as they allow a wide range of posterior distributions to be simulated and information on their parameters found numerically.

In BAT, an implementation of the Metropolis algorithm is used to create a Markov Chain where the stationary probability density corresponds to the desired posterior probability density function. The basic idea is that, for a given initial point $\boldsymbol{\theta_0}$, a new sample is produced for each iteration $t = 1...N$:

1. Propose a new point $\tilde{\boldsymbol{\theta}}$
2. Sample a value x between 0 and 1 from a uniform distribution
3. If $x < \frac{P(\tilde{\boldsymbol{\theta}}|D)}{P(\boldsymbol{\theta_{t-1}}|D)}$, $\boldsymbol{\theta_t} = \tilde{\boldsymbol{\theta}}$
4. Else $\boldsymbol{\theta_t} = \boldsymbol{\theta_{t-1}}$

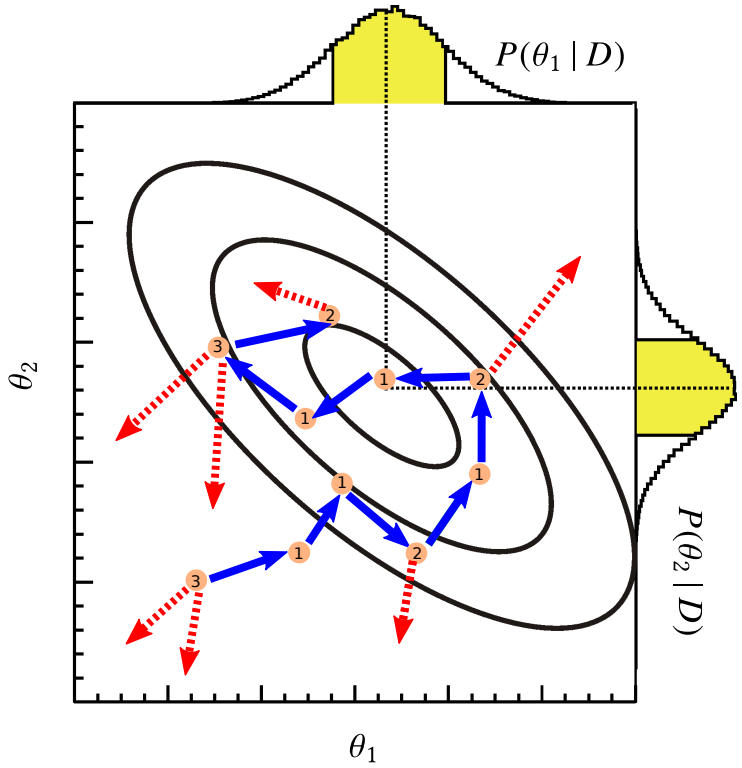

Figure 6.2: Example of a 2D random walk with the Metropolis algorithm. The black contours are isolines of constant probability. The arrows point to proposed values, with the blue arrows being accepted and the red arrows being rejected. Figure taken from [133].

An example of this sort of random walk using the Metropolis algorithm is shown in Fig. 6.2, where the state $\boldsymbol{\theta} = (\theta_1, \theta_2)$ is 2-dimensional. In the example, the chain begins in the lower left, and proposes two points which are rejected (red dashed arrows) followed by a point which is accepted (blue solid arrow). The circled number denotes the number of iterations for which the chain remains at a given point. The marginal distributions are updated for each iteration, t, in the case of the 1D marginals $P(\theta_i|\overrightarrow{D})$ by adding the ith coordinate to a histogram. To approximate the 2D marginals this is repeated for each pair of coordinates.

In BAT, the proposal of new points is handled by a "proposal function", as this is not specified in the Metropolis algorithm. The Markov property requires that the proposal may depend only on the current point $\boldsymbol{\theta_t}$ and not on any previous points. The general form is either a Gaussian or a Student's t-distribution, the default being a Student's t-distribution with one degree of freedom (i.e. a Cauchy distribution). The covariance of the chosen distribution is learned from the covariance of samples in a *pre-run*, which is used to determine an efficient proposal function, and marginalisation is performed in the *main run*. For a chain of finite length, the initial point has some effect on the Markov Chain output. To mitigate this, multiple chains can

be run from different initial positions, and convergence declared if the chains then turn out to explore the same region of parameter space, in which case the chains have forgotten their initial point.

6.4 Performance with Truth Smearing

To establish the feasibility of the KF method, an approach neglecting correlations between the quantities in $\overrightarrow{D}$, and assuming the detector resolutions are perfectly understood is first used. This section presents these tests in two parts. First, generated events with no QED radiation present are used, and the resulting kinematic resolutions for such events presented. The second part introduces QED radiation, and along with the kinematic resolutions, the ability of this method to reconstruct the energy of ISR photons is considered.

6.4.1 No QED Radiation

For these initial studies, events are generated using the Djangoh event generator with QED radiation turned off. The $18 \times 275\,\mathrm{GeV}^2$ maximum EIC centre-of-mass energy beam configuration is chosen, with kinematic cuts of $0.001 < x < 1$, $0.01 < y < 0.95$, $1 < Q^2 < 100\,000\,\mathrm{GeV}^2$, and $W > 1.4\,\mathrm{GeV}$. These cuts are chosen such that events are generated in the DIS regime, and a reasonable efficiency is achieved for cuts applied as part of the reconstruction procedure. A smearing procedure is applied to the generated values to mimic the detector response. The smearing function for each of the quantities in $\overrightarrow{D}$ is a normal distribution with standard deviation corresponding to a conservative estimate of the resolution of the quantity, as determined from full simulation studies [134] (refer to Section 6.5), or the Yellow Report requirement matrix [10]. The smearing width for the electron quantities is chosen to be $\sigma(E_e)/E_e = 11\,\%/\sqrt{E_e} \oplus 2\,\%$ and $\sigma(\theta_e) = 0.1\,\mathrm{mrad}$, and for the HFS quantities $\sigma(\delta_h)/\delta_h = 25\,\%$ and $\sigma(p_t^h)/p_t^h = 25\,\%$. The smearing procedure is outlined below.

1. Find true values of quantities in $\overrightarrow{D}$ and $\overrightarrow{\lambda}$.
2. If scattered electron is outside of central detector acceptance $-4 < \eta < 4$, discard event.
3. Draw smearing value f randomly from normal distribution for each quantity in $\overrightarrow{D}$.
4. Set reconstructed quantity to $f_i \times D_i$.

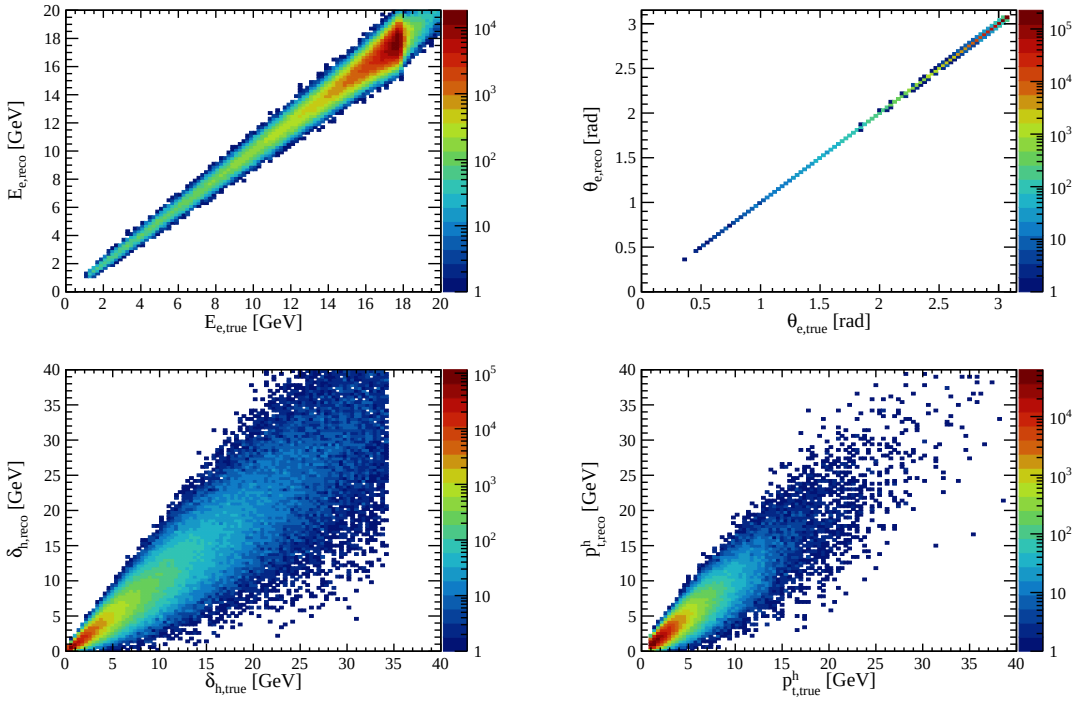

Figure 6.3: Correlation between the true scattered electron and HFS quantities, and the smeared quantities simulating those that would be reconstructed by the detector.

The distributions of the reconstructed and true quantities are shown in Fig. 6.3, and display broadly similar behaviour to the equivalent plots from full simulation shown in Fig. 5.1, but without the long tails present in the full simulation quantities.

To apply the KF method to full simulations or real data, the resolutions of the quantities in $\overrightarrow{D}$ must be found from dedicated studies using Monte-Carlo, test beams, or other approaches, in order for a likelihood function to be constructed. In the truth smearing approach, these resolutions are used as the smearing parameters and so are already known, and the likelihood function is constructed as in Eq. 6.6.

The kinematic fit is applied using BAT, and the reconstructed values of x, y, and E_γ are extracted from the global mode of the posterior distribution for each event. The range of values which each parameter may take is specified, with x and y occupying the range $[0, 1]$. E_γ may in principle take any value in the range $0 < E_\gamma < 18\,\text{GeV}$, but since these events were not generated with QED radiation present, E_γ was fixed to 0 for the fit in these first studies. Examples of the marginalised posterior distributions for x and y after fitting for an event with true x and y of 0.104 and 0.197 respectively, are shown in Fig. 6.4. The hollow circle denotes the position of the global mode, the solid circle and arrows shows the mean and standard deviation of the marginal distribution, and the highlighted regions show three credibility inter-

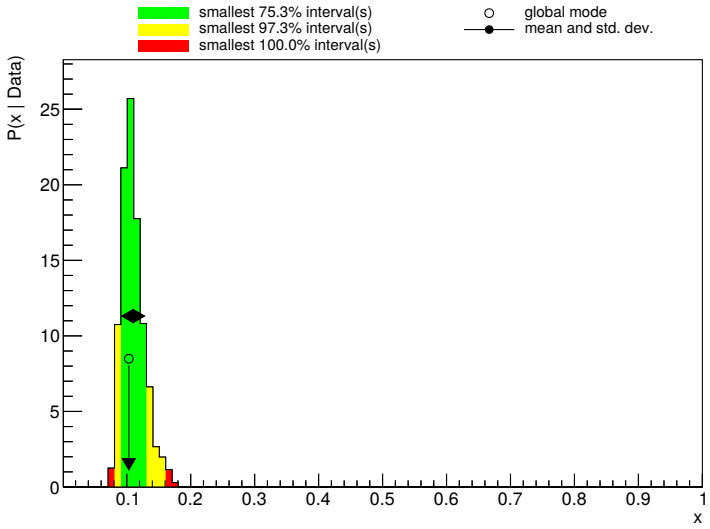

(a) x posterior

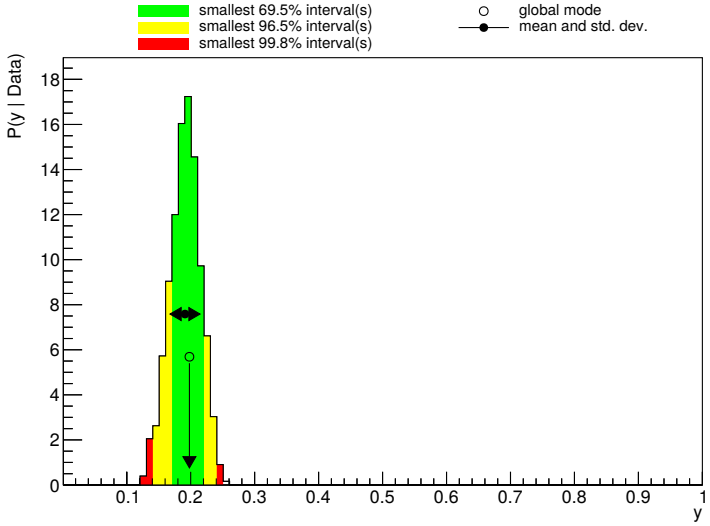

(b) y posterior

Figure 6.4: 1D marginalised posterior distributions for (a) x and (b) y from BAT for a single event with true x and true y of 0.104 and 0.197 respectively. Three credibility intervals are shown. The global mode of the posterior is marked by a hollow point, the mean of the 1D posterior by a solid point with arrows, and the standard deviation by the attached arrows.

vals. A posterior distribution, along with estimates of x, y, and E_γ, and their errors, are found on an event-by-event basis.

The y and Q^2 resolutions for the KF method and various conventional methods in different y bins are shown in Fig. 6.5 and Fig. 6.6 respectively. It can be seen that for the lowest y bin, the $\Delta y/y$ distributions for the Σ, JB, and KF method are almost identical and show the best resolution. For this y bin the Double Angle method performs somewhat worse, and the electron method gives a very poor reconstruction, as is discussed in more detail in Section 5.3. At low y, and in the absence of ISR, y reconstruction using the Σ method and JB method are essentially equivalent:

$$y_h = \frac{\delta_h}{2E_0}, \qquad y_\Sigma = \frac{\delta_h}{\delta_h + E_e(1-\cos\theta_e)}. \tag{6.11}$$

This is because at low y the value of δ_h is very small, and the well measured scattered electron contributes more to the denominator of the y calculation, so $\delta_h + E_e(1-\cos\theta_e) \simeq 2E_0$. The kinematic fit implicitly weights the contributions of the electron and hadronic quantities such that the best resolution is achieved, so at low y where the electron quantities give a worse reconstruction, the value of y predicted by the fit approaches that of the JB and Σ methods. For the other bins where $y > 0.05$, the KF method actually exceeds the performance of the conventional methods. This improvement in resolution is achieved through the optimal weighting of each of the input quantities, and the additional reduction in variance that is possible with a constrained fit.

Similar results are seen for the Q^2 resolutions of the conventional methods as were seen in Section 5.3, with the DA method giving the best reconstruction for the lower y bins and the electron method for higher y. The KF method matches the performance of the DA method in the lowest y bin and exceeds the performance of conventional methods for $y > 0.05$ in this configuration.

6.4.2 QED Radiation On

In a DIS experiment, some amount of ISR is unavoidable, and measures must be taken to understand and account for its contribution. For the results in this section, events are generated in the same manner as before, but with QED radiation included. The smearing procedure is as described in the previous section, with a correction for the inclusion of FSR. The "true" scattered electron four vector in an event containing FSR is the four vector before the emission of FSR. This four vector is equivalent to the summed four vectors of the FSR photon and the scattered electron after FSR emission. In a detector, FSR is typically emitted collinear to the scattered electron and the summed energy measured in the calorimeter, so these quantities are naturally summed. To mimic this in the smearing procedure, the MC scattered electron and FSR photon four vectors are simply merged before the smearing factor is applied.

In a typical inclusive DIS analysis, a cut is often applied on the quantity Σ_{tot} to remove hard ISR events, and a correction for softer (lower energy) ISR is applied as part of the unfolding procedure. For the smearing approach, the reconstructed Σ_{tot} distribution is Gaussian and is centred on $2E_0$ for events with no ISR emission. A

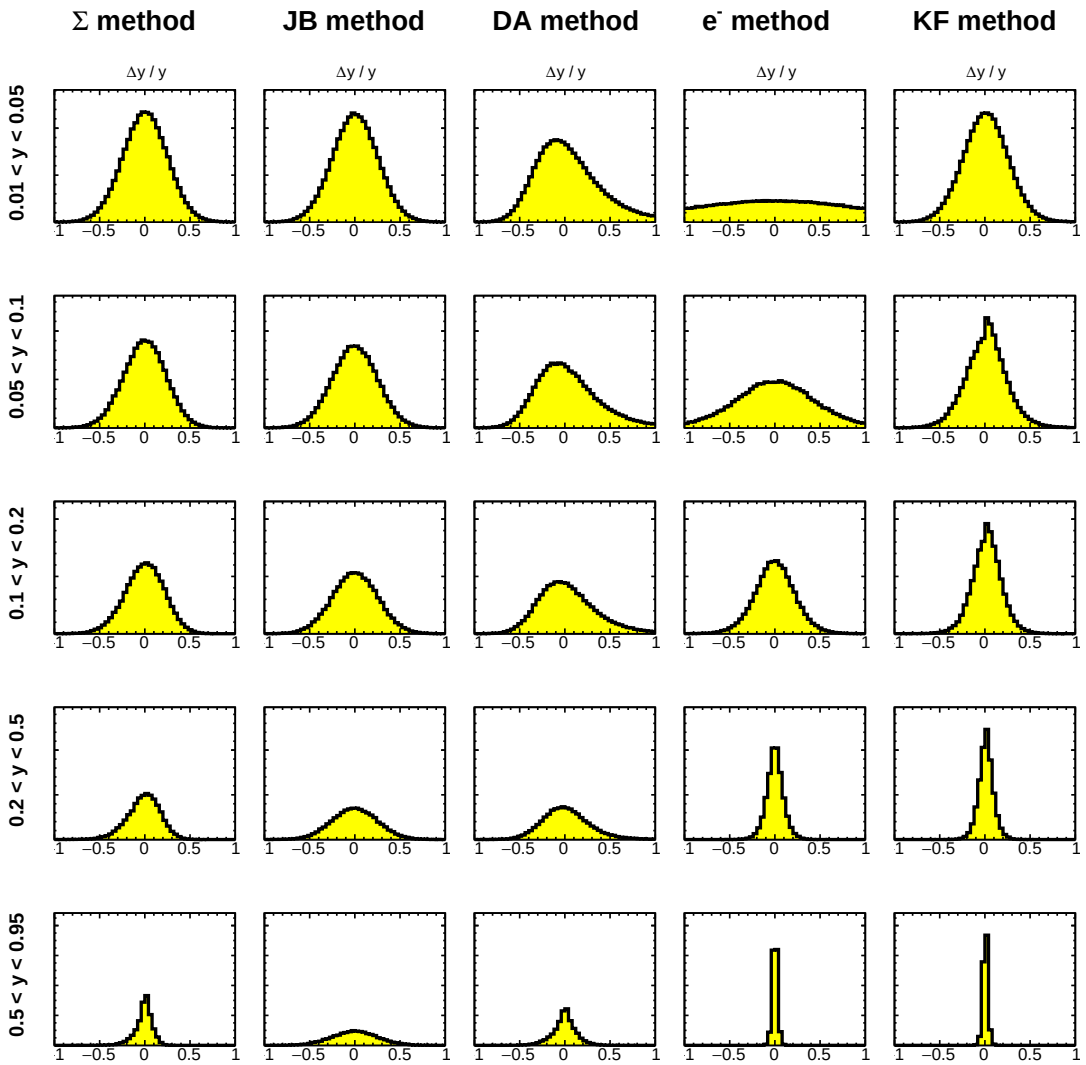

Figure 6.5: $\Delta y/y$ distributions in different y ranges for smeared Djangoh MC when reconstructed using several reconstruction methods. The Q^2 range is $Q^2 > 1\,\mathrm{GeV}^2$ and the beam configuration is $18 \times 275\,\mathrm{GeV}^2$ e^- on p.

similar distribution, but with an additional tail to the left of the peak is seen when ISR is included, as shown in Fig. 6.7a. A minimum Σ_{tot} cut is chosen to reduce the number of events in the sample containing large levels of ISR, thus reducing the size of the necessary radiative corrections. For these studies, a minimum Σ_{tot} cut of 31 GeV is chosen, with the aim of reducing the number of events requiring large ISR corrections while keeping a high efficiency. Of the reconstructed events, 96.5 % passed this cut. The effect of this cut on the levels of QED ISR is presented in Fig. 6.7b, where it can be seen that the events passing the cut are those with lower levels of ISR.

Having prepared the sample, the performance of the various reconstruction methods is once again evaluated, this time with QED radiation effects included. A comparison

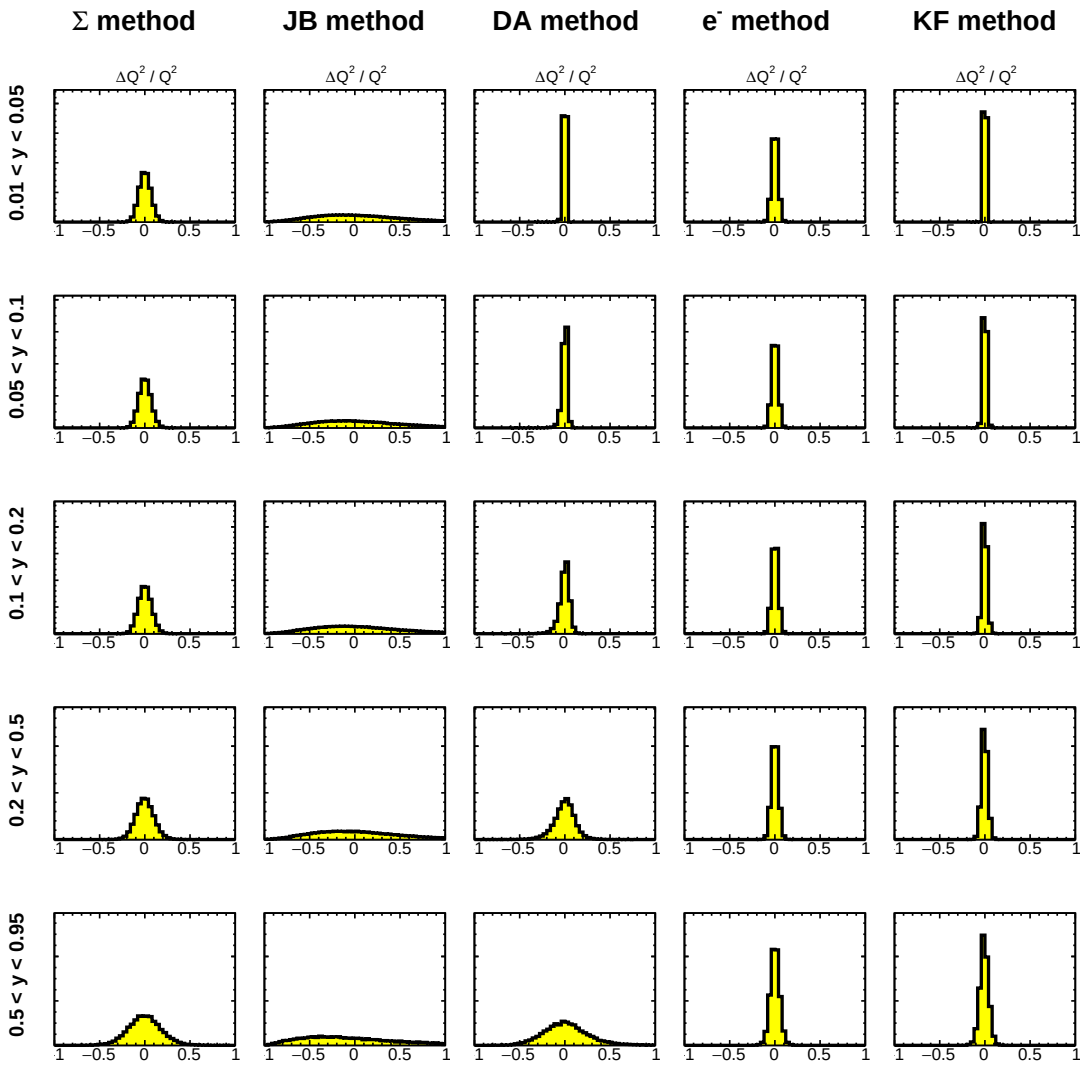

Figure 6.6: $\Delta Q^2/Q^2$ distributions in different y ranges for smeared Djangoh MC when reconstructed using several reconstruction methods. The Q^2 range is $Q^2 > 1\,\mathrm{GeV}^2$ and the beam configuration is $18 \times 275\,\mathrm{GeV}^2$ e^- on p.

of the y and Q^2 resolutions as a function of y is made in Fig. 6.8, with the same y binning as used in the earlier 1-dimensional y and Q^2 distribution plots. The comparison is made between the various reconstruction methods, with and without the inclusion of ISR events, and with the $\Sigma_{tot} > 31\,\mathrm{GeV}$ cut applied throughout to reduce the impact of events containing hard ISR. It can be seen that the KF method typically matches or exceeds the performance of the conventional methods as before, and that the effect of ISR on the kinematic resolutions is small when an appropriate Σ_{tot} cut is applied, as has typically been done in previous experiments. Prior to the inclusion of ISR, the Double Angle method demonstrated the best Q^2 reconstruction in the lowest y bin. However with ISR included the four methods give more similar reconstruction performance in this bin.

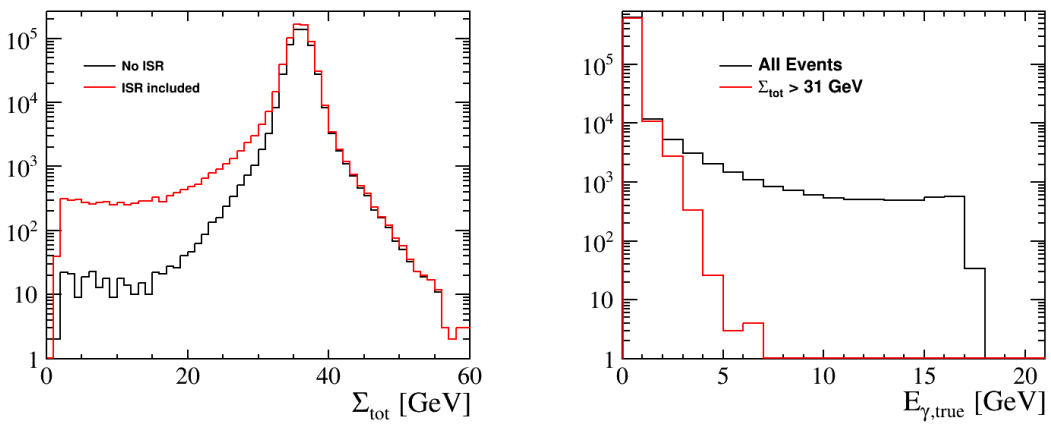

(a) (b)

Figure 6.7: (a) Reconstructed Σ_{tot} for events with no ISR photon emitted (black) and all events (red). (b) Frequency of events containing an ISR photon with true energy E_γ with no cut (black) and a minimum Σ_{tot} cut of 31 GeV (red).

6.4.3 ISR Tagging and Measurement

An advantage of the KF method is that in addition to reconstructing the inclusive DIS variables, it also yields the energy of a possible ISR photon. In the kinematic fit this is achieved by allowing the electron beam energy to vary as part of the fitting procedure, with the energy of the possible ISR photon relating to the reduced electron beam energy E_r as $E_r = E_0 - E_\gamma$. This approach assumes that the ISR photon is emitted collinear to the electron beam. The limiting quantity in the extraction of the ISR photon using the kinematic fit is the resolution of Σ_{tot}. For collinear ISR and in the absence of detector resolution effects, the relation $\Sigma_{tot} \simeq 2E_r$ is followed. For hard ISR, the measured value of Σ_{tot} is usually much less than $2E_0$. The probability of measuring a value of $\Sigma_{tot} \ll 2E_0$ as the result of a detector resolution effect is low, so hard ISR can be identified with a high efficiency.

The same events as in the previous studies were used here, consisting of a full MC sample of $18 \times 275\,\text{GeV}^2$ ep events with $Q^2 > 1\,\text{GeV}^2$, generated with QED radiative effects turned on, and smeared according to the parametrised detector resolutions. In these studies, events containing hard ISR are of partular interest, and so the minimum Σ_{tot} cut is removed such that the full energy spectrum of ISR is considered.

Fig. 6.9 shows the frequencies of generated E_γ and the distribution of E_γ predicted by the kinematic fit. It can be seen that there is good agreement between the number of events predicted by the kinematic fit and the number of generated events for energies $E_\gamma > 3\,\text{GeV}$, with the ratio of "reconstructed" to true falling in the range $0.7 - 1.3$ for these bins, and within $0.9 - 1.1$ for $E_\gamma > 4\,\text{GeV}$. For events where the

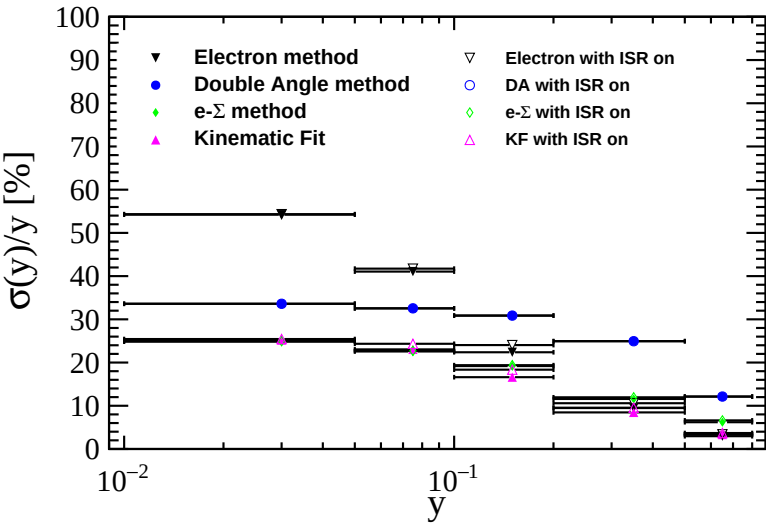

(a) y resolution

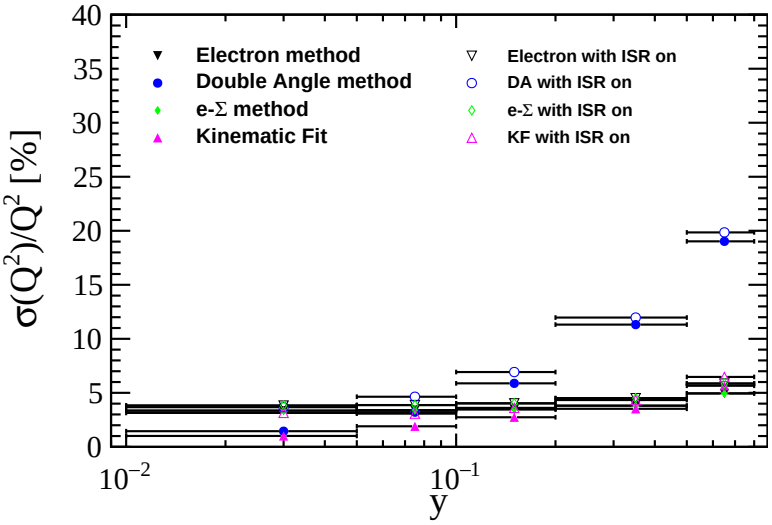

(b) Q^2 resolution

Figure 6.8: (a) y resolution and (b) Q^2 resolution in five y bins spanning $0.01 < y < 0.8$ with and without ISR present, reconstructed using several reconstruction methods. A cut of $\Sigma_{tot} > 31\,\text{GeV}$ is applied throughout.

energy of the ISR photons $E_\gamma < 3\,\text{GeV}$, the true value of Σ_{tot} is greater than 30 GeV. It is clear from Fig. 6.7a that a measured value of $\Sigma_{tot} > 30\,\text{GeV}$ could equally be attributed to a detector resolution effect. The ISR factor of the prior in Eq. 6.10 rises as $E_\gamma \to 0$. This means that the likelihood function must be strongly peaked away from $E_\gamma = 0$ in order for the posterior distribution to have its maximum at $E_\gamma > 0$. The numbers of events in the $1 < E_\gamma < 3\,\text{GeV}$ bins in Fig. 6.9 are significantly underestimated, with events generated in these bins usually being reconstructed in the $0 < E_\gamma < 1\,\text{GeV}$ bin. For these events, the discrepancy between the predicted kinematics from the scattered electron and HFS is not enough to overcome the effect of the prior, which pulls the predicted value of E_γ towards 0. The extent to which the events migrate between these low E_γ bins, and the direction in which they migrate, depends on the choice of prior for ISR [135]. However, the influence of the ISR

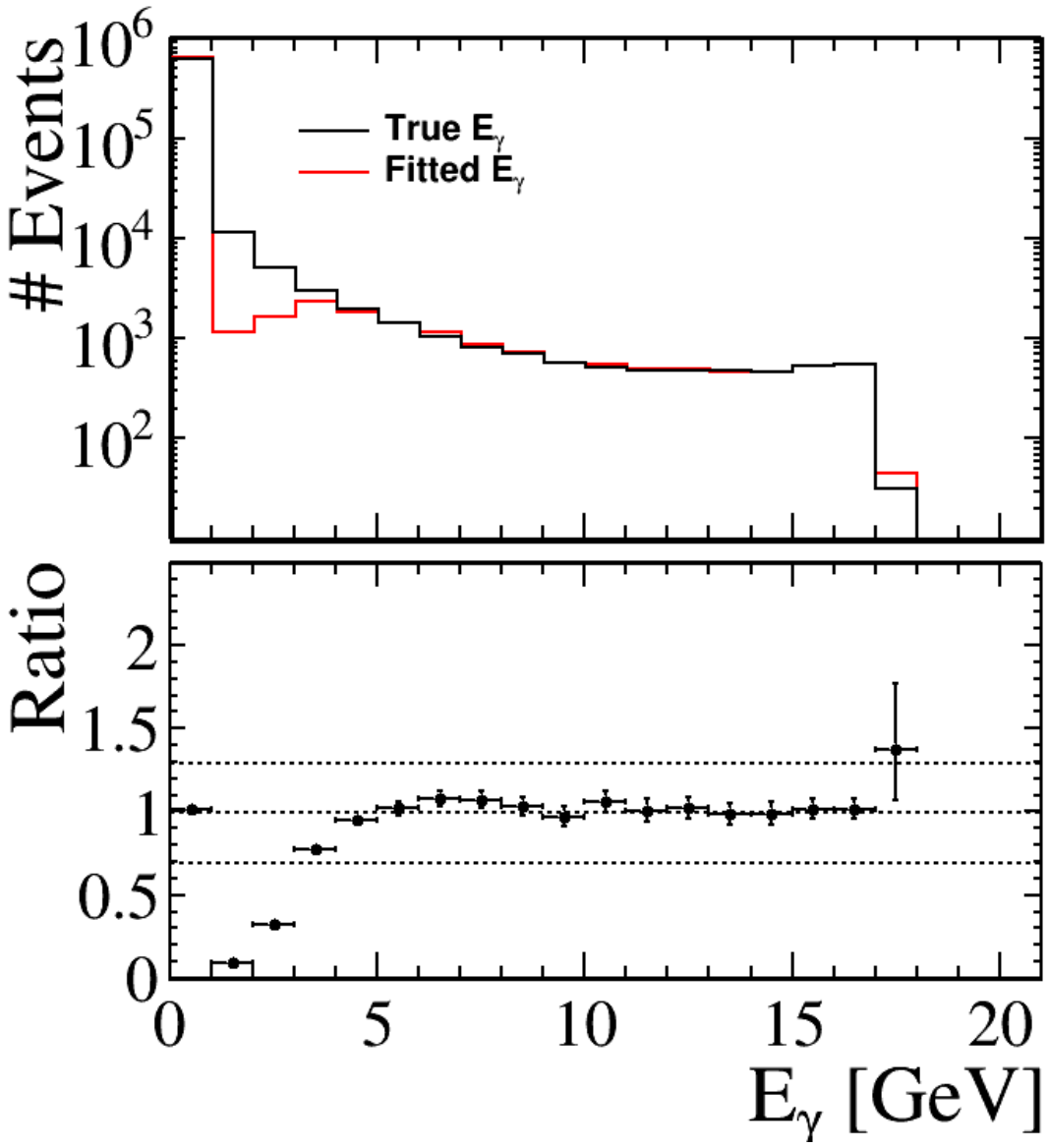

Figure 6.9: (Top) Distributions of the true values of E_γ from the MC, $E_{\gamma,true}$, and the E_γ prediction from the kinematic fit, $E_{\gamma,fitted}$. (Bottom) Ratio of number of fitted to true events in each E_γ bin.

prior does not extend beyond this low E_γ region, and any reasonable prior for E_γ produces the same distribution beyond $E_\gamma \sim 3\,\text{GeV}$, including a prior that is flat in E_γ (see [135]). As such, the role of the ISR prior is to ensure that the distribution of E_γ predicted by the fit reproduces the true distribution as well as possible at low E_γ.

The correlation between the values of E_γ predicted by the kinematic fit, $E_{\gamma,fitted}$, and the true values from the MC, $E_{\gamma,true}$ is shown in Fig. 6.10. There is a strong correlation between $E_{\gamma,fitted}$ and the true value, with minimal bias. The number of events reconstructed at low values of $E_{\gamma,true}$ is underestimated, which is consistent with the behaviour seen in Fig. 6.9. The ratio of the value E_γ predicted by the kinematic fit to the true value of E_γ is shown in Fig. 6.11, and is used to extract

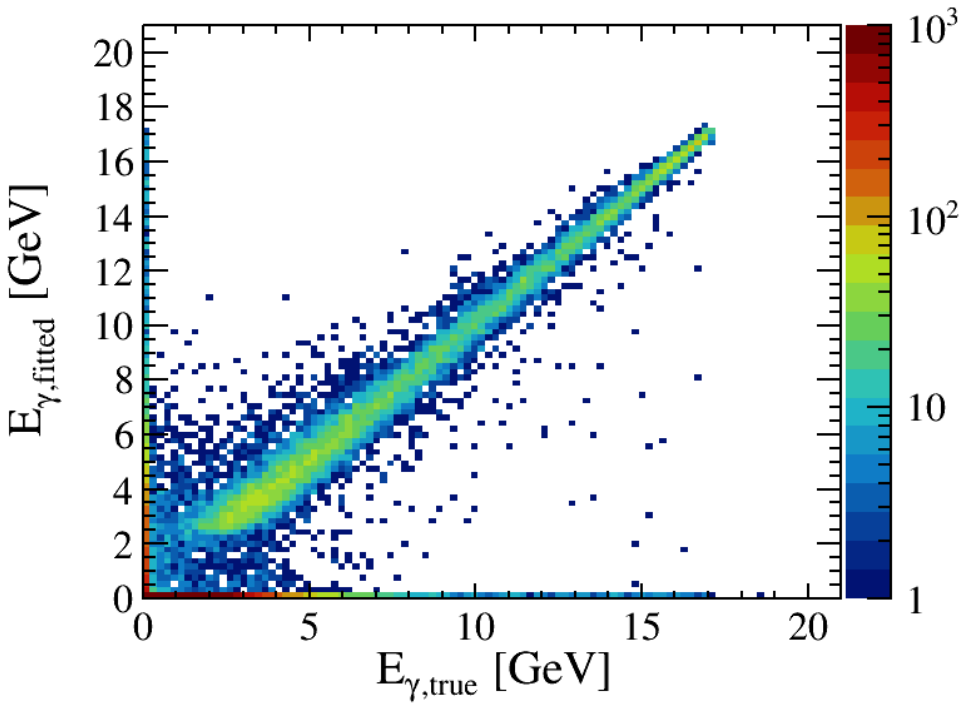

Figure 6.10: Correlation between values of E_γ predicted by kinematic fit, $E_{\gamma,fitted}$, and true value of E_γ from the MC, $E_{\gamma,true}$. Note the logarithmic scale in z.

the energy resolution at fixed energies. The resolution improves as E_γ increases, with a resolution of $\sim 11\,\%$ at $5\,\text{GeV}$, $\sim 5\,\%$ at $10\,\text{GeV}$, and $\sim 1.5\,\%$ at $15\,\text{GeV}$. The $E_{\gamma,fitted}/E_{\gamma,true}$ distribution at $E_{\gamma,true} = 5\,\text{GeV}$ exhibits positive skewness as a result of negative fluctuations in the $E - p_z$ measured by the detector. This is due to events with $E_\gamma < 5\,\text{GeV}$ having a larger probability of being reconstructed when Σ_{tot} is underestimated.

6.5 KF Method at ePIC

The smeared MC studies show that if the detector resolutions are perfectly described by the likelihood function, the KF method yields an equivalent or superior reconstruction performance compared to conventional reconstruction methods. In a realistic experiment, the detector resolutions are often non-Gaussian, and there may be effects due to noise or background events that interfere with the reconstruction, making the estimation of the likelihood function a more complicated procedure. Simulated full events produced using the ePIC software framework in the same manner as for Chapter 5 provide a more realistic detector output, with which the resolution of the KF method may once again be studied and compared to conventional methods.

The sample of simulated events used in these studies is generated using Pythia6, with beam effects applied using the afterburner (see Section 5.2) to apply the crossing

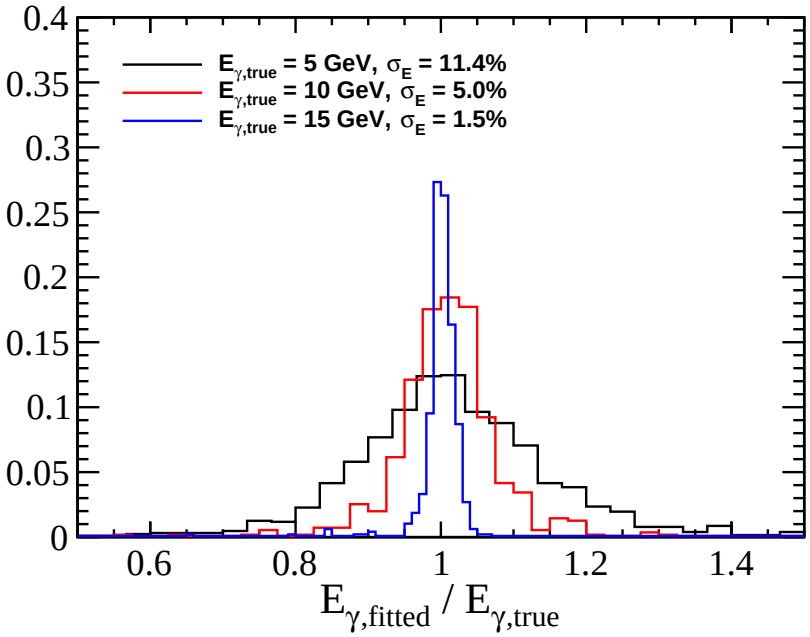

Figure 6.11: Distributions of $E_{\gamma,fitted}/E_{\gamma,true}$ for three different values of $E_{\gamma,true}$. An arbitrary binning scheme and y-axis scaling are used for visibility. The energy resolution, σ_E, is indicated for each $E_{\gamma,true}$, where the resolution is the width of a Gaussian fit to the distribution.

angle and beam effects. The sample used a relatively high minimum Q^2 threshold for the EIC of $100\,\mathrm{GeV}^2$. The sample is restricted to events for which the polar angle of the true scattered electron is within the barrel tracker acceptance of $45 < \theta < 135°$ ($-0.88 < \eta < 0.88$) as this region is well studied in ePIC simulations. The tracking detector which is used for charged particle reconstruction in the ePIC software is expected to provide a superior resolution compared to the calorimeters for this region. The momentum and polar angle resolutions for the scattered electrons, as determined from simulations of single electrons, are shown in Fig. 6.12, for the barrel tracker region. The tracker implemented in simulations is symmetric over this range, so only resolutions for positive η are shown. The resolutions shown in these plots are used to determine the Gaussian widths used in the likelihood function.

The electron variables E_e and θ_e only require a single particle to be measured, and so the simulated resolution on these variables is simply the resolution shown in Fig. 6.12. The HFS variables p_t^h and δ_h are reconstructed as the sum of track and calorimeter measurements, each with their own resolution. As a consequence, the distributions of $\delta_{h,reco}/\delta_{h,true}$ and $p^h_{t,reco}/p^h_{t,true}$ from the ePIC simulation are sharply peaked, with long tails, as shown in Fig. 6.13. The development of reconstruction algorithms for the inclusive HFS in the ePIC software is ongoing, with the eventual goal being a full particle flow algorithm. Given the current status of the reconstruc-

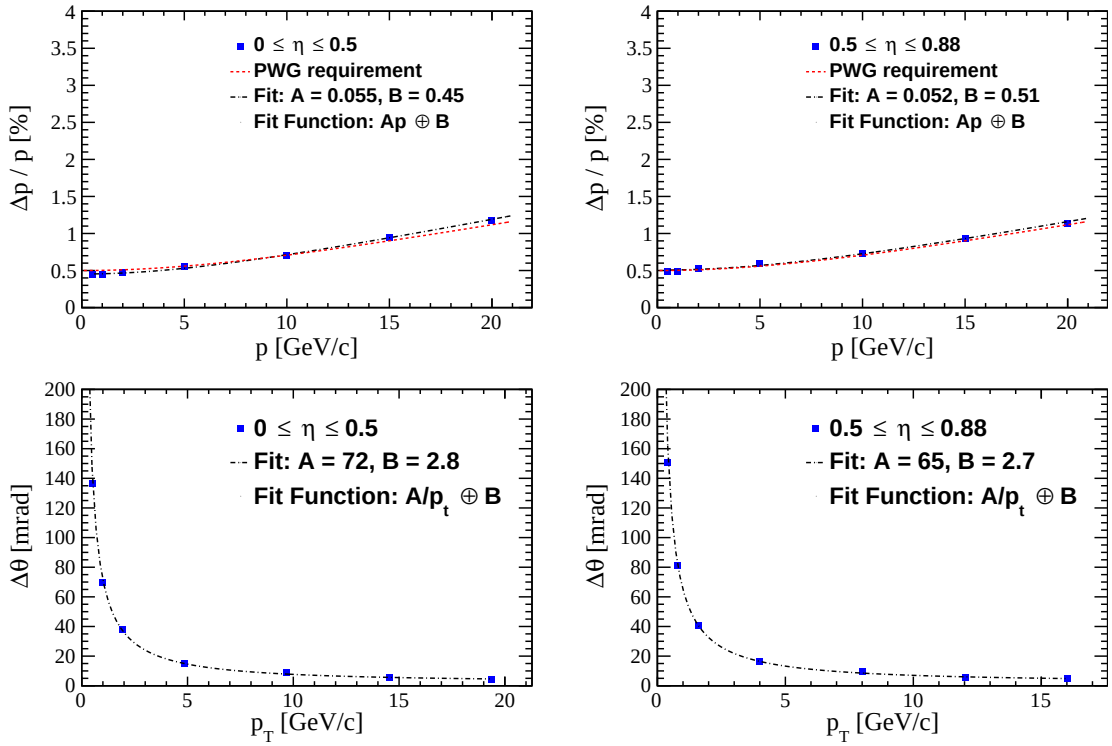

Figure 6.12: (Top) Relative momentum resolution and (Bottom) polar angle resolution for electrons in the barrel region of the tracking detector, as determined from single electron simulations in the ePIC software framework.

tion, detailed studies of the resolutions of the inclusive HFS are yet to be performed. To match the simple likelihood function used in the kinematic fit so far, a simple parametrisation of the δ_h and p_t^h resolutions is made by approximating the distributions in Fig. 6.13 with Gaussians with widths of 25 %.

As the distributions are non-Gaussian, this description of the HFS variables in the likelihood function is not perfect. Broadly speaking, the KF method weights the electron and HFS information according to the expected resolution for an event with a given x and Q^2, with HFS information generally being preferred at low y, and electron information at high y. At intermediate y, events are typically reconstructed with a value somewhere between the electron method and JB method predictions, and so an improved model of the resolutions of the HFS quantities may in future yield an improved KF method performance at moderate y.

The final parametrisation used for the likelihood function in the kinematic fit uses the factorisation in Eq. 6.6, with Gaussian widths given by

$$\sigma_E = 0.055 \cdot p \oplus 0.45 \text{ in GeV}$$
$$\sigma_\theta = 72/p_t \oplus 2.8 \text{ in mrad}$$

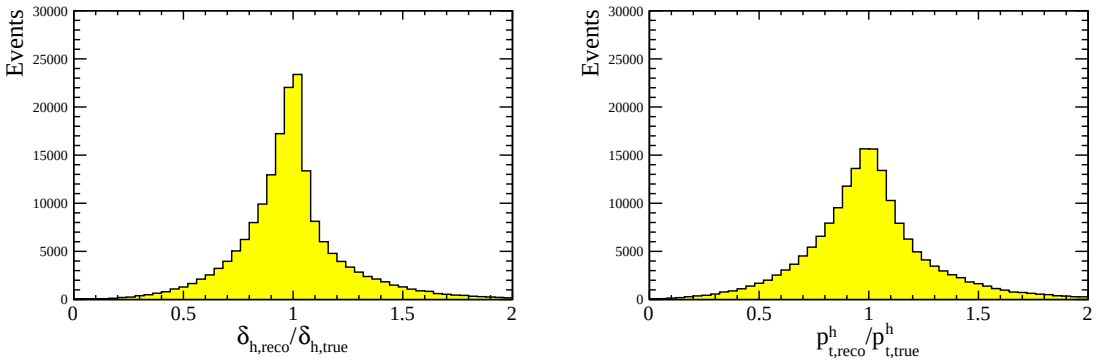

Figure 6.13: Distributions of $\delta_{h,reco}/\delta_{h,true}$ and $p^h_{t,reco}/p^h_{t,true}$ as determined from full simulations with Pythia6 events at $Q^2 > 100\,\mathrm{GeV}^2$, where the scattered electron is measured in the barrel region of the tracking detector and all other final state particles are included in the δ_h and p^h_t sum.

for the electron variables if the electron is scattered in the range $|\eta| < 0.5$, or

$$\sigma_E = 0.052 \cdot p \oplus 0.51$$
$$\sigma_\theta = 65/p_t \oplus 2.7$$

if scattered in the range $0.5 < |\eta| < 0.88$. The HFS variables are given by

$$\sigma_{\delta_h} = 0.25 \cdot \delta_h \text{ in GeV}$$
$$\sigma_{p^h_t} = 0.25 \cdot p^h_t \text{ in GeV}.$$

A summary of the $\Delta y/y$ distributions for the KF method and various conventional methods in different y bins is shown for fully simulated ePIC events in Fig. 6.14. A similar comparison for y resolutions extracted from ePIC full simulations is shown in Fig. 5.2 in Chapter 5, for the performance of conventional methods in the range $1 < Q^2 < 10\,\mathrm{GeV}^2$. In the lower Q^2 range, the scattering angle of the DIS electron is typically small and the resolution on θ_e is large as a result, leading to a poor resolution for the DA method at low Q^2, while the best y reconstruction is provided by the JB method at low y or the electron method at high y. In the higher Q^2 event sample used for Fig. 6.14, only events containing electrons scattered in the range $45 < \theta_e < 135°$ are considered, for which the electron polar angle is measured with high precision. Consequently, a significant improvement in the resolution of the DA method is observed for this event sample, which now offers the best y reconstruction for $y \lesssim 0.2$.

As previously discussed, the y reconstruction performance of the KF method generally tends towards the better performing method between the electron method and the JB method for a given y bin. It can be seen however, that for these high Q^2

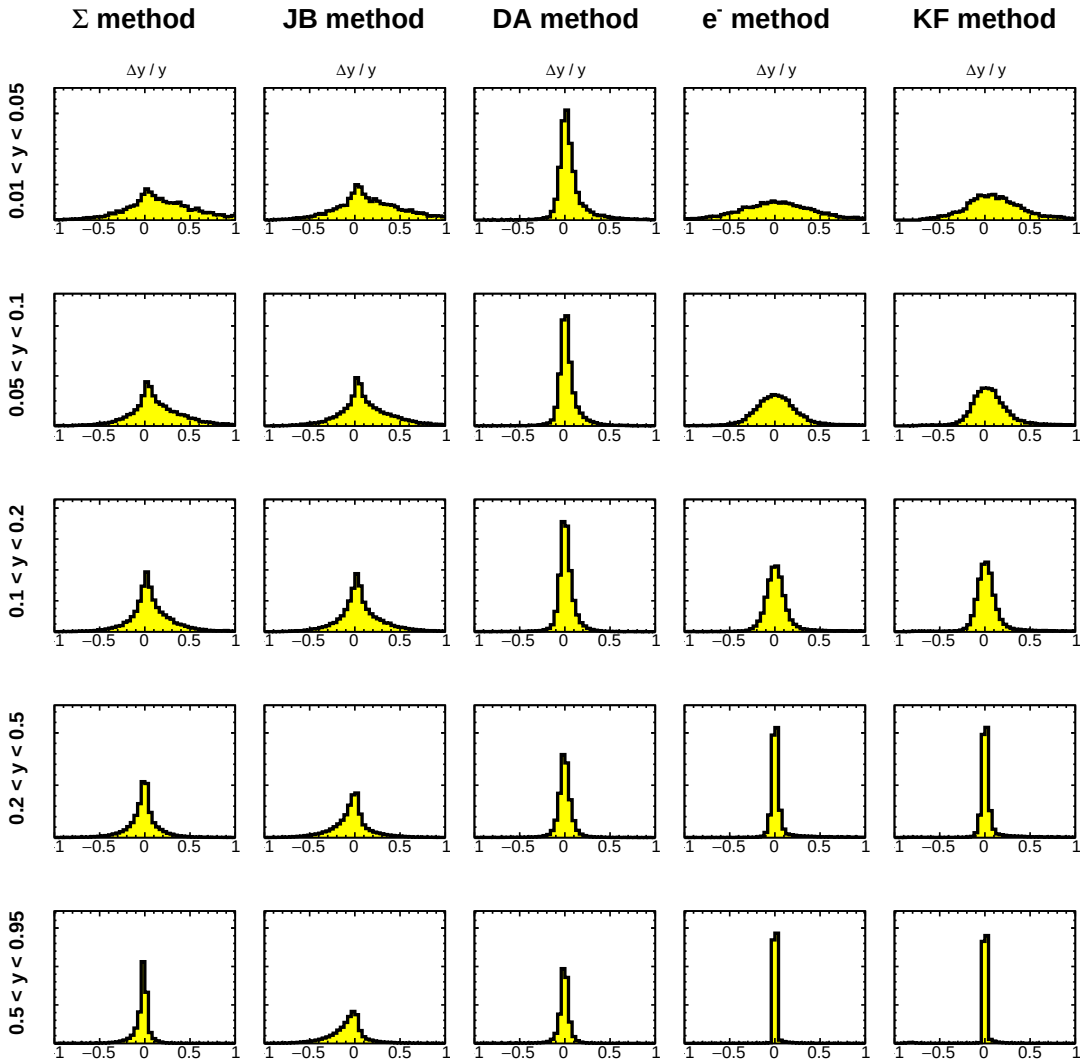

Figure 6.14: $\Delta y/y$ distributions in different y ranges for fully simulated ePIC events when reconstructed using several reconstruction methods. The Q^2 range is $Q^2 > 100\,\mathrm{GeV}^2$ and the beam configuration is $18 \times 275\,\mathrm{GeV}^2$ e^- on p.

events all methods are significantly outperformed by the DA method for $y \lesssim 0.2$. If the measured quantities are truly used simultaneously in an optimal matter, then the KF method is expected to provide performance comparable to that of the best conventional reconstruction method for a given y. However, in Fig. 6.14 is appears that the DA method significantly exceeds the performance of the KF method at low y. As will become clear from the following studies that this behaviour is attributable to the correlation between the HFS quantities δ_h and p_t^h. The same tracks and calorimeter clusters are used in the energy sum for both HFS quantities, meaning that a positive (negative) fluctuation in the measured value of δ_h with respect to the true value is usually accompanied by a positive (negative) fluctuation in the measured p_t^h. The HFS angle used in the DA method is defined by

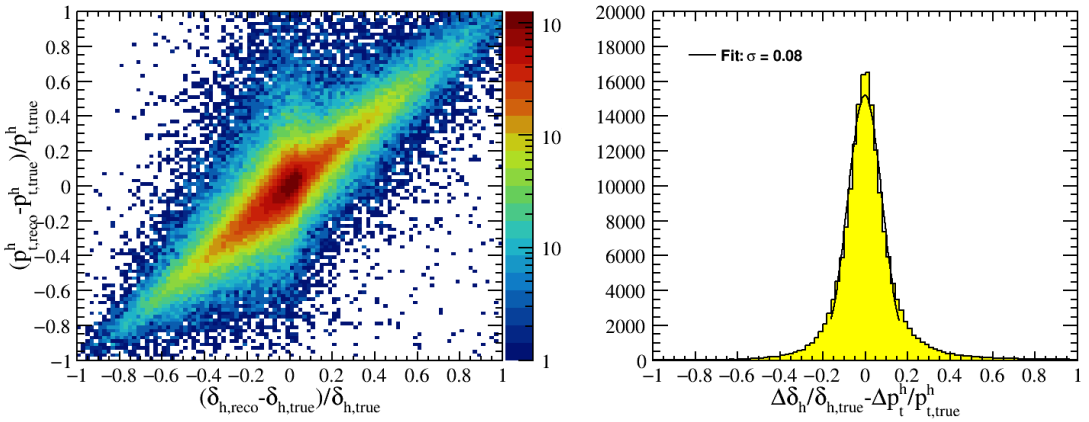

Figure 6.15: (left) Correlation plot for the fractional difference between the reconstructed and true values of p_t^h and δ_h as found from ePIC full simulations. (right) The distribution of $\Delta\delta_h/\delta_{h,true} - \Delta p_t^h/p_{t,true}^h$ as found from ePIC full simulations, where $\Delta\delta_h = \delta_{h,reco} - \delta_{h,true}$ and $\Delta p_t^h = p_{t,reco}^h - p_{t,true}^h$). A Gaussian fit is applied over a range $\pm 2\sigma$, and the width determined from the fit shown on the plot.

$$\tan\gamma_h = \frac{\delta_h}{p_t^h} = \frac{E_h(1-\cos\gamma_h)}{E_h \sin\gamma_h}, \tag{6.12}$$

such that any fluctuation in the total energy measured by the calorimeters does not change the value of $\tan\gamma_h$, and the correlation between δ_h and p_t^h is implicitly accounted for in the determination of the inclusive HFS angle. This is clearly not the case for the electron and Σ methods. In the implementation of the KF described in Eq.6.6, δ_h and p_t^h are treated as independent, and so do not benefit from the reduction in variance due to the correlation.

If the HFS variables are given by $\delta_h = E_h(1-\cos\gamma_h)$ and $p_t^h = E_h \sin\gamma_h$, they are highly correlated, and it follows that

$$c = \frac{\delta_{h,reco} - \delta_{h,true}}{\delta_{h,true}} - \frac{p_{t,reco}^h - p_{t,true}^h}{p_{t,true}^h} \simeq 0, \tag{6.13}$$

with c defined by the above equation. In the perfectly correlated case, the resulting c distribution would be a δ function. If the quantities are instead completely uncorrelated, then the resulting c distribution would be Gaussian with a width given by the sum of the δ_h and p_t^h resolutions in quadrature, i.e. for resolutions of 25 % the width σ_{corr}, of the c distribution, would be given by $\sigma_{corr} = \sigma(\delta_h)/\delta_h \oplus \sigma(p_t^h)/p_t^h = 35\,\%$. For partially correlated variables, the c distribution is a Gaussian with a smaller width than for uncorrelated variables, and can hence be parametrised and used to introduce an additional constraint to the kinematic fit. The correlation of the fractional difference between the reconstructed and true values of δ_h and p_t^h is investigated in Fig. 6.15, where it can be seen that the width of the c distribution defined

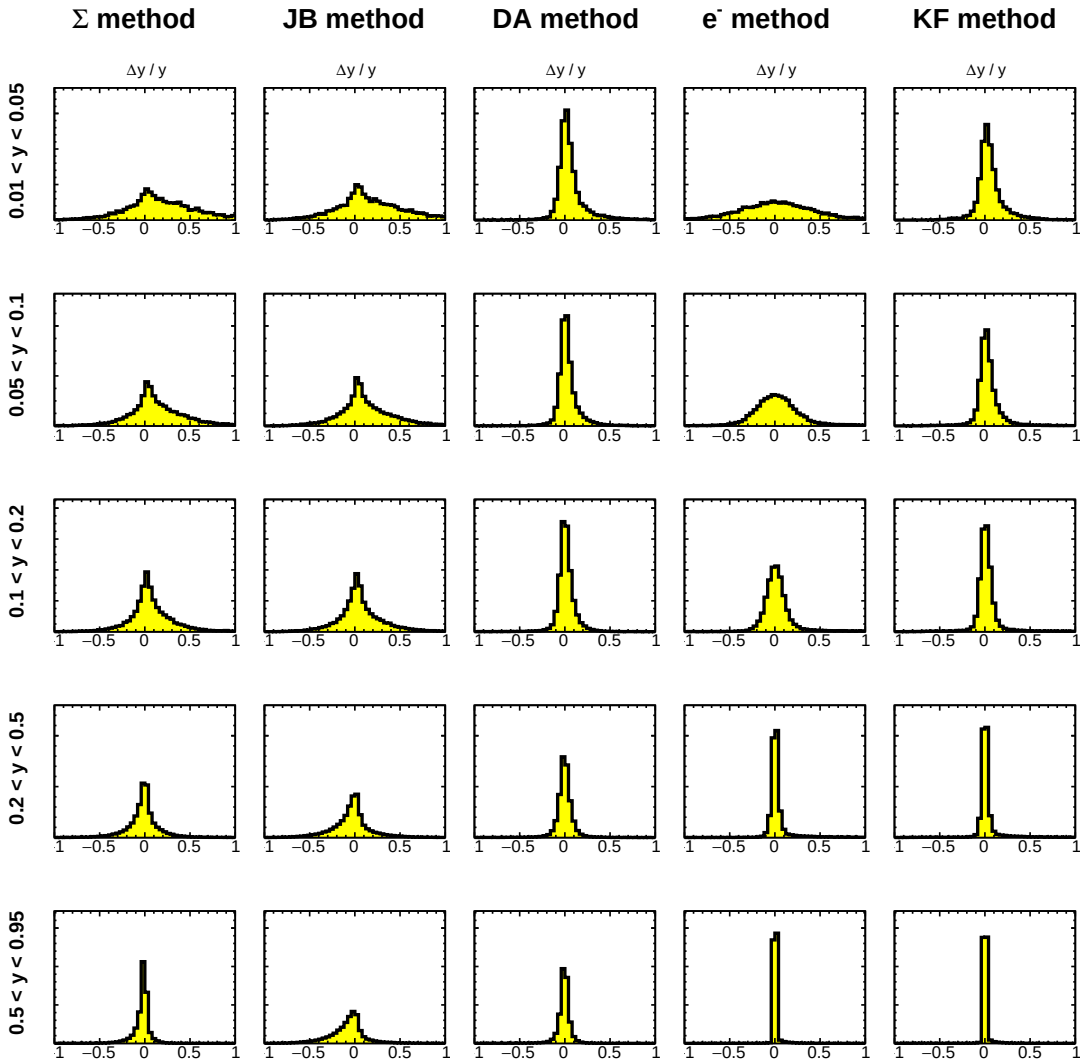

Figure 6.16: $\Delta y/y$ distributions in different y ranges for fully simulated ePIC events when reconstructed using several reconstruction methods. The KF method is modified to include an additional constraint to account for correlations. The Q^2 range is $Q^2 > 100\,\mathrm{GeV}^2$ and the beam configuration is $18 \times 275\,\mathrm{GeV}^2$ e^- on p.

by Eq. 6.13 is $\sim 8\,\%$. With this information, the likelihood function described by Eq. 6.6, denoted now as $P(\overrightarrow{D}|\overrightarrow{\lambda})_{uncorr}$, can be modified to include this additional constraint as

$$P(\overrightarrow{D}|\overrightarrow{\lambda})_{corr} = P(\overrightarrow{D}|\overrightarrow{\lambda})_{uncorr} \frac{1}{\sqrt{2\pi}\sigma_{corr}} \cdot \exp -\frac{(c-c^{\lambda})^2}{2\sigma_{corr}^2}, \tag{6.14}$$

with $\sigma_{corr} = 0.08$, as determined from the fit in Fig. 6.15.

Comparisons of the y and Q^2 resolutions of various methods with the KF method with this additional constraint are shown in Fig. 6.16 and Fig. 6.17, respectively. The inclusion of the constraint results in a significant improvement in the resolution at low y when reconstructing using the KF method, which now exhibits a perfor-

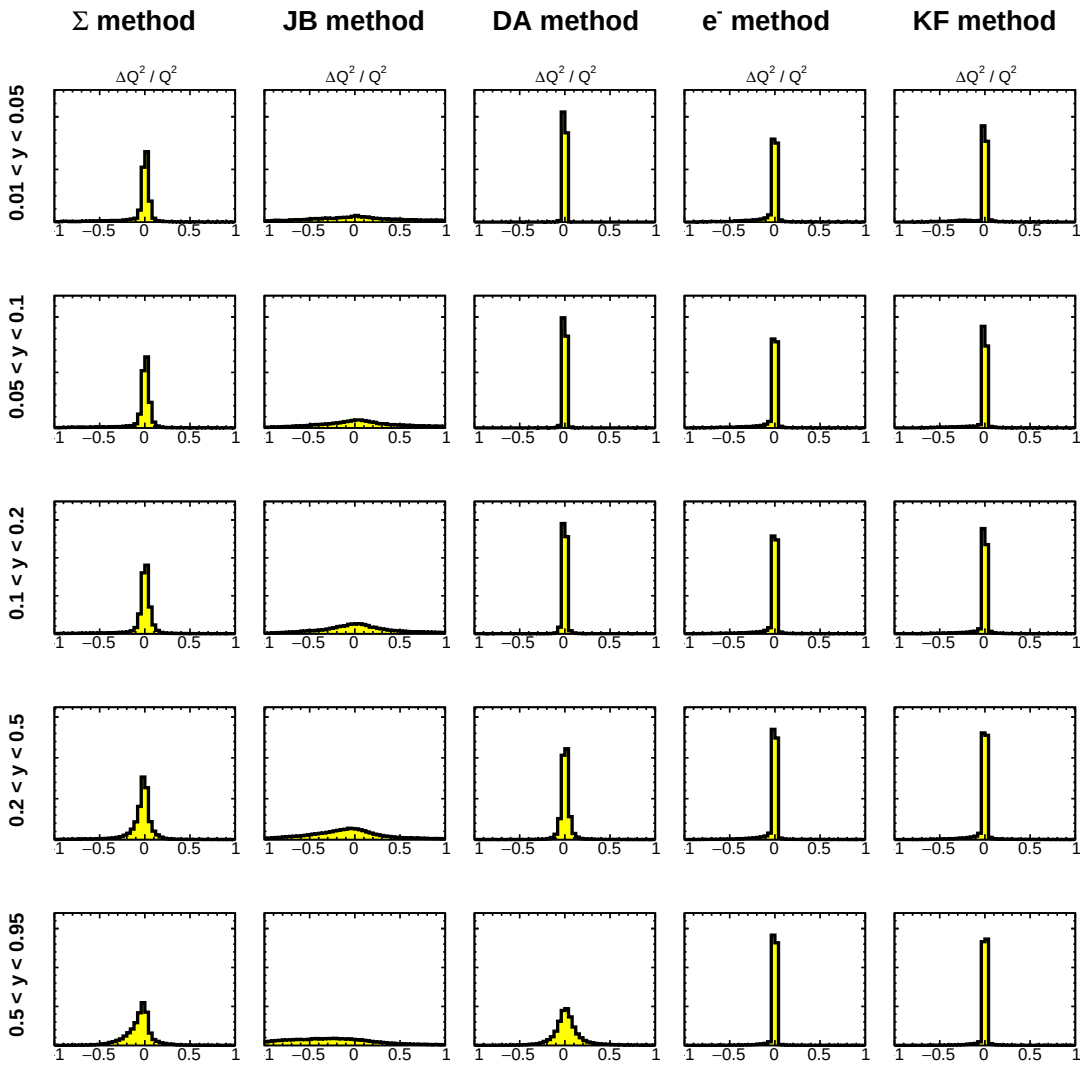

Figure 6.17: $\Delta Q^2/Q^2$ distributions in different y ranges for fully simulated ePIC events when reconstructed using several reconstruction methods. The KF method is modified to include an additional constraint to account for correlations. The Q^2 range is $Q^2 > 100\,\mathrm{GeV}^2$ and the beam configuration is $18 \times 275\,\mathrm{GeV}^2$ e^- on p.

mance comparable to the DA method in the low y bins, and overall provides a reconstruction in line with the best conventional method for all y bins throughout the range $0.01 < y < 0.95$.

Further improvements should be possible through a more rigorous determination of the contribution of the HFS quantities to the likelihood function. Taking the variables δ_h and p_t^h to be Gaussian distributed with width 25 % is sufficient to reconstruct events with good precision using the KF method, as their likelihood is peaked at the correct position, and the 25 % resolution gives a reasonable approximation for their weighting relative to the electron variables. However, an improved description of the HFS quantities requires more than simply optimising the Gaussian widths used

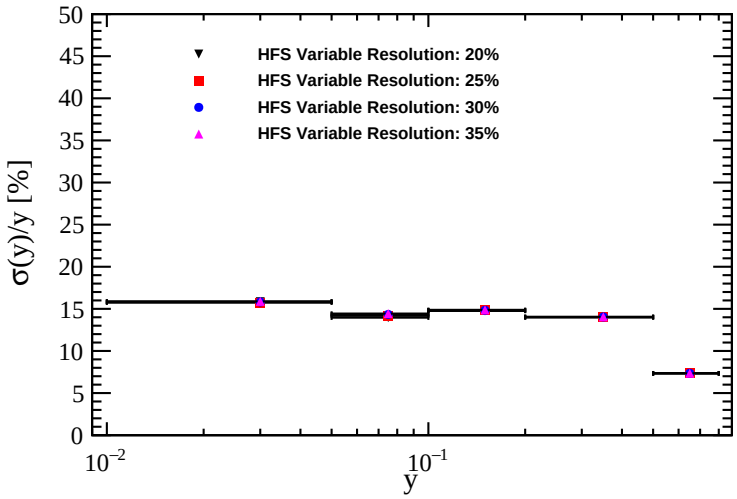

(a) y resolution

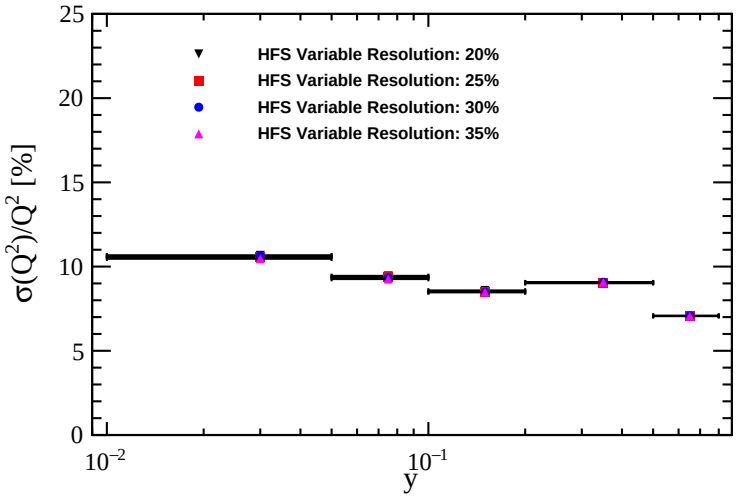

(b) Q^2 resolution

Figure 6.18: Comparison between the y (left) and Q^2 (right) resolutions for the KF method including the treatment of correlations, for Gaussian parametrisations of the HFS variable resolutions with four different Gaussian widths in the likelihood function.

in the likelihood function, as can be seen in Fig. 6.18, which compares four different Gaussian widths used as inputs to the kinematic fit to reconstruct the same sample, where any difference in the measured kinematic resolution is at the $< 1\,\%$ level. It is concluded that for an optimal description of the HFS variables, and thus an optimal reconstruction using the KF method, the parametrisation will need to be adjusted in favour of a parametrisation that more accurately reflects the distributions shown in Fig. 6.13. Through improvements to the description of the correlations for both the electron and HFS variables, and by refining the description of the HFS resolutions, the KF method should be able to match or exceed the resolutions of all conventional methods throughout the kinematic plane.

6.6 KF Method at H1

The resolution and ISR tagging studies based on applying the KF method to the ePIC full simulations provide a useful indicator of the performance of the method in the context of the EIC. However, as ePIC will not begin data taking for several years, and the simulation and reconstruction software are still being developed, we must rely on previous experiments to validate the behaviour of the KF method in a fully realistic experimental environment.

The H1 experiment was one of two general purpose detectors at HERA which took data from $e^{\pm}p$ collisions between 1992 and 2007. MC from H1 are an excellent tool with which to test the KF method. The simulations are tuned to data, and include backgrounds and radiative corrections, such that the simulated output accurately reflects that of the experiment. Furthermore, the KF method can be verified using real DIS data taken by H1, and additionally may be used to check for discrepancies between H1 data and MC. The following studies with H1 aim to demonstrate that the KF method is viable as part of a realistic analysis that includes all of the difficulties associated with a DIS experiment. Additionally, it is verified that the performance with simulations and data match, and generated H1 events are used to investigate the ability of the method to tag ISR events.

6.6.1 The H1 Experiment

The H1 detector used an asymmetric detector design that was optimised for the measurement of high energy ep collisions. It consisted of various subsystems for tracking, calorimetry, and muon detection positioned around the interaction point, as well as luminosity systems further along the beamline in the electron-going direction. A comprehensive description of the H1 detector can be found elsewhere [136], and only the subsystems most relevant to these studies are briefly described here. The coordinate system is as outlined in Section 2.3.1, with the positive z-axis aligned with the proton beam direction. The main detectors used in these studies are the Liquid Argon (LAr) calorimeter, and the inner tracking detectors. Both subsystems are subject to a 1.16 T axial magnetic field provided by a superconducting solenoid.

The central tracking system spans an overall range in polar angle of $15° < \theta < 165°$, and consists of drift and proportional chambers, complemented by a silicon vertex detector for which the outer layer extends over a polar angle range of $30° < \theta < 150°$ [137]. The tracking system provides a transverse momentum resolution for charged particles of $\sigma_{p_t}/p_t = 0.2\,\% \cdot p_t \oplus 1.5\,\%$. The LAr calorimeter spans $4° <$

$\theta < 154^\circ$ in polar angle, and consists of an electromagnetic section which uses 20-30 radiation lengths of lead absorber plates and a hadronic section with steel absorber plates giving a total depth of 4.5-8 interaction lengths. The energy resolution for leptons is $\sigma_E/E = 11\,\%/\sqrt{E} \oplus 1\,\%$, and for charged pions $\sigma_E/E \approx 50\,\%/\sqrt{E} \oplus 3\,\%$, as determined from test beam measurements [138, 139].

6.6.2 H1 Simulations

For these studies, fully simulated samples of DIS events containing both QED and QCD radiative effects are required. The events are generated using the DJANGOH 1.4 [140] leading order matrix element MC simulation toolkit, for which QED radiation and electroweak effects are provided by HERACLES 4.6 [141]. Higher order parton emissions are simulated according to the colour dipole model implementation in ARIADNE [142], which includes an implementation of the JETSET software toolkit for the calculation of hadronisation, fragmentation, and decay. DIS samples were generated with a minimum Q^2 of $60\,\mathrm{GeV}^2$ for use in these studies. Background processes such as photoproduction, Charged-Current DIS, and QED Compton are not included in the MC sample.

The detector response was simulated using a detailed simulation of the H1 detector based on Geant [143]. The simulation includes a time-dependent model of the experimental conditions, such as detector noise, beam optics, polarisation, and inefficient channel maps, such that the simulations reflect the conditions throughout the data taking period.

6.6.3 Event Selection

Operations in the 2003 to 2007 run period were performed using the upgraded HERA-II collider, which collided 27.6 GeV electrons or positrons with 920 GeV protons for a total integrated luminosity of $351.1\,\mathrm{pb}^{-1}$ [144]. The studies detailed in this section were performed using only data collected during the 2003 to 2004 run period, where positrons (henceforth referred to as electrons) were collided with protons for a total integrated luminosity of $99.4\,\mathrm{pb}^{-1}$.

A trigger requirement is imposed in which a high energy cluster must be found in the electromagnetic section of the LAr calorimeter. Electron candidates are taken as LAr clusters that have been matched to a track, subject to isolation criteria, the scattered electron being chosen as the candidate with the largest transverse momentum. Events containing scattered electrons with $E_e > 11\,\mathrm{GeV}$ are retained for analysis. Background processes such as those arising from cosmic rays, photo-

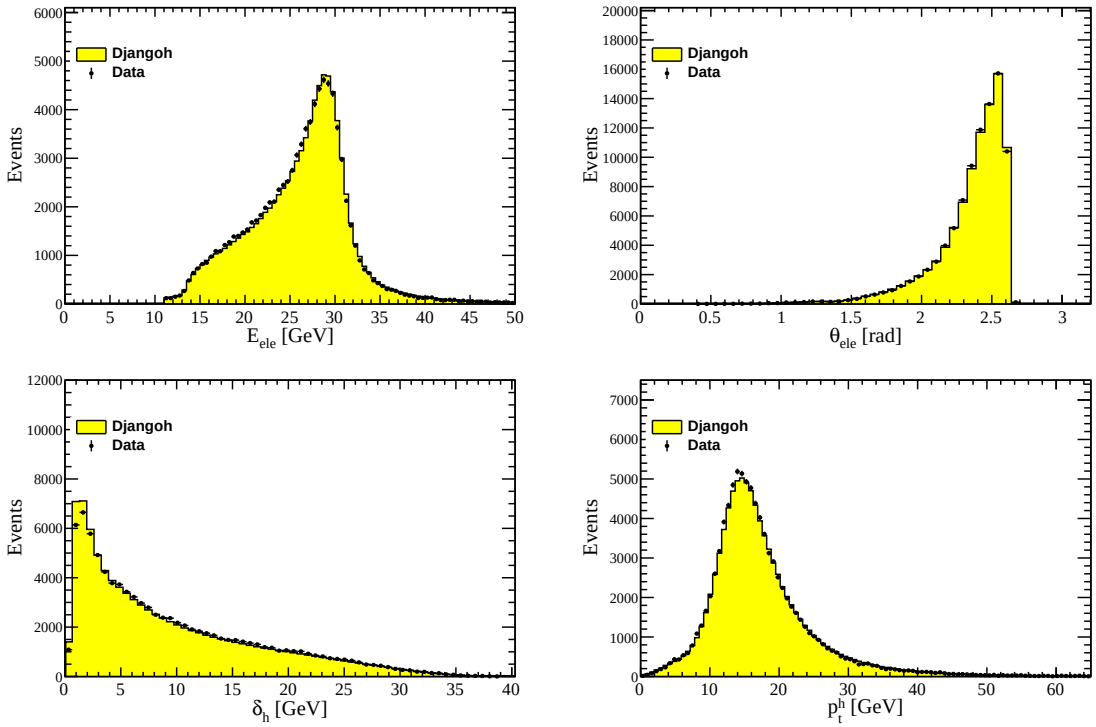

Figure 6.19: Control distributions comparing the reconstructed quantities E_e, θ_e, δ_h, and p_t^h for H1 2003/2004 e^+p data and a pure DIS MC sample (Djangoh), after event selection and cuts.

production, beam-gas interactions, charged current DIS, and QED Compton, are vetoed according to dedicated selection requirements [145].

The same reconstruction and analysis algorithms used for event selection were applied to both data and simulated events. Further analysis cuts were applied to remove events on the edges of the acceptance, ensuring a clean sample. The electron trigger requirement naturally limits the kinematic range to $Q^2 \gtrsim 150\,\mathrm{GeV}^2$, due to the maximum polar angle coverage of the LAr calorimeter, and $y \lesssim 0.7$ due to the minimum electron energy requirement. This range was restricted by analysis cuts of $Q^2_{e\Sigma} > 200\,\mathrm{GeV}^2$ and $y_{e\Sigma} < 0.6$, and a cut of $y_{e\Sigma} > 0.01$ is introduced to maintain reasonable kinematic resolutions. Lower and upper cuts around Σ_{tot} are often applied to control the contribution from QED radiation, as well as reducing the background from photoproduction events. Since ISR is desirable for the present studies, the lower Σ_{tot} cut is not applied, though an upper cut of $\Sigma_{tot} < 60\,\mathrm{GeV}$ is applied in order to filter events for which a DIS event is coincident with a beam-gas interaction that leaves energy deposits in the calorimeters.

Control distributions comparing data and MC after the event selection and cuts for the measured quantities that are inputs to the kinematic reconstruction methods are

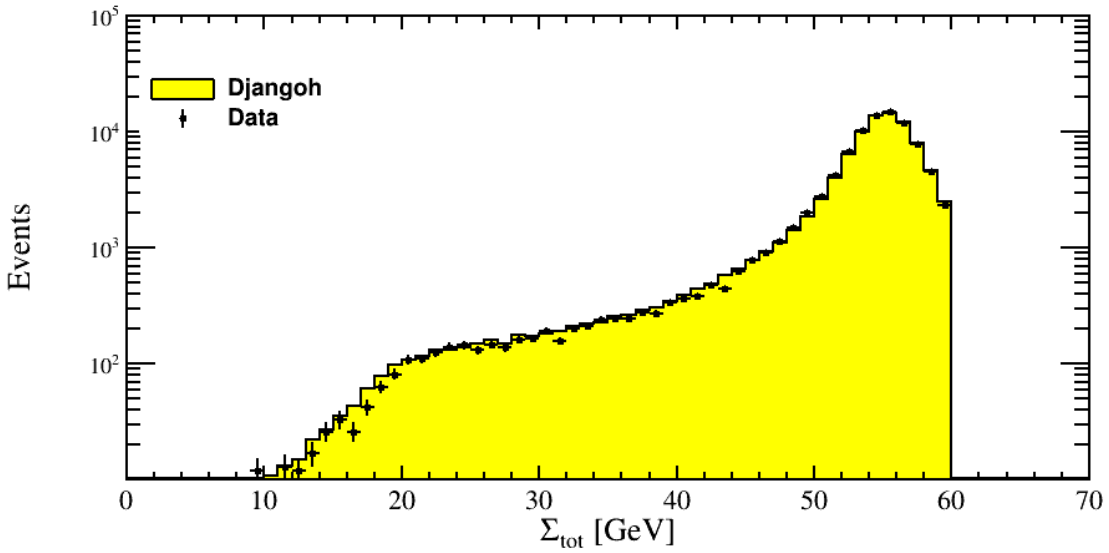

Figure 6.20: Control distribution comparing Σ_{tot} for H1 2003/2004 e^+p data and a pure DIS MC sample (Djangoh), after event selection and cuts.

shown in Fig. 6.19, and the control distribution for Σ_{tot} is shown in Fig. 6.20. The pure DIS MC sample is in good agreement with the data with these cuts applied for each distribution, and so is used in further studies without simulating background processes. The Σ_{tot} distribution is shown with a logarithmic y-scale so that the $\Sigma_{tot} \lesssim 50\,\text{GeV}$ region, for which hard ISR dominates, is visible. The ISR tail is well described by the MC.

6.6.4 Kinematic Fit

The same kinematic fitting procedure outlined in Section 6.2 and Section 6.3 was used to reconstruct the H1 data and MC, with the likelihood function being constructed according to a parametrisation of H1 detector resolutions. The energy resolution of the H1 LAr calorimeter is well studied, and since the LAr is the only system used for the scattered electron energy measurement, the quoted resolution of $\sigma(E_e)/E_e \approx 11\,\%/\sqrt{E_e} \oplus 1\,\%$ [136] may be used directly. The resolution on the polar angle of the scattered electron θ_e, as well as the HFS quantities δ_h and p_t^h, were parametrised through dedicated studies of the current MC sample. The polar angle resolution is taken to be constant, with no dependence on E_e or θ_e, leading to a resolution of $\sigma(\theta_e) = 4\,\text{mrad}$. A simplified approximation was used for the resolution of δ_h, where the Gaussian width of the $\delta_{h,reco}/\delta_{h,true}$ distribution is used, from which a resolution parametrisation of $\sigma(\delta_h) = 13.5\,\% \times \delta_h$ is obtained. The resolution on p_t^h is parametrised based on the calorimeter energy resolution, as $\sigma(p_t^h)/p_t^h = 54\,\%/\sqrt{p_t^h} \oplus 4\,\%$, which is comparable to the quoted LAr energy

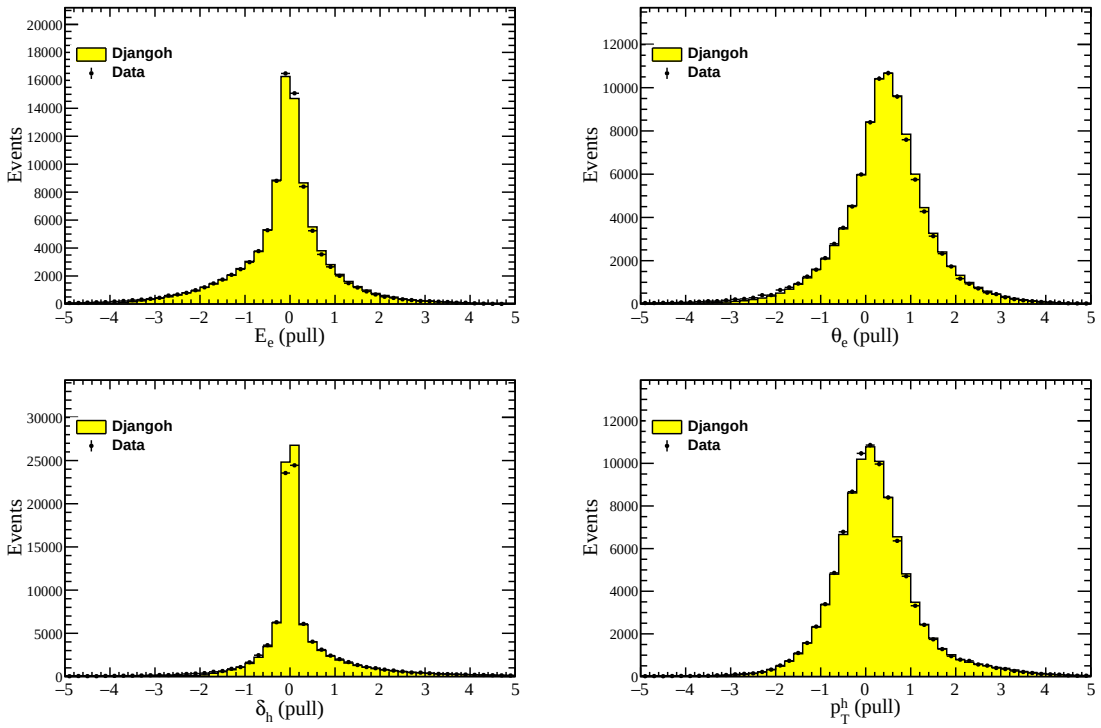

Figure 6.21: Distributions comparing the pulls obtained from the kinematic fit for the quantities $E_e, \theta_e, \delta_h,$ and p_t^h for H1 2003/2004 e^+p data and a pure DIS MC sample (Djangoh), after event selection and cuts.

resolution for hadrons of $\sigma_E/E \approx 50\,\%/\sqrt{E} \oplus 3\,\%$ [136]. The likelihood function constructed using these parametrisations is sufficient for ISR tagging studies, but more detailed studies of the resolutions of the measured quantities should be performed if the goal is to optimise the kinematic resolutions.

It is important to ensure that data and MC behave compatibly during the kinematic fitting procedure, so a set of pulls for the quantities in the vector $\overrightarrow{D}$ at the output of the kinematic fit are studied. The pull g may be defined by

$$g = \frac{x - \mu}{\sigma} \tag{6.15}$$

which, for a random variable x generated from a Gaussian distribution with mean μ and standard deviation σ, will be distributed as a Gaussian centred at 0, with unit width [146]. The quantities in $\overrightarrow{D}$ may be non-Gaussian, so for these studies the pull is instead defined by

$$g = \frac{D_{i,fitted} - D_{i,reco}}{RMS_{MC}}, \tag{6.16}$$

where $D_{i,reco}$ ($D_{i,fitted}$) is the reconstructed (fitted) value of the quantity in the vector $\overrightarrow{D}$, and RMS_{MC} is the root mean square (RMS) of the $D_{i,reco} - D_{i,true}$ distribution

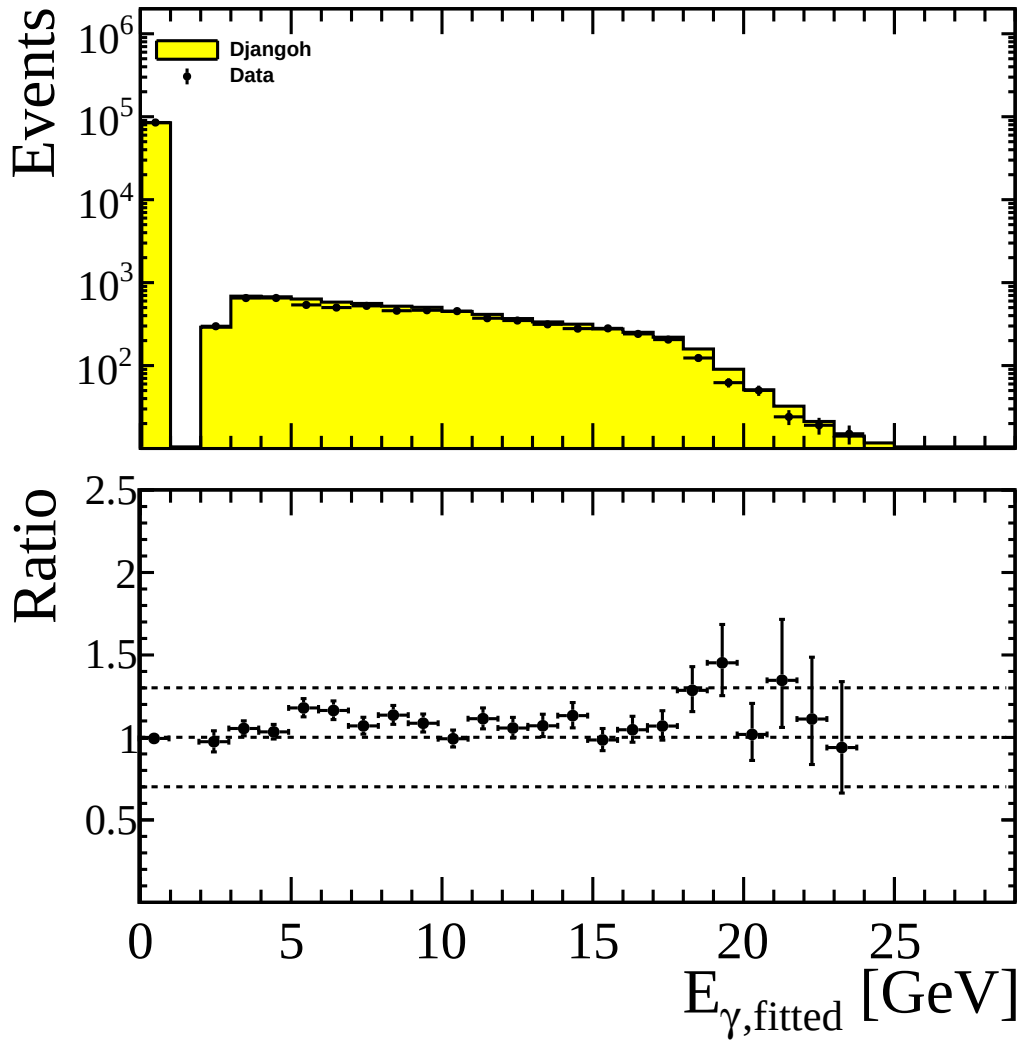

Figure 6.22: (Top) Control distribution comparing $E_{\gamma,fitted}$ for H1 2003/2004 e^+p data and a pure DIS MC sample (Djangoh), after event selection and cuts. (Bottom) Ratio of the number of MC to Data events reconstructed by the KF.

of the MC sample, such that the pull distributions for the MC sample have an RMS of 1 by construction. The pull distributions for the quantities at the output of the kinematic fit are shown in Fig. 6.21, and good agreement is found between the distributions produced by data and MC. A discrepancy between the pull distributions would indicate a bias between the data and the MC; as such the pulls may be used to set limits on systematic uncertainties in future studies.

6.6.5 ISR Tagging and Measurement

A control distribution comparing the values of E_γ predicted by the kinematic fit with the distribution from real H1 data is shown in Fig. 6.22, with a logarithmic y-

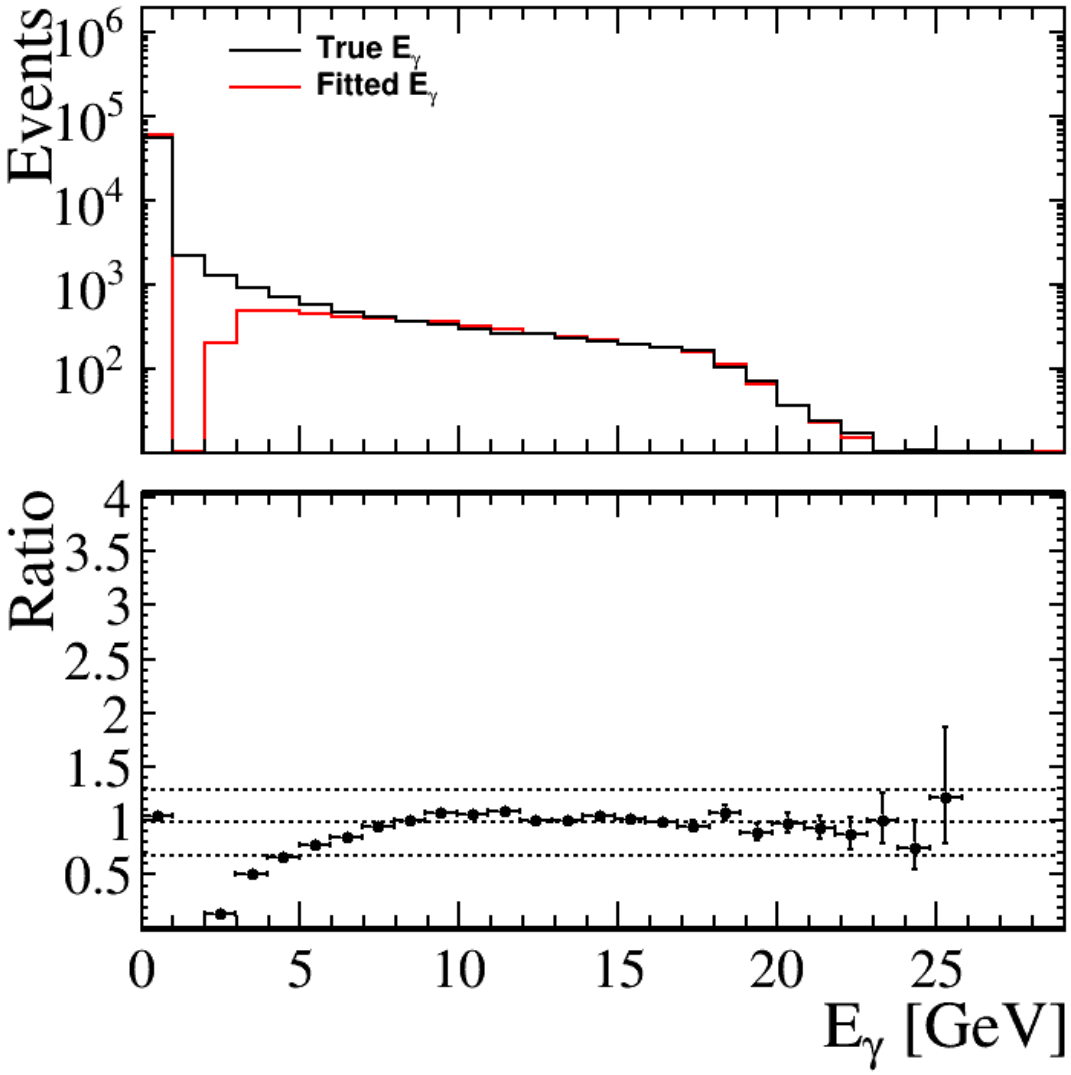

Figure 6.23: (Top) Distributions of the true values of E_γ from the MC, $E_{\gamma,true}$, and the E_γ prediction from the kinematic fit, $E_{\gamma,fitted}$. (Bottom) Ratio of number of fitted to true events in each E_γ bin (True or Fitted).

scale. For this sample, the number of events rapidly decreases for $E_{\gamma,fitted} \gtrsim 17\,\text{GeV}$, whereas the equivalent distribution using smeared MC, shown in Fig. 6.9, flattens out at the largest $E_{\gamma,fitted}$. This behaviour is a consequence of the minimum scattered electron energy $E_e > 11\,\text{GeV}$ requirement. In cases where the ISR is emitted with energy $E_\gamma > 17\,\text{GeV}$, the electron beam energy is reduced to $E_0 < 11\,\text{GeV}$. In order to pass the selection criteria the electron must be scattered with a larger energy than the (reduced) beam energy which, while possible, is heavily suppressed. The distribution of ISR energies predicted by the fit for the data and for the MC are in reasonably good agreement across the full range.

The distributions for the MC sample of predicted and true energies of ISR photons, and the ratio of the number of events predicted by the kinematic fit to the true

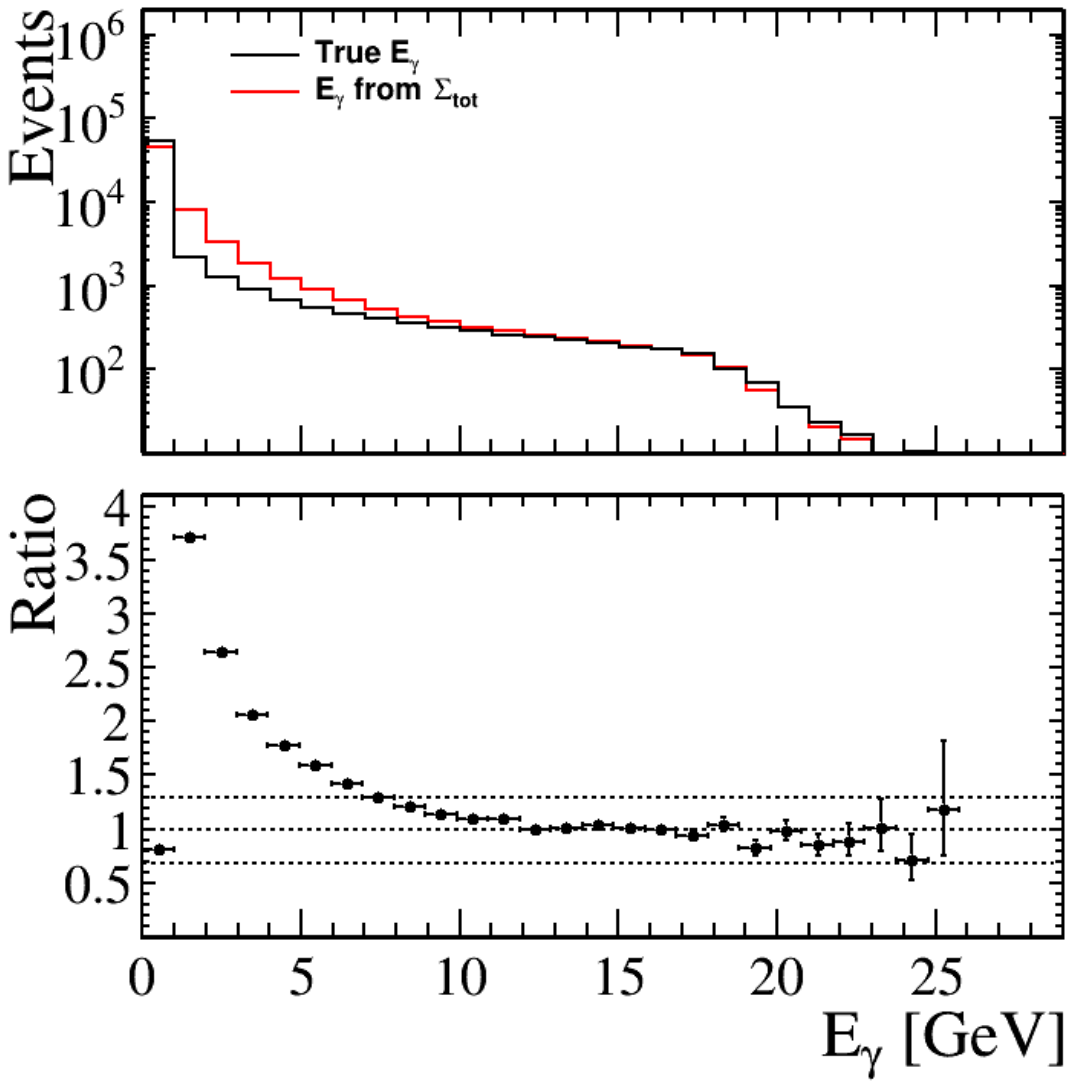

Figure 6.24: (Top) Distributions of the true values of E_γ from the MC, $E_{\gamma,true}$, and the E_γ prediction from the Σ_{tot} constraint, $E_{\gamma,\Sigma}$. (Bottom) Ratio of number of predicted to true events in each E_γ bin (True or from prediction). Events for which $E_{\gamma,\Sigma}$ is calculated to be negative are added to the $0 < E_\gamma < 1\,\text{GeV}$ bin.

number of events at a given energy, are shown in Fig. 6.23. We see that the true E_γ distribution is well reproduced by the kinematic fit prediction, at all but the smallest values of E_γ, where the prediction underestimates the number of events. The kinematic fit is able to extract the energy of ISR photons by leveraging the over-constraint in the kinematics. The Σ methods are insensitive to QED radiation for similar reasons, as they use more than two measured quantities to reconstruct the kinematics. The electron beam energy in these methods is replaced using the Σ_{tot} constraint, so the methods account for ISR photons with energy given by

$$E_{\gamma,\Sigma} = \frac{1}{2}(2E_0 - \Sigma_{tot}). \tag{6.17}$$

This relation can be directly used to predict the energy of possible ISR photons, and

compare them to the prediction from the kinematic fit. The distribution of true ISR photon energies and the energies predicted by the Σ_{tot} constraint, as well as the ratio of predicted to true events, are shown in Fig. 6.24. Comparing the distributions and ratios between the two different E_γ prediction approaches, Fig. 6.23 and 6.24 both converge to the truth values at large ISR energies, $E_\gamma \gtrsim 9\,\text{GeV}$. The two approaches differ in their predictions in the $1 < E_\gamma < 9\,\text{GeV}$ region. The prediction based on the Σ_{tot} constraint increasingly overestimates the number of events for a given E_γ bin with decreasing E_γ, while the kinematic fit increasingly underestimates. The overestimation in the Σ_{tot} approach in Fig. 6.24 results from negative fluctuations in the measured Σ_{tot} for events containing low energy ISR, or no ISR at all. As events with $E_{\gamma,true} < 1\,\text{GeV}$ drastically outnumber those with $E_{\gamma,true} > 1\,\text{GeV}$, and the width of the Σ_{tot} peak is larger than 1 GeV, the migration of events from $0 < E_\gamma < 1\,\text{GeV}$ generation bin to the $1 < E_\gamma < 2\,\text{GeV}$ generation bin is common. Consequently, the majority of the events reconstructed in the $1 < E_{\gamma,\Sigma} < 4\,\text{GeV}$ bins using the Σ_{tot} constraint were generated in the $0 < E_{\gamma,true} < 1\,\text{GeV}$ bin. It should be noted that the value of E_γ predicted using Eq. 6.17 can be negative, so in Fig. 6.24 events with $E_{\gamma,\Sigma} < 0$ are set to 0, and added to the $0 < E_\gamma < 1\,\text{GeV}$ bin.

The underestimation of the number of events by the kinematic fit in Fig. 6.23 as $E_\gamma \to 0$ is consistent with the behaviour seen with smeared MC, and occurs due to the ISR prior pulling the E_γ to 0, as is discussed in Section 6.4.3. The underestimation of the number of events by the kinematic fit of H1 data and MC is substantial compared to the underestimation for the smeared EIC MC, with no events being reconstructed in the $1 < E_\gamma < 2\,\text{GeV}$ bin for the H1 simulations/data. This can be attributed to the poorer resolution on the measured value of Σ_{tot} for H1 compared to the resolution in the smeared MC studies. The Σ_{tot} peak in the H1 case is wide enough that the likelihood function for events with $1 < E_\gamma < 2\,\text{GeV}$ is consistent with zero, and so the estimation of E_γ by the kinematic fit is pulled towards zero by the prior.

The role of the prior is to improve the description of low energy ISR beyond what is possible with a naive prediction based on the Σ_{tot} constraint. It is largely successful in this regard, as can be seen from the fact that the fitted versus true ratio falls within the tolerance of $0.7 - 1.3$ for events with $E_\gamma > 4\,\text{GeV}$ (and $0.9 - 1.1$ for $E_\gamma > 7\,\text{GeV}$) for the kinematic fit prediction. The tolerance was chosen to maintain a reasonable error contribution from acceptance corrections. The Σ_{tot} approach, which is used implicitly in the Σ methods, achieves this tolerance for $E_\gamma > 7\,\text{GeV}$. It can therefore be concluded that the KF method extends the energy range for which ISR photons can be identified with good efficiency compared to the Σ methods.

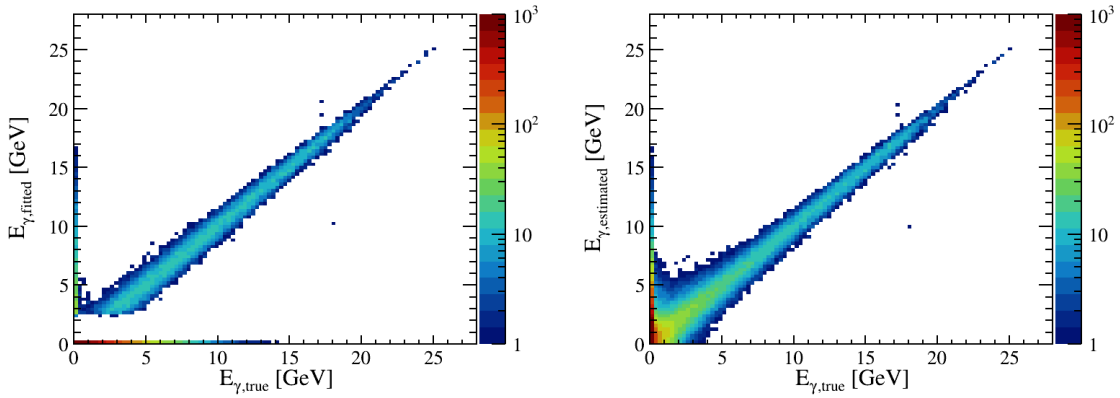

(a) Kinematic Fit **(b)** Σ_{tot} constraint

Figure 6.25: Correlation between values of E_γ predicted by (a) the kinematic fit, $E_{\gamma,fitted}$, and (b) the Σ_{tot} constraint, $E_{\gamma,\Sigma}$, and the true value of E_γ from the MC, $E_{\gamma,true}$. Note the logarithmic scale in z.

The correlations between the predicted value of E_γ and the true values from the MC are shown in Fig. 6.25, for the prediction at the output of the kinematic fit, and a prediction using the Σ_{tot} constraint. At relatively large values, there is a strong correlation between $E_{\gamma,fitted}$ and $E_{\gamma,true}$, with good resolution and minimal bias for moderate and high energy ISR, as was the case with the kinematic fit of the smeared MC. It can be seen from the fine binning of $E_{\gamma,fitted}$ in Fig. 6.25a that the kinematic fit does not predict the values of E_γ in the range $0 < E_\gamma \lesssim 3\,\text{GeV}$, and the predicted E_γ for events in this range is usually 0. The kinematic fit does more than a simple cut at 2.5 GeV could, however, as can be seen by comparison with Fig. 6.25b where the energy of ISR photons with $0.5 \lesssim E_{\gamma,true} \lesssim 4\,\text{GeV}$ is often overestimated when using the Σ_{tot} constraint, while such events are filtered out by the kinematic fit. The distribution of the ratio $E_{\gamma,fitted}/E_{\gamma,true}$ for three different values of $E_{\gamma,true}$ is shown for the KF method in Fig. 6.26, with information on the Gaussian width of each distribution, i.e. the energy resolution. The energy resolution improves as $E_{\gamma,true}$ increases, as was seen for smeared MC in Fig. 6.11, though with comparitively larger resolutions of $\sim 16\,\%$ at 5 GeV, $\sim 8\,\%$ at 10 GeV, and $\sim 4\,\%$ at 15 GeV.

While a study of ISR is useful by itself, the accurate reconstruction of ISR energies means that events containing hard ISR, which would typically be removed by a Σ_{tot} cut, can be used in an analysis. Furthermore, events containing hard ISR significantly reduce the electron beam energy, and so electrons at a fixed Q^2 scatter through a larger angle. This effectively extends the detector acceptance to lower values of Q^2. This is shown in Fig. 6.27, which compares the distribution of events in $x - Q^2$ for events containing no ISR and with hard ISR ($E_\gamma > 7\,\text{GeV}$), from the

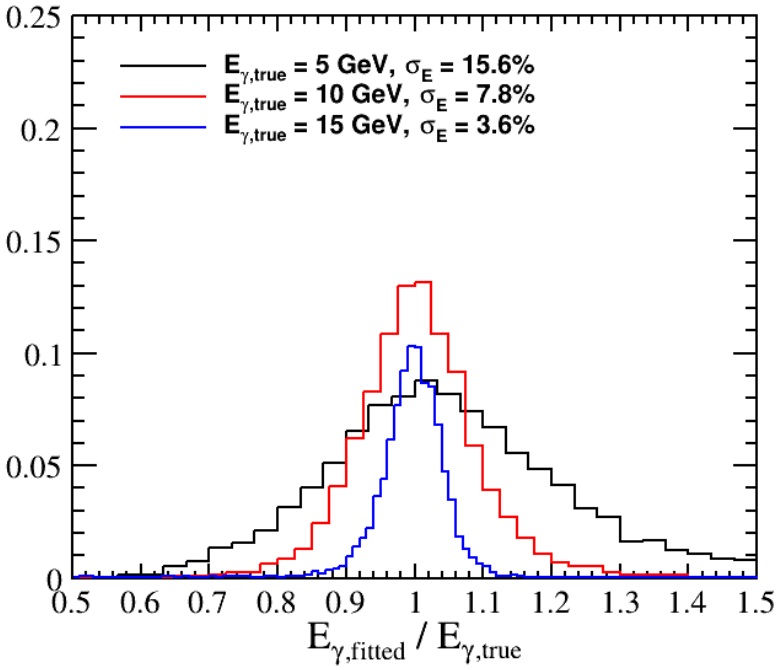

Figure 6.26: Distributions of $E_{\gamma,fitted}/E_{\gamma,true}$ for three different values of $E_{\gamma,true}$. An arbitrary binning scheme and y-axis scaling are used for visibility. The energy resolution, σ_E, is indicated for each $E_{\gamma,true}$, where the resolution is the width of a Gaussian fit to the distribution.

same H1 MC or data sample. The top plot shows the distributions in $x_{fitted}-Q^2_{fitted}$, for events in the H1 data sample with $E_{\gamma,fitted} = 0$, meaning that the kinematic fit predicts that there is no ISR in the event, and with $E_{\gamma,fitted} > 7\,\text{GeV}$. The bottom plot shows the distribution in $x_{true} - Q^2_{true}$ for events in the H1 MC sample with $E_{\gamma,true} = 0$ and $E_{\gamma,true} > 7\,\text{GeV}$. It can be seen that the events with $E_\gamma = 0$ are limited by the detector acceptance, and events do not extend below than $Q^2 \sim 100\,\text{GeV}^2$ in this configuration. The events with $E_\gamma > 7\,\text{GeV}$ do not reach the same maximum Q^2 as the events that do not contain ISR, however there is considerable overlap in the $x - Q^2$ coverage, as well as an extension of coverage to lower Q^2 values. The same features are observed in both the $x - Q^2$ distributions for the kinematic fit in the data, and the reconstructed-level MC.

By using the data for which the predicted E_γ is large, measurements of the F_2 structure function may be obtained, both in the regions of the phase space that have been explored in previous measurements, and the low Q^2 region that is not usually accessible using the central detector. It should be noted that for low Q^2 measurements, scattered electrons are usually measured by the H1 spaghetti calorimeter (SpaCal), rather than the LAr calorimeter used in these studies. At H1, measurements of F_2 were performed down to $Q^2 \sim 0.5\,\text{GeV}^2$ for the nominal vertex position, and down

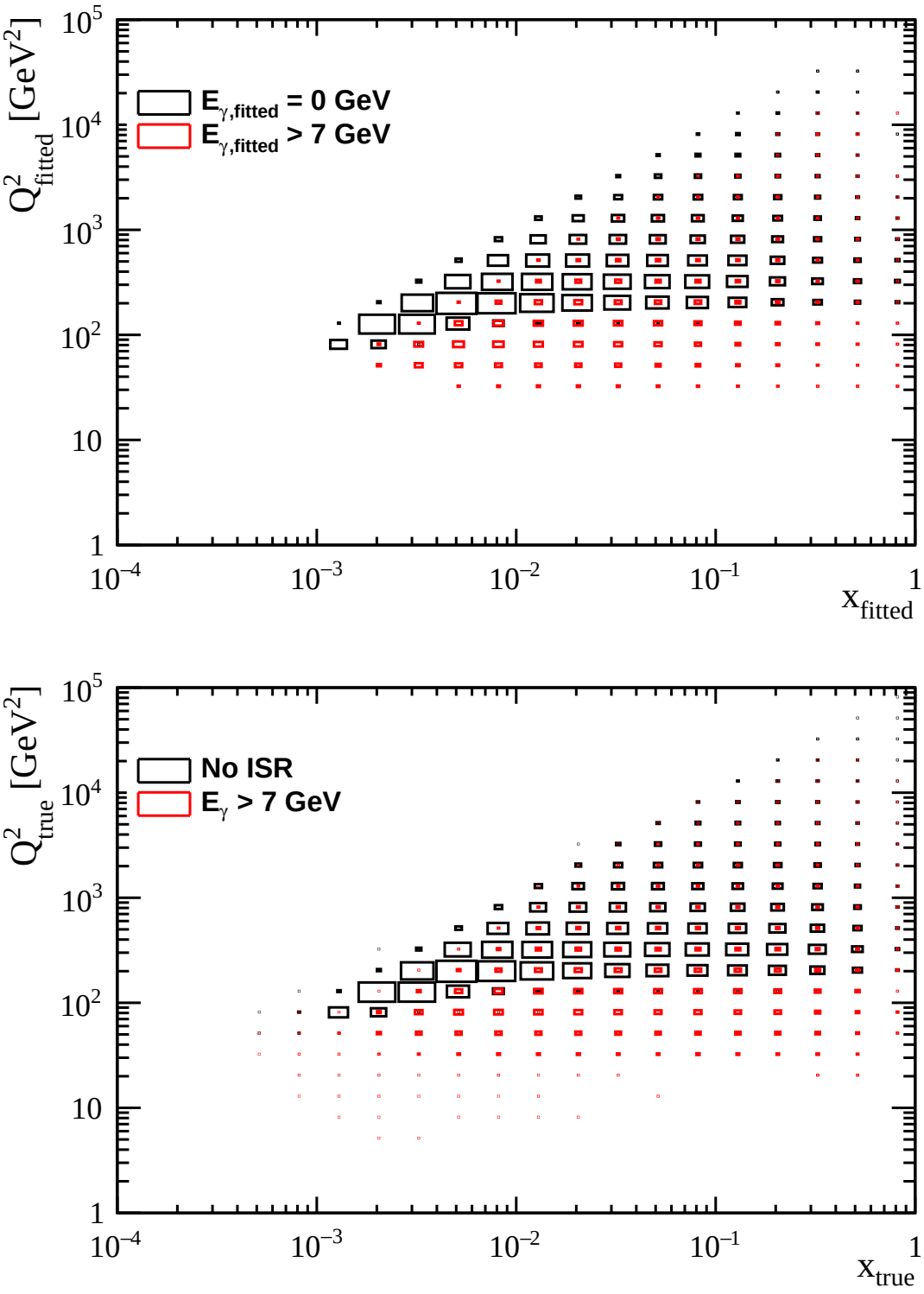

Figure 6.27: (Top) Distribution of $x_{fitted} - Q^2_{fitted}$ for H1 03/04 data for events where the kinematic fit E_γ prediction is 0, or $E_{\gamma,fitted} > 7\,\text{GeV}$. The y and Q^2 analysis cuts are removed. (Bottom) Distribution of $x_{true} - Q^2_{true}$ for H1 MC sample (Djangoh) for events where the $E_{\gamma,true} = 0$, or $E_{\gamma,true} > 7\,\text{GeV}$. The size of the boxes are proportional to the number of events in each bin.

to $Q^2 \sim 0.2\,\mathrm{GeV}^2$ through dedicated runs with the z position of the interaction point shifted along the proton beam direction by 70 cm [147]. The kinematic fit approach is applicable to data sets for low Q^2 based on electron measurements in the SpaCal, and may also be used with measurements for the shifted vertex runs. This has the potential to extend the kinematic reach even further, with the caveat that dedicated studies of the scattered electron and HFS resolutions would need to be performed. The longitudinal structure function F_L is extracted using a Rosenbluth plot, for which the reduced cross section σ_r is plotted against y/Y_+, such that F_L is the slope of a line fitted to the data points (see Eq. 2.21). To vary y/Y_+ for a fixed bin in $x - Q^2$, the centre-of-mass energy must be varied. For most of the HERA running period, the centre-of-mass energy was fixed at 300/318 GeV, so dedicated runs at the end of the HERA II running period were performed using reduced proton beam energies of $E_p = 565\,\mathrm{GeV}$ and $E_p = 460\,\mathrm{GeV}$, with the aim of measuring F_L [148]. Tagging hard ISR events with the kinematic fit allows for the centre-of-mass energy to be varied without changing the beam energy, which could be used to obtain additional data points for a Rosenbluth plot, though a limiting factor in this approach are the low statistics for hard ISR events, and the energy resolution on $E_{\gamma,fitted}$.

Whilst these possibilities, enabled by the KF method, are exciting, further studies will be required to investigate their feasibility and expected performance.

Chapter 7

Summary and Conclusions

7.1 Tracking Simulations

The tracking simulations are split into three sections. Initial studies using tracker designs that were considered for the Yellow Report baseline detector with 1.5 T and 3 T magnetic fields are first presented. This is followed by dedicated studies of a Silicon + MPGD hybrid tracker using a 3 T magnetic field, for the ATHENA detector proposal. Finally, studies are shown covering the evolution of a reference tracking detector design starting from a 1.5 T magnetic field, to the current ePIC tracking design based on a 1.7 T magnetic field.

From the initial studies it is concluded that two approaches may be used in order to achieve the required tracking performance. If the magnetic field strength provided by the magnet chosen for the experiment is 3 T, the required tracking performance can be achieved using a tracker with a reduced lever arm (~ 20 cm) of high precision silicon layers in all cases other than the relative momentum resolution in the electron endcap. However, it is anticipated that the insufficient momentum resolution from tracking measurements in this region can be recovered with measurements by the calorimetry systems. If a magnet with a lower field strength of ~ 1.5 T is chosen, the momentum resolution is degraded, and so the required tracking performance in the barrel cannot be achieved without a larger lever arm of silicon (~ 40 cm), while the momentum resolution requirements at larger pseudorapidities ($|\eta| > 1$) cannot be met using the tracking system alone.

Studies for the ATHENA tracking system demonstrated that the material budget and lever arm of the disks are key parameters in the optimisation of the endcap tracking systems. To maximise the performance in this region, the material seen by

charged particles traversing the disks must be minimised. The material budget of the endcap disks is determined by the results of dedicated R&D for the disk design, while the lever arm available to the endcap tracker is limited by the positioning of the PID systems. The material budget is hence minimised by using a design with fewer MAPS disks, with 5 disks determined to be the minimum number that can still provide the necessary angular coverage and redundancy.

A gold coating is applied to the interior of the beampipe to attenuate Synchrotron Radiation (SR) entering the central detector. The coating is not found to significantly impact the relative momentum resolution. However, the transverse pointing resolution sees a degradation at low p_t, most prevalently for $|\eta| > 2.5$. The pointing resolution requirement is still within reach with a thin coating applied, but to avoid an unacceptable degradation in the performance, the thickness of the coating should be kept below 10 µm, providing that the reduction in SR remains adequate.

The final pitch of the sensors that will be used in the MAPS layers for the EIC project detector is determined by the outcomes of the ALICE ITS3 development. The tracking resolutions are seen to deteriorate at large (transverse) momenta with a large pixel pitch. However, configurations that meet the requirements at low momenta will still meet the requirement at large momenta regardless of the pixel pitch. As such, a sensor based on the ITS3 technology is capable of delivering the required performance with a pixel pitch of ~ 20 µm.

AC-LGAD timing layers are an appealing technology for low momentum PID at the EIC, and have the added benefit that they may provide a high precision space-point measurement for use in track reconstruction. An AC-LGAD time-of-flight layer positioned at $r \sim 50$ cm, with a spatial resolution of 15 µm or 30 µm in $r\phi$ is found to provide a significant improvement in the momentum resolution at large momenta.

Studies for the tracking system in the reference detector, based on the design presented in the ECCE proposal, evolving to the current ePIC tracking system, showed once again that momentum resolution targets in the barrel region can be challenging with a magnetic field strength of 1.5 T. A reconfiguration of the barrel silicon layers allows the central momentum resolution requirements to be met, by positioning the third vertexing layer at a radius of $r \sim 12$ cm while maintaining the 0.05 % X_0 material budget of the first two layers, and by maximising the lever arm of the outermost MAPS barrel layer. The vertexing layers are also moved out to account for constraints placed by the sensor size, and to provide sufficient clearance for the innermost layer during beampipe bake-out. The larger radius of 36 mm for the first

vertexing layer does not significantly degrade the transverse pointing resolution with the second vertexing layer positioned at 48 mm.

In the realistic experimental environment of the EIC, the primary vertex at which particles are produced may deviate from the origin by up to $\sim 10\,\text{cm}$ in z. This is found to not impact the tracking resolutions, except at specific angles corresponding to the service cone material, where the increase in the average material traversed by charged particles degrades the average momentum resolution by a factor of ~ 1.25 for pions generated with $0 < p_t < 10\,\text{GeV}$.

Studies of the barrel region have assessed the role of the μRWELL layer and determined that it does not contribute to the momentum resolution, except in the case that both the barrel AC-LGAD and the outermost MAPS layer fail. This result indicates that the primary function of this layer is for pattern recognition.

Studies of the angular acceptance of the disk region have shown that a realistic disk implementation may provide partial tracking acceptance up to $|\eta| \sim 3.6$. The angular acceptance of the range $3.2 \lesssim |\eta| \lesssim 3.4$ deviates from 100 % when the disks have $< 100\,\%$ efficiency, as there are only three MAPS disks in the path of particles produced with this pseudorapidity. This impacts the low Q^2 acceptance, with a corresponding drop appearing for $Q^2 \lesssim 3\,\text{GeV}^2$. Nevertheless, coverage is provided down to $Q^2 \sim 1\,\text{GeV}^2$, which is sufficient for many inclusive DIS measurements.

Studies of the expected beam related backgrounds for the tracking detector have shown that both the fluence and total ionising dose remain within tolerable levels for the SVT, based on a worst case estimate in which the collider runs for 6 months per year, for 10 years, at top luminosity. The hit occupancy of the MAPS layers is found to be dominated by the beam related backgrounds, but remains manageable for the sensor and readout electronics.

The current ePIC tracking design is found to give relative momentum and transverse pointing resolutions that are consistent with, or within reach of, the Yellow Report requirements for much of the η and p range. In the regions where the requirements are not met, notably $-3.5 < \eta < -2.5$, tracking measurements can be supplemented with measurements from the calorimetry systems such that the physics can still be achieved.

7.2 Kinematic Reconstruction

The kinematic variable precision achieveable at the EIC has been assessed in terms of the resolutions of the reconstructed values of the kinematic variables x, y, and Q^2, using full simulations in the ePIC software framework. Pythia6 is used to generate $18 \times 275\,\mathrm{GeV}^2$ ep collisions, the highest centre-of-mass energy considered for the EIC, which are passed through the simulated ePIC geometry and reconstructed using the ePIC software. The scattered electron and the HFS are reconstructed using tracking information for all charged particles (including the DIS electron) and calorimetry for neutrals. The kinematic variables are reconstructed using the energies and polar angles of the scattered electron and HFS, in a manner corresponding to five different reconstruction methods: The electron method, the JB method, the Double Angle method, and the Σ and $e-\Sigma$ methods.

The kinematic resolutions have been compared for the reconstructed kinematic variables using each method, and the optimal method identified across the $x-Q^2$ plane. The kinematic variable y is found to be best reconstructed by the electron method at large-y, the $e-\Sigma$ method at low-y and low-Q^2, and the DA method at low-y and large-Q^2. If the y resolution, defined as the RMS of the $y_{reco} - y_{true}/y_{true}$ distribution, is considered, the JB method may appear to provide the best reconstruction for much of the low y region. However, the JB method often exhibits significant bias, and a significantly worse Q^2 resolution across the phase space. The JB method is thus the least effective method for reconstructing the kinematics with high precision, and is therefore reserved for Charged-Current DIS events, where it is the only option.

A sample binning scheme has been evaluated, with four logarithmically spaced bins in x and Q^2 per decade, for reconstruction using the electron, Double Angle, and $e-\Sigma$ methods. If the most appropriate reconstruction method for a given bin is chosen, a purity and stability of 30 % or more is possible for each bin in the range $0.01 < y < 0.95$ and $Q^2 > 1\,\mathrm{GeV}^2$. Such values were often deemed acceptable for analyses at HERA, with this also expected to be the case at the EIC.

7.3 Kinematic Fitting

A method for the reconstruction of the kinematic variables x, y, and Q^2, based on a kinematic fit with a Bayesian prior, is presented and compared to conventional reconstruction methods. The method leverages an over-constraint from the measured quantities to extract, in addition to the DIS kinematic variables, the energy of a possible ISR photon.

The method is validated using an approach whereby DIS events are generated, and the detector response mimicked by smearing the true quantities that would be measured by the detector (the electron and HFS energies and polar angles) by estimates of the resolution of an EIC detector in a Gaussian approximation. The smearing quantities are used to construct a likelihood function that perfectly describes the "reconstructed" data. For a generator sample that does not include QED ISR/FSR, the resolution with which y and Q^2 are reconstructed by the kinematic fit matches or exceeds the resolution with the conventional methods throughout the phase space.

A sample that includes QED ISR/FSR is also considered. Initially, a cut of $\Sigma_{tot} > 31\,\text{GeV}$ is applied to reduce the amount of high energy ISR, as would be done in a typical DIS analysis. The kinematic resolutions are not found to significantly change between the ISR-free sample and the sample that includes ISR with the Σ_{tot} cut applied, for any of the considered conventional methods or the kinematic fit.

The ability of the KF method to reconstruct ISR has also been studied with the Σ_{tot} cut removed. It is found that the ratio of the number of events predicted by the kinematic fit for a given E_γ bin, and the true number generated in the bin, is close to unity for high energy E_γ bins. The ratio lies in the range $0.7 - 1.3$ for all bins with $E_\gamma > 3\,\text{GeV}$, and so it is concluded that the KF method reconstructs ISR efficiently in this range. The ratio decreases for $E_\gamma < 3\,\text{GeV}$, as the detector resolutions that make-up the likelihood function are not good enough to overcome the Bayesian prior that pulls the E_γ prediction towards 0.

The kinematic fit was also applied to events not containing ISR, that were passed through the ePIC geometry and reconstructed using the ePIC software. The likelihood function was set according to single particle resolution studies of the tracker for the scattered electron, and a simple resolution study of the HFS for fully simulated DIS events. The y resolution obtained using the KF method, which gave the best performance at all y for the smearing based reconstruction, matches the performance of the electron method at high y (the best method in this range), but is beaten at low y by the Double Angle method.

A hypothesis that the superior performance of the DA method compared to the kinematic fit at low y arises from the correlation of the two HFS variables is considered. A quantity expressing the correlation is introduced to the likelihood function. With the inclusion of the correlation, the excellent performance of the KF method is recovered. It can therefore be concluded that it is necessary to include correlations

if the optimal resolution is to be obtained, and that further investigations into the correlations and the parametrisation of the HFS variables may further improve the resolution.

Studies are perfomed in which the kinematic fit is applied to a sample of H1 MC and data, to evaluate the performance in particular for ISR events. Pull distributions are produced that confirm the behaviour of the kinematic fit to be consistent between data and MC. The distribution of ISR energies predicted by the kinematic fit is compared to a prediction using the Σ_{tot} constraint, as is done implicitly in the Σ methods. The number of events at low E_γ is increasingly overestimated as E_γ approaches 0 for the prediction based on the Σ_{tot} constraint. Conversely, the prediction by the kinematic fit underestimates the number of events at low E_γ. The behaviour of the KF prediction is attributed to the Bayesian prior, which peaks at $E_\gamma \sim 0$. Where a detector resolution effect leads to a deviation of Σ_{tot} from $2E_0$, the prior pulls the E_γ prediction to 0. The result is that the KF method reproduces the E_γ distribution for a larger energy range than the Σ_{tot} constraint. This gives the possibility that the KF method could be used in studies with a reduced electron beam energy, enabling possible cross section measurements in an extended Q^2 range, and a subsequent F_2 extraction and potentially also F_L.

Chapter 8

Future Work

A major topic of this thesis has been the layout dependence of the tracking resolutions. While changes to the details of the geometry remain possible, the main features of the ePIC tracking detector are expected to remain the same. The main focus of future simulation studies will be increasing the realism of the detector geometry implemented in simulations. Work has progressed on the design of the silicon outer barrel layers, with concepts that include the placement of sensors, and structures for support, powering, and cooling. In a "realistic" design such as this, passive material is introduced at specific positions along the staves, which may result in performance degradation at certain values of η and ϕ. A realistic material budget for these layers may significantly impact the momentum resolution, as the material estimates used in the current design (0.25 % and 0.55 % X_0 in L3 and L4 respectively) are approximations, and are averaged across the entire length of the barrel layers in the simulations. Deviations from these approximate values are inevitable, and it is a distinct possibility that the L3 material budget estimate may not be reached, while the L4 material budget estimate may be improved upon. Additionally, depending on the stave design, the radial positions at which the layers are placed is also likely to change. Such changes are important to include in simulations, as the impact on the tracking performance could be significant.

Realism of the detector simulation is also needed for physics studies, where an accurate description of the detector acceptance is crucial. Studies in this thesis investigated the acceptance around the inner openings of the MAPS disks, where regions of partial acceptance are present due to the offset of the beampipe and the tiling of sensors on the disks. The implementation of "realistic" disks within the ePIC software framework, such that the large η acceptance is properly modelled in physics studies, is a necessary step for the development of the framework.

The development of track and vertex reconstruction algorithms within the ePIC software framework is also key, as the current implementation is only suitable for use with single particle events. The future work in this area may consist of: tuning of the parameters used by the seed finder to search for valid seeds; disambiguation of duplicate seeds; seed reconstruction performance in full DIS events and the inclusion of beam related backgrounds; and the development of vertexing algorithms for the identification of primary and secondary vertices. With each of these developments, there are tracking resolution or physics performance studies that may be useful, such as the resolutions of the inclusive DIS variables with fully realistic track reconstruction and PID, or heavy flavour reconstruction based on vertexing information.

Developments of the ePIC software framework are also needed for the optimal combination of tracker and calorimeter information. An initial goal of studies of this kind may be the matching of tracks to calorimeter clusters. Progress in this area may allow for the development of an electron finding algorithm, which can be evaluated in terms of its efficiency, and also the optimisation of the scattered electron resolution by considering the performance offered by the tracking and calorimetry subsystems in combination across the detector acceptance. Additionally, the development of a full particle flow algorithm is needed for the reconstruction of the overall hadronic final state four-vector.

A fully realistic detector simulation and reconstruction, starting from the generation of minimum bias DIS events with QED effects, as well as beam-related and physics backgrounds, is also synergistic with the needs of the DIS group for the EIC, which targets fully simulated measurements of F_2, F_L, and spin-sensitive asymmetries.

Further improvements to the reconstruction of the inclusive DIS kinematics using the KF method are also forseen, in the form of a detailed treatment of the correlations between the electron quantities as well as the HFS quantities, and resolution studies that may be used to improve the description of the HFS in the likelihood function. Physics studies will then be possible that leverage the identification of ISR using the KF method in order to extend the kinematic reach of a given detector, with both ePIC and H1 being considered. A determination of the reduced cross section for low Q^2 events, containing high energy ISR photons identified using the KF method, may allow the extraction of the F_2 structure function in a challenging region of the kinematic plane, as well as F_L from the centre-of-mass variation of events containing high energy ISR.

Appendices

Appendix A

Kinematic Resolutions Supporting Plots

This appendix contains summaries of the distributions comparing the different conventional methods for kinematic reconstruction that were introduced in Section 5.3. The methods are compared in terms of their respective $\Delta x/x$, $\Delta y/y$, and $\Delta Q^2/Q^2$ distributions, for three Q^2 intervals: $1 < Q^2 < 10\,\mathrm{GeV}^2$, $10 < Q^2 < 100\,\mathrm{GeV}^2$, and $100 < Q^2 < 1000\,\mathrm{GeV}^2$. Note that Fig. A.2 also appears in the main text of this thesis as Fig. 5.2.

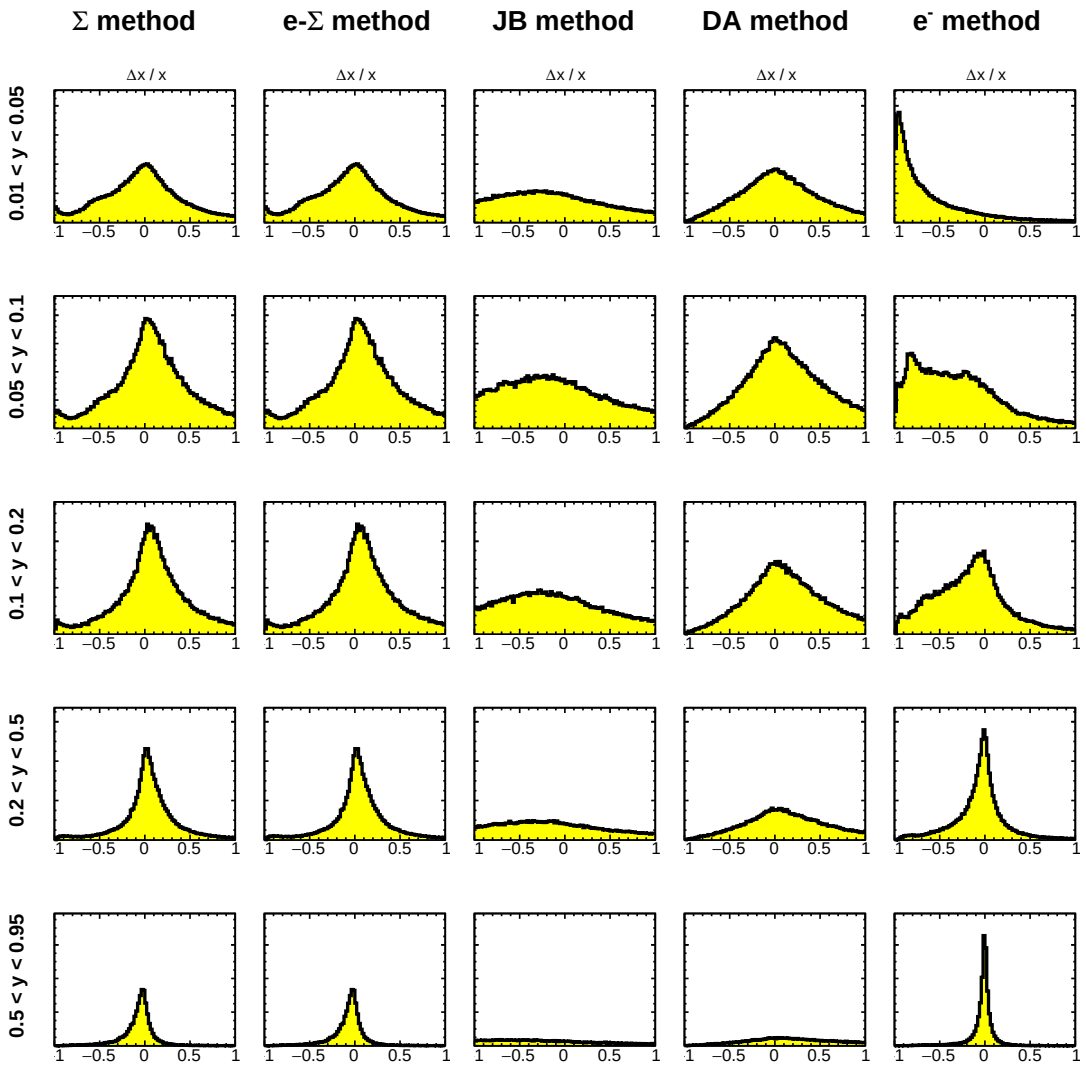

Figure A.1: Distributions of $\Delta x/x = (x_{reco} - x_{true})/x_{true}$ for different ranges in y_{true}, when reconstructed using several reconstruction methods. The Q^2 range is $1 < Q^2 < 10\,\mathrm{GeV}^2$ and the beam configuration is $18 \times 275\,\mathrm{GeV}^2$ e^- on p.

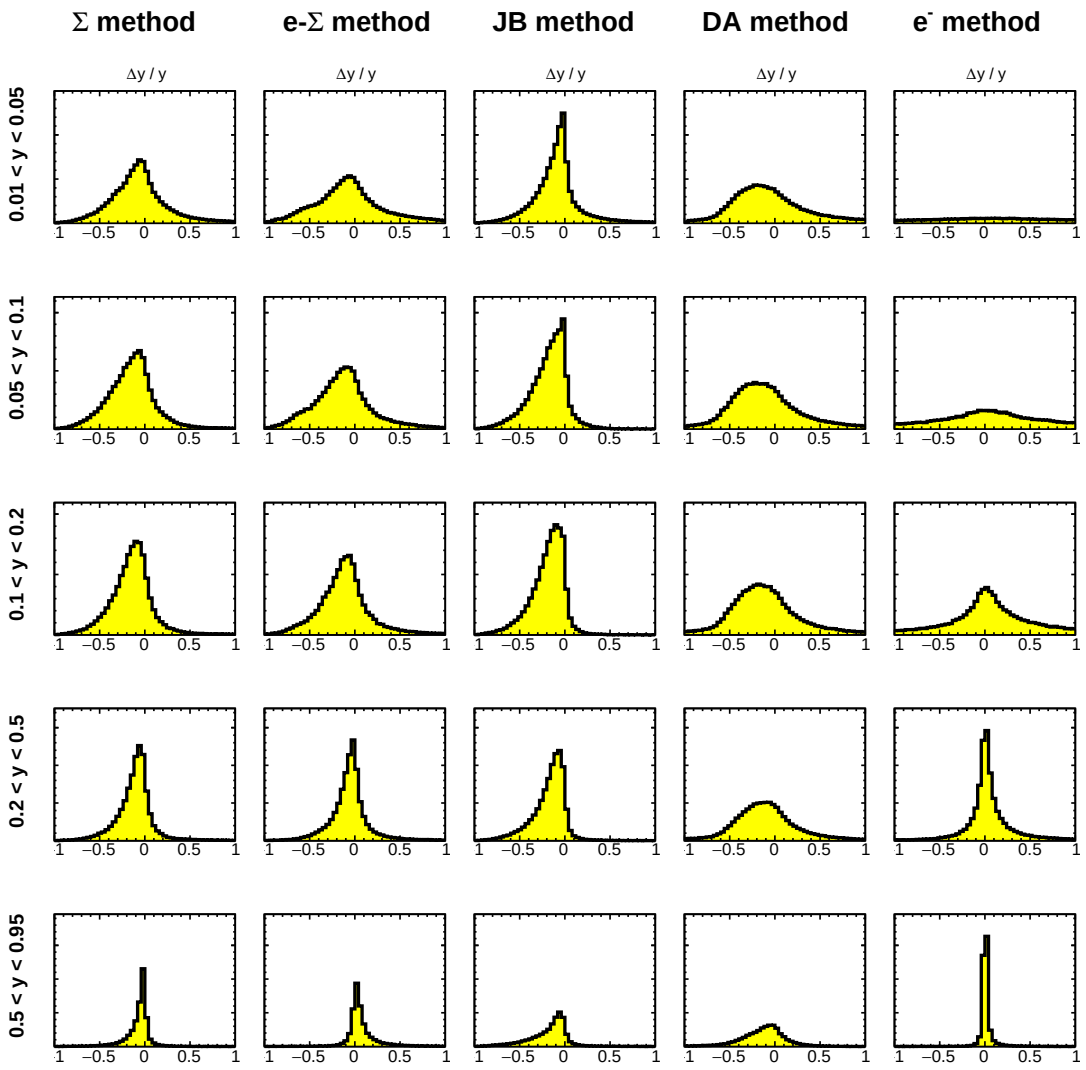

Figure A.2: Distributions of $\Delta y/y = (y_{reco} - y_{true})/y_{true}$ for different ranges in y_{true}, when reconstructed using several reconstruction methods. The Q^2 range is $1 < Q^2 < 10\,\mathrm{GeV}^2$ and the beam configuration is $18 \times 275\,\mathrm{GeV}^2$ e^- on p. This figure also appears in the main text as Fig. 5.2.

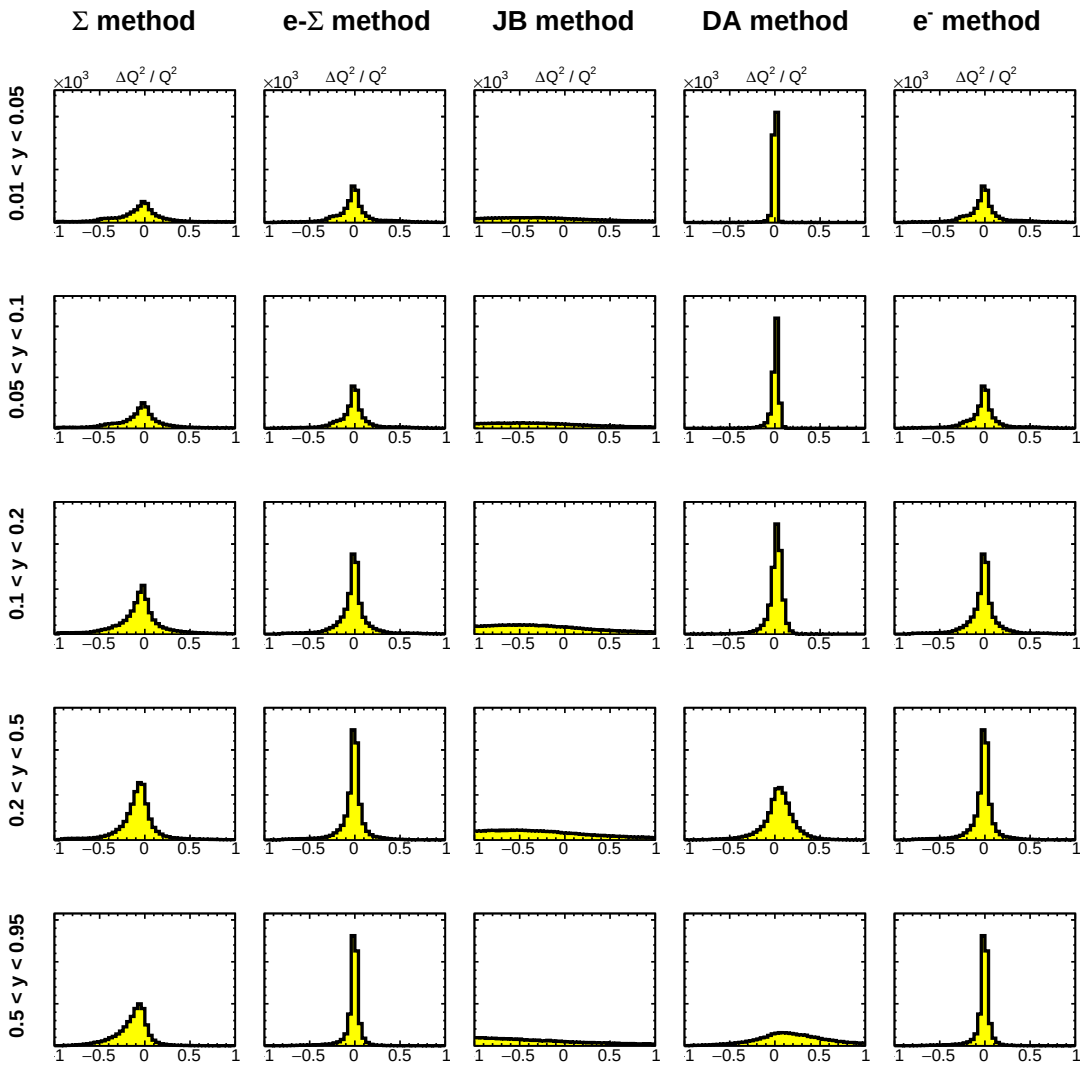

Figure A.3: Distributions of $\Delta Q^2/Q^2 = (Q^2_{reco} - Q^2_{true})/Q^2_{true}$ for different ranges in y_{true}, when reconstructed using several reconstruction methods. The Q^2 range is $1 < Q^2 < 10\,\mathrm{GeV}^2$ and the beam configuration is $18 \times 275\,\mathrm{GeV}^2$ e^- on p.

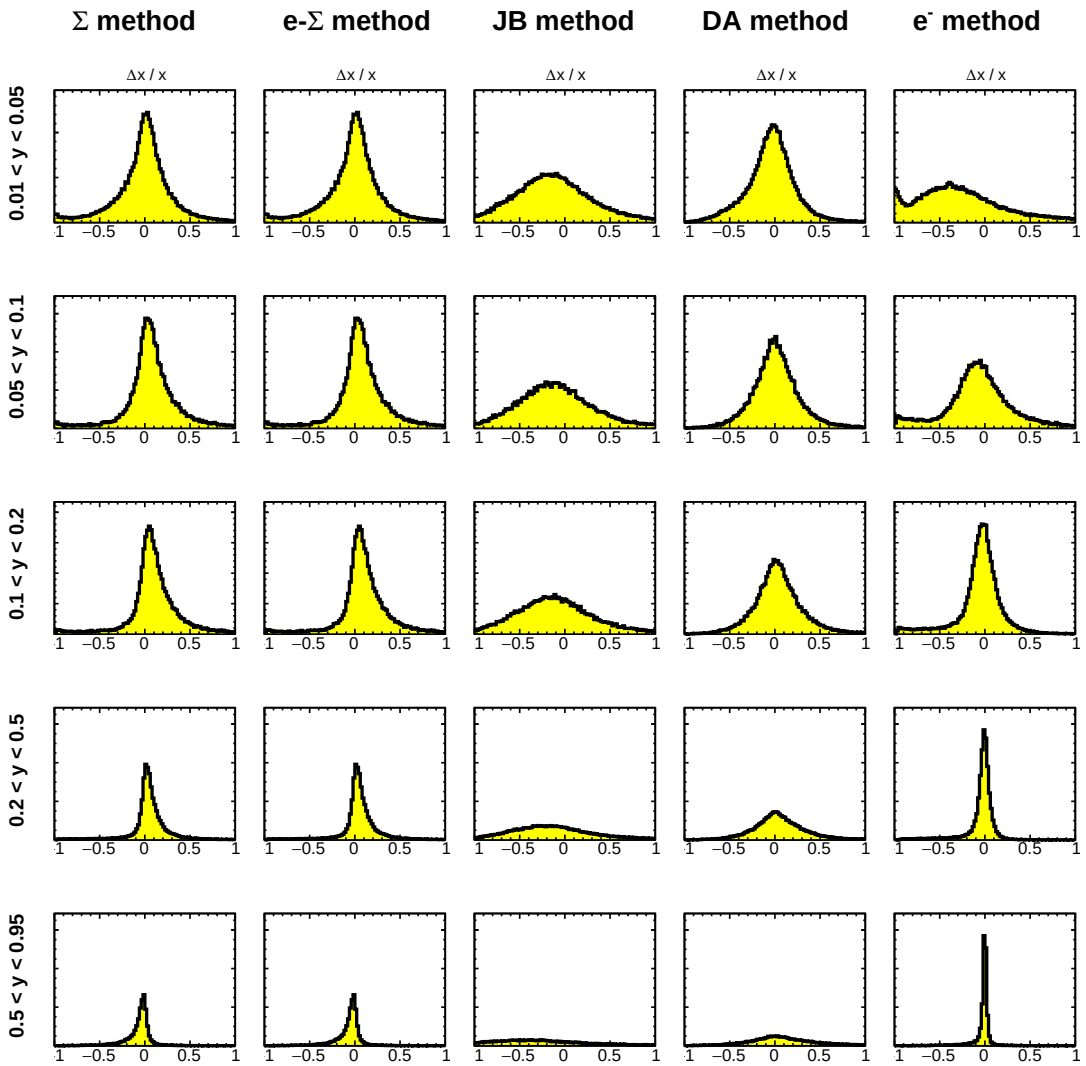

Figure A.4: Distributions of $\Delta x/x = (x_{reco} - x_{true})/x_{true}$ for different ranges in y_{true}, when reconstructed using several reconstruction methods. The Q^2 range is $10 < Q^2 < 100\,\mathrm{GeV}^2$ and the beam configuration is $18 \times 275\,\mathrm{GeV}^2$ e^- on p.

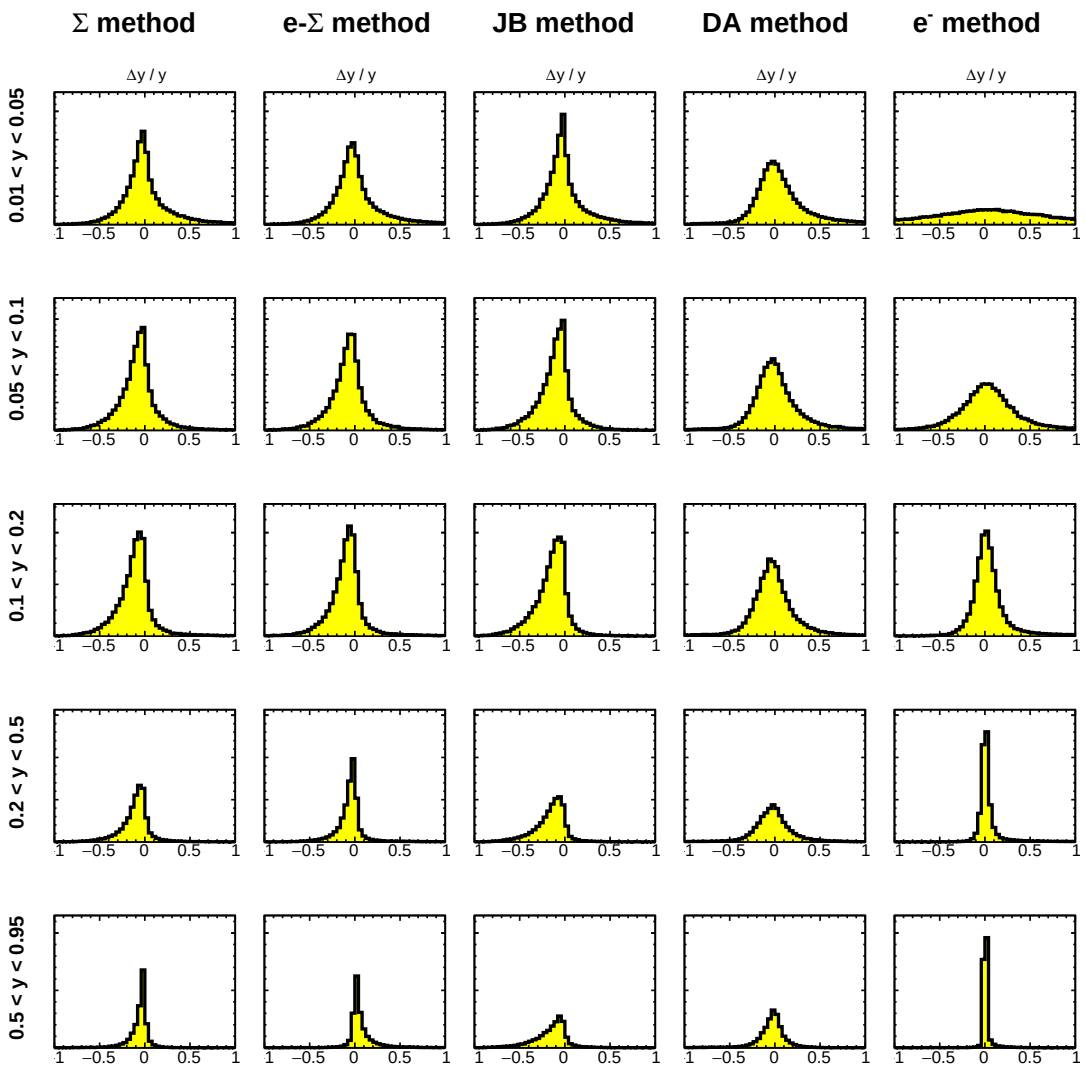

Figure A.5: Distributions of $\Delta y/y = (y_{reco} - y_{true})/y_{true}$ for different ranges in y_{true}, when reconstructed using several reconstruction methods. The Q^2 range is $10 < Q^2 < 100\,\mathrm{GeV}^2$ and the beam configuration is $18 \times 275\,\mathrm{GeV}^2$ e^- on p.

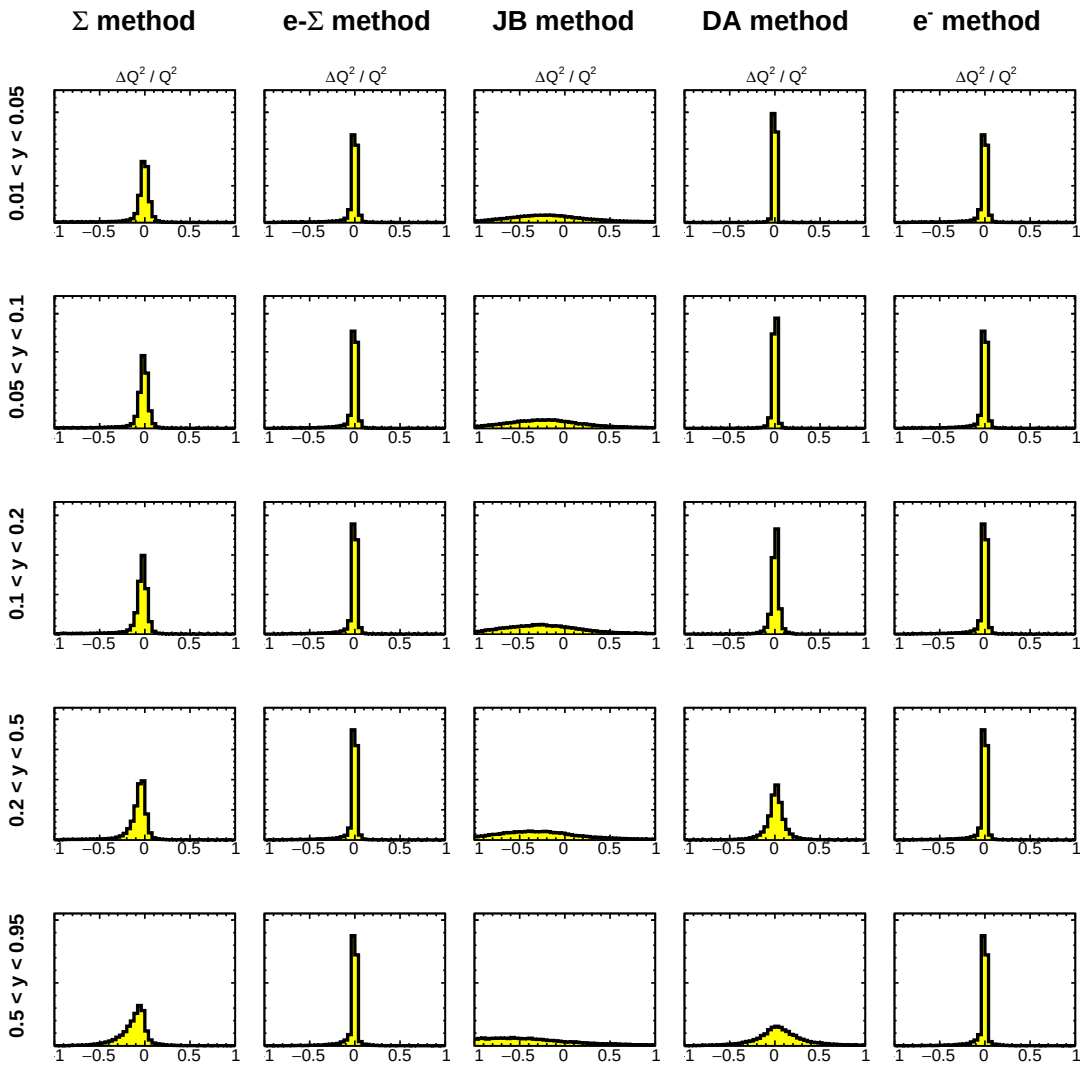

Figure A.6: Distributions of $\Delta Q^2/Q^2 = (Q^2_{reco} - Q^2_{true})/Q^2_{true}$ for different ranges in y_{true}, when reconstructed using several reconstruction methods. The Q^2 range is $10 < Q^2 < 100\,\mathrm{GeV}^2$ and the beam configuration is $18 \times 275\,\mathrm{GeV}^2$ e^- on p.

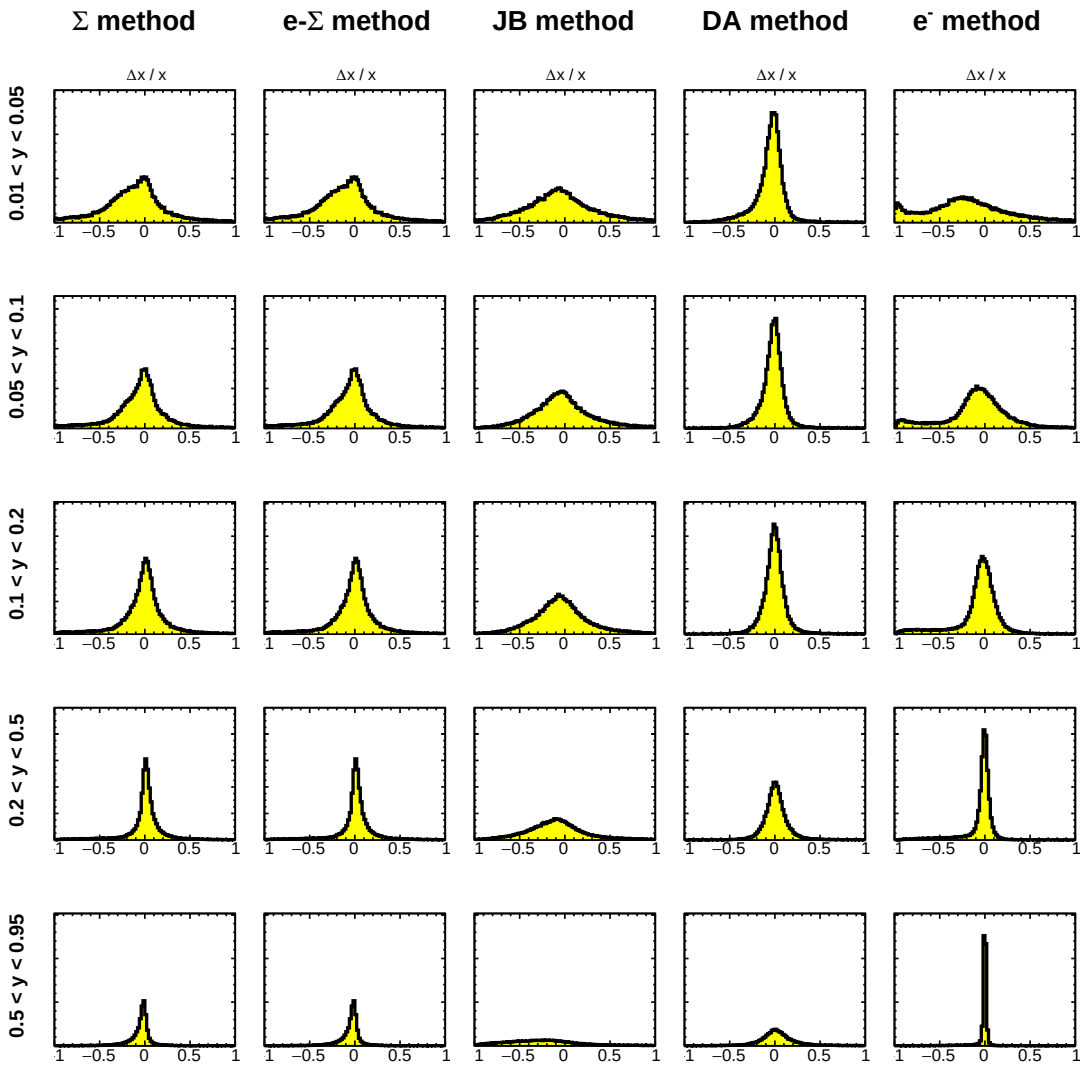

Figure A.7: Distributions of $\Delta x/x = (x_{reco} - x_{true})/x_{true}$ for different ranges in y_{true}, when reconstructed using several reconstruction methods. The Q^2 range is $100 < Q^2 < 1000\,\mathrm{GeV}^2$ and the beam configuration is $18 \times 275\,\mathrm{GeV}^2$ e^- on p.

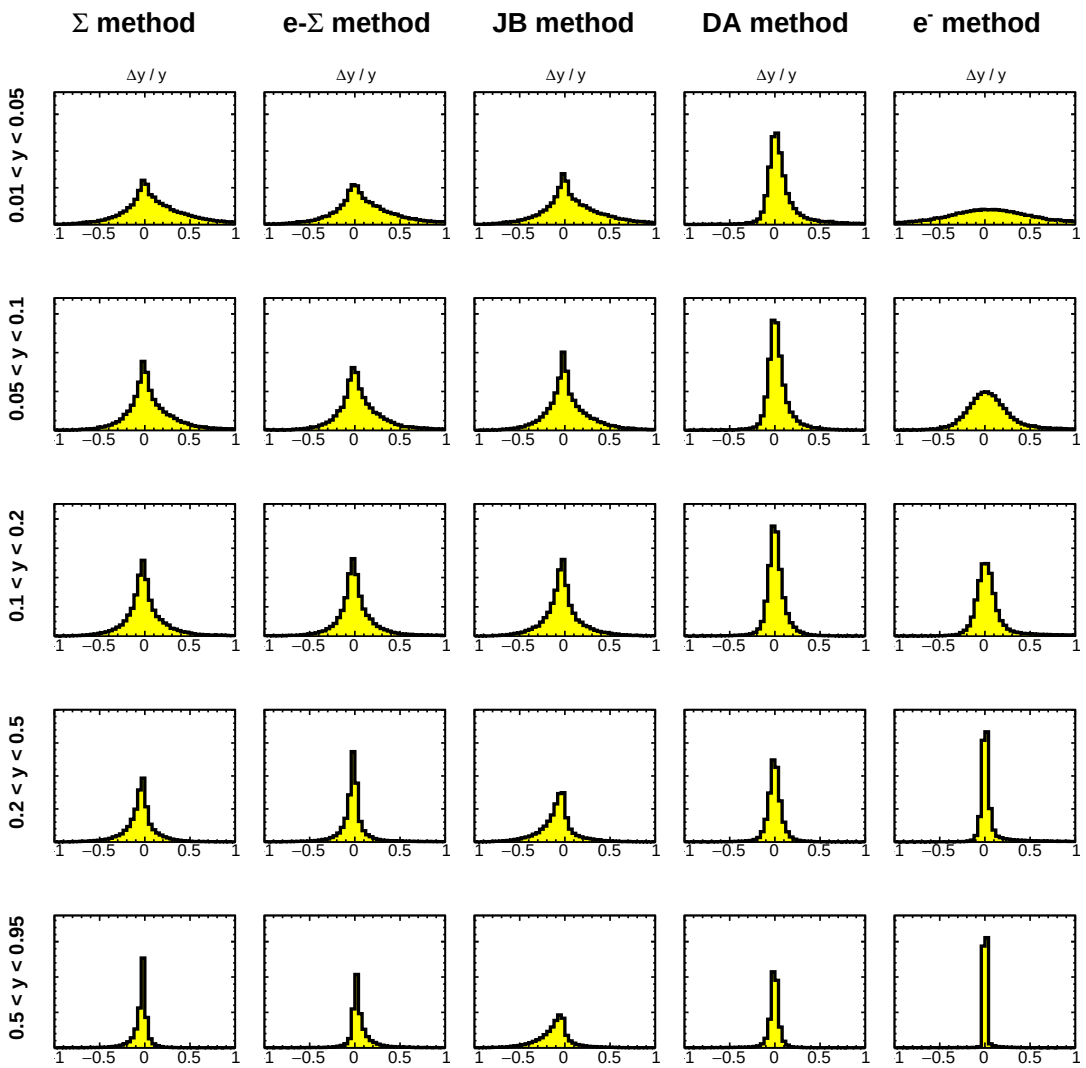

Figure A.8: Distributions of $\Delta y/y = (y_{reco} - y_{true})/y_{true}$ for different ranges in y_{true}, when reconstructed using several reconstruction methods. The Q^2 range is $100 < Q^2 < 1000\,\mathrm{GeV}^2$ and the beam configuration is $18 \times 275\,\mathrm{GeV}^2$ e^- on p.

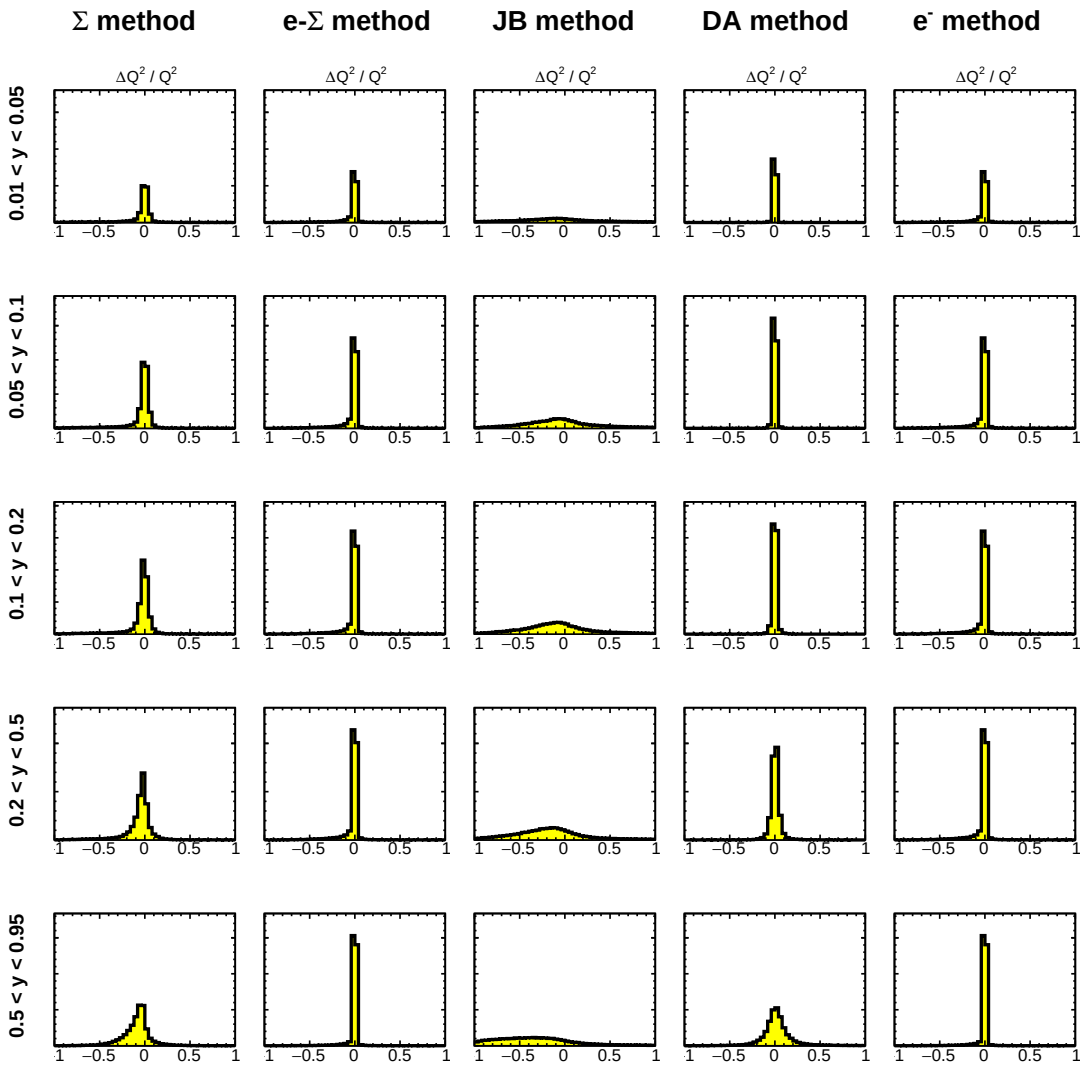

Figure A.9: Distributions of $\Delta Q^2/Q^2 = (Q^2_{reco} - Q^2_{true})/Q^2_{true}$ for different ranges in y_{true}, when reconstructed using several reconstruction methods. The Q^2 range is $100 < Q^2 < 1000\,\mathrm{GeV}^2$ and the beam configuration is $18 \times 275\,\mathrm{GeV}^2$ e^- on p.

Bibliography

[1] E. Rutherford, "The scattering of alpha and beta particles by matter and the structure of the atom," *Phil. Mag. Ser. 6*, vol. 21, pp. 669–688, 1911.

[2] R. W. McAllister and R. Hofstadter, "Elastic scattering of 188-mev electrons from the proton and the alpha particle," *Phys. Rev.*, vol. 102, pp. 851–856, May 1956. [Online]. Available: https://link.aps.org/doi/10.1103/PhysRev.102.851

[3] E. D. Bloom *et al.*, "High-Energy Inelastic e p Scattering at 6-Degrees and 10-Degrees," *Phys. Rev. Lett.*, vol. 23, pp. 930–934, 1969.

[4] J. D. Bjorken, "CURRENT ALGEBRA AT SMALL DISTANCES," *Conf. Proc. C*, vol. 670717, pp. 55–81, 1967.

[5] C. G. Callan, Jr. and D. J. Gross, "High-energy electroproduction and the constitution of the electric current," *Phys. Rev. Lett.*, vol. 22, pp. 156–159, 1969.

[6] S. Kullander, "Highlights of the European Muon Collaboration," *Nucl. Phys. A*, vol. 518, pp. 262–296, 1990.

[7] NuTeV Collaboration and J. Yu et. al, "Strange sea and alpha-s measurements from nu-n deep inelastic scattering at ccfr/nutev," 1998.

[8] J. Ashman *et al.*, "A Measurement of the Spin Asymmetry and Determination of the Structure Function g(1) in Deep Inelastic Muon-Proton Scattering," *Phys. Lett. B*, vol. 206, p. 364, 1988.

[9] A. Accardi *et al.*, "Electron Ion Collider: The Next QCD Frontier: Understanding the glue that binds us all," *Eur. Phys. J. A*, vol. 52, no. 9, p. 268, 2016.

[10] R. Abdul Khalek *et al.*, "Science Requirements and Detector Concepts for the Electron-Ion Collider: EIC Yellow Report," *Nucl. Phys. A*, vol. 1026, p. 122447, 2022.

[11] F. Willeke, "Electron Ion Collider Conceptual Design Report 2021," 2 2021.

[12] F. Halzen and A. Martin, *Quarks & Leptons: An Introductory Course in Modern Particle Physics*, ser. Wiley student edition. Wiley India Pvt. Limited, 2008. [Online]. Available: https://books.google.co.uk/books?id=ITQy9G62H0gC

[13] J. Thomson, *The Corpuscular Theory of Matter*, ser. Marilee E. Thomas and Robert C. Thomas Science and Related Subjects Collection. Scribner's Sons, 1907.

[14] N. F. Mott, "The polarisation of electrons by double scattering," *Proceedings of the Royal Society of London. Series A, Containing Papers of a Mathematical and Physical Character*, vol. 135, no. 827, pp. 429–458, 1932. [Online]. Available: http://www.jstor.org/stable/95868

[15] M. N. Rosenbluth, "High energy elastic scattering of electrons on protons," *Phys. Rev.*, vol. 79, pp. 615–619, Aug 1950. [Online]. Available: https://link.aps.org/doi/10.1103/PhysRev.79.615

[16] K. S. Krane, *Introductory nuclear physics*. New York, NY: Wiley, 1988. [Online]. Available: https://cds.cern.ch/record/359790

[17] W. Xiong *et al.*, "A small proton charge radius from an electron–proton scattering experiment," *Nature*, vol. 575, no. 7781, pp. 147–150, 2019.

[18] R. Devenish and A. Cooper-Sarkar, *Deep Inelastic Scattering*. Oxford University Press, 2004. [Online]. Available: https://books.google.co.uk/books?id=LsSumroE7nsC

[19] R. L. Workman and Others, "Review of Particle Physics," *PTEP*, vol. 2022, p. 083C01, 2022.

[20] K. Prytz, "Approximate determination of the gluon density at low-x from the f2 scaling violations," *Physics Letters B*, vol. 311, no. 1, pp. 286–290, 1993. [Online]. Available: https://www.sciencedirect.com/science/article/pii/0370269393905708

[21] G. Altarelli and G. Parisi, "Asymptotic Freedom in Parton Language," *Nucl. Phys. B*, vol. 126, pp. 298–318, 1977.

[22] C. Adloff *et al.*, "On the rise of the proton structure function F(2) towards low x," *Phys. Lett. B*, vol. 520, pp. 183–190, 2001.

[23] A. De Rújula, S. L. Glashow, H. D. Politzer, S. B. Treiman, F. Wilczek, and A. Zee, "Possible non-regge behavior of electroproduction structure functions," *Phys. Rev. D*, vol. 10, pp. 1649–1652, Sep 1974. [Online]. Available: https://link.aps.org/doi/10.1103/PhysRevD.10.1649

[24] A. Dubak, "Measurement of the e^+p Neutral Current DIS Cross Section and the F_2, F_L, xF_3 Structure Functions in the H1 Experiment at HERA," Other thesis, 4 2003.

[25] T. Carli, A. Cooper-Sarkar, J. Feltesse, A. Glazov, C. Gwenlan, M. Klein, T. Lastoviicka, G. Lastoviicka-Medin, S. Moch, B. Reisert, G. P. Salam, and F. Siegert, "Experimental determination of parton distributions," 2005. [Online]. Available: https://cds.cern.ch/record/941457

[26] F. D. Aaron *et al.*, "Inclusive Deep Inelastic Scattering at High Q^2 with Longitudinally Polarised Lepton Beams at HERA," *JHEP*, vol. 09, p. 061, 2012.

[27] S. Bailey, T. Cridge, L. A. Harland-Lang, A. D. Martin, and R. S. Thorne, "Parton distributions from LHC, HERA, Tevatron and fixed target data: MSHT20 PDFs," *Eur. Phys. J. C*, vol. 81, no. 4, p. 341, 2021.

[28] R. Windmolders, "Review of recent results in spin physics," *Nucl. Phys. B, Proc. Suppl.*, vol. 79, pp. 51–64, 1999. [Online]. Available: http://cds.cern.ch/record/388591

[29] I. Borsa, G. Lucero, R. Sassot, E. C. Aschenauer, and A. S. Nunes, "Revisiting helicity parton distributions at a future electron-ion collider," *Phys. Rev. D*, vol. 102, no. 9, p. 094018, 2020.

[30] A. Martin and M. Ryskin, "Higher twists in deep inelastic scattering," *Physics Letters B*, vol. 431, no. 3, pp. 395–404, 1998. [Online]. Available: https://www.sciencedirect.com/science/article/pii/S0370269398005711

[31] A. Guskov, "Drell-Yan measurements with COMPASS," Tech. Rep., 2011. [Online]. Available: https://cds.cern.ch/record/1494176

[32] M. Alekseev *et al.*, "Collins and Sivers asymmetries for pions and kaons in muon-deuteron DIS," *Phys. Lett. B*, vol. 673, pp. 127–135, 2009.

[33] M. Aghasyan *et al.*, "First measurement of transverse-spin-dependent azimuthal asymmetries in the Drell-Yan process," *Phys. Rev. Lett.*, vol. 119, no. 11, p. 112002, 2017.

[34] A. Airapetian *et al.*, "Single-spin asymmetries in semi-inclusive deep-inelastic scattering on a transversely polarized hydrogen target," *Phys. Rev. Lett.*, vol. 94, p. 012002, 2005.

[35] E. C. Aschenauer, I. Borsa, R. Sassot, and C. Van Hulse, "Semi-inclusive Deep-Inelastic Scattering, Parton Distributions and Fragmentation Functions at a Future Electron-Ion Collider," *Phys. Rev. D*, vol. 99, no. 9, p. 094004, 2019.

[36] G. Xie, W. Kou, Q. Fu, Z. Ye, and X. Chen, "Deeply virtual compton scattering at future electron-ion colliders," *Eur. Phys. J. C*, vol. 83, no. 10, p. 900, 2023.

[37] A. C. Aguilar *et al.*, "Pion and Kaon Structure at the Electron-Ion Collider," *Eur. Phys. J. A*, vol. 55, no. 10, p. 190, 2019.

[38] J. Wagner, "Timelike compton scattering," Slides presented at the 1st EIC Yellow Report Workshop at Temple University, March 2020. [Online]. Available: https://indico.bnl.gov/event/7449/contributions/35847/attachments/27234/41518/Wagner_Temple2020.pdf

[39] M. Lomnitz and S. Klein, "Exclusive vector meson production at an electron-ion collider," *Phys. Rev. C*, vol. 99, no. 1, p. 015203, 2019.

[40] A. Bylinkin *et al.*, "Detector requirements and simulation results for the EIC exclusive, diffractive and tagging physics program using the ECCE detector concept," *Nucl. Instrum. Meth. A*, vol. 1052, p. 168238, 2023.

[41] M. Diehl, "Imaging partons in exclusive scattering processes," in *20th International Workshop on Deep-Inelastic Scattering and Related Subjects*, 2012, pp. 307–310.

[42] U. Amaldi *et al.*, "Report from the study group on detectors for charged current events," in *ECFA Study of an ep Facility for Europe*, 1979, pp. 377–414.

[43] U. Bassler and G. Bernardi, "On the kinematic reconstruction of deep inelastic scattering at HERA: The Sigma method," *Nucl. Instrum. Meth. A*, vol. 361, pp. 197–208, 1995.

[44] S. Bentvelsen, J. Engelen, and P. Kooijman, "Reconstruction of (x, Q**2) and extraction of structure functions in neutral current scattering at HERA," in *Workshop on Physics at HERA*, 1 1992.

[45] J. Breitweg *et al.*, "Measurement of high Q^2 neutral current e^+p deep inelastic scattering cross-sections at HERA," *Eur. Phys. J. C*, vol. 11, pp. 427–445, 1999.

[46] C. Schwanenberger, "The jet calibration in the h1 liquid argon calorimeter," in *Calorimetry in Particle Physics*. World Scientific, Jan. 2003. [Online]. Available: http://dx.doi.org/10.1142/9789812704894_0095

[47] K. Piotrzkowski, "Challenging luminosity measurements at the Electron-Ion Collider," *JINST*, vol. 16, no. 09, p. P09023, 2021.

[48] E. Aschenauer *et al.*, "Electron-ion collider detector requirements and r&d handbook," 2020, version 1.2, February 25.

[49] V. Fadin, "Phys. lett. b60 1975 50; ea kuraev, ln lipatov and vs fadin," *Sov. Phys. JETP*, vol. 44, p. 45, 1976.

[50] I. Balitsky, "Operator expansion for high-energy scattering," *Nucl. Phys. B*, vol. 463, pp. 99–160, 1996.

[51] J. Jalilian-Marian, A. Kovner, A. Leonidov, and H. Weigert, "The BFKL equation from the Wilson renormalization group," *Nucl. Phys. B*, vol. 504, pp. 415–431, 1997.

[52] F. Gelis, E. Iancu, J. Jalilian-Marian, and R. Venugopalan, "The Color Glass Condensate," *Ann. Rev. Nucl. Part. Sci.*, vol. 60, pp. 463–489, 2010.

[53] I. Redondo, "Open charm production at HERA," *J. Phys. G*, vol. 28, pp. 939–952, 2002.

[54] M. Arratia, Y. Furletova, T. J. Hobbs, F. Olness, and S. J. Sekula, "Charm jets as a probe for strangeness at the future Electron-Ion Collider," *Phys. Rev. D*, vol. 103, no. 7, p. 074023, 2021.

[55] C.-P. Wong, X. Li, M. Brooks, M. J. Durham, M. X. Liu, A. Morreale, C. da Silva, and W. E. Sondheim. (2020, Sep) A Proposed Forward Silicon Tracker for the Future Electron-Ion Collider and Associated Physics Studies.

[56] T. Ullrich, "Summary of studies and challenges for vmp in e+a collisions at eic," Slides presented at the 1st EIC Yellow Report Workshop at Temple University, March 2020. [Online]. Available: https://wiki.bnl.gov/eicug/images/6/67/Xvmp_ullrich_mar19_2020.pdf

[57] T. Toll and T. Ullrich, "Exclusive diffractive processes in electron-ion collisions," *Phys. Rev. C*, vol. 87, no. 2, p. 024913, 2013.

[58] J. Repond, "Eic detectors: An overview," Slides presented at the 13th International Workshop on High-pT Physics in the RHIC/LHC era, March 2019.

[59] G. Wei, V. Morozov, F. Lin, F. Pilat, Y. Zhang, Y. Nosochkov, and M.-H. Wang, "Integration of the full-acceptance detector into jleic," in *Proceedings of the 8th International Particle Accelerator Conference (IPAC 2017)*. Copenhagen, Denmark: SLAC National Accelerator Laboratory, May 2017, sLAC–PUB–17388.

[60] A. Adare *et al.*, "Concept for an Electron Ion Collider (EIC) detector built around the BaBar solenoid," Feb 2014.

[61] J. Adam *et al.*, "ATHENA detector proposal — a totally hermetic electron nucleus apparatus proposed for IP6 at the Electron-Ion Collider," *JINST*, vol. 17, no. 10, p. P10019, 2022.

[62] J. K. Adkins *et al.*, "Design of the ECCE Detector for the Electron Ion Collider," Sep 2022.

[63] R. Alarcon *et al.*, "CORE – a COmpact detectoR for the EIC," Sep 2022.

[64] Electron-Proton/Ion Collider Experiment, "Main page — electron-proton/ion collider experiment," 2024, [Accessed 23-June-2024]. [Online]. Available: https://wiki.bnl.gov/EPIC/index.php?title=Main_Page&oldid=1961

[65] H. Bethe and W. Heitler, "On the Stopping of fast particles and on the creation of positive electrons," *Proc. Roy. Soc. Lond. A*, vol. 146, pp. 83–112, 1934.

[66] T. Sjostrand, S. Mrenna, and P. Z. Skands, "PYTHIA 6.4 Physics and Manual," *JHEP*, vol. 05, p. 026, 2006.

[67] M. Zurek, "Barrel imaging calorimeter at eic," Slides presented at the January 2024 ePIC Collaboration Meeting, Jan 2024. [Online]. Available: https://indico.cern.ch/event/1316311/contributions/5827458/

[68] I. Brewer, R. Caputo, M. Negro, R. Leys, C. Kierans, I. Peric, J. Metcalfe, and J. Perkins, "Astropix: Investigating the potential of silicon pixel sensors in the future of gamma-ray astrophysics," 2021.

[69] H. Klest, "Calorimetry for the epic experiment," Slides presented at The XXXI International Workshop on Deep Inelastic Scattering and Related Subjects (DIS2024), Grenoble, France, Apr 2024.

[70] C. A. Aidala *et al.*, "Design and Beam Test Results for the 2-D Projective sPHENIX Electromagnetic Calorimeter Prototype," *IEEE Trans. Nucl. Sci.*, vol. 68, no. 2, pp. 173–181, 2021.

[71] A. Adare *et al.*, "An Upgrade Proposal from the PHENIX Collaboration," Jan 2015.

[72] F. Bock *et al.*, "Design and simulated performance of calorimetry systems for the ECCE detector at the electron ion collider," *Nucl. Instrum. Meth. A*, vol. 1055, p. 168464, 2023.

[73] T. Frisson, V. Boudry, A. Specka, and F. Moreau, "Luminosity measurement in h1," *Nuclear Instruments and Methods in Physics Research Section A: Accelerators, Spectrometers, Detectors and Associated Equipment*, vol. 640, no. 1, pp. 49–53, 2011. [Online]. Available: https://www.sciencedirect.com/science/article/pii/S0168900210030226

[74] L. Adamczyk *et al.*, "Measurement of the luminosity in the zeus experiment at hera ii," *Nuclear Instruments and Methods in Physics Research Section A: Accelerators, Spectrometers, Detectors and Associated Equipment*, vol. 744, pp. 80–90, 2014. [Online]. Available: https://www.sciencedirect.com/science/article/pii/S0168900214001041

[75] T. Haas and V. Makarenko, "Precision calculation of processes used for luminosity measurement at the ZEUS experiment," *Eur. Phys. J. C*, vol. 71, p. 1574, 2011.

[76] A. Jentsch, "Forward detection in epic," Slides presented at the workshop "Towards improved hadron femtography with hard exclusive reactions 2023", Jefferson Lab, 7–11 Aug, 2023.

[77] A. Jentsch, "Physics Opportunities in the Far-forward Region at the Future Electron–Ion Collider," *Acta Phys. Polon. Supp.*, vol. 16, no. 7, pp. 7–A13, 2023.

[78] "Letter of Intent: A Forward Calorimeter (FoCal) in the ALICE experiment," Jun 2020.

[79] R. Turchetta, N. Guerrini, and I. Sedgwick, "Large area cmos image sensors," *Journal of Instrumentation*, vol. 6, no. 01, p. C01099, Jan 2011. [Online]. Available: https://dx.doi.org/10.1088/1748-0221/6/01/C01099

[80] J. Sonneveld, "ITS3: A truly cylindrical inner tracker for ALICE," *PoS*, vol. HardProbes2023, p. 077, 2024.

[81] I. Giomataris, P. C. Rebourgeard, J. P. Robert, and G. Charpak, "Micromegas: a high-granularity position-sensitive gaseous detector for high particle-flux environments," *Nucl. Instrum. Methods Phys. Res., A*, vol. 376, no. 1, pp. 29–35, 1996. [Online]. Available: https://cds.cern.ch/record/299159

[82] G. Bencivenni, R. De Oliveira, G. Morello, and M. P. Lener, "The micro-Resistive WELL detector: a compact spark-protected single amplification-stage MPGD. The Resistive-WELL detector: a compact spark-protected single amplification-stage MPGD," *JINST*, vol. 10, p. P02008, 2016. [Online]. Available: https://cds.cern.ch/record/2238861

[83] A. Acker *et al.*, "The CLAS12 Micromegas Vertex Tracker," *Nucl. Instrum. Meth. A*, vol. 957, p. 163423, 2020.

[84] H. L. O. Wennlöf, "Development of a silicon vertex tracker for the electron-ion collider," Ph.D. dissertation, University of Birmingham, May 2021.

[85] R. L. Gluckstern, "Uncertainties in track momentum and direction, due to multiple scattering and measurement errors," *Nucl. Instrum. Meth.*, vol. 24, pp. 381–389, 1963.

[86] F. Ragusa and L. Rolandi, "Tracking at LHC," *New J. Phys.*, vol. 9, p. 336, 2007.

[87] X. Ai *et al.*, "A Common Tracking Software Project," *Comput. Softw. Big Sci.*, vol. 6, no. 1, p. 8, 2022.

[88] P. Gessinger-Befurt, "Development and improvement of track reconstruction software and search for disappearing tracks with the atlas experiment," May 2021, available from INIS: http://inis.iaea.org/search/search.aspx?orig_q=RN:53004640; Available from INIS in electronic form. Also available from: http://dx.doi.org/10.25358/openscience-5901.

[89] P. V. C. Hough, "Machine Analysis of Bubble Chamber Pictures," *Conf. Proc. C*, vol. 590914, pp. 554–558, 1959.

[90] B. Denby, "Neural networks and cellular automata in experimental high energy physics," *Computer Physics Communications*, vol. 49, no. 3, pp. 429–448, 1988. [Online]. Available: https://www.sciencedirect.com/science/article/pii/0010465588900045

[91] S. Farrell *et al.*, "The hep.trkx project: deep neural networks for hl-lhc online and offline tracking," *EPJ Web Conf.*, vol. 150, p. 00003, 2017. [Online]. Available: https://doi.org/10.1051/epjconf/201715000003

[92] R. E. Kalman, "A New Approach to Linear Filtering and Prediction Problems," *Journal of Basic Engineering*, vol. 82, no. 1, pp. 35–45, March 1960. [Online]. Available: https://doi.org/10.1115/1.3662552

[93] R. Frühwirth and A. Strandlie, *Pattern Recognition, Tracking and Vertex Reconstruction in Particle Detectors*, ser. Particle Acceleration and Detection. Springer, 11 2020.

[94] C. Pinkenburg *et al.*, "Fun4All," Slides presented at the EIC Software Meeting, September 2015. [Online]. Available: https://www.jlab.org/conferences/eicsw/

[95] K. F. Read, *The Phenix Experiment*. Boston, MA: Springer US, 1999, pp. 91–99. [Online]. Available: https://doi.org/10.1007/978-1-4615-4719-8_9

[96] S. Agostinelli *et al.*, "GEANT4: A simulation toolkit," *Nucl. Instrum. Meth.*, vol. A506, pp. 250–303, 2003.

[97] R. Brun and F. Rademakers, "Root - an object oriented data analysis framework," in *AIHENP'96 Workshop, Lausane*, vol. 389, 1996, pp. 81–86.

[98] C. Höppner, S. Neubert, B. Ketzer, and S. Paul, "A novel generic framework for track fitting in complex detector systems," *Nuclear Instruments and Methods in Physics Research Section A: Accelerators, Spectrometers, Detectors and Associated Equipment*, vol. 620, no. 2–3, p. 518–525, Aug. 2010. [Online]. Available: http://dx.doi.org/10.1016/j.nima.2010.03.136

[99] M. Frank, F. Gaede, C. Grefe, and P. Mato, "DD4hep: A detector description toolkit for high energy physics experiments," vol. 513, no. 2, p. 022010, Jun 2014. [Online]. Available: https://doi.org/10.1088/1742-6596/513/2/022010

[100] W. Deconinck *et al.*, "Eicrecon: v1.12.0," https://doi.org/10.5281/zenodo.10946715, Apr. 2024.

[101] A. Salzburger *et al.*, "A common tracking software (acts)," https://doi.org/10.5281/zenodo.5707179, 2021.

[102] H. T. Klest, "A Compact TPC for the sPHENIX Experiment," *J. Phys. Conf. Ser.*, vol. 2374, no. 1, p. 012147, 2022.

[103] "Energy spectrum of synrad+ events," ePIC wiki page, May 2024. [Online]. Available: https://wiki.bnl.gov/EPIC/index.php?title=Synchrotron_Radiation

[104] L. Greiner, "Estimates for material in for eic si structures/services," Slides presented at the 2nd EIC Yellow Report Workshop at Pavia University, May 2020. [Online]. Available: https://indico.bnl.gov/event/8231/contributions/37955/

[105] L. Greiner, "A possible method for adding services load to the eic simulations," Slides presented at the 1st EIC Yellow Report Workshop at Temple University, March 2020. [Online]. Available: https://indico.bnl.gov/event/7449/contributions/36038/

[106] L. Greiner, "Design of mechanics and services," Slides presented at EIC Silicon Consortium meeting, July 2021. [Online]. Available: https://indico.bnl.gov/event/12512/

[107] G. Aglieri, "Developments of stitched monolithic pixel sensors towards the alice its3," *Nuclear Instruments and Methods in Physics Research Section A: Accelerators, Spectrometers, Detectors and Associated Equipment*, vol. 1049, p. 168018, 2023. [Online]. Available: https://www.sciencedirect.com/science/article/pii/S0168900223000086

[108] J. Liu, "Alice its3: a truly cylindrical vertex detector based on bent, wafer-scale stitched cmos sensors," Presented at the 13th International "Hiroshima" Symposium on the Development and Application of Semiconductor Tracking Detectors (HSTD13), Vancouver, Canada, Dec 2023.

[109] G. Aglieri *et al.*, "Monolithic active pixel sensor development for the upgrade of the alice inner tracking system," *Journal of Instrumentation*, vol. 8, no. 12, p. C12041, Dec 2013. [Online]. Available: https://dx.doi.org/10.1088/1748-0221/8/12/C12041

[110] B Abelev et al and (The ALICE Collaboration), "Technical design report for the upgrade of the alice inner tracking system," *Journal of Physics G: Nuclear and Particle Physics*, vol. 41, no. 8, p. 087002, Jul 2014. [Online]. Available: https://dx.doi.org/10.1088/0954-3899/41/8/087002

[111] M. Tornago *et al.*, "Resistive ac-coupled silicon detectors: Principles of operation and first results from a combined analysis of beam test and laser data," *Nuclear Instruments and Methods in Physics Research Section A: Accelerators, Spectrometers, Detectors and Associated Equipment*, vol. 1003, p. 165319, Jul. 2021. [Online]. Available: http://dx.doi.org/10.1016/j.nima.2021.165319

[112] X. Li, "Latest vertex and tracking detector developments for the future Electron-Ion Collider," in *31st International Workshop on Vertex Detectors*, 5 2023.

[113] M. Posik, "Report on erd6 and erd22 activities," Slides presented at the 1st EIC Yellow Report Workshop at Temple University, March 2020. [Online]. Available: https://indico.bnl.gov/event/7449/contributions/35957/

[114] G. Bencivenni, G. Felici, M. Gatta, M. Giovannetti, G. Morello, M. P. Lener, R. de Oliveira, A. Ochi, and E. Tskhadadze, "High space resolution μ-rwell for high rate applications," *Journal of Physics: Conference Series*, vol. 1498, no. 1, p. 012003, apr 2020. [Online]. Available: https://dx.doi.org/10.1088/1742-6596/1498/1/012003

[115] ANSYS. (2016) Ansys fluent - cfd software — ansys. [Online]. Available: http://www.ansys.com/products/fluids/ansys-fluent

[116] B. Eng, "Eic beryllium section thermal analysis status," Slides presented at EIC Silicon Consortium meeting, Jun 2022. [Online]. Available: https://indico.bnl.gov/event/16164/

[117] N. Apadula, "Air cooling studies and beam pipe bakeout studies," Slides presented at EIC Silicon Consortium meeting, Feb 2023. [Online]. Available: https://indico.bnl.gov/event/18525

[118] R. Rajput-Ghoshal, "Detector solenoid design overview," Slides presented at the January 2024 ePIC Collaboration Meeting, Jan 2024. [Online]. Available: https://indico.bnl.gov/event/20473/contributions/84201/

[119] J. Adam *et al.*, "Accelerator and beam conditions critical for physics and detector simulations for the electron-ion collider," Internal Note, Jul 2021. [Online]. Available: https://github.com/eic/documents/blob/master/reports/general/Note-Simulations-BeamEffects.pdf

[120] P. Jones, "Study of disks tiling," Slides presented at EIC Silicon Consortium meeting, Sep 2022. [Online]. Available: https://indico.bnl.gov/event/17073/

[121] C. Bierlich *et al.*, "A comprehensive guide to the physics and usage of PYTHIA 8.3," *SciPost Phys. Codeb.*, vol. 2022, p. 8, 2022.

[122] "Radiation doses," ePIC wiki page, Jun 2024. [Online]. Available: https://wiki.bnl.gov/EPIC/index.php?title=Radiation_Doses

[123] "Starsim : Star detector simulation tool," Jun 2024. [Online]. Available: https://www.star.bnl.gov/public/comp/simu/newsite/gstar/gstar.html

[124] T. A. Gabriel, J. D. Amburgey, and B. L. Bishop, "CALOR: A Monte Carlo Program Package for the Design and Analysis of Calorimeter Systems," Apr 1977.

[125] "Displacement damage in silicon," Aug 2000. [Online]. Available: https://rd50.web.cern.ch/NIEL/

[126] L. Musa, "Letter of Intent for an ALICE ITS Upgrade in LS3," CERN, Geneva, Tech. Rep., 2019. [Online]. Available: http://cds.cern.ch/record/2703140

[127] M. Arratia, D. Britzger, O. Long, and B. Nachman, "Reconstructing the kinematics of deep inelastic scattering with deep learning," *Nuclear Instruments and Methods in Physics Research Section A: Accelerators, Spectrometers, Detectors and Associated Equipment*, vol. 1025, p. 166164, Feb. 2022. [Online]. Available: http://dx.doi.org/10.1016/j.nima.2021.166164

[128] M. Diefenthaler, A. Farhat, A. Verbytskyi, and Y. Xu, "Deeply learning deep inelastic scattering kinematics," *The European Physical Journal C*, vol. 82, no. 11, Nov. 2022. [Online]. Available: http://dx.doi.org/10.1140/epjc/s10052-022-10964-z

[129] A. Gelman, J. Carlin, H. Stern, D. Dunson, A. Vehtari, and D. Rubin, *Bayesian Data Analysis, Third Edition*, ser. Chapman & Hall/CRC Texts in Statistical Science. Taylor & Francis, 2013. [Online]. Available: https://books.google.co.uk/books?id=ZXL6AQAAQBAJ

[130] J. Schwartz, "Experimental Study of Initial State Radiative Events at HERA and a Measurement of the Proton Longitudinal Structure Function," Ph.D. dissertation, McGill U., 2011.

[131] A. Caldwell, D. Kollár, and K. Kröninger, "Bat – the bayesian analysis toolkit," *Computer Physics Communications*, vol. 180, no. 11, p. 2197–2209, Nov. 2009. [Online]. Available: http://dx.doi.org/10.1016/j.cpc.2009.06.026

[132] S. Brooks, "Markov chain monte carlo method and its application," *Journal of the Royal Statistical Society: Series D (The Statistician)*, vol. 47, no. 1, pp. 69–100, January 2002. [Online]. Available: https://doi.org/10.1111/1467-9884.00117

[133] F. Beaujean, A. Caldwell, D. Greenwald, K. Kröninger, and O. Schulz, "Bat release, version 1.0.0," Jul. 2018. [Online]. Available: https://doi.org/10.5281/zenodo.1322675

[134] S. Maple, "Kinematic reconstruction," Slides presented at the January 2023 ePIC Collaboration Meeting, Jan 2023. [Online]. Available: https://indico.bnl.gov/event/17621/contributions/71753

[135] R. Aggarwal and A. Caldwell, "Kinematic fitting of neutral current events in deep inelastic ep collisions." *JINST*, vol. 17, no. 09, p. P09035, 2022.

[136] I. Abt *et al.*, "The H1 detector at HERA," *Nucl. Instrum. Meth. A*, vol. 386, pp. 310–347, 1997.

[137] D. Pitzl *et al.*, "The H1 silicon vertex detector," *Nucl. Instrum. Meth. A*, vol. 454, pp. 334–349, 2000.

[138] B. Andrieu *et al.*, "Results from pion calibration runs for the H1 liquid argon calorimeter and comparisons with simulations," *Nucl. Instrum. Meth. A*, vol. 336, pp. 499–509, 1993.

[139] B. Andrieu *et al.*, "Beam tests and calibration of the H1 liquid argon calorimeter with electrons," *Nucl. Instrum. Meth. A*, vol. 350, pp. 57–72, 1994.

[140] G. A. Schuler and H. Spiesberger, "DJANGO: the interface for the event generators HERACLES and LEPTO," in *Physics at HERA Proceedings Vol 3*, G. Ingelman, Ed., Germany, 1992, p. 422.

[141] A. Kwiatkowski, H. Spiesberger, and H. J. Mohring, "Heracles: An Event Generator for *ep* Interactions at HERA Energies Including Radiative Processes: Version 1.0," *Comput. Phys. Commun.*, vol. 69, pp. 155–172, 1992.

[142] L. Lönnblad, "Ariadne version 4 — a program for simulation of qcd cascades implementing the colour dipole model," *Computer Physics Communications*, vol. 71, no. 1, pp. 15–31, 1992. [Online]. Available: https://www.sciencedirect.com/science/article/pii/001046559290068A

[143] R. Brun, F. Bruyant, M. Maire, A. C. McPherson, and P. Zanarini, *GEANT 3: user's guide Geant 3.10, Geant 3.11; rev. version.* Geneva: CERN, 1987. [Online]. Available: https://cds.cern.ch/record/1119728

[144] F. D. Aaron *et al.*, "Determination of the Integrated Luminosity at HERA using Elastic QED Compton Events," *Eur. Phys. J. C*, vol. 72, p. 2163, 2012, [Erratum: Eur.Phys.J.C 74, 2733 (2014)].

[145] V. Andreev *et al.*, "Measurement of multijet production in *ep* collisions at high Q^2 and determination of the strong coupling α_s," *Eur. Phys. J. C*, vol. 75, no. 2, p. 65, 2015.

[146] L. Demortier and L. Lyons. (2002) Everything you always wanted to know about pulls. [Online]. Available: https://hep-physics.rockefeller.edu/~luc/technical_reports/cdf5776_pulls.pdf

[147] F. D. Aaron *et al.*, "Measurement of the Inclusive *ep* Scattering Cross Section at Low Q^2 and x at HERA," *Eur. Phys. J. C*, vol. 63, pp. 625–678, 2009.

[148] M. Klein and R. Yoshida, "Collider Physics at HERA," *Prog. Part. Nucl. Phys.*, vol. 61, pp. 343–393, 2008.